



**University of
Leicester**

***XMM-Newton* observations of ultraluminous
X-ray sources and their host galaxies**

Ann-Marie Stobbart

Supervisors:

Robert Warwick

Tim Roberts

Thesis submitted for the degree of
Doctor of Philosophy
at the University of Leicester.

X-ray & Observational Astronomy Group
Department of Physics and Astronomy
University of Leicester

December 14, 2006

UMI Number: U218901

All rights reserved

INFORMATION TO ALL USERS

The quality of this reproduction is dependent upon the quality of the copy submitted.

In the unlikely event that the author did not send a complete manuscript and there are missing pages, these will be noted. Also, if material had to be removed, a note will indicate the deletion.



UMI U218901

Published by ProQuest LLC 2013. Copyright in the Dissertation held by the Author.
Microform Edition © ProQuest LLC.

All rights reserved. This work is protected against
unauthorized copying under Title 17, United States Code.



ProQuest LLC
789 East Eisenhower Parkway
P.O. Box 1346
Ann Arbor, MI 48106-1346

Declaration

I hereby declare that no part of this thesis has been previously submitted to this or any other University as part of the requirement for a higher degree. The work described herein was conducted by the undersigned except for contributions from colleagues as acknowledged in the text.

Ann-Marie Stobbart

December 2006

***XMM-Newton* observations of ultraluminous X-ray sources and their host galaxies**

Ann-Marie Stobbart

ABSTRACT

X-ray observations of nearby galaxies have shown them to be extended and complex sources of X-ray emission. The excellent sensitivity of the current generation of missions is now permitting detailed studies of their discrete X-ray source populations as well as diffuse thermal emission from hot interstellar gases. This thesis presents X-ray observations from the *XMM-Newton* Space Observatory of a variety of nearby galaxies, and some of the most luminous X-ray sources they host.

The work begins with an investigation into the properties of a luminous extra-nuclear X-ray source in the Magellanic-type galaxy NGC 55. The observed X-ray luminosity of this source ($> 10^{39} \text{ erg s}^{-1}$) places it in the ultraluminous X-ray source (ULX) regime, a class of sources that may host a new, ‘*intermediate-mass*’ class of black-holes, though this interpretation is currently being hotly debated. This particular source exhibits complex and rapid variability including a gradual increase in flux and pronounced dips in its X-ray light curve. In addition, the spectral analysis revealed an unusual X-ray spectral shape with curvature at high energies ($> 2 \text{ keV}$).

Detailed studies of the X-ray properties of NGC 55 as well as the nearby spiral galaxy NGC 4945 are then presented. The X-ray emission from NGC 55 is dominated by its discrete X-ray source population which, on the basis of an X-ray colour classification scheme, largely consists of accreting X-ray binaries. The galaxy also displays evidence of soft diffuse X-ray emission in and around its disc. NGC 4945 is a much more energetic galaxy, hosting a heavily obscured active nucleus as well as a nuclear starburst. The galaxy has a more luminous discrete X-ray source population than NGC 55 and shows clear evidence for diffuse X-ray emission along its disc as well as a possible outflow perpendicular to the galactic plane. The observed luminosities of these galaxies are consistent with the luminosities predicted on the basis of their star-formation rates.

Finally, a detailed analysis of the deepest *XMM-Newton* observations of a sample of ULXs is then presented with the aim of addressing their true underlying nature. Interestingly, this work provides new evidence that the high energy spectral curvature seen first in the NGC 55 ULX may be prevalent throughout this class. Such curvature may be evidence for a cool optically thick Comptonising corona in these systems which is unlike most Galactic binaries, and poses new challenges to the intermediate-mass black-hole interpretation for these systems.

Publications

A significant amount of work contained in this thesis has been published in the following papers:

Chapter 3—Stobbart, A.-M., Roberts, T. P., Warwick, R. S., 2004, “**A dipping black hole X-ray binary candidate in NGC 55**”, *MNRAS*, 351, 1063

Chapter 4—Stobbart, A.-M., Roberts, T. P., Warwick, R. S., 2006, “**The X-ray properties of the dwarf Magellanic-type galaxy NGC 55**”, *MNRAS*, 370, 25

Chapter 6—Stobbart, A.-M., Roberts, T. P., Wilms, J., 2006, “**XMM-Newton observations of the brightest ultraluminous X-ray sources**”, *MNRAS*, 368, 397

Acknowledgements

I would like to say thank you to the following people for all their help and support throughout my time working on this PhD.

Firstly, I would like to thank my 'official' supervisor Bob Warwick for providing incredibly thorough help and assistance in so many aspects of this thesis. Thanks for this must also go to my 'unofficial' supervisor Tim Roberts, who has probably been harassed with more questions than any supervisor would like. I am extremely grateful for the patience you have both shown in explaining things to me multiple times, and for your consistent guidance which has been essential in completing this research.

I would also like to thank the brilliant office mates that I've shared my days with over the last few years; from the early days of Pam, Leigh, Levan and Simpson to the latest recruits of Becks, Jonny and Silvia, you've all made it a lot more enjoyable to come to work! Thanks especially to Leigh who helped me find my feet with the joys of SAS, XSPEC and Q, and more importantly for her friendship throughout. I also thank Andrew for making sure the days were never as dull (or as productive) as they might otherwise have been. Thanks also to Becks for the many laughs and conversations which were much needed in the last few months of writing this thesis!

I would also like to thank my friends at Carisbrooke who have helped to alleviate the stress of thesis writing with lots of tennis, food and parties. Thanks especially to Fiona, Rachel and Louisa for being excellent tennis partners and friendly competitors throughout. In particular I would like to thank Louisa who has been a great friend since the early days of undergraduate and the best pool partner around.

Of course I owe my greatest thanks to the many members of my family who have helped and encouraged me every step of the way. Thanks especially to my Mam, Dad and sisters Victoria and Shannon for all your love and support. A very special thanks must also go to my Granda, who always takes care of me and still makes sure I have a car full of food after every visit home!

And finally, enormous thanks go to Mark, for your friendship, encouragement and invaluable support in everything over the last few years. You've been amazing.

Dedication

This thesis is dedicated to the memory of my grandparents, Sally & Alan Cowell and especially to Mary Stobbart for her unwavering belief in me and who would no doubt have taken this to the bingo to show everyone she could!

CONTENTS

1	Introduction	1
1.1	A brief history of X-ray astronomy	1
1.2	X-ray physical processes	5
1.2.1	Fundamental Processes	6
1.2.2	Power source	12
1.3	X-rays from galaxies	14
1.3.1	Active Galactic Nuclei	18
1.3.2	Diffuse X-ray emission	20
1.3.3	Supernova remnants	21
1.3.4	X-ray binaries	23
1.3.5	Ultraluminous X-ray sources	26
1.4	Overview of this thesis	30

2	Instrumentation	31
2.1	The <i>XMM-Newton</i> Space Observatory	31
2.1.1	European Photon Imaging Cameras	33
2.2	Comparison with other X-ray missions	37
2.3	Data reduction	39
2.3.1	Filtering event lists	40
2.3.2	Filtering high background flaring	40
2.3.3	Images, light curves and spectra	41
2.3.4	Source detection	42
3	A dipping BHB	47
3.1	Introduction	47
3.2	The XMM-Newton observations and preliminary data analysis	49
3.3	The X-ray properties of XMMU J001528.9-391319	51
3.3.1	X-ray light curve	51
3.3.2	X-ray spectra	54
3.4	Discussion	59
3.4.1	XMMU J001528.9-391319 as a BHB candidate	59
3.4.2	XMMU J001528.9-391319 as a dipping BHB candidate	62
3.5	Conclusions	64

4	The X-ray properties of NGC 55	65
4.1	Introduction	65
4.2	Observations and data screening	67
4.3	X-ray Sources in the Field of NGC 55	67
4.3.1	The source catalogue	67
4.3.2	X-ray sources associated with NGC 55	75
4.3.3	Cross-correlation with other catalogues	76
4.4	The brightest discrete X-ray sources	79
4.4.1	Light curves	80
4.4.2	X-ray Spectra	82
4.5	X-ray colours	87
4.6	Residual disc emission	93
4.7	Discussion	99
4.7.1	The brightest sources in NGC 55	99
4.7.2	NGC 55 - a typical Magellanic-type galaxy	101
4.8	Summary	103
5	The X-ray properties of NGC 4945	105
5.1	Introduction	105
5.2	Observations and data analysis	108

5.3	X-ray Sources in the Field of NGC 4945	109
5.3.1	Source catalogue	109
5.3.2	X-ray sources associated with NGC 4945	114
5.3.3	Cross correlation	115
5.4	The brightest discrete X-ray sources	117
5.4.1	Light curves	117
5.4.2	X-ray Spectra	118
5.5	X-ray colours	125
5.6	Residual disc emission	126
5.7	Discussion	132
5.7.1	The bright sources	132
5.7.2	Comparison with NGC 55	133
5.8	Summary	135
6	<i>XMM</i> observations of the brightest ULXs	137
6.1	Introduction	137
6.2	The Sample	141
6.3	Observations and data analysis	143
6.4	Spectral properties	146
6.4.1	Simple models	146

6.4.2	Power-law + MCD model	154
6.4.3	Dual thermal models	159
6.4.4	Why do Ho II X-1 and NGC 4395 X-1 not conform?	160
6.4.5	Physical models	164
6.5	L_X - kT relationship	167
6.6	Discussion	169
6.7	Conclusions	173
7	Conclusions	174
7.1	Overview	174
7.2	Thesis highlights	175
7.2.1	A dipping black-hole X-ray binary candidate in NGC 55	175
7.2.2	The X-ray properties of the dwarf Magellanic-type galaxy NGC 55	176
7.2.3	The X-ray properties of the spiral galaxy NGC 4945	177
7.2.4	<i>XMM-Newton</i> observations of the brightest ULXs	177
7.3	Future Work	178
7.3.1	Future X-ray missions	181
	References	186

Chapter 1

Introduction

1.1 A brief history of X-ray astronomy

The study of the highest energy processes in the Universe, *i.e.*, those that produce/involve X-ray and γ -ray radiation, is a relatively new science. This is because the Earth's atmosphere is opaque to high energy radiation, requiring X-ray observatories to be placed high above the Earth's surface. Initial attempts at X-ray astronomy involved launching radiation detectors onboard sounding rockets and high altitude balloons, which could take them above most of the atmosphere. In 1949, one such rocket experiment discovered that our Sun is a source of X-rays. However, the main disadvantage of rocket flights is that they can only spend a few minutes above the atmosphere before falling back to Earth. The balloon flights were able to carry instruments up to ~ 40 – 50 km above sea level (*i.e.*, above most of the atmosphere) and were able to operate for longer than the initial rocket experiments. However, even at these altitudes, much of the X-ray spectrum is absorbed and only energetic X-rays (> 35 keV) can be detected. Although the Sun had been discovered to emit X-rays, detectable emission from anything else was not expected (it was thought that even the next nearest stars would be too far away and thus too faint). However, a rocket flight experiment launched in 1962 by a group at American Science and Engineering successfully detected the first cosmic source of X-ray emission (which became known as Sco X-1; the first source in the constellation of Scorpius). This came as something of a surprise as the group had officially developed the X-ray detectors to search for X-ray emission from the surface of the Moon (Giacconi et al., 1962). The mission was also the first to detect the X-ray background – a

diffuse background of X-ray emission emanating across the whole sky. These new discoveries lead to an explosion of study in X-ray astronomy and to date there have been 32 dedicated scientific missions launched into orbit, 7 of which are still active, with several more planned for the future. Such X-ray telescopes have revolutionised our current understanding of the high energy Universe.

The first in a long line of dedicated X-ray astronomy satellites was the NASA sponsored *UHURU* mission (also known as the Small Astronomical Satellite 1: SAS-1), which was launched on 12th December 1970. *UHURU* extended the time of observation from minutes to years and provided the first comprehensive all sky survey (Giacconi et al., 1971). The *UHURU* Catalog contains 339 objects, consisting primarily of binary stellar systems, supernova remnants (SNRs), Seyfert galaxies and clusters of galaxies.

This satellite was followed by a succession of other X-ray observatories in the 1970s, which include Ariel 5, SAS-3, OSO-8, and HEAO-1. These missions discovered X-ray bursts, numerous pulsars, and obtained the first detailed X-ray spectra. Particularly important missions were the NASA series of very large scientific payloads called High Energy Astrophysical Observatories (HEAO) beginning in 1977 with HEAO-1. This was the first major observatory to be flown and yielded a catalog of 842 point sources (Wood et al., 1984), allowed the first comprehensive measurement of the diffuse X-ray background spectrum and performed time variability studies on millisecond time scales. NASA's follow-up mission HEAO-2 (also known as the *Einstein* Observatory; Giacconi et al. 1979) launched in 1978, proved to be the most revolutionary of the HEAO programme. *Einstein* carried the largest X-ray telescope ever built and was the first fully imaging X-ray telescope placed in orbit. It used a grazing incidence telescope over the 0.2–4 keV energy range, which provided a huge increase in sensitivity with *Einstein* observing sources 10^4 times fainter than *UHURU*. *Einstein* also provided improved positional accuracy (from $<1'$ to $\sim \text{few}''$) and resolved numerous X-ray sources in M31 and the Magellanic Clouds (van Speybroeck et al. 1979 and Long et al. 1981 respectively). It was also the first observatory with the capability to resolve extended objects such as X-ray emitting gas in galaxies and clusters of galaxies.

During the 1980s the European, Russian, and Japanese space agencies continued to launch successful X-ray astronomy missions including the European X-ray Observatory Satellite (*EXOSAT*), *Granat* (the *Kvant* module of the Mir space station), *Tenma* and *Ginga*. These missions were more modest in scale than the previous HEAO program and were directed towards in-depth studies of known phenomena.

Further great advances were made in the 1990s with the launch of satellites that provided an unprecedented view of the X-ray Universe. June 1990 saw the launch of *ROSAT*, a cooperative program between Germany, the United States and the United Kingdom (for more details see § 2.2). *ROSAT* carried two imaging telescopes operating in the soft X-ray (0.1–2.4 keV) and extreme ultraviolet (EUV: 0.06–0.2 keV) ranges, and discovered 125,000 X-ray and 479 EUV sources. In addition, the *ROSAT* All Sky Survey (RASS) mapped $\sim 98\%$ of the sky in the $\frac{1}{4}$ keV, $\frac{3}{4}$ keV and 1.5 keV bands (*e.g.*, see Snowden et al. 1995), revealing considerable structure that had not been previously observed (Fig. 1.1). Also, deep *ROSAT* surveys resolved 70–80% of the 0.5–2 keV X-ray background into discrete point sources (Hasinger et al., 1998).

ASCA, a joint Japanese-American project, was launched in 1993 and was the first satellite to use CCD detectors for X-ray astronomy, with moderate imaging optics up to 10 keV. The mission was primarily designed to study the detailed spectra of X-ray sources, *e.g.*, SNRs, active galactic nuclei (AGN) and galaxy clusters. A key result from the *ASCA* mission was that it provided the first evidence of gravitational redshift due to the strong gravitational field around a black-hole (Tanaka et al., 1995).

Another important satellite of this decade was the Rossi X-ray Timing Explorer (*RXTE*) which was launched in December 1995. *RXTE* does not have focusing X-ray mirrors but was instead designed to study time variability in the emission from X-ray sources (*e.g.*, white-dwarf stars, X-ray binaries [XRBs], neutron stars, pulsars, and black-holes) over a wide range of X-ray energies (2–250 keV) and timescales (milliseconds–years). While *RXTE* was originally designed for a required lifetime of 2 yrs with a goal of 5 yrs, it has now been operational for more than 10 yrs and is still performing well. During this time *RXTE* has identified many X-ray transients and played a vital role in the discovery and study of accretion-driven millisecond X-ray pulsars (*e.g.*, Wijnands & van der Klis 1998) and kilohertz quasi-periodic oscillations (kHz QPOs; *e.g.*, Strohmayer et al. 1996; van der Klis et al. 1996).

BeppoSax was launched soon afterwards in April 1996 and was a major program of the Italian Space Agency (ASI) with participation from the Netherlands Agency for Aerospace Programs (NIVR). It was the first X-ray mission with a scientific payload covering more than three decades of energy (0.1–300 keV) with a relatively large effective area, medium energy resolution and imaging capabilities in the range of 0.1–10 keV. *BeppoSax* operated for 6 years and proved to be especially useful in the field of gamma-ray burst (GRB) research¹. In particular, this mission determined GRB positions with an un-

¹GRBs are brief, intense flashes of γ -rays, going off at a rate of about one per day all over the sky.

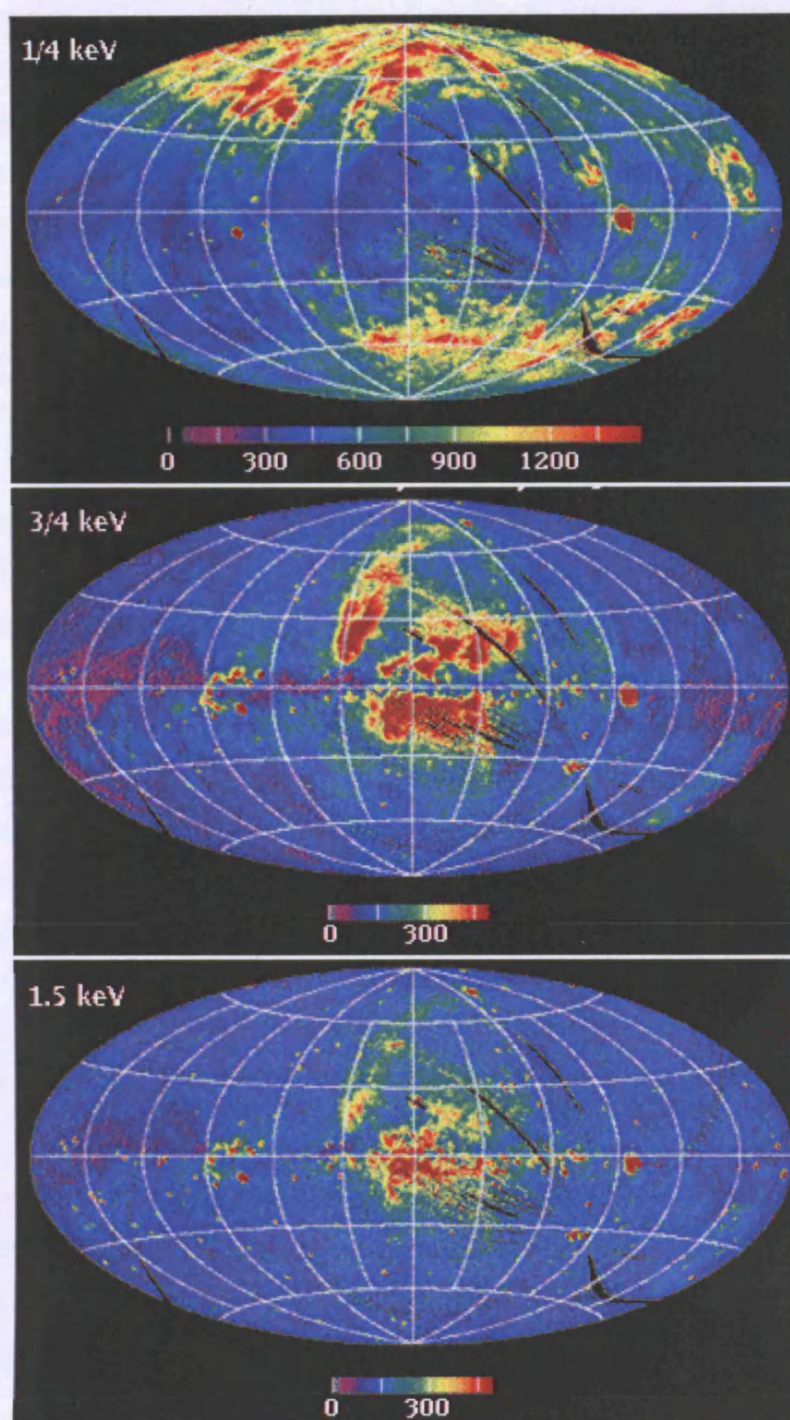


Figure 1.1: *ROSAT* All Sky Survey (RASS) maps in three energy bands: $\frac{1}{4}$ keV, $\frac{3}{4}$ keV and 1.5 keV. The colour scale shows the intensity measured in units of $\times 10^{-6}$ counts s^{-1} arcmin $^{-2}$. Images available from <http://image.gsfc.nasa.gov/docs/features/news/02dec96.html>.

precedented precision, which enabled the first ever detection of a GRB X-ray afterglow (GRB 970228; Costa et al. 1997). In addition, van Paradijs et al. (1997) reported the detection of the first GRB optical afterglow for this source, which appeared to be associated with a faint galaxy. This suggested a cosmological origin for GRBs, consistent with previous observations (with the BATSE instrument on-board the *Compton Gamma-Ray Observatory*) which showed an isotropic distribution of these events. However, by the time of its discovery the afterglow had become too faint to detect its spectrum and definitively prove this. The first confirmation of their extragalactic nature actually came with the discovery of another *BeppoSax* GRB—GRB 970508, which was identified with a dwarf galaxy at $z \sim 0.835$ (Metzger et al. 1997a,b).

X-ray astronomy has made even further progress in recent years due to the larger effective areas and improved spatial and spectral resolutions offered by *Chandra* and *XMM-Newton*, both launched in 1999. *Chandra's* superb imaging resolution ($<1''$) is complemented by the large collecting area of *XMM-Newton* and together these observatories have revolutionised the field; *e.g.*, they have collectively provided the first high-resolution X-ray spectra of a wealth of astrophysical sources, significantly advanced the studies of discrete X-ray populations within galaxies, permitted detailed studies of the structure of SNRs and expanded galaxy and cluster samples to higher redshifts. Some of these examples are discussed later in more detail. Fig. 1.2 shows some examples of the variety of astrophysical sources looked at by these observatories.

1.2 X-ray physical processes

There are several mechanisms that can occur in astrophysical objects which lead to the production of X-rays. Each physical process produces a characteristic spectral shape which can be examined to gain an insight into the nature of the X-ray source. A brief description of the X-ray production mechanisms mentioned in this thesis are described below.

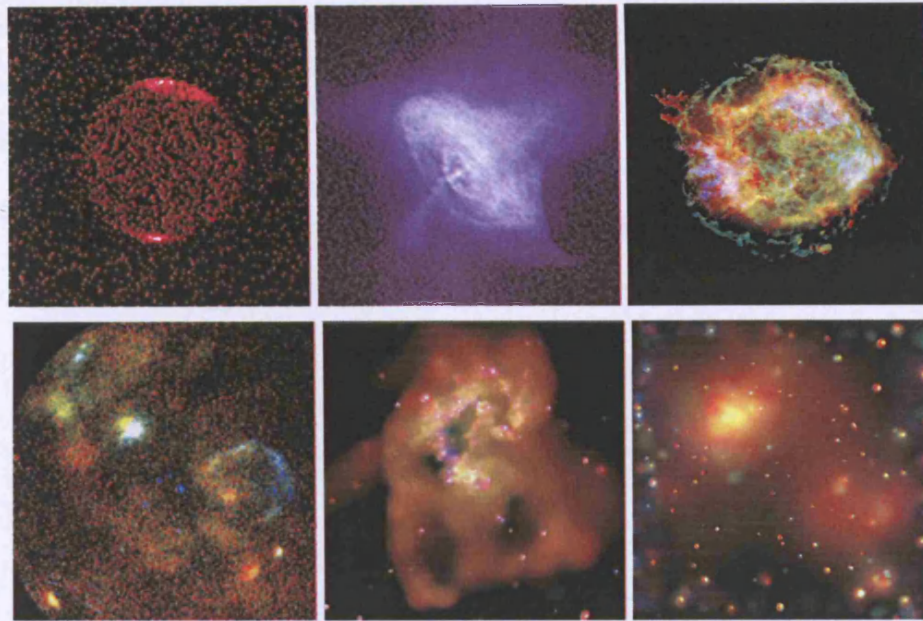


Figure 1.2: *Top panel from left to right: Chandra images of Jupiter, the Crab Nebula and the SNR Cassiopeia A (credit: NASA/CXC/SWRI/G.R.Gladstone et al., NASA/CXC/SAO, NASA/CXC/PSU/S.Park et al. and NASA/CXC/GSFC/U.Hwang et al. respectively). Bottom panel from left to right: An XMM-Newton image of LMC 30 Dor, a Chandra image of the Antennae galaxies and a Chandra image of the galaxy cluster Abell 2125 (credit: the University of Leicester, NASA/CXC/SAO/G. Fabbiano et al. and NASA/CXC/UMass/Q.D.Wang et al. respectively). Images available from <http://chandra.harvard.edu/photo/> and <http://astro.sci.muni.cz/pub/xmm2000>.*

1.2.1 Fundamental Processes

Blackbody radiation

A blackbody is an object that absorbs all radiation incident upon it and re-emits this radiation at all wavelengths. All dense objects with a temperature above 0°K will produce thermal blackbody emission. This is represented by a continuous spectrum with the peak wavelength directly related to the source temperature in accordance with Wien's Law: $\lambda_{max}T = 0.29 \text{ cm K}$ (see Fig 1.3). In astronomy, the most precisely measured blackbody spectrum was determined for the cosmic microwave background, as measured by NASA's COsmic Background Explorer (COBE). In addition, a number of astrophysical objects have demonstrated blackbody emission in the X-ray regime. For example, the

surface of a neutron star emits blackbody radiation at X-ray wavelengths if sufficiently hot enough ($\sim 10^6$ K). In this thesis, blackbody radiation is described using the `bbbody` model in the X-ray spectral fitting package `XSPEC`.

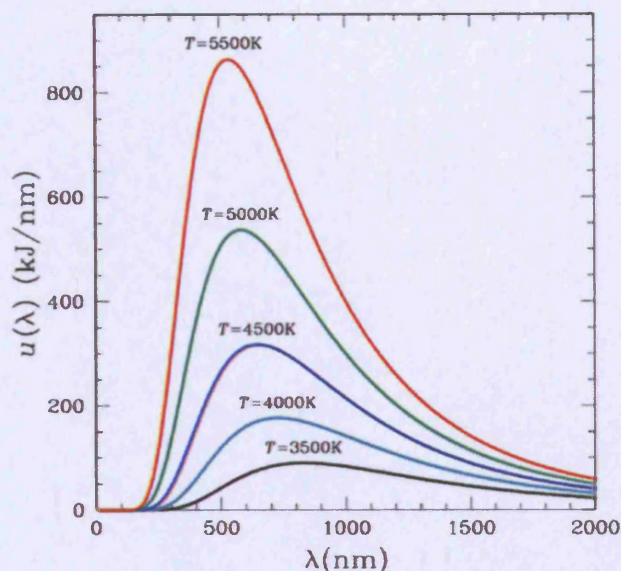


Figure 1.3: Graphical representation of the blackbody spectrum as a function of wavelength, taken from <http://en.wikipedia.org/wiki/Image:Bbs.jpg>.

Bremsstrahlung

‘Bremsstrahlung’ is a German word meaning ‘braking radiation’ and is used to describe the radiation which is emitted when charged particles are decelerated or ‘braked’. Usually this occurs when a fast-moving electron is deflected by the electric field surrounding a positively charged atomic nucleus, causing it to lose energy (see Fig. 1.4). This process is also known as free-free emission as the electrons are not bound to an atom before or after the event that causes the emission. The most common occurrence is the emission from a hot gas produced by the rapid and continuous motions of the particles in the plasma. This so-called ‘thermal bremsstrahlung’ produces a continuous characteristic spectrum. In addition, lines can appear super-imposed on this spectrum, corresponding to the ejection of electrons from atoms due to collisions with other atoms or interactions with incident photons. As such, high resolution X-ray spectroscopy can provide information on the abundance of elements present in the

emitting source based on characteristic spectral features.

Throughout this thesis, emission from a hot plasma is modelled by either the `brems` (Kellogg et al., 1975) or the `mekal` (Mewe et al., 1995) component in XSPEC. The `brems` model represents a continuum resulting from free-free emission, while the `mekal` model includes line emissions from several elements and a continuum emission consisting of free-free emission, free-bound emission and two-photon emission (Kaastra & Mewe, 1993).

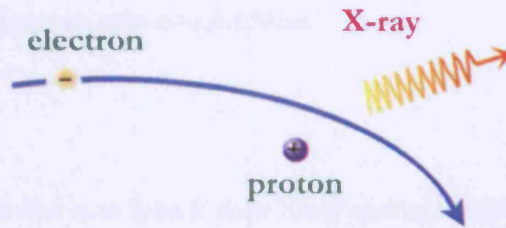


Figure 1.4: Graphical representation of the bremsstrahlung emission process, taken from http://chandra.harvard.edu/xray_astro/xrays.html.

Comptonisation

Compton scattering occurs when a photon collides with a free electron and transfers some of its energy. The scattered photon has a lower frequency than that of the incoming photon, while the electron has an increased kinetic energy. However, in Astronomy, the reverse process *i.e.*, *inverse* Comptonisation, in which low energy photons gain energy from collisions with energetic electrons is often more important (see Fig. 1.5). For example, the very high state seen in XRBs (see § 1.3.4) is thought to be due to the scattering of photons from the underlying accretion disc in a non-thermal corona (Gierliński et al. 1999; Zdziarski et al. 2001). The X-ray spectrum has a strong non-thermal component (observed to extend up to ~ 1 MeV) which is well described by an unbroken power-law model.

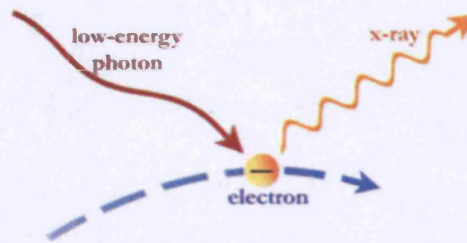


Figure 1.5: Graphical representation of inverse Compton scattering, taken from http://chandra.harvard.edu/xray_astro/xrays2.html.

Discrete line emission

Some sources show discrete emission lines in their X-ray spectra, which are produced when electrons make downward transitions from higher to lower energy states. Such transitions can occur when the electrons in an element are excited to higher energy levels (*e.g.*, via collisions or interactions with incident photons), and then relax to lower energy levels, emitting photons in the process (see Fig. 1.6). Alternatively, if an electron is ejected from the atom then an electron in a higher energy state drops down to replace it, which also results in the emission of a photon. The emitted photons are characteristic of the energy difference between the energy states and appear as discrete spectral lines at the appropriate energies. While each energy state is separated by a discrete amount of energy, the atoms for each element have their own unique sets of energy states. Therefore a hot gas may yield a spectrum composed of many emission lines depending on the various elements within it. As such, analysis of the discrete line emission can provide information on the temperature and abundance of the emitting material.

Although in theory, specific atomic transitions correspond to the emission of photons with a specific frequency, spectral lines are observed to extend over a range of frequencies. There are three main processes responsible for this broadening of spectral lines and each mechanism produces its own distinctive line shape (line profile). Natural broadening is a consequence of the Heisenberg uncertainty principle which relates the lifetime of an excited state with the precision of the energy, *i.e.*, $\Delta E \Delta t \geq \hbar$. Doppler broadening occurs due to the random motion and different thermal velocities of the atoms in the gas. Pressure (and collisional) broadening occurs when the orbitals of an atom are perturbed either due to a close encounter involving the electric field of an ion or due to collisions with nearby atoms. In

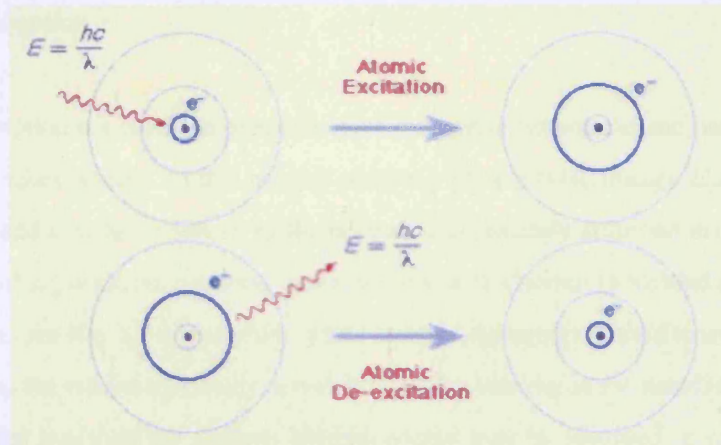


Figure 1.6: Graphical representation of discrete line emission, taken from <http://www.astro.wisc.edu/bank/index.html>.

addition, the centre of the line may be shifted from its nominal central wavelength. This frequency shift in astronomical objects arises from the relative motion of the object to the observer (*i.e.*, the Doppler Effect).

Emission lines are observed from a wide range of astronomical sources. For example, bright normal galaxies exhibit emission lines due to the prevalence of hot interstellar plasma (see the ‘**Bremsstrahlung**’ section above). Many soft X-ray emission lines have also been detected in the X-ray spectra of some AGNs. One particularly interesting result from AGN X-ray spectral studies is the detection of a broad neutral Fe-K α line at 6.4 keV (*e.g.*, Pounds et al. 1989). It is thought that this emission is due to a fluorescence line from the K-shell of iron, generated through the irradiation of the cold (weakly ionised) disc by a source of hard X-rays (*e.g.*, an optically thin Comptonising corona). The observed broadness of the line implies relativistic velocities which in turn suggests that the line emission originates from the inner accretion disc close to the central black-hole. Thus, the study of Fe-K α profiles in AGN provides the means to probe the immediate environment of a black-hole and represents one of the few cases where general relativistic effects can be directly measurable. Broadened Fe-K α lines have also been detected in Galactic black-hole binaries (BHBs) and are again thought to arise in the inner accretion disc. A wealth of lines have been observed in the X-ray spectra from SNRs, arising from elements such as Fe, O, Mg, S, Si, Na, Ca, Ni, Ne and Ar. SNR spectra may also show an Fe-K line at 6.7 keV which originates from highly ionised iron *i.e.*, from hot plasma emission.

Photoelectric absorption

Photoelectric absorption is a common phenomenon in astrophysical sources and particularly dominates for low energy incident X-rays. In this process an X-ray photon (with energy $E_{ph} = h\nu$, where h is Planck's constant and ν is the frequency of the photon) is completely absorbed in the collision with an atom of some absorbing material, resulting in the ejection of an electron (with binding energy $E_b \leq h\nu$) from the atom (*e.g.*, see Fig. 1.7). Therefore, while some of the energy is used to overcome the binding energy of the atom, the remaining energy serves to impart a velocity to the recoiling electron. Photons which have energies less than the electron binding energy may be absorbed or scattered but will not photoionise the atom. The overall process is characterised by the photoelectric cross-section of the atoms in the absorbing material which is also dependent on the energy of the incident photon. Usually the absorbing material is dominated by hydrogen because this is the most abundant element. To ionise hydrogen, photons need an energy greater than 13.6 eV, therefore in this case the energy of the emitted photoelectron is given by: $\frac{1}{2}mv^2 = h\nu - 13.6 \text{ eV}$.

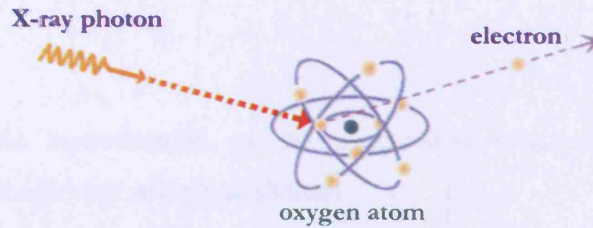


Figure 1.7: Graphical representation of the photoelectric absorption process, taken from http://chandra.harvard.edu/xray_astro/absorption.html.

Photoelectric absorption can give rise to absorption edges in the X-ray spectrum, corresponding to energy changes within the electron orbitals of the absorbing material *i.e.*, transitions of electrons to higher states. These edges are element specific and shift to higher energies when the atomic number increases.

In this thesis, the absorption component of the X-ray data is modelled with either the Wisconsin absorption model (*wabs*) of Morrison & McCammon (1983) or with the Tuebingen-Boulder interstellar medium (ISM) absorption model (*tbabs*) with abundances and absorption cross-sections tabulated by Wilms et al. (2000). The *tbabs* model is intended as a replacement for the *wabs* component and uses

revised abundances and updated cross-sections for X-ray absorption by the ISM.

Synchrotron

Synchrotron radiation is a non-thermal component produced by relativistic electrons spiralling along magnetic field lines (see Fig. 1.8). Depending on the electron's energy and the strength of the magnetic field, the maximum intensity will occur as radio waves, visible light, or X-rays. The radiation is concentrated in the direction of the electron's motion and is strongly plane polarised. Assuming the electron energy spectrum obeys a power-law then the resulting synchrotron spectrum is also represented by a power-law.

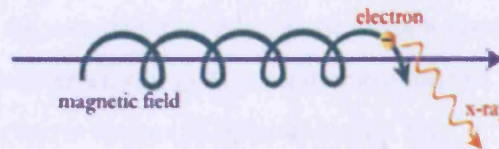


Figure 1.8: Graphical representation of the synchrotron emission process, taken from http://chandra.harvard.edu/xray_astro/xrays3.html.

1.2.2 Power source

X-ray observations probe extreme environments such as those found near black-holes. While the above section describes processes that give rise to X-ray emission, this section describes a key power source that creates an environment in which such processes can occur.

Accretion

Accretion is an important astrophysical process which can result in the growth of a massive object by gravitationally attracting more matter, typically through an accretion disc. Accretion discs are thought to be involved in diverse phenomena ranging from the formation of stars and planets to the powering

of quasars. Accretion discs themselves are formed when a large gravitational source attracts nearby material towards it. Instead of accreting directly (due to its high angular momentum) the material orbits the central object and eventually forms a disc. The best studied discs reside in interacting binary systems. For simplicity, Shakura & Sunyaev (1973) pictured the disc as a thin, flat gaseous object with a negligible gravitational field compared to that of the central object. Therefore, matter in the accretion disc moves in a series of Keplerian orbits, such that the velocity at a radius r is given by:

$$v_{Kep} = \left(\frac{GM}{r} \right)^{1/2} \quad (1.1)$$

where G is the gravitational constant and M is the mass of the central compact object. Viscosity causes the orbiting gases to spiral in towards the compact object. As it does so, angular momentum is transferred outward through the accretion disc. Also, as the gas falls inwards it is heated to increasingly higher temperatures as the lost orbital energy is converted into thermal energy. Therefore the energy released through accretion is due to the loss of potential energy, *i.e.*,

$$E_{acc} = \frac{GMm}{r} \quad (1.2)$$

which gives an accretion luminosity of

$$L_{acc} = \frac{dE_{acc}}{dt} = \frac{GM\dot{M}}{r} \quad (1.3)$$

where m is the mass of the material being accreted, M is the mass of the compact object, \dot{M} is the mass accretion rate and r is the radius of the compact object.

While this process is highly efficient, there is a limit to the luminosity that can be liberated by accretion, known as the Eddington limit. This occurs when the outward radiation pressure is equal to the inward gravitational force, preventing further mass infall. Assuming that the infalling matter is fully ionized and that the radiation pressure is due to Thomson scattering of the radiation by electrons in the plasma, then the limit is given by:

$$\frac{\sigma_T L_{acc}}{4\pi r^2 c} = \frac{GMm_H}{r^2} \quad (1.4)$$

$$\Rightarrow L_{Edd} = \frac{4\pi GMm_p c}{\sigma_T} \sim 1.3 \times 10^{38} \left(\frac{M}{M_\odot} \right) \text{ ergs}^{-1} \quad (1.5)$$

where $m_H = m_p + m_e \approx m_p$ and σ_T is the Thomson scattering cross section. Thus, the Eddington limit is the maximum luminosity which a spherically symmetric source of mass M can emit in a steady state. While neutron stars and white dwarfs have a solid surface onto which matter can be accreted, the size of a black-hole is represented by its event horizon, which occurs at the Schwarzschild radius, defined as $R_S = 2 \left(\frac{GM}{c^2} \right)$. No information (*i.e.*, as matter, radiation) can propagate outward from this radius. For accretion discs around black-holes, the material spirals inward gradually through a sequence of nearly circular orbits until it reaches the innermost stable circular orbit (ISCO). Once inside the ISCO, gas can fall into the black-hole without any further loss of angular momentum. The ISCO is located well outside the event horizon (at $\sim 3 R_S$) for a nonrotating black-hole and approaches the horizon (at $\sim \frac{1}{2} R_S$) for a rapidly spinning black-hole, provided that the gas is orbiting in the same sense as the black-hole's rotation.

Throughout this thesis, accretion discs are assumed to be optically thick and geometrically thin, and are modelled as multiple blackbody components with a continuous spectrum corresponding to the local disc temperature at each radial distance. One such model has been formulated by Mitsuda et al. (1984) and Makishima et al. (1986) and is known as the multi-colour disc blackbody (MCD) model which is represented by the `diskbb` model in XSPEC. Another model used to described the blackbody spectrum of an accretion disc is the `diskpn` model in XSPEC. This is an extension of the `diskbb` model and assumes that the inner edge of the accretion disc extends down to the ISCO, *i.e.*, $R_{in} = 6 \left(\frac{GM}{c^2} \right)$, as well as including corrections for the temperature distribution near the black-hole (Gierliński et al., 1999).

1.3 X-rays from galaxies

This thesis is based on X-ray observations of nearby galaxies and as such it is pertinent to give a review of the X-ray emission from such systems. Before the launch of the *Einstein* observatory, only four

normal galaxies *i.e.*, those without an active nucleus (see next section) had been detected in X-rays: the Milky Way, M31 and the Magellanic Clouds (*e.g.*, see Helfand 1984). *Einstein* was the first X-ray observatory sensitive enough to detect a large number of normal galaxies and provide further information about their X-ray properties. The significant advancement in this area is reflected by the 493 galaxies observed with the IPC and HRI imaging instruments, catalogued by Fabbiano et al. (1992). These observations showed that galaxies of all morphological types are extended sources of X-ray emission with observed X-ray luminosities in the range of $10^{38} - 10^{42} \text{ erg s}^{-1}$ (Fabbiano, 1989). However, a more detailed analysis of the X-ray morphology and spectral characteristics were limited to the very closest systems (*i.e.*, M31, M33 and the Magellanic Clouds) at this time. Such observations revealed that a large fraction of the X-ray emission from Local Group galaxies is due to bright sources, such as accreting binaries and SNRs (*e.g.*, Helfand 1984 and references therein). In addition, *Einstein* revealed the presence of diffuse X-ray emission in some galaxies (*e.g.*, M33; Trinchieri et al. 1988).

The X-ray spectra of more distant galaxies were also consistent with the hard spectra expected for XRBs (Fabbiano & Trinchieri, 1987). However, only a few very bright discrete sources could be detected in such galaxies (*e.g.*, Fabbiano & Trinchieri 1987). In the case of bright spiral galaxies, most of these sources reside in the spiral arms and are very luminous. In fact, a number of spiral galaxies were shown to possess sources which exceeded the Eddington limit for accretion onto a $1 M_{\odot}$ object ($> 1.3 \times 10^{38} \text{ erg s}^{-1}$), and some achieved luminosities in excess of $10^{39} \text{ erg s}^{-1}$. Several ideas have been proposed to explain the highest luminosities seen in these so-called ultraluminous X-ray sources (ULXs), as discussed below in § 1.3.5. However, while the *Einstein* results suggest that the X-ray emission from spiral galaxies is dominated by evolved sources, a hot ISM component was discovered to dominate the emission from elliptical and S0 galaxies (Forman et al. 1979, Fabbiano 1989). *Einstein* also detected hot outflows from nearby starburst galaxies *i.e.*, galaxies with an enhanced star formation rate (Watson et al. 1984, Fabbiano 1988b).

The softer energy band of *ROSAT* meant that it was more suited to searches for hot ISM components. Indeed, the first evidence for such a component in spiral galaxies was provided by a *ROSAT* observation of NGC 891 (Bregman & Pildis, 1994). *ROSAT*'s much improved spatial and spectral resolution coupled with its lower internal background meant that it provided a substantial improvement in this field compared to previous X-ray imaging instruments. In particular, the hot ISM was detected in many nearby spiral galaxies including the edge-on spiral galaxy NGC 4631 which showed extended emission more than 8 kpc above the galactic plane (Wang et al., 1995). Numerous individual galaxy

studies have been performed with *ROSAT* which have been complimented by studies of nearby spiral galaxy samples that were analysed uniformly. For example, Read et al. (1997) presented an analysis of *ROSAT* PSPC observations of 17 nearby spiral galaxies, covering a range of activity and inclination. These results showed that nearby non-active spiral galaxies have 0.1–2.0 keV luminosities in the range $10^{38} - 10^{41} \text{ erg s}^{-1}$, consistent with the *Einstein* results (Fabbiano et al., 1992). Almost all of the systems in this survey showed evidence for significant amounts ($\lesssim 10^9 M_{\odot}$) of low metallicity diffuse hot gas ($1 - 8 \times 10^6 \text{ K}$). This hot gas component has been shown to dominate the soft X-ray emission of high-activity systems, whereas the low-activity systems appear to be dominated by discrete sources (XRBs, SNRs etc.) which span a wide range of X-ray luminosities ($\text{few} \times 10^{35} - \text{few} \times 10^{40} \text{ erg s}^{-1}$). Therefore one of the key *ROSAT* results is that spiral galaxies have complex X-ray emission, with various contributions coming from accreting sources, SNRs and hot phases of the ISM.

The launch of the *Chandra* and *XMM-Newton* observatories with their significantly improved resolution and sensitivity, has advanced current understanding in most aspects of the high energy Universe. For example, the X-ray data of ULXs pre-*Chandra* were spatially limited to the extent that they could not always be distinguished from moderately compact complexes of X-ray-emitting sources. *Chandra* has made significant advances in this field due to its order-of-magnitude improvement in spatial resolution, which for example, permitted the first identification of an optical counterpart to such a source (Roberts et al., 2001). Prior to the launch of *XMM-Newton*, the spectra of these sources had been successfully described with single component models. However, *XMM-Newton* observations provided unprecedented spectral quality and were the first to statistically require two component modelling (e.g., Miller et al. 2003; Miller, Fabian & Miller 2004b) providing further clues to their true physical nature.

Further results to emerge from *Chandra* and *XMM-Newton* observations of nearby galaxies are provided by the high spectral resolution of their dispersive spectrometers. In the case of *XMM-Newton*, the high resolving power of the Reflection Grating Spectrometer (RGS) is coupled to a very large collecting area, which makes this an ideal instrument for detailed spectroscopic investigations. For example, *XMM-Newton* RGS spectra of the starburst galaxies M82 and NGC 253 yielded detailed information on their emission line ratios, which permitted the determination of elemental abundances and physical states of the emitting regions and surrounding environments (Read & Stevens 2002, Pietsch et al. 2001 respectively).

Also, while the X-ray populations of Local Group galaxies have been classified in detail by earlier X-

ray missions (*e.g.*, *Einstein*, *ROSAT*, *ASCA*), these observatories were unable to resolve X-ray sources in more distant galaxies. However, *Chandra*'s superb spatial resolution has enabled many sources in more distant galaxies to be resolved. Furthermore, X-ray colour analyses on these sources have revealed significant differences between bulge and disc systems. These differences have been used as a basis to classify sources into various types *e.g.*, XRBs, SNRs and supersoft sources (Prestwich et al., 2003). *Chandra*'s sub-arcsecond spatial resolution has also provided direct evidence of the existence of populations of low-mass X-ray binaries (LMXBs) in all E and S0 galaxies (*e.g.*, Sarazin et al. 2001; Angelini et al. 2001; Kim & Fabbiano 2003). Interestingly, these observations have shown that a significant fraction (up to $\sim 70\%$) of LMXBs in elliptical galaxies are located within globular clusters (*e.g.*, Sarazin et al. 2001; Angelini et al. 2001), suggesting that globular clusters are the dominant sites of LMXB formation in galaxies with old stellar populations.

Source population studies with *Chandra* and *XMM-Newton* has also made significant contributions to the X-ray luminosity functions (XLFs) of galaxies². The first *Chandra* studies of XLFs suggest trends related to the morphological type of the parent galaxy and/or the age of the prevalent stellar population. For example, XLFs of early-type galaxies appear to have a break at the Eddington luminosity of neutron star XRBs (*e.g.*, Blanton et al. 2001; Sarazin et al. 2001; Irwin et al. 2002), although some argue that this may be due to incompleteness (*e.g.*, Kim & Fabbiano 2003). The XLFs of star forming galaxies tend to follow a single power-law with the slope related to the star formation rate (*e.g.*, Zezas et al. 2001; Bauer et al. 2001; Kilgard et al. 2002).

These observatories have also revolutionised studies of the X-ray background and the sources that comprise it. In particular, most (*i.e.*, $\gtrsim 60\% - 80\%$) of the 2–8 keV background has now been resolved into point sources (*e.g.*, Brandt et al. 2000, Mushotzky et al. 2000, Hasinger et al. 2001, Giacconi et al. 2001). Also, high-quality *Chandra* positions also allow these sources to be matched unambiguously to (often faint) multiwavelength counterparts, the vast majority of which are AGN. Also at faint soft band fluxes ($\lesssim 3 \times 10^{-16}$ erg cm⁻² s⁻¹) these observations showed the emergence of a population of apparently normal galaxies (including moderately star-forming galaxies and elliptical galaxies), which contribute as much as 5%–10% of the X-ray background flux in the 0.5–2 keV band. As well as improving our understanding of the X-ray emission from nearby galaxies (< 20 Mpc), these missions have enabled the study of the X-ray properties of normal galaxies at cosmological distances (*e.g.*, Hornschemeier et al. 2001, Brandt et al. 2001).

²XLFs of galaxy source populations are a measure of the number of sources at a given luminosity.

Such observations have detected galaxies with $0.1 \lesssim z \lesssim 1.0$ in appreciable numbers at fluxes below $1 \times 10^{-15} \text{ erg cm}^{-2} \text{ s}^{-1}$ (0.5–2 keV).

The following sections describe the main components of the X-ray emission from galaxies in more detail.

1.3.1 Active Galactic Nuclei

While it is thought that most galaxies contain central massive black holes (*e.g.*, Bertola et al. 2003), only those which are adequately fuelled are classed as active. The nuclear regions of such galaxies have been observed to greatly outshine the rest of the galaxy, leading to the name Active Galactic Nuclei (AGN). Such objects are the most consistently luminous sources in the Universe with bolometric luminosities up to $10^{48} \text{ erg s}^{-1}$. It is now widely believed that AGN are powered by the accretion of matter onto a supermassive black-hole (SMBH) of $\sim 10^6 - 10^9 M_{\odot}$ (Lynden-Bell, 1969). This radiation can be emitted across most of the electromagnetic spectrum, as infrared, radio waves, UV, X-ray and γ -rays. However, the observed characteristics vary greatly between individual examples, leading to many subclasses of AGN; Seyferts, quasars (or QSOs: quasi-stellar objects), blazars, LINERs (Low-Ionization Nuclear Emission Region Galaxies) and radio-galaxies to name but a handful. Seyfert galaxies were the first recognised AGN and tend to be spiral galaxies. They were originally classified by Carl Seyfert (Seyfert, 1943) but were later subdivided into two main types, Type 1 or 2, depending on whether their spectra show narrow and broad emission lines, or only narrow lines respectively. The narrow lines are thought to originate in regions further from the AGN than for the broad lines, with the broad component obscured by dust and/or viewing angle for Seyfert 2's. However, in some Type 2 Seyfert galaxies, the broad component can be observed in polarised light. In this case it is thought that light from the broad-line region is scattered by a hot, gaseous halo surrounding the nucleus, allowing it to be viewed indirectly. The first example of this was found for the Seyfert 2 galaxy NGC 1068 (Antonucci & Miller, 1985) and gave rise to the so-called ‘unification model’ (*e.g.*, Antonucci 1993). The current paradigm of this model is that the ultimate energy source in all AGN is similar, and that the observed characteristics are secondary effects of their environment and our viewing angle *e.g.*, with dust obscuration and relativistic beaming causing the observational differences. A sketch of this AGN unification model is shown in Fig. 1.9. It is thought that Seyfert nuclei of both types reside in $\sim 10\%$ of all galaxies (Ho et al., 1997b), whereas the more common (but least luminous of the classifications)

LINERs occur in up to 30% of all galaxies. The majority of galaxies are in fact quiescent, including our own Milky Way.

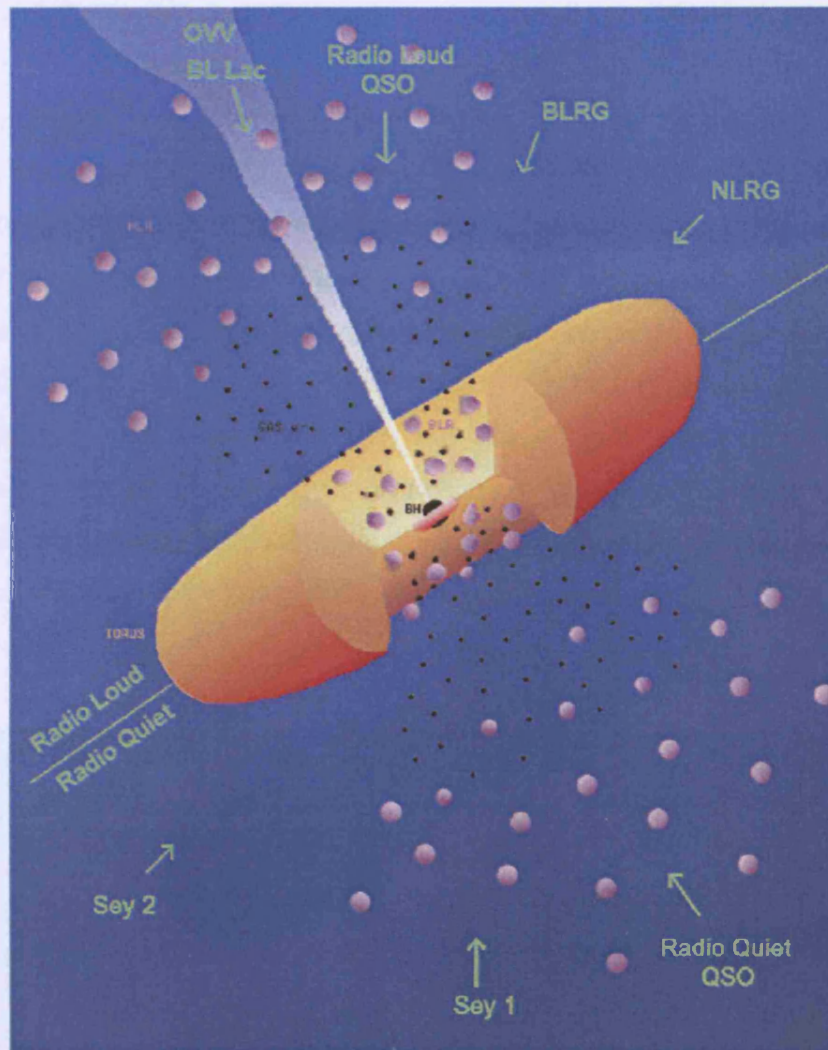


Figure 1.9: A schematic diagram showing the basic assumptions of the unified theory of AGN. Taken from <http://www.asdc.asi.it/bepposax/calendar/>, adapted from Urry & Padovani (1995).

1.3.2 Diffuse X-ray emission

Einstein and *ROSAT* observations showed that spiral galaxies emit soft X-rays (0.1–2.4 keV) with luminosities of $10^{38} - 10^{40} \text{ erg s}^{-1}$ (e.g., Fabbiano et al. 1992, Read et al. 1997). However, before the advent of *Chandra* and *XMM-Newton*, studies of the morphology of this diffuse emission was only possible for a few cases (e.g., M101, Snowden & Pietsch 1995; M51 Ehle et al. 1995; NGC 891, Bregman & Houck 1997) due to lack of spatial resolution. The improved spatial resolution of *Chandra* and *XMM-Newton* has enabled separation between diffuse hot gas and point sources as well as a more precise morphological study of the diffuse emission. Normal spiral galaxies typically exhibit only low levels of diffuse emission (typically well described by two soft low-metallicity thermal plasmas, e.g., Kuntz et al. 2003; Carpano et al. 2005) and there is very little mass, energy or metal losses via hot diffuse gas. While some normal galaxies only appear to show true diffuse gas in their centres (e.g., M31, Shirey et al. 2001), much more diffuse emission is seen in the more active normal galaxies (e.g., M101 and M83 which show strong diffuse emission associated with star-forming regions in their spiral arms; see Fig. 1.10).

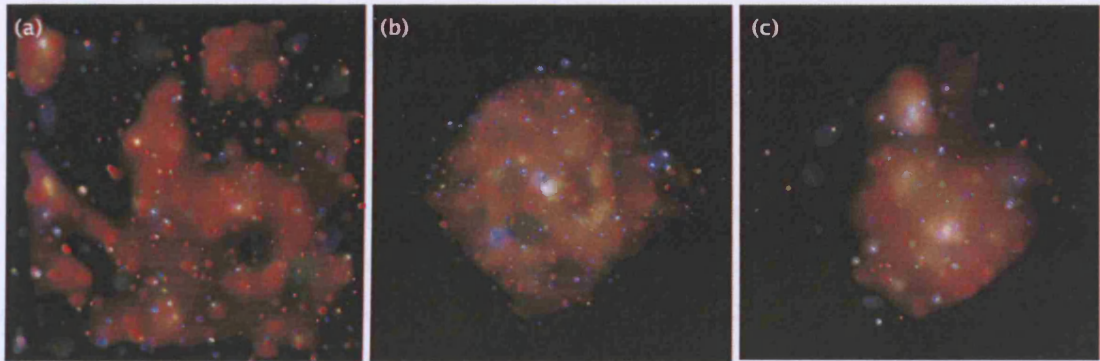


Figure 1.10: *Chandra* images of the diffuse emission in face-on spiral galaxies, taken from <http://chandra.harvard.edu/photo/2004/m101/more.html> (Credit: NASA/CXC/SAO/R.DiStefano et al.). Color Code: Red: 0.3–1.0 keV, Green: 1.0–2.0 keV, Blue: 2.0–8.0 keV. The galaxies are (a) M101, (b) M83, (c) M51.

Chandra and *XMM-Newton* imaging have shown that the diffuse emission can have a variety of morphologies, particularly in starburst galaxies. These galaxies typically display greater levels of diffuse emission and hotter gas components than normal galaxies. Also, the gas appears in the form of out-

flows *i.e.*, from superwinds (*e.g.*, Heckman et al. 1990), as well as coronae and halos. It is thought that the X-ray emitting gas is associated with supernovae and winds from young massive stars. In particular, superwinds occur after there has been a strong star-formation episode, where the collective power of a large number of supernovae drives the high-pressure, high-temperature gas out of the disc of the host galaxy at high speeds (from a few $\times 10^2$ to 10^3 km s $^{-1}$; Heckman 2001). During the process, cool dense gas from the disc and halo regions are accelerated and shocked, giving rise to soft X-ray and optical H α emission. Extra-planar gas has been detected in many starburst galaxies (Strickland et al. 2004a, Strickland et al. 2004b) as shown in Fig. 1.11. As superwinds can transport large amounts of material, including the newly synthesized heavy elements created by the supernovae, into the intergalactic medium (IGM), it is thought that they play a key role in the metallicity evolution of galaxies (*e.g.*, Edmunds 1990). X-ray observations of superwinds are particularly important as they can provide information about their energetics and composition, and hence the transport of energy and metal-enriched gas into the IGM.

1.3.3 Supernova remnants

As the name suggests, a SNR contains the remnants of a star which has undergone a supernova explosion. Such an explosion causes the outer layers of the star to be ejected into the ISM at faster than the speed of sound. This results in a shock wave which moves outwards from the central object. The expanding material plows outwards into the ISM and sweeps up any surrounding dust and gas. There are three main morphological types of SNR: shell-like which have a shell-like structure, centre-filled (also known as Crab-like remnants) which contain a pulsar (*i.e.*, a rotating neutron star) at its centre and composite remnants which can appear as shell-like or Crab-like depending on the energy band they are observed in. SNRs are generally powerful radio and X-ray sources, and may also be visible at optical wavelengths in *e.g.*, H α . Thermal X-ray emission is produced as the ambient material is compressed and heated as a result of the expanding shock wave and/or if the core of the star forms a neutron star. Shell-like remnants also show non-thermal radio synchrotron emission as a result of relativistic electrons produced within the shock gyrating around magnetic field lines. Filled remnants also exhibit non-thermal synchrotron emission (from radio through to γ -rays) via relativistic electrons produced by the central pulsar.

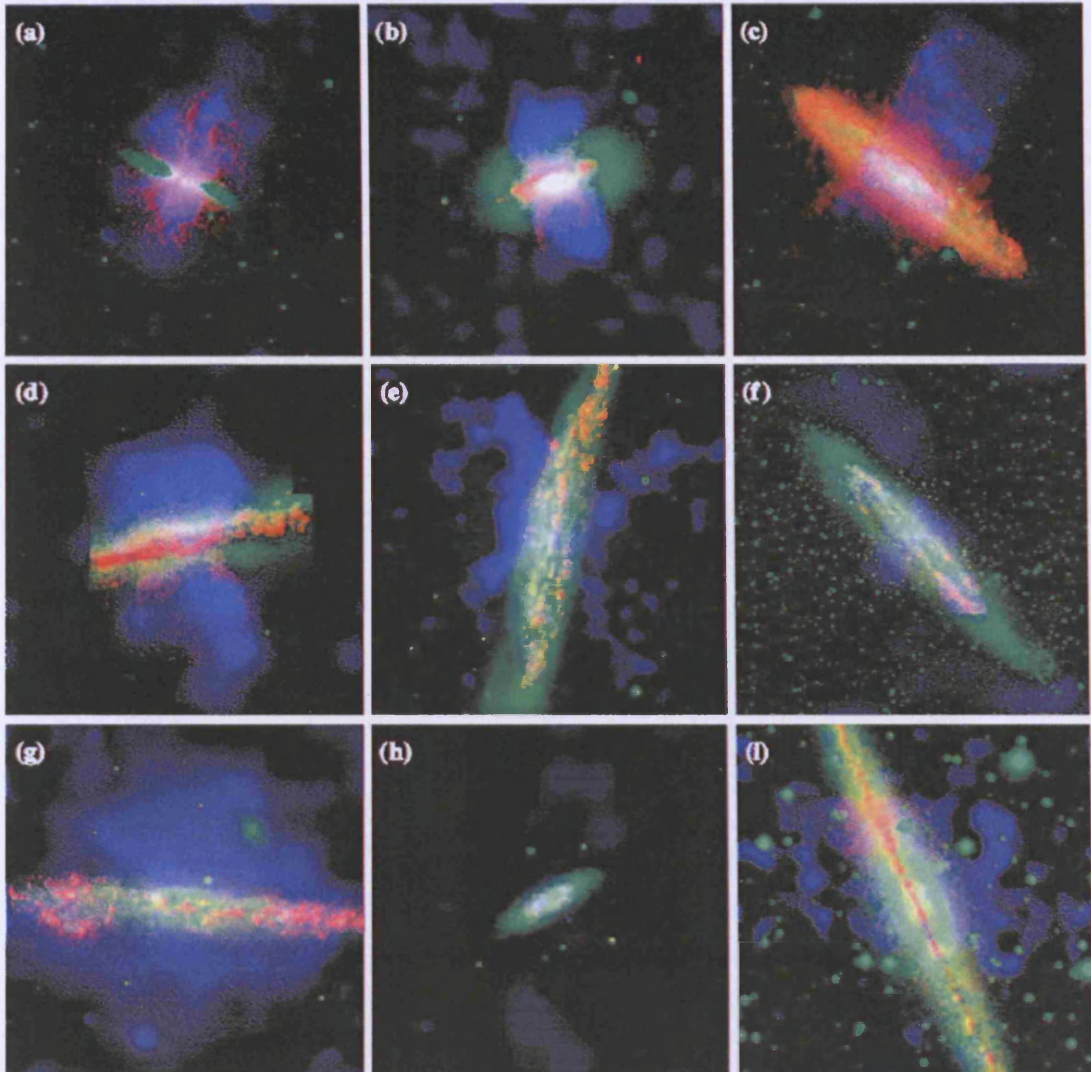


Figure 1.11: False colour images ($20 \text{ kpc} \times 20 \text{ kpc}$) from a *Chandra* survey of the diffuse emission in the halos of edge-on starforming disc galaxies, taken from (Strickland et al., 2004b). Red: optical $\text{H}\alpha$ emission, Green: optical R-band emission (starlight), Blue: Diffuse soft (0.3–2 keV) X-ray emission. The galaxies are (a) M82, (b) NGC 1482, (c) NGC 253, (d) NGC 3628, (e) NGC 3079, (f) NGC 4945, (g) NGC 4631, (h) NGC 6503, (i) NGC 891.

1.3.4 X-ray binaries

XRBs are mentioned extensively in this work, therefore the next few sections give an introduction to these systems and describe their key characteristics. XRBs were the first X-ray sources to be discovered outside the Solar System (*e.g.*, Sco X-1, Giacconi et al. 1962; Cyg X-1, Bowyer et al. 1965) and constitute the brightest class of discrete X-ray sources in the sky. Their discovery posed two main problems *i.e.*, firstly explaining the production of the X-ray emission and then explaining the high X-ray luminosities. It was soon realised that both of these could be explained by the accretion of mass under the influence of gravity onto a compact object in these systems. In fact, an XRB contains either a neutron star or a black-hole accreting from a companion star (see Fig 1.12) and in many cases they have been shown to represent the dominant component of the X-ray emission from normal and star-forming galaxies.

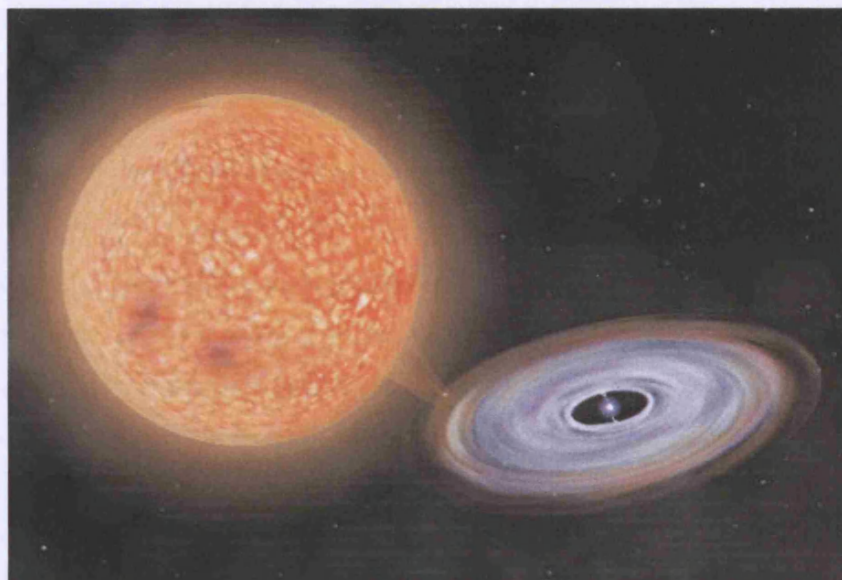


Figure 1.12: Artists impression of an X-ray binary system, showing material being pulled away from the companion star onto the accretion disc of its partner. Image courtesy of Chris Moran, using the Celestia software (<http://www.shatters.net/celestia>).

Mass exchange in an XRB system occurs in two main ways *i.e.*, via Roche Lobe overflow or stellar wind accretion, depending on the nature of the companion star and the orbital separation. Roche Lobe overflow occurs if the companion star increases in size or the binary separation shrinks, such that the outer layers of the companion star crosses into a region of space dominated by the gravitational pull of

Table 1.1: Properties of the two main classes of strong Galactic X-ray sources

	HMXB	LMXB
X-ray spectra:	$kT \geq 15$ keV, hard	$kT \leq 10$ keV, soft
Type of time variability:	Regular X-ray pulsations No X-ray bursts	Only a very few pulsars Often X-ray bursts
Accretion process:	Wind	Roche-lobe overflow
Timescale of accretion:	10^5 yr	$10^7 - 10^9$ yr
Accreting compact star:	high \vec{B} -field NS (or BH)	low \vec{B} -field NS (or BH)
Spatial distribution:	Galactic plane	Galactic centre and spread around the plane
Stellar population:	Young, age $< 10^7$ yr	Old, age $> 10^9$ yr
Companion stars:	Luminous, $L_{\text{opt}}/L_X > 1$ early type O(B)-stars $> 10 M_\odot$ (Pop. I)	Faint, $L_{\text{opt}}/L_X \ll 0.1$ blue optical counterparts $\leq 1 M_\odot$ (Pop. I and II)

NOTES: Table from Tauris & van den Heuvel (2006).

the compact object. Alternatively, the companion star may gradually eject much of its mass in the form of a stellar wind, some of which is then gravitationally captured by the compact object. More than 90% of strong Galactic XRBs appear to fall into two distinct groups depending on the mass of the companion star: high-mass X-ray binaries (HMXBs) which have a high-mass companion star to the neutron star or black-hole and low-mass X-ray binaries (LMXBs) which have a low-mass companion star (Tauris & van den Heuvel, 2006). The large difference in the companion masses between HMXBs and LMXBs leads to a number of additional differences between these two classes of systems as summarised in Table 1.1 and described in the following text.

HMXBs

HMXBs contain an early type (OB) companion star with a mass of $\gtrsim 10 M_\odot$. These high-mass stars usually have an intense wind that is easily captured by the neutron star or black-hole to release X-rays. The mass transfer rate is determined by the strength and speed of the wind and orbital separation.

Neutron star HMXBS (NS-HMXBs) are much more common than the black-hole systems and many appear as accretion powered pulsars. This is a consequence of the high magnetic field ($\sim 10^{12}$ G) in such systems, which disrupts the accretion flow and channels it onto the magnetic poles. However, such pulses are not seen in black-hole HMXBs (BH-HMXBs) due to the presence of the event horizon, which does not allow for any stable features to be anchored to the rotation of the compact object. The lifetimes of these systems are determined by the evolution of the high-mass companions and are relatively short ($\sim 10^5 - 10^7$ yr). Therefore HMXBs are distributed along the Galactic plane, as is the case for young stellar populations. The optical luminosity is dominated by the emission from the companion star while the X-ray luminosity is either powered by stellar wind accretion or, in the case of the brighter systems, by Roche-lobe overflow via an accretion disc. NS-HMXB spectra are usually hard while the X-ray spectra of the black-hole systems tend to vary depending on their spectral state (see later).

LMXBs

LMXBs have old companion stars with masses of $\lesssim 1 M_{\odot}$. The orbital separation is generally smaller than in a typical HMXB because the companion is smaller. Accretion occurs via Roche Lobe overflow from the companion star (either as a consequence of the compact orbit or if the companion increases in size). If the compact object is a neutron star, then they often display X-ray bursts *i.e.*, sudden thermonuclear fusion of accreted matter at the surface. However, such bursts are suppressed in the presence of high magnetic fields (*e.g.*, $\vec{B} > 10^{11}$ G), which is why they are not observed in NS-HMXBs (Lewin & Joss, 1983). Also, such bursts are absent for BH-LMXBs due to the lack of a material surface. Although LMXBs are very seldom X-ray pulsars due to their relatively weak magnetic fields ($10^9 - 10^{11}$ G), they have been observed to contain millisecond pulsars (*e.g.*, Wijnands & van der Klis 1998). These are thought to arise from the prolonged phase of accretion which suppresses the magnetic field and spins up the neutron star (Psaltis & Remillard, 2006). The lifetimes of LMXBs are determined by the mass transfer process and are longer than those of HMXBs (*i.e.*, $\sim 10^7 - 10^9$ yr). Also, most LMXBs in our Galaxy are located in the bulge and in globular clusters, consistent with an old stellar population. The spectrum of the optical companion can only be observed in the widest of these systems or if the source becomes quiescent. Otherwise the optical emission is dominated by thermal emission from the accretion disc.

X-ray spectral states

Galactic BHBs have been observed to occupy a number of X-ray spectral/temporal states defined in the 1–10 keV band (van der Klis 1994; Tanaka & Lewin 1997; Tanaka & Shibazaki 1996). In addition, their X-ray spectra has shown transitions between these states, the first example of which was observed in Cyg X-1 (Tananbaum et al., 1972). Further evidence of spectral state changes in BHBs led to the suggestion that they may be connected with changes in the accretion process. The three most familiar X-ray bright states are the low/hard (LH), high/soft (HS, also described as ‘thermal dominated’) and the very high (VH, or ‘steep power-law’) states (see McClintock & Remillard 2006 for further details). The X-ray emission of BHBs has different spectral characteristics depending on which X-ray state the system is in. At lower mass accretion rates, a BHB usually enters the LH state where their X-ray emission is dominated by a hard power-law component ($\Gamma \sim 1.7$), thought to arise from Comptonisation of soft photons by a hot optically thin corona³. In this state, the disc is either undetected (*e.g.*, Belloni et al. 1999) or appears truncated at a much larger inner radius and hence cooler than the parameters derived for the soft state (Wilms et al. 1999, McClintock et al. 2001). The soft X-ray state is generally seen at a higher luminosity (*i.e.*, the HS state) and is best explained as ~ 1 keV thermal emission from a multi-temperature accretion disc (*i.e.*, modelled with a MCD component). In this state, the spectrum may also display a hard tail that contributes a small percentage of the total flux. The VH state is in many cases the most luminous state and is characterised by an unbroken power-law spectrum extending out to a few hundred keV or more. The photon index is typically steeper (≥ 2.5) than found in the LH state and generally coincides with the onset of strong X-ray QPOs. A MCD component may also be present in the VH state and the *EXOSAT* era demonstrated that some of the QPOs occur when both disc and power-law components contribute substantial luminosity (van der Klis, 1997).

1.3.5 Ultraluminous X-ray sources

Einstein observations revealed that some galaxies contain extremely bright non-nuclear point sources with X-ray luminosities in excess of 10^{39} erg s⁻¹. These so-called ultraluminous X-ray sources (ULXs) were of great interest as they were brighter than any discrete sources observed in our Galaxy or in our nearest large neighbor galaxy M31. Further observations revealed that they also displayed evi-

³However this is still a topic of debate, with the main alternative for the X-ray power-law emission being synchrotron emission from the radio jet that is associated with this state (*e.g.*, Falcke & Biermann 1995; Markoff, Falcke & Fender 2001).

dence for both short- and long-term X-ray variability, suggesting an accreting nature (Miller & Colbert, 2004). However, at these luminosities they exceed the theoretical limit (the Eddington limit) for spherical accretion onto a stellar mass ($\sim 10 M_{\odot}$) black-hole. Their luminosities are actually *intermediate* between normal black-hole XRBs and those of AGN. Therefore, ULXs have attracted considerable interest over recent years (*e.g.*, see Makishima et al. 2000 and references therein) as one simple way of evading the Eddington limit is to assume larger black-hole masses than typically found as the endpoints of stellar evolution. A brief description of this scenario as well as the other competing models currently proposed to explain the high luminosities in ULXs, is given below.

Intermediate mass black-holes

The idea that ULXs contain more massive black-holes than typically found as the endpoints of stellar evolution is a current hot topic of ULX research (*e.g.*, Colbert & Mushotzky 1999). Such *intermediate-mass* black-holes (IMBHs) with $M \sim 10^2 - 10^4 M_{\odot}$ would provide the ‘missing link’ between the stellar-mass black-holes and the SMBHs in the nuclei of galaxies. They are an attractive scenario for ULXs because sub-Eddington accretion onto such objects could easily explain the observed high luminosities. In particular, it is thought that those ULXs at the upper-end of the luminosity range ($L_X \geq 10^{40} \text{ erg s}^{-1}$) are perhaps the best candidates for harbouring IMBHs. Indeed, the current best ULX candidate for an IMBH is M82 X-1, which also happens to be amongst the most luminous ULXs observed so far ($L_X \sim 9 \times 10^{40} \text{ erg s}^{-1}$; Matsumoto et al. 2001; Kaaret et al. 2001). The measured luminosities of this source correspond to an IMBH mass of $\sim 500 - 900 M_{\odot}$, for accretion at the Eddington limit (Matsumoto et al. 2001; Kaaret et al. 2001). In addition to its extreme luminosity, a QPO was also discovered in the X-ray flux from M82 X-1, which was the first detection from a ULX (Strohmayer & Mushotzky, 2003). This QPO discovery establishes the compact nature of the source and argues against beaming.

The X-ray spectra of some ULXs have been successfully fitted with the same MCD plus power-law model used for Galactic BHBs. However, the temperature of the MCD component in some ULXs has been observed to be much cooler than in Galactic systems, which typically have $kT_{in} \sim 1 - 2 \text{ keV}$ (King, 2003). According to the MCD model, the temperature of the innermost edge of an accretion disc decreases as the mass of the compact object increases ($kT_{in} \propto M^{-1/4}$). Therefore cooler accretion discs suggest more massive black-holes, and thus provide supporting evidence for IMBHs. This is the

case for the spectra of some of the more luminous ($L_X \geq 10^{40} \text{ erg s}^{-1}$) ULXs which show accretion disc components with $kT_{in} \sim 0.1 - 0.2 \text{ keV}$ (Miller et al., 2004a), implying black-hole masses of $\sim 1000 M_\odot$.

However, there are several challenges to the IMBH model of ULXs. In particular the large numbers of ULXs associated with regions of star formation (*e.g.*, Zezas et al. 2002a, Gao et al. 2003, Wolter & Trinchieri 2004) argues against IMBHs constituting a large fraction of the ULX population (King, 2004). Also, recent X-ray spectral fitting results of high quality ULX data suggests that it may not be necessary to invoke IMBHs even in the more luminous ULXs (see Chapter 6).

Anisotropic radiation

An alternative scenario to the IMBH picture is that ULXs are actually a type of stellar mass ($\gtrsim 10 M_\odot$) BHB accreting around their Eddington limit. The idea that ULXs are in fact the extreme end of a HMXB population provides a natural explanation for the large numbers observed in star forming regions. One model to explain the high luminosities from such binaries assumes mildly anisotropic radiation patterns (beaming factors $\lesssim 10$) from sources emitting at or below the Eddington limit (King et al., 2001). Such radiation patterns (as opposed to the isotropic scenario assumed for IMBHs) could trivially allow apparent luminosities up to $\sim 10^{40} \text{ erg s}^{-1}$, compatible with the majority of claimed ULXs (King et al., 2001). As well as the large numbers of ULXs found in sites of star formation, further support for this model comes from some ULX spectra. In many cases the X-ray spectra of ULXs are consistent with thermal components at $kT_{in} \sim 1 - 2 \text{ keV}$ (see Chapter 6 for further details), which is a natural temperature for a stellar-mass object (King, 2003). However, while mild anisotropic emission could explain the apparent high luminosities up to $\sim 10^{40} \text{ erg s}^{-1}$, the most luminous objects would require much larger beaming factors (> 100) for which there are no known mechanisms other than relativistic effects (Mushotzky, 2004).

A further problem for this model has arisen from studies of the environments around ULXs; *e.g.*, Pakull & Mirioni (2002) discovered that the optical nebula surrounding the ULX Holmberg-II X-1 has substantial He II $\lambda 4686 \text{ \AA}$ emission. This line is produced by the recombination of fully ionised helium, and therefore requires a high energy source. High resolution imaging of the nebula with the *Hubble Space Telescope* showed that Holmberg II X-1 is the ionisation source powering the line emission, and

that the morphology of the nebula is inconsistent with narrow beaming of the X-ray emission (Kaaret et al., 2004). Furthermore, the flux in the He II line implies that the total luminosity of the ionisation source is $\gtrsim 6 \times 10^{39} \text{ erg s}^{-1}$, suggesting that the compact object is truly ultraluminous.

Relativistic beaming

Mirabel & Rodríguez (1999) suggested that a number of nearby galaxies should host microblazars *i.e.*, microquasars with relativistically beamed jets pointed towards the observer. This implies that the spectra of some XRBs could be explained by a coupled disc/jet model, where some of the X-ray emission is relativistically beamed and is produced by synchrotron and inverse-Compton radiation in a jet (Körding et al., 2001). A possible ULX microblazer is M74 X-1, which exhibits extreme variability and behaviour that resembles stellar-mass Galactic microquasars (Krauss et al., 2005). Therefore the emission mechanism may be related to relativistically beamed jets which produce the high observed X-ray luminosity (up to $\sim 1.2 \times 10^{40} \text{ erg s}^{-1}$; Krauss et al. 2005). A further example of stellar-mass microblazar was suggested by Soria et al. (2006) for NGC 5408 X-1, which is one of the few ULXs with a radio counterpart (Kaaret et al., 2003). In this case the extreme luminosity ($L_X \sim 10^{40} \text{ erg s}^{-1}$) would be due to Doppler boosting, its radio emission would be synchrotron from the jet; its X-ray spectrum could be produced by synchrotron self-Compton or inverse-Compton scattering of low energy photons (from the disc or donor star) by the relativistic jet (Körding et al., 2002). As with anisotropic radiation, this model reduces the required ULX black-hole mass to standard values (*i.e.*, $< 10 M_\odot$).

Super-Eddington accretion discs

Begelman (2002) suggested that some observed ULXs are actually due to thin, super-Eddington accretion discs orbiting stellar-mass black-holes. Such discs may arise as a result of strong density inhomogeneities which produces a photon-bubble instability and causes the disc to become ‘leaky’. In this way the disc becomes porous to radiation leakage which means that more radiation can escape without inflating the disc, thereby permitting the luminosity to exceed the Eddington limit while the disc remains geometrically thin. Such models suggest that accretion discs around stellar-mass black-holes could radiate as much as ~ 10 times the Eddington limit.

1.4 Overview of this thesis

The main aim of this thesis is to investigate the underlying nature and physical properties of ULXs using deep *XMM-Newton* observations. This thesis also examines the overall X-ray properties of two nearby galaxies which harbour such objects. Chapter 2 presents the instrumentation and data analysis techniques. Chapter 3 presents an in depth analysis of the spectral and temporal properties of a ULX in the nearby Magellanic-type galaxy NGC 55. Chapter 4 proceeds to present an analysis of this Magellanic-type galaxy, concentrating on the discrete source population and underlying diffuse emission. Chapter 5 presents a similar analysis on the X-ray properties of the more active spiral galaxy NGC 4945. Chapter 6 focuses on the ULX phenomenon by investigating the spectral properties of the best quality datasets to date. A review of this work is given in Chapter 7 followed by a discussion of further work in the field and how this may be addressed with current and future X-ray observatories.

Chapter 2

Instrumentation and Data Analysis

2.1 The *XMM-Newton* Space Observatory

The work in this thesis is based on observational data from the *XMM-Newton* satellite (Jansen et al., 2001). *XMM-Newton* is the largest scientific observatory (4 tonne, 10 m long) developed by the European Space Agency (ESA) and is the second ‘Cornerstone’ mission of ESA’s Horizon 2000 Programme. An artists impression of the spacecraft (erroneously shown in low-Earth orbit) is given in Fig. 2.1.

The satellite was launched on 10th December 1999 and placed in a 48 hour highly elliptical orbit (7000 km perigee, 114 000 km apogee), inclined at 40° to the equator. This orbit was chosen to allow the onboard instruments to be passively cooled to between -80°C and -100°C. The lowest portion of this orbit is contained within the radiation belts, so operations are limited to altitudes above 60 000 km. However, this choice of orbit still permits long, uninterrupted observations (up to ~ 40 hours out of the 48 hour orbit are available for scientific observations above the radiation belts).

XMM-Newton comprises two large payload modules, located either end of a long carbon fibre tube which forms the telescope optical bench (Fig. 2.2). In addition to most of the spacecraft sub-systems, the service module (left-hand side of Fig. 2.2) contains a 30 cm optical/UV telescope (Optical Monitor [OM]) which reflects light through a filter-wheel to detectors in its focal plane. The OM detectors

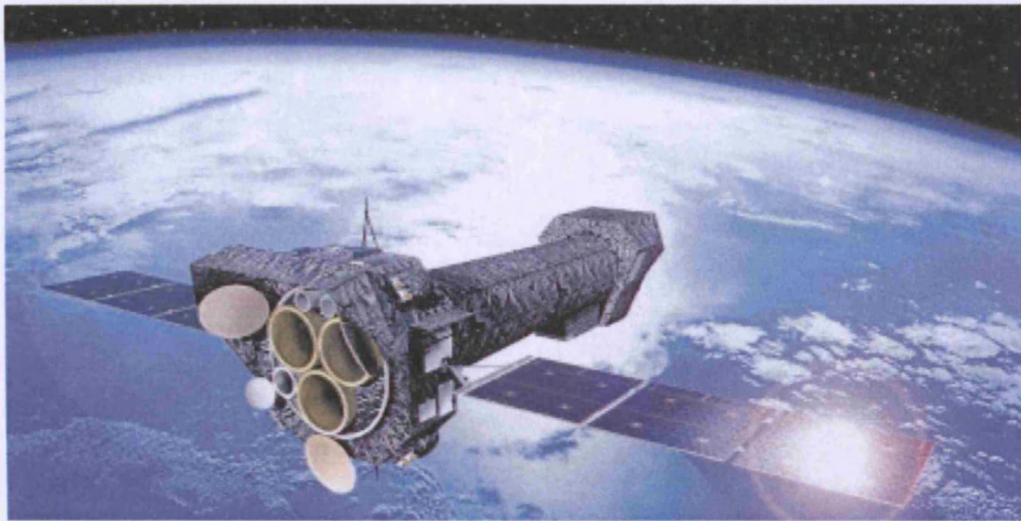


Figure 2.1: Artists impression of the *XMM-Newton* Observatory, taken from http://www.terma.com/multimedia/space_xmm_courtesy_esa_420.jpg.

consist of micro-channel plate (MCP) intensified CCDs (MICs)¹. Photons coming from the mirror hit a photocathode which is optimised for the UV and blue and provides a sensitivity from 160 nm to 600 nm, from where the signal is amplified ($\sim 10^5$ times) by three consecutive MCPs. After this the electrons hit a phosphor layer, from which the resulting photons are imaged onto a CCD. The service module also contains three X-ray Mirror Modules, each with 58 Wolter-I high-precision concentric mirrors, which are nested to offer the largest collecting area. The OM is co-aligned with the X-ray telescopes, providing complementary data on the X-ray sources *e.g.*, monitoring and identification of optical/UV counterparts.

Each X-ray telescope has a different CCD detector in its focal plane (located on the focal plane assembly; right-hand side of Fig. 2.2), collectively known as the European Photon Imaging Cameras (EPIC). Two of the cameras contain seven identical front illuminated Metal Oxide Semi-conductor (MOS) CCD arrays each (MOS-1, MOS-2; Turner et al. 2001), while the third camera consists of a single silicon wafer containing twelve back-illuminated pn CCDs (Strüder et al., 2001). The telescopes containing the MOS cameras are also fitted with Reflection Grating Spectrometers (RGS; den Herder et al. 2001) which perform high resolution dispersive X-ray spectroscopy. The MOS cameras receive just 44%

¹ A simple CCD is not good enough to achieve the desired limiting sensitivity of 24th magnitude with just a 30 cm diameter telescope.

of the incident flux due to a 50% diversion of flux from the spectrometers and 6% from structural obscuration. However, the third telescope with the pn camera at its focus has an unobstructed beam.

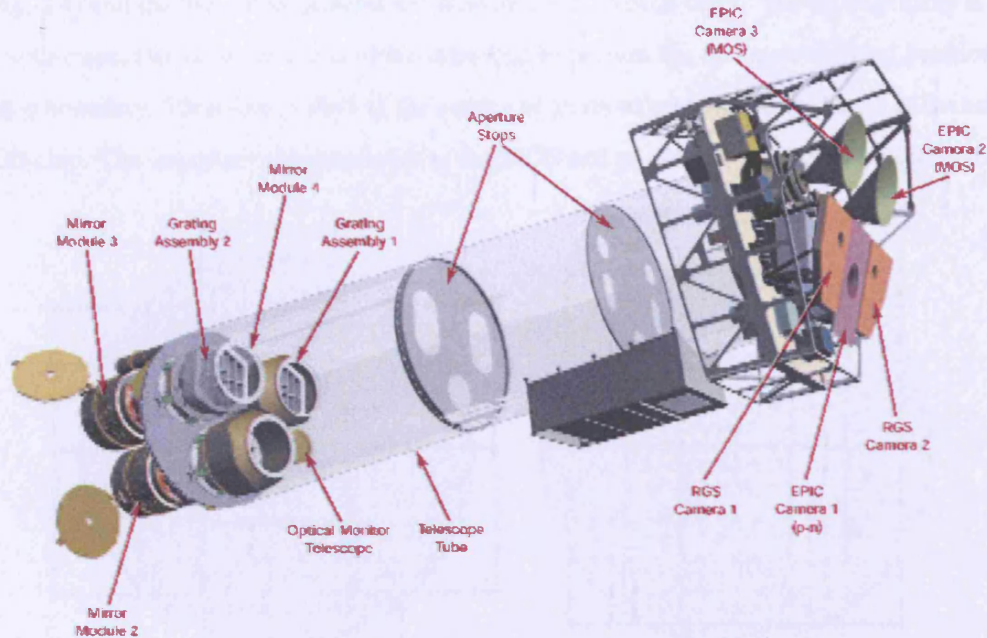


Figure 2.2: Sketch of the *XMM-Newton* payload, taken from <http://esapub.esrin.esa.it/bulletin/bullet100/BAGNASCO.pdf>.

The six science instruments onboard *XMM-Newton* (*i.e.*, 3 EPIC detectors, 2 RGS instruments and the OM) operate simultaneously unless prohibited *e.g.*, by target brightness constraints. However, the instruments themselves work independently (*i.e.*, exposures of the individual instruments do not necessarily have the same start or stop times) and each can have different modes of data acquisition (see next section). The work in this thesis focuses on data from the EPIC instruments, therefore these detectors are described in more detail in the following section.

2.1.1 European Photon Imaging Cameras

The EPIC cameras can perform sensitive imaging observations over a 30' field-of-view (FOV) and a 0.15–15 keV energy range. However, the MOS and pn CCDs are fundamentally different with respect to chip geometry and instrumental characteristics (*e.g.*, different readout times and detector quantum efficiencies). Fig. 2.3 shows a rough sketch of the detector layout and the sensitive area of each detector.

The 7 MOS CCDs each measure $10.9' \times 10.9'$, while the 12 chips of the pn camera each measure $13.6' \times 4.4'$. The detector edges of the MOS chips slightly overlap each other creating unusable areas (see Fig. 2.4) and the two MOS cameras are rotated at 90° to each other. The pn chip array is slightly offset with respect to the optical axis of the telescope to prevent the on axis observing position falling on a chip boundary. Therefore $\geq 90\%$ of the energy of an on-axis point source can be collected on one pn CCD chip. The important characteristics of the MOS and pn detectors are summarised in Table 2.1.

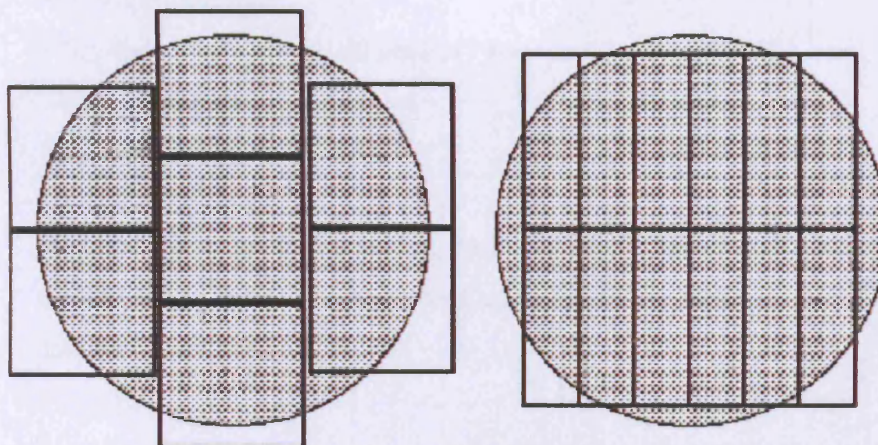


Figure 2.3: A comparison of the focal plane organisation of the EPIC MOS (*left*) and pn (*right*) cameras. The shaded circle depicts a $30'$ diameter area.

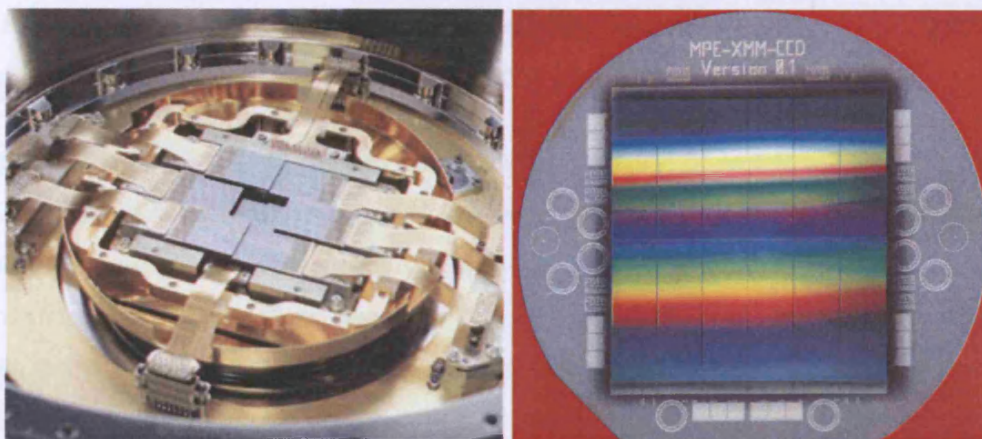


Figure 2.4: EPIC MOS and pn CCDs, taken from <http://xmm.vilspa.esa.es>.

Table 2.1: An overview of the *XMM-Newton* EPIC instrumental characteristics

Instrument	EPIC-MOS	EPIC-pn
Bandpass	0.15–12 keV	0.15–15 keV
Orbital target visibility ^a	5–135 ks	5–135 ks
Sensitivity ^b	$\sim 10^{-14}$ erg cm ⁻² s ⁻¹	$\sim 10^{-14}$ erg cm ⁻² s ⁻¹
Field-of-view	30'	30'
PSF (<i>FWHM/HEW</i>)	5'' /14''	6'' /15''
Pixel size	40 μ m (1.1'')	150 μ m (4.1'')
Timing resolution ^c	1.5 ms	0.03 ms
Spectral resolution ^d	~ 70 eV	~ 80 eV

NOTES: ^a Total time available for science per orbit, ^b after 10 ks in the range 0.15–15 keV, ^c in fast data acquisition mode *i.e.*, timing mode for the EPIC detectors, ^d at 1 keV.

The EPIC cameras can be operated in several modes of data acquisition. For the MOS cameras, the central CCD can be operated separately in 4 different observing modes, while the 6 outer CCDs remain in standard imaging mode. This ensures that all CCDs are always gathering data, independent of the choice of operating mode. The pn camera has 6 different modes of operation; 3 of which involve all four quadrants of the detector (full frame, extended full frame and large window mode), while the other 3 modes (small window, timing and burst) can be operated with one single CCD. The operating modes for the MOS and pn detectors are shown in Fig. 2.5.

The EPIC CCDs are not only sensitive to X-ray photons, but also to IR, visible and UV light. Therefore the X-ray signal from an astronomical target may become contaminated by those photons if the source also has a high optical flux. To prevent this each EPIC camera is also equipped with a set of four aluminised optical blocking filters; two thin filters, one medium filter and one thick filter. The EPIC cameras can be operated in closed and open filter positions. The former is used to protect the CCDs from soft protons in orbit, while the open position could be used for observations when no filter is needed *i.e.*, where the light flux is very low.

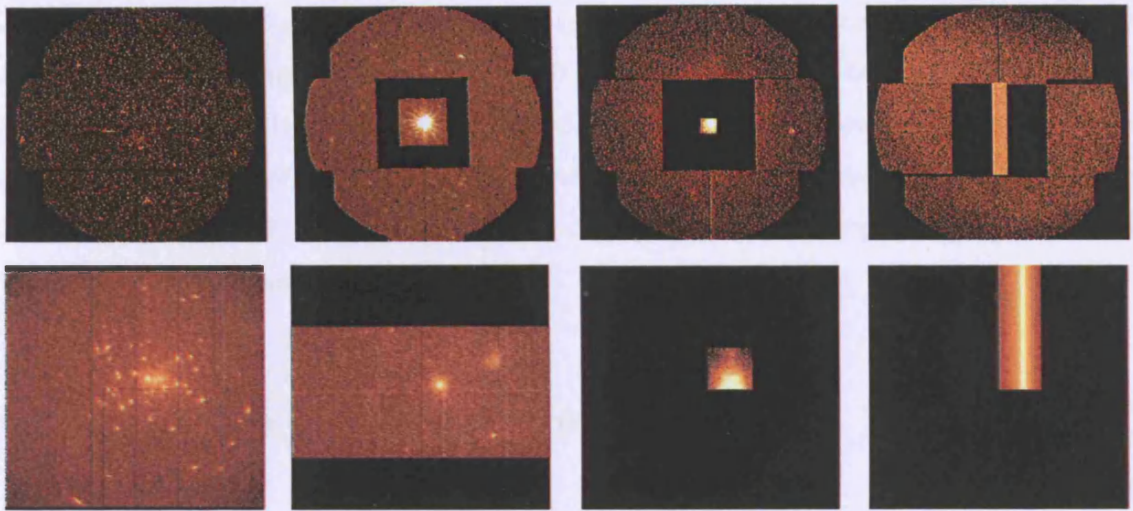


Figure 2.5: Operating modes for the MOS (*top panel*) and pn (*bottom panel*) CCD cameras—from left to right: full frame modes, large window modes, small window modes and timing modes.

CCD cameras degrade when exposed to the extreme environment of space due to radiation, temperature and low pressure effects. Such degradation includes gradual changes over timescales of years, or it can be more sudden due to solar activity or particle/micro-meteorite impacts. This can lead to effects ranging from a change in the Charge Transfer Efficiency (CTE) of the CCDs (*i.e.*, the amount of charge successfully moved from one pixel to another as an X-ray event is read out), to a fatal failure of the whole instrument. Therefore it is essential to monitor the health of the system throughout the mission to ensure sustained performance of the instruments and to preserve the quality of the scientific data. Indeed, the instrument health of *XMM-Newton* has been steadily monitored since the beginning of the mission. To date the EPIC detectors have suffered 4 events interpreted as micrometeoroid impacts (Kirsch et al., 2005), the most recent of which led to the loss of EPIC-MOS1 CCD6 (one of the 7 CCDs in the EPIC-MOS1 focal plane). Such impacts are thought to be the cause of additional hot pixels seen in the EPIC cameras. On 6–7 November 2002, the MOS cameras (which are qualified to operate down to -130°C) were cooled from their nominal operating temperatures (-100°C) down to -120°C . This had a curative effect on the bright pixels produced from such impacts and also improved the MOS energy resolution and reduced the number of bad pixels in the Current Calibration Files (CCFs). One of the main surprises and concerns after launch was the high fluctuations and variability of the particle background in the cameras. This background consists of two main components: a relatively quiescent component due to the interaction of high energy particles ($> 100\text{ MeV}$) with the detector

structure (and perhaps the detectors themselves) and its associated fluorescence, and a variable and flaring component attributed to soft protons (< 100 MeV) which are funnelled towards the detectors by the X-ray mirrors. It is believed that the soft proton population is somehow related to the radiation belts as the probability of soft proton flaring decreases with the distance from the Earth. Overall up to 15%–20% of the *XMM-Newton* observing time can be lost due to radiation flaring although this is highly variable from observation to observation.

2.2 Comparison with other X-ray missions

While the work in this thesis is based on *XMM-Newton* data, there are references and comparisons to other X-ray missions throughout. Therefore this section details the basic characteristics of three other X-ray missions mentioned in this work, namely *ASCA*, *ROSAT* and *Chandra* (with much of this information taken from the *XMM-Newton* Users Handbook²). Table 2.2 shows several parameters which describe the capabilities of each satellite. One particularly important feature for X-ray missions is the effective area of the telescope's mirrors, as this is the best measure of its photon collecting power. A comparison of the effective areas of *XMM-Newton*, *Chandra*, *ROSAT* and *ASCA* is shown in Fig 2.6. It is clear that *XMM-Newton* has provided a huge increase in the collecting power of X-ray telescopes.

Table 2.2: Comparison of *XMM-Newton* with other X-ray satellites

Satellite	Energy range (keV)	Mirror PSF ^a FWHM / HEW (″)	Mirror effective area ^b (cm ²)	Orbital target visibility (hr)
<i>XMM-Newton</i>	0.1–15	6/15	4650	40
<i>Chandra</i>	0.1–10	0.2/0.5	800	50
<i>ROSAT</i>	0.1–2.4	3.5/7	400	1.3 ^c
<i>ASCA</i>	0.5–10	73/174	350	0.9 ^c

NOTES: ^a FWHM (Full Width at Half Maximum), HEW (Half Energy Width)—the diameter of the circle within which half of the photons fall, ^b at 1 keV, ^c low orbit with Earth occultation.

²http://xmm.vilspa.esa.es/external/xmm_user_support/documentation/uhb.2.1/

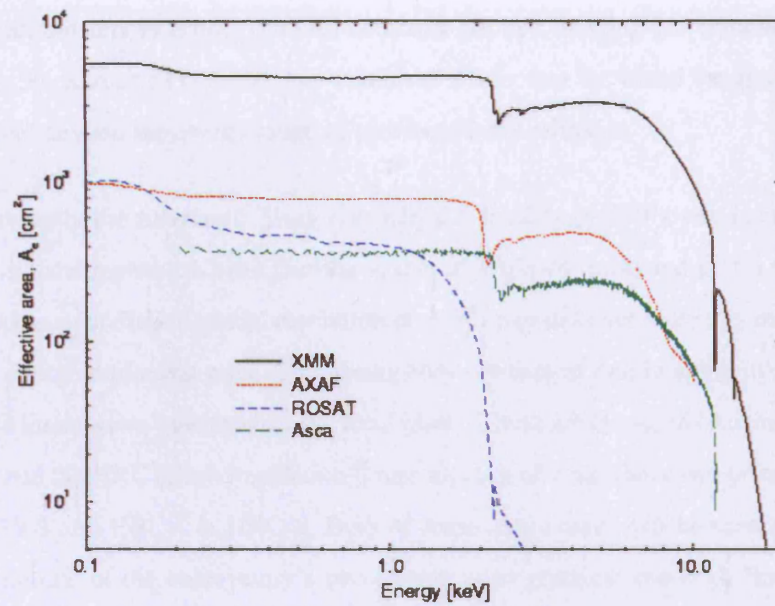


Figure 2.6: The effective area of all *XMM-Newton* mirror modules, in comparison with those of other X-ray satellites (logarithmic scale).

ROSAT – The Roentgen satellite was launched on 1st June 1990 and operated for almost 9 years. The satellite consisted of one X-ray telescope which could be used in conjunction with either the Position Sensitive Proportional Counter (PSPC) or the High Resolution Imager (HRI) over 0.1–2.5 keV. The first 6 months of the mission were dedicated to an All-Sky Survey using the PSPC with a 2° diameter FOV, followed by a pointed phase. The HRI had a smaller FOV of $\sim 0.6^\circ$ square, but an improved spatial resolution. Also on-board was a Wide Field Camera (WFC) with its own mirror system and a FOV of 5° diameter, which operated in the EUV range of 62–206 eV. Science highlights include an X-ray All-Sky Survey catalogue with more than 150,000 objects and an EUV All-Sky Survey catalogue (479 objects).

ASCA – The Advanced Satellite for Cosmology and Astrophysics was launched on the 20th February 20, 1993 and operated successfully until the 15th July 2000. *ASCA* was the first X-ray mission to combine imaging capability with a broad bandpass, good spectral resolution, and a large effective area (Tanaka et al., 1994). The satellite comprised four X-ray telescopes working in conjunction with either solid-state imaging spectrometers (SIS; 0.4–10 keV) or gas imaging spectrometers (GIS; 0.8–10 keV). The two SIS detectors are identical CCD cameras with a maximum FOV of $22' \times 22'$, and were the first

X-ray CCD spectrometers in orbit. The GIS detectors are two imaging gas scintillation proportional counters with a 50' diameter FOV. One key feature of *ASCA* was the broad bandpass which provided spectra of sources beyond the energy range of previous X-ray missions.

Chandra – Previously the Advanced X-ray Astrophysics Facility (AXAF), was launched on 23rd July 1999 into an elliptical high-earth orbit (similar to that of *XMM-Newton*) and is still in operation today. *Chandra* provides unparalleled spatial resolution of $< 1''$, operates over an energy range of 0.1–10 keV and possesses a large collecting area. The observatory consists of one imaging telescope which may have one of two instruments inserted into the focal plane. These are the ACIS (Advanced CCD Imaging Spectrometer) and the HRC (High Resolution Camera), each of which have two principal components–ACIS-I & ACIS-S and HRC-I & HRC-S. Both of these instruments can be used on their own or in conjunction with one of the observatory's two transmission gratings: the High Energy Transmission Grating Spectrometer (HETGS) and the Low Energy Transmission Grating Spectrometer (LETGS) which are dedicated to high resolution spectroscopy. Each spectrometer is activated by swinging an assembly into position behind the mirrors, where they diffract the intercepted X-rays by an amount which depends sensitively on the X-ray energy.

2.3 Data reduction

XMM-Newton has its own suite of software tools specifically developed to perform data reduction, extraction and some data analysis. These programs and scripts are collectively known as the Science Analysis Software (SAS), which is developed and maintained by the Science Operations Centre (SOC: Madrid, Spain) and the Survey Science Centre (SSC: Leicester, UK). *XMM-Newton* data are available in two formats; Observation Data Files (ODFs) and Pipeline Processing System (PPS) products. For every *XMM-Newton* observation, the SOC produces an ODF file which contains science telemetry and housekeeping for each instrument, as well as uncalibrated products. The SSC then processes all the ODFs through an automated analysis pipeline, to yield the PPS products. These contain validated scientific products including event lists, images and source lists. These are then returned to the SOC with the original ODFs, for distribution to the scientific community. The analysis presented in this thesis uses EPIC MOS and pn event lists produced by the SAS, to create images, spectra, lightcurves and source detection products as described below.

2.3.1 Filtering event lists

Each EPIC CCD operates in photon counting mode and produces an associated event list. Event lists are tables consisting of one line per received photon, listing attributes of the photon such as the pixel position on the CCD on which it was registered, the arrival time, energy and the type of the event. These event lists can be filtered to reject spurious data and to select good events on which to perform subsequent analysis. This filtering is applied using a ‘selection expression’ and can be based on the pixel position, energy, timing criteria, ‘PATTERN’ and ‘FLAG’ (see below) of the event. The type of the event is specified by the ‘PATTERN’ parameter, and describes how the charge cloud released by the in-falling photon is distributed over the pixels. Therefore ‘PATTERN’ assignments are related to the number of CCD pixels that record a deposit of charge for a given event. The expression ‘PATTERN == 0’ corresponds to single pixel events (*i.e.*, the energy of a photon was released in one CCD pixel only), whereas ‘PATTERN in [1:4]’, ‘PATTERN in [5:8]’ and ‘PATTERN in [9:12]’ correspond to double, triple and quadruple pixel events respectively. For very bright sources, there may be an accumulation of events in the same pixel during the time the CCD is read out (known as ‘pile-up’). These events are interpreted as one single event and therefore cause flux loss and spectral distortion. In these cases, only single pixel events should be used and the inner region of the source should be excluded in the analysis. Fortunately there were no sources in this thesis for which pile up was a problem. Throughout this analysis the ‘PATTERN’ selections were ‘PATTERN ≤ 12’ for the MOS detectors (which maximises the signal-to-noise ratio against non X-ray events) and ‘PATTERN ≤ 4’ for the pn detector (for which spectral analysis calibrations are available). Further screening can be applied using the ‘FLAG’ criteria, which defines the quality of the data. The expression ‘#XMMEA_EM’ is used for the MOS detectors (‘#XMMEA_EP’ for pn) and screens for various event condition flags *e.g.*, near to hot pixels, chip edges or outside the FOV. In some cases (see individual Chapters for more details) a more conservative screening was applied to the pn detectors using ‘FLAG == 0’ which ensures that all events at the edge of a CCD and adjacent to a bad pixel are excluded.

2.3.2 Filtering high background flaring

One of the preliminary steps in EPIC data analysis is to inspect the full-field light curves (see next section) for high background periods. Such periods have measured intensities many factors above the quiescent level and are attributed to soft proton flaring *i.e.*, \sim few 100 keV solar protons which are

accelerated by solar magnetospheric reconnection events. These protons are funnelled towards the *XMM-Newton* detectors by the X-ray mirrors, in the same way as the X-ray photon events. As well as contaminating the X-ray light curves, their spectral variability is also problematic for spectral studies. These flaring events are not flagged in the pipeline processing so must be excluded from future analysis by using a temporal filter in the selection expression. Unfortunately, this screening also causes the loss of ‘good’ data during these intervals.

The data analysis presented in this thesis has included temporal filtering where necessary. In some cases this was as simple as defining a single time region from the light curve which neglected the flaring period. However, other cases which suffered more flaring periods required the use of a specific Good Time Interval (GTI) file. These GTI files were created using the SAS task `tabgtigen` together with a suitable count rate threshold based on the full-field light curves in each case (*i.e.*, just above the quiescent rate). This produces a table (in FITS format) in which only those periods with desirable count rates are listed, thereby excluding those periods with higher count rates from further analysis.

2.3.3 Images, light curves and spectra

Images, light curves and spectra were created from the EPIC event lists using ‘PATTERN’, ‘FLAG’ and temporal filters in the selection expression. Images were created using the SAS task `evselect` (or via the analogous `xmmselect` GUI) and were binned into 4'' per pixel. Additional filtering was applied to select particular energy ranges for the image extraction, as described in the relevant chapters.

Similarly, light curves were extracted using `evselect` (or `xmmselect`), using ‘PATTERN’, ‘FLAG’, energy and temporal filtering. As described in the previous section, full-field light curves were extracted in each case to check for soft proton flaring events. In addition to this, background subtracted light curves for individual sources were also created to examine how the source count rate varies over the course of the observation. Such light curves were created by subtracting nearby source-free background light curves from the source+background light curves (using circular extraction apertures in both cases) to correct for background contamination. The light curves were binned in time bins that provided at least 20 counts per bin, to ensure Gaussian statistics were valid. Where possible, the light curve extraction regions were centred on the same RA and DEC co-ordinates in each EPIC detector.

X-ray spectra were extracted using the SAS task `especget` which produced a source and background

spectrum together with the appropriate Ancillary Response File (ARF) and Redistribution Matrix File (RMF) required in the spectral fitting. Similar to the light curve extraction, circular apertures were used for the spectral extraction of the discrete sources. The position of the background extraction regions were chosen to optimise the calibration where possible. For the MOS detectors, the background was extracted from the same chip as the source, while for the pn detector the background was extracted from the same RAWY position as the source extraction region (although not necessarily the same chip)³.

The final step before spectral analysis was the grouping of the spectra based on a minimum number of counts in each bin. This was performed using the FTOOLS task `grppha` and the binning was chosen to provide at least 20 counts per bin, ensuring Gaussian statistics.

The X-ray spectral analysis was performed using the spectral fitting package XSPEC. In order for XSPEC to predict the spectrum that would be detected by a given instrument, it must know the specific characteristics of the instrument. This information is known as the detector response. For *XMM-Newton* data, the response matrix is the product of the RMF and ARF files mentioned above. These files are created using the SAS tasks `rmfgen` and `arfgen`, which are automatically run by `especget` but can be run separately if desired. The `rmfgen` task creates the correct RMF for the input spectrum by reading the observation mode, observation date, source position and 'PATTERN' selection from the file header. The RMF describes the response of the instrument as a function of energy at the source position. The `arfgen` task calculates the instrument effective area from various contributions, *i.e.*, telescope effective area, vignetting, filter transmission, quantum efficiency, encircled energy correction and the flux loss due to CCD gaps, bad pixels and offset columns⁴. XSPEC also applies the proper renormalisation to the background spectra, using the value of the 'BACKSCAL' keyword in the header of the spectral file(s). This BACKSCAL value is calculated by the SAS task `backscale` (which is automatically run when a spectrum is extracted via `especget`) and takes into account CCD gaps, bad pixels and the size of the extraction region.

2.3.4 Source detection

This section details the source detection routines that were utilised in Chapters 4 & 5. In each case, the MOS-1 and MOS-2 events were combined using the SAS task `merge` (in order to increase the

³RAWY is the long axis of the CCD.

⁴see *XMM-Newton* Users Handbook for further details.

sensitivity of the MOS data), such that the routines were performed on the combined MOS (*i.e.*, MOS-1 plus MOS-2) and pn data as separate channels. The source detection was performed on MOS and pn images (pixel size of $4'' \times 4''$) in three energy bands, chosen to provide a good signal-to-noise coverage of the EPIC data: 0.3–1 keV (soft), 1–2 keV (medium) and 2–6 keV (hard). Corresponding exposure maps (which contain the values of the exposure at each position on the detector) were created from these images using the SAS task `eexpmap`. These exposure maps were then used to create MOS and pn detector masks (via the SAS task `emask`), which show the area to be searched by the source detection tasks.

The main stages in source detection are to detect the sources and record their positions, and then to perform maximum likelihood fits to the sources to characterise them. This thesis has utilised two different methods to initially detect the X-ray sources: a sliding box detection method (`eboxdetect`) and a wavelet detection algorithm (`ewavelet`), both of which were performed separately for the MOS and pn detectors. The `eboxdetect` task is a standard SAS routine and has two different modes of operation. The first mode is the ‘local’ detection mode in which the images are scanned by a sliding square box, and if the signal to noise of the source centred in the box is greater than a specified threshold value, it is marked as an object⁵. The derived source positions were then provided as input for the task `esplinemap` which constructs background maps using source-free regions of the image. These background maps are then utilised in a further run of `eboxdetect` in ‘map’ mode, leading to an improved detection sensitivity and the final `eboxdetect` source list for the detector used. The `eboxdetect` method performs simultaneous detection runs over all three energy bands resulting in output source tables (one each for MOS and pn) containing one row per input image for each detected source, plus a summary row for each source containing the broad band results. Therefore the `eboxdetect` source list contains information for each detected source in all three energy bands as well as the broad band. Limitations of this procedure include difficulties in detecting extended features, close objects and sources near the detection limit.

For this reason the `ewavelet` routine was also implemented which uses a mexican hat wavelet algorithm. The algorithm detects both point sources and extended sources provided that the source extent is not too large ($< 1/8$ th the image size). This method also provides good suppression of multiple false detections in extended sources and is typically better at separating close sources. Unlike the

⁵The signal is derived from the pixel values inside a 5×5 pixel window, and the local background and noise level is estimated from the surrounding 56 pixels (within a full 9×9 pixel window).

`eboxdetect` method, `ewavelet` only has one mode of operation which produces a wavelet source list. Also the `ewavelet` source detection algorithm performs on a single input image, and thus produces separate soft (S), medium (M) and hard (H) source lists for each detector.

After the initial source detection, the `eboxdetect` and the `ewavelet` source lists were analysed separately using a maximum likelihood technique with the SAS task `emldetect`. For an input list of source locations, this task performs simultaneous maximum likelihood point spread function (PSF) fits to the source count distribution in the specified energy band(s) for a particular EPIC detector. The task requires the input source lists in `eboxdetect` format (therefore the `ewavelet` source lists were converted into this format using `FTOOLS`). The task also requires the EPIC images in the S, M and H energy bands, the corresponding exposure and background maps as well as a detector map for each instrument. First-order background maps already existed based on the `eboxdetect` source list but needed to be created in the same way (*i.e.*, via `esplinemap`) based on the `ewavelet` source lists.

Again, while the maximum likelihood fits were performed simultaneously on the three energy bands of the `eboxdetect` source lists for a particular detector, they were performed separately on each band and detector for the `ewavelet` method. This provided output `emldetect` source lists which contain various derived source parameters including the significance of the detection. However, in order to accurately determine the significance of a detected source, an accurate modelling of the background is required. Therefore these `emldetect` source lists were used by the `asmooth` task to create improved adaptively-smoothed background maps from source-excluded regions. A further run of `emldetect` was made using these improved background maps to produce a standardised set of source parameters. A further iteration of the `asmooth` and `emldetect` procedures were performed to create the final `emldetect` source lists from each method.

The resultant source lists were then compared and any additional sources detected via the `ewavelet` method were added to the `eboxdetect` lists that were originally produced from the `eboxdetect` ‘map’ mode run. This provided complete lists of MOS and pn sources detected from both methods which needed to undergo the final parameterisation process. As such, the `emldetect` and `asmooth` iterations mentioned above were performed on these combined source lists. This provided consistent multi-band parameterised MOS and pn source lists for each observation which contain the following derived parameters: source count rate (total and in each band), likelihood of detection (total and in each band), likelihood of source extent, and two hardness ratios ($HR1 = (M - S)/(M + S)$ and

$HR2 = (H - M)/(H + M)$). Energy Conversion Factors (ECFs) were calculated for each instrument and energy band from a power-law continuum spectrum with $\Gamma = 1.7$ absorbed by the Galactic foreground column towards the galaxy in question. These ECFs were used by `emldetect` to convert vignetting corrected count rates into fluxes. Sources were classified as significant detections if they had a likelihood (DET_ML) value of 10 or more (corresponding to a detection significance of $> 4\sigma$) in at least one of the S/M/H energy bands, not just in the combined summary band. Therefore as a final quality check, any sources that did not pass the significance test in at least one of the S/M/H energy bands were removed, as were sources deemed to be unreliable based on a visual inspection of the images (*e.g.*, unconvincing sources at chip edges or gaps).

The final step in the source detection process was to merge the final `emldetect` source lists into the final galaxy source list using the `srcmatch` task, which correlated sources co-located within their 4σ centroiding errors plus a $1''$ systematic error. The first galaxy on which source detection was performed had two observations which were slightly offset from each other which resulted in four source lists (one for each of the detectors and observations) to be combined with `srcmatch`. However, when this was attempted the final source list contained multiple detections of the same source in a number of cases. This was remedied by applying the task `eposcorr` to the four source lists prior to `srcmatch`. The `eposcorr` task checked for astrometric offsets by correlating the source lists with the USNO A2.0 optical catalogue and derived the ‘optimum offsets’ for each observation. These offsets are then used by the task to correct the X-ray source positions to the USNO frame of reference. The corrected source lists were then combined using `srcmatch` to produce the final galaxy source list. It was not deemed necessary to perform the `eposcorr` task on the output source lists of the other galaxy as these correlated well with `srcmatch` without any correction. A flow chart summarising the source detection process is shown in Fig. 2.7.

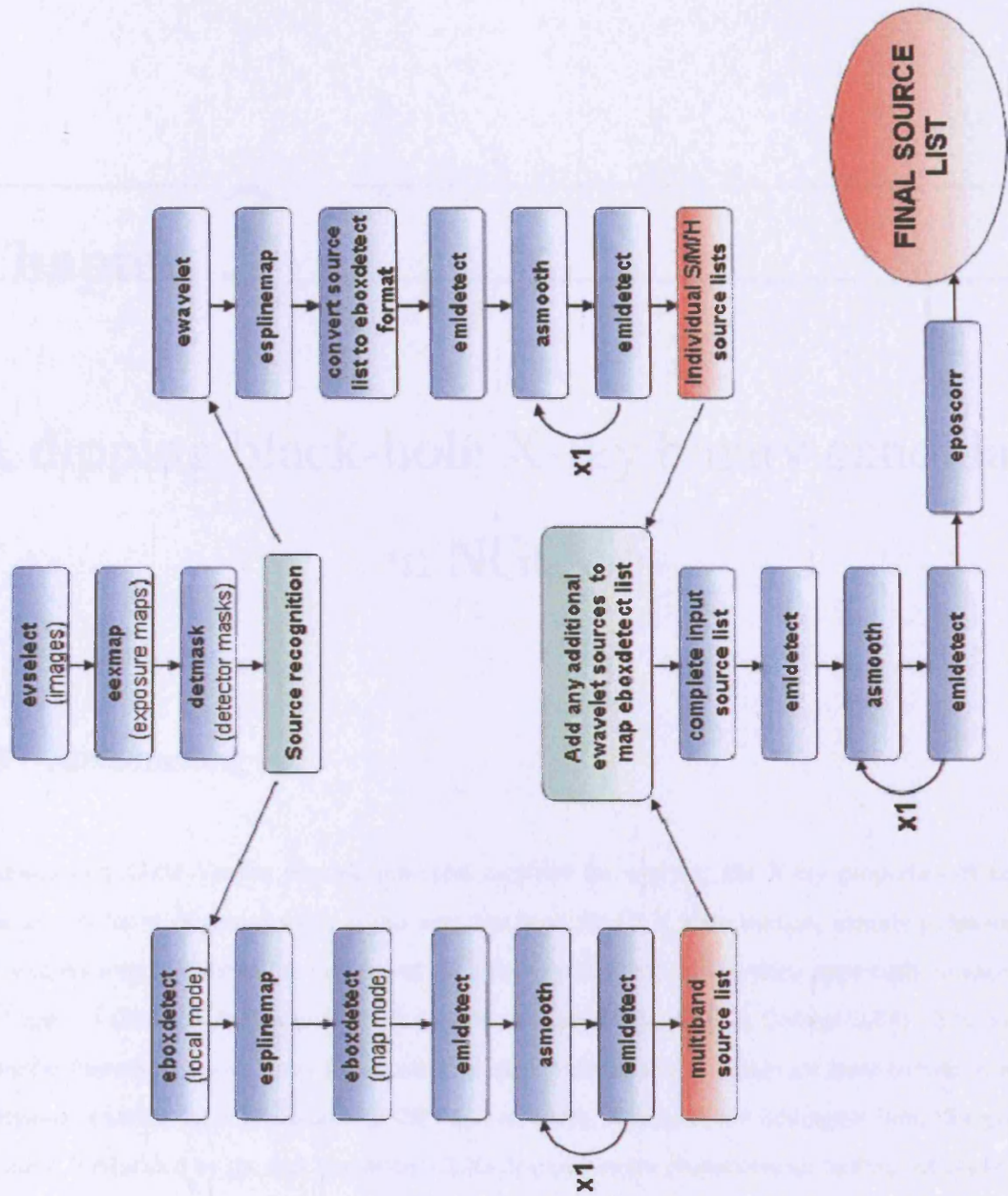


Figure 2.7: Source detection flow chart followed separately for each detector and observation. The procedure shown produces: one multi-band eboxdetect source list and one S/M/H ewavlet source list. stage to produce a source list in each band). Any additional S/M/H ewavlet sources are incorporated into the multi-band eboxdetect ‘map’ source list. The combined list is then analysed and (in one case) is corrected for astrometric offsets using `eposcorr`, providing a complete source list for a particular detector and observation. The process is repeated to achieve all the required detector/observation combinations and the resultant source lists are combined into the final galaxy source list using `srcmatch`.

Chapter 3

A dipping black-hole X-ray binary candidate in NGC 55

3.1 Introduction

Chandra and *XMM-Newton* provide powerful facilities for studying the X-ray properties of nearby galaxies. A focus of recent work in this area has been the ULX phenomenon, namely point-like X-ray sources located outside the nucleus of the galaxy with X-ray luminosities apparently in excess of $10^{39} \text{ erg s}^{-1}$ (Roberts & Warwick 2000; Colbert & Ptak 2002; Miller & Colbert 2004). It is entirely plausible that sources with X-ray luminosities at, or just above, this threshold are mass-transfer binaries containing a stellar mass black-hole ($3\text{--}20 M_{\odot}$) radiating at close to the Eddington limit. Supporting evidence is provided by the fact that many ULXs display similar characteristics to those of established BHBs (*e.g.*, Makishima et al. 2000). However, as previously mentioned the nature of the subset of ULXs with X-ray luminosities in excess of a few $\times 10^{39} \text{ erg s}^{-1}$ is less certain, since these could be systems harbouring IMBHs (Colbert & Mushotzky, 1999), radiating anisotropically (King et al., 2001) or possessing truly super-Eddington discs (Begelman, 2002).

It has been estimated that an accreting black-hole, as opposed to a neutron star, is present in at least 10% of all bright XRBs (McClintock & Remillard, 2006). At the present time there are only 18 dynamically-confirmed stellar-mass BHBs, most of which were discovered as X-ray novae in our own

Galaxy (McClintock & Remillard, 2006). A further 20 or more candidate objects, which exhibit all the characteristics of black-hole systems, can be added to this sample (McClintock & Remillard, 2006). Using *Chandra* and *XMM-Newton*, an individual bright XRB can be studied out to a distance of about 10 Mpc, hence studies of nearby galaxies have the potential for greatly extending our knowledge of luminous XRBs of all types, including black-hole systems. For example, M31 has been a prime target for recent observations (*e.g.*, Kong et al. 2002; Shirey et al. 2001; Osborne et al. 2001), and at least one good BHB candidate has been identified on the basis of its X-ray properties (RX J0042.3+4115; Barnard et al. 2003). The other major Local Group galaxy, M33, also hosts many discrete X-ray sources (*e.g.*, Haberl & Pietsch 2001), including the most luminous persistent X-ray source in the Local Group (M33 X-8; Trinchieri, Fabbiano & Peres 1988). This source is another good black-hole candidate, with recent *Chandra* observations revealing characteristics consistent with accretion onto a $> 5 M_{\odot}$ object (La Parola et al., 2003). Yet a further example is the discovery of an eclipsing XRB in NGC 253 (Pietsch et al., 2003). This Chapter discusses the properties of the brightest X-ray source detected in NGC 55. This source sits right on the boundary of the ‘normal’ binary/ULX categorisation and, on the basis of its X-ray luminosity and spectral properties, is most probably a black-hole system.

NGC 55 is a member of the nearby Sculptor group of galaxies, located in the region of the South Galactic Pole at a distance of 1.78 Mpc (Karachentsev et al., 2003). It is morphologically similar to the Large Magellanic Cloud but viewed edge-on with its bar pointing almost along the line of sight ($i = 90^{\circ}$, Tully 1988). NGC 55 has previously been studied in the X-ray band through *ROSAT* PSPC (Read, Ponman & Strickland 1997; Schlegel, Barrett & Singh 1997) and HRI (Roberts, 1997) observations. The PSPC data revealed seven bright point-like X-ray sources coincident with the galaxy (Schlegel et al. 1997). A subsequent re-analysis of the PSPC data, in conjunction with the HRI data, revealed 25 X-ray point sources coincident with, or in close proximity to, the disc of the galaxy (Roberts, 1997). The *ROSAT* observations showed one particular object, located $\sim 7'$ to the east of the main bar complex, to be several times brighter than any other X-ray source in the galaxy (Source 7 of Schlegel et al. 1997; Source 6 of Read et al. 1997; and Source N55-14 of Roberts 1997). The *ROSAT* PSPC data further revealed this source to be spectrally soft (bremsstrahlung temperature $kT \sim 0.8 - 1.0$ keV or power-law photon index $\Gamma \sim 3 - 4$) and mildly absorbed ($N_H \sim 2 - 4 \times 10^{21}$ atoms cm^{-2}) with a derived X-ray luminosity of $\sim 7 \times 10^{38}$ erg s^{-1} in the 0.1 – 2.4 keV *ROSAT* band, adopting a distance of 1.78 Mpc. Crucially, both long- and short-term variability were seen, suggesting this is a luminous accretion-powered XRB. This source is revisited in the present Chapter, using new, high quality *XMM-*

Newton observations to investigate its spectral and temporal behaviour. The Chapter is structured as follows: § 3.2—details of the observations and data reduction, § 3.3—details of the temporal and spectral analyses, § 3.4—a discussion of the results and finally, the conclusions are summarised in § 3.5.

3.2 The XMM-Newton observations and preliminary data analysis

Two observations of NGC 55 were carried out by *XMM-Newton* in the period 14th–15th November 2001 (revolution 354), with the second observation commencing 2.2 ks after the termination of the first. The pointings were offset by $\sim 7'$ in opposite directions with respect to the centre of the galaxy so as to image the full extent of the edge-on galaxy disc (see Table 3.1). The EPIC MOS and pn cameras were operated in the full window mode with the thin filter deployed. The datasets were pipeline processed and reduced using standard tools of the XMM-SAS version 5.4.1. Whilst the instrument background was at a constant low level during the first observation, the second was affected by soft proton flaring towards the end of the exposure. A time filter was used to reject the flaring episode and also to select only those data recorded when all three cameras (MOS-1, MOS-2 and pn) were in operation. This resulted in a net exposure time of 30.4 ks and 21.5 ks of data for the first and second observation respectively with a gap of 6.2 ks between the two datasets.

Table 3.1: The *XMM-Newton* observations of NGC 55

Obs ID	R.A. (J2000)	Dec. (J2000)	Date	UT _{start}
0028740201	00 15 46.0	-39 15 28	2001-11-14	14:20:08
0028740101	00 14 32.9	-39 10 46	2001-11-15	00:24:43

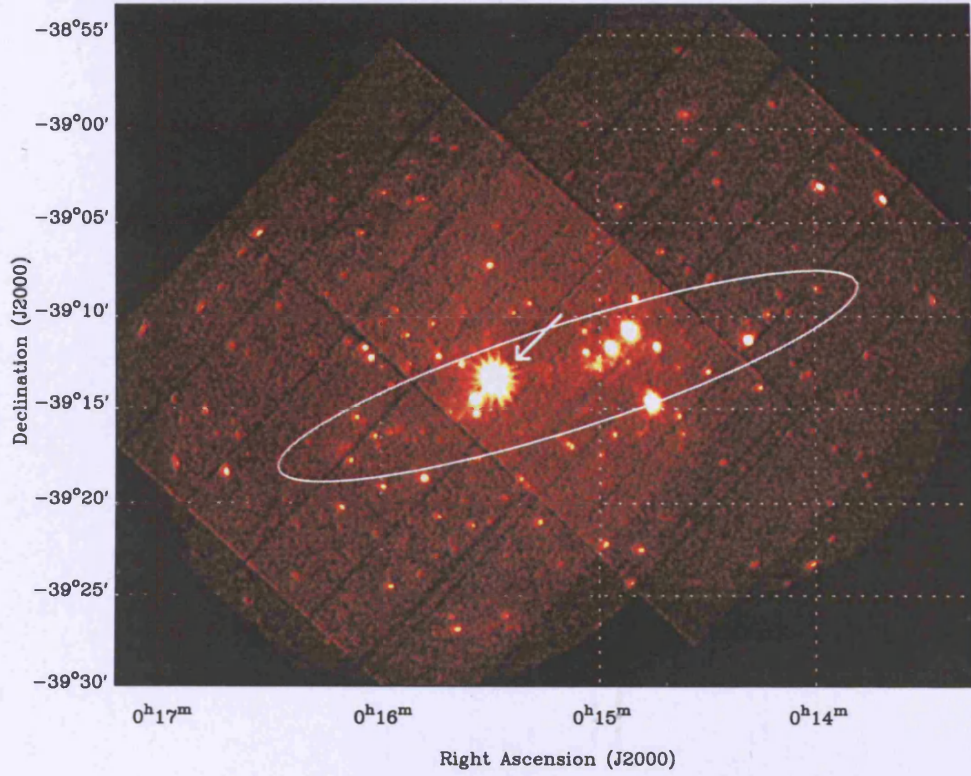


Figure 3.1: The *XMM-Newton* image of the NGC 55 field in a broad (0.3–10.0 keV) bandpass. The field centre is at R.A. $00^{\text{h}}15^{\text{m}}18.0^{\text{s}}$, Dec $-39^{\circ}13'33''$ (J2000) and the image size is $40' \times 40'$. The position of XMMU J001528.9-391319 is highlighted by the arrow. North is up and East is to the left.

Images were produced in the 0.3–10.0 keV energy band for each observation and for each camera and were then combined using the *emosaic* SAS task. The resulting mosaiced X-ray image is shown in Fig. 3.1. The corresponding DSS-2 optical image of the galaxy with X-ray contours overlaid is shown in Fig. 3.2. The brightest source in the earlier *ROSAT* observations retains this distinction in the *XMM-Newton* observations. Its position has been determined as R.A. $00^{\text{h}}15^{\text{m}}28.95^{\text{s}}$, Dec. $-39^{\circ}13'19.1''$ (J2000) with an uncertainty of $\sim 1''$ and has been given the source designation XMMU J001528.9-391319.

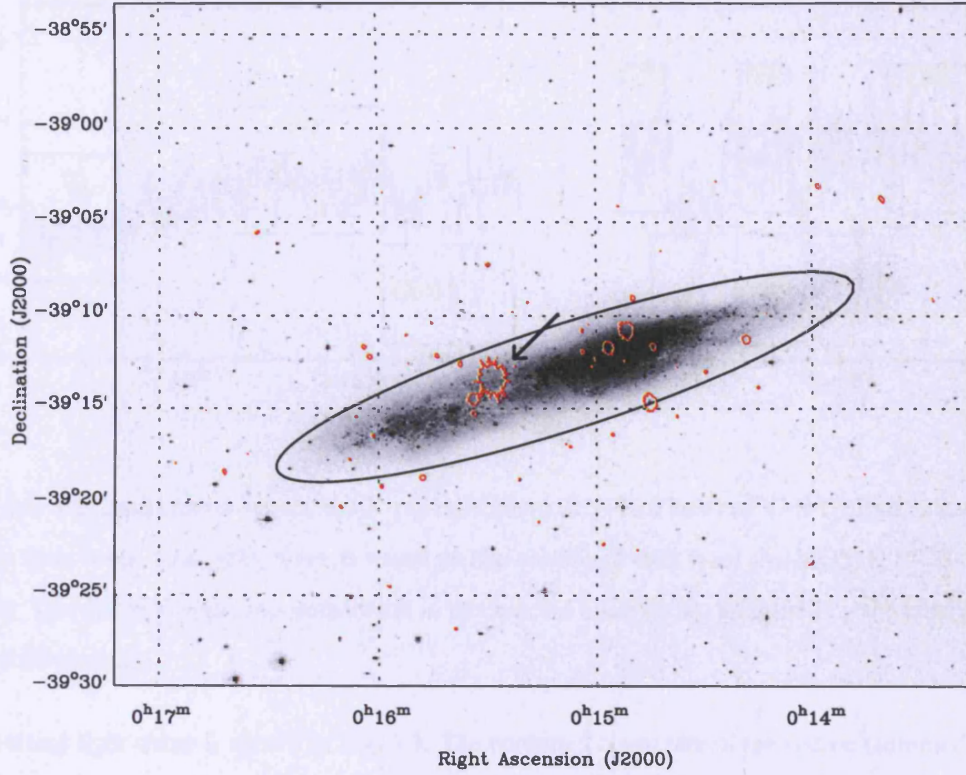


Figure 3.2: Optical DSS-2 (blue) image of NGC 55, with the rotation angle aligned precisely to a North-South projection. The red contour, which is derived from a lightly smoothed version of the X-ray image (using a circular Gaussian mask with $\sigma = 1$ pixel = $4''$), corresponds to a surface brightness of $16 \text{ count pixel}^{-1}$. North is up and East is to the left.

3.3 The X-ray properties of XMMU J001528.9-391319

3.3.1 X-ray light curve

A background-subtracted source light curve based on the combined data from the three EPIC cameras was extracted from each observation in the 0.3–10.0 keV band. A circular source extraction region of radius $52''$ was used as well as a nearby background region of the same dimension. When combining the two datasets, a scaling factor of 2.1 was applied to the count rates measured in the second exposure, so as to account for the extra vignetting arising from the large off-axis angle of the source in this observation.

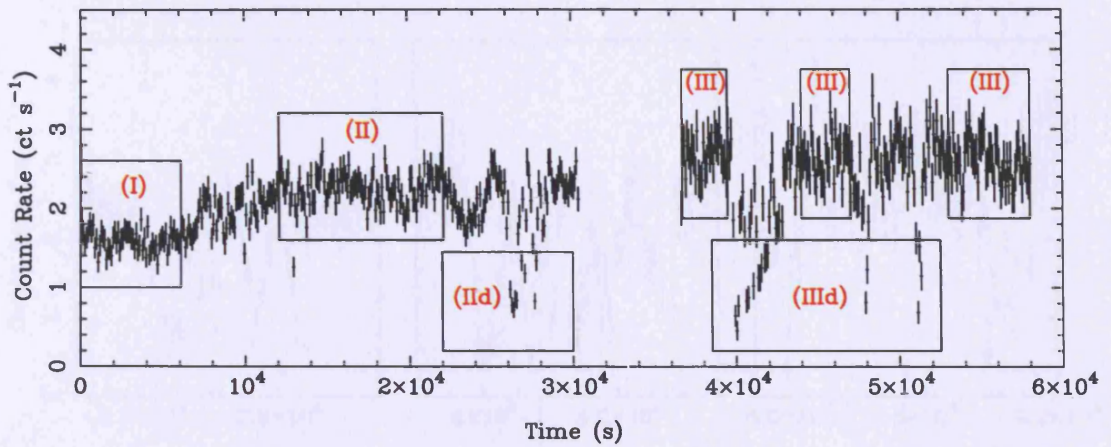


Figure 3.3: The background-subtracted X-ray light curve (0.3–10.0 keV) of XMMU J001528.9-391319 in 100 s time bins. This light curve is based on the combined data from the MOS-1, MOS-2 and pn cameras. The different segments considered in the spectral analysis are identified by the labelled boxes (see text for details).

The resulting light curve is shown in Fig. 3.3. The corrected count rate of the source (summed over the three EPIC cameras) varies from 0.5–3.5 count s^{-1} with considerable temporal structure including a marked upward drift, a significant level of underlying chaotic activity and pronounced dips. Fig. 3.4 illustrates the structure of the dips in more detail and shows that a typical dip lasts between 100–300 s and that some of the dips correspond to a 80%–90% reduction in the source flux in the 0.3–10.0 keV band.

The variability of the source was further investigated by extracting light curves, using the method described above, in three energy bands which optimised the signal to noise ratio: 0.5–1.0 keV (soft), 1.0–2.0 keV (medium) and 2.0–4.5 keV (hard), as shown in Fig. 3.5. These light curves show that the upward drift apparent in the broad-band light curve throughout the observation is due largely to changes above 1.0 keV. The dips are present in all three energy bands although the depth of the dips appears to be somewhat greater in the harder bands, such that the maximum flux diminution approaches 100% in the 2.0–4.5 keV band.

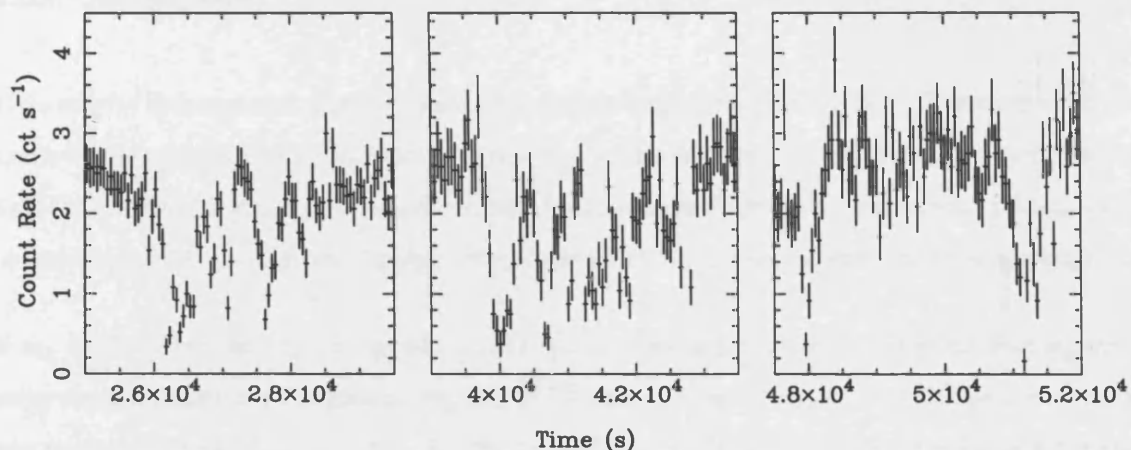


Figure 3.4: Zoomed in regions of the X-ray light curve shown in Fig. 3.3, with 50 s time binning. *Left panel*: the dipping episode from the first observation, *centre panel*, the first dipping episode from the second observation, *right panel*: remaining dip episodes of the second observation.

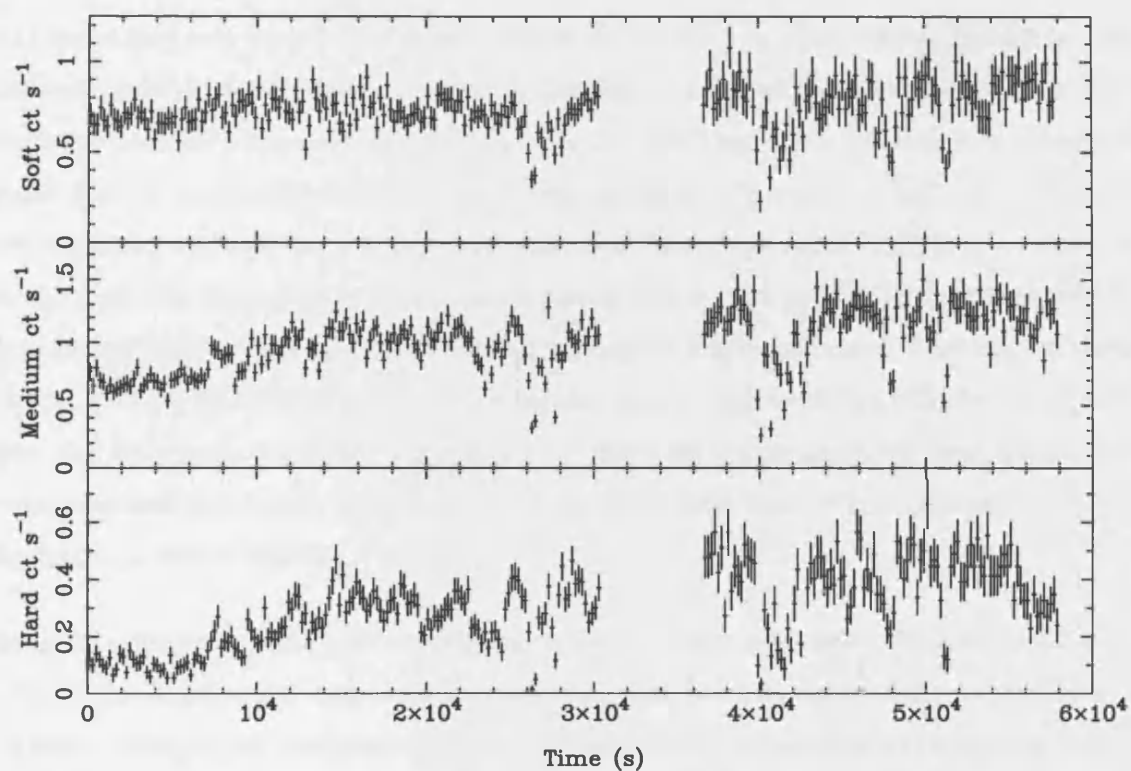


Figure 3.5: The XMMU J001528.9-391319 X-ray light curve in three energy bands with 200 s time binning. *From top to bottom*: 0.5–1.0 keV (soft), 1.0–2.0 keV (medium) and 2.0–4.5 keV (hard).

3.3.2 X-ray spectra

The different data segments used for spectral extraction are illustrated in Fig. 3.3¹. These represent different flux states of the source as follows: (I) the initial low flux state; (II) a relatively steady part of the light curve when the flux was at an intermediate level; (III) the highest flux state reached during these observations; (IIId) & (IIIId), the dipping states observed in the first and second exposures respectively.

X-ray spectra were extracted (using *especget* as described in § 2.3.3) for the different data segments using circular source and background regions of 75'' and 110'' radii respectively. The spectral analysis was performed using *XSPEC* v. 11.0.1. The pn, MOS-1 and MOS-2 spectra for each data segment were fitted simultaneously, but with constant multiplicative factors to allow for calibration differences between the cameras. Spectra were initially extracted in the 0.3–10.0 keV band. However, since very few counts were recorded above 7.0 keV and there were possible calibration uncertainties below 0.5 keV, the spectral fitting was restricted to the 0.5–7.0 keV range.

As a preliminary step, the spectra recorded while the source was in its initial low flux state (state I) were fitted with a simple absorbed power-law model. This resulted in a good match to the data ($\chi^2/\text{degrees of freedom} = 341/346$) with parameter values $N_H \sim 4 \times 10^{21} \text{ cm}^{-2}$ and $\Gamma \sim 4$. The former is considerably higher than the line of sight column density through our Galaxy ($N_H = 1.55 \times 10^{20} \text{ cm}^{-2}$; Stark et al. 1992) and may represent the column density within NGC 55 or material intrinsic to the source itself. A variety of other single-component continuum models were also attempted to fit the X-ray spectra but none of these improved upon the power-law fit; for example a single-temperature blackbody component yielded $\chi^2/\text{dof} = 459/346$, whereas a MCD spectrum gave $\chi^2/\text{dof} = 400/346$. The low state spectra were also fitted with a combination of a power-law plus a MCD component, but found that the latter component contributed only $\sim 10\%$ of the total X-ray flux and the resulting improvement in χ^2 was not significant ($\chi^2/\text{dof} = 338/344$).

Given the evidence from the light curves of the presence of a relatively steady soft component together with a more variable hard component, attempts were made to fit the intermediate and high states of the source (states II and III respectively) with an absorbed two component model comprising a power-law plus an additional component. In the event, trials showed that a MCD model provided the best match to the spectral shape of the hard emission, with the power-law dominant at soft X-ray energies.

¹The data were selected using GTI files based on either time or count-rate criteria.

The full analysis was conducted by fitting the spectra for states I, II and III *simultaneously* with the column density, photon index, power-law normalisation and the inner disc temperature kT_{in} of the MCD component tied across the three states. Therefore the normalisation of the MCD component for each state provided the remaining free parameters of the model. The results of fitting this two-component model are summarised in Table 3.2, where the errors are quoted at the 90% confidence level for one interesting parameter. This prescription resulted in a reasonable fit to the three spectral datasets ($\chi^2/\text{dof} = 1615/1436$).

The combination of a MCD component with a power-law is the spectral model generally employed for BHB systems (McClintock & Remillard 2006). However, in the ‘standard’ BHB spectral model the power-law invariably represents the hard tail of the emission rather than the softest emission (as above). In essence, the best fit model has reversed the role of the two components compared to the standard picture. As a check of this procedure, the X-ray spectra for the three states were fitted with the power-law component representing *the harder emission* in line with the standard model. Paralleling the previous approach (*i.e.*, the soft component remains constant over the three states), the column density, inner disc temperature kT_{in} , MCD normalisation and photon index are tied, while the power-law normalisation varies across the states. The results are also summarised in Table 3.2 under the heading ‘standard model’, and show that the standard description is not the preferred option in this case. In the best fitting ‘non-standard’ picture, the MCD component provides a good match to the curvature of the hard spectrum whereas the soft emission appears to have a simple power-law form (after allowing for modest excess absorption). Fig. 3.6 illustrates the changing form of the spectrum between states I and II, due to the increase in the MCD component.

The source luminosity (excluding the dips) increases by a factor ~ 2 over the course of the 60 ks interval of the observation, from $8.5 \times 10^{38} \text{ erg s}^{-1}$ in the early stages (I) to a maximum of $1.6 \times 10^{39} \text{ erg s}^{-1}$ during the latter part (III) of the observation (Table 3.2). Here the luminosities are quoted for the broad 0.5–7.0 keV band, assuming a distance to NGC 55 of 1.78 Mpc.

Finally the spectral properties of the dips were investigated by fitting the spectra from states II_d and III_d. Since the light curve analysis indicates that the relative depth of the dips increases with energy, this immediately rules out models in which the dipping is the result of obscuring material entering the line of sight so as to fully cover both spectral components simultaneously. This is true for either photoelectric absorption or pure electron scattering. Therefore, the energy dependence of the dipping was modelled

Table 3.2: Simultaneous spectral fitting results for states (I),(II) & (III) of XMMU J001528.9-391319

Model	N_H^a	Γ^b	A_{PL}^c	kT_{in}^d	A_{MCD}^e	χ^2/dof	f_X^f	L_X^g
Non-standard ¹	4.2 ± 0.2	4.2 ± 0.1	3.0 ± 0.2	0.86 ± 0.02	0.00 ± 0.10 (I)	1615/1436	2.2 (I)	0.9 (I)
					0.24 ± 0.03 (II)		3.9 (II)	1.5 (II)
					0.29 ± 0.04 (III)		4.2 (III)	1.6 (III)
Standard ²	$1.6^{+0.2}_{-0.1}$	2.0 ± 0.1	$0.05^{+0.06}_{-0.03}$ (I)	$0.41^{+0.01}_{-0.02}$	$7.21^{+1.51}_{-1.02}$	2173/1436	2.2 (I)	0.8 (I)
			$0.56^{+0.10}_{-0.05}$ (II)				4.2 (II)	1.6 (II)
			$0.67^{+0.11}_{-0.05}$ (III)				4.6 (III)	1.8 (III)

NOTES: ^a Column density including Galactic (10^{21} cm^{-2}), ^b power-law photon index, ^c power-law normalisation ($10^{-3} \text{ photon cm}^{-2} \text{ s}^{-1} \text{ keV}^{-1}$), ^d MCD inner-disc temperature (keV), ^e MCD normalisation ($((R_{in}/km)/(D/10kpc))^2 \cos i$, where R_{in} is the inner disc radius, D is the distance to the source and i is the inclination angle of the disc). NB. The spectra of states (I), (II) & (III) were fitted simultaneously with: ¹ N_H , Γ , A_{PL} and kT_{in} tied across all three states, with A_{MCD} allowed to vary, ² N_H , Γ , kT_{in} and A_{MCD} tied across all three states, with A_{PL} allowed to vary. Also shown are the observed 0.5–7.0 keV X-ray flux^f ($10^{-12} \text{ erg cm}^{-2} \text{ s}^{-1}$) and corresponding 0.5–7.0 keV X-ray luminosity^g ($10^{39} \text{ erg s}^{-1}$) for each of the three states.

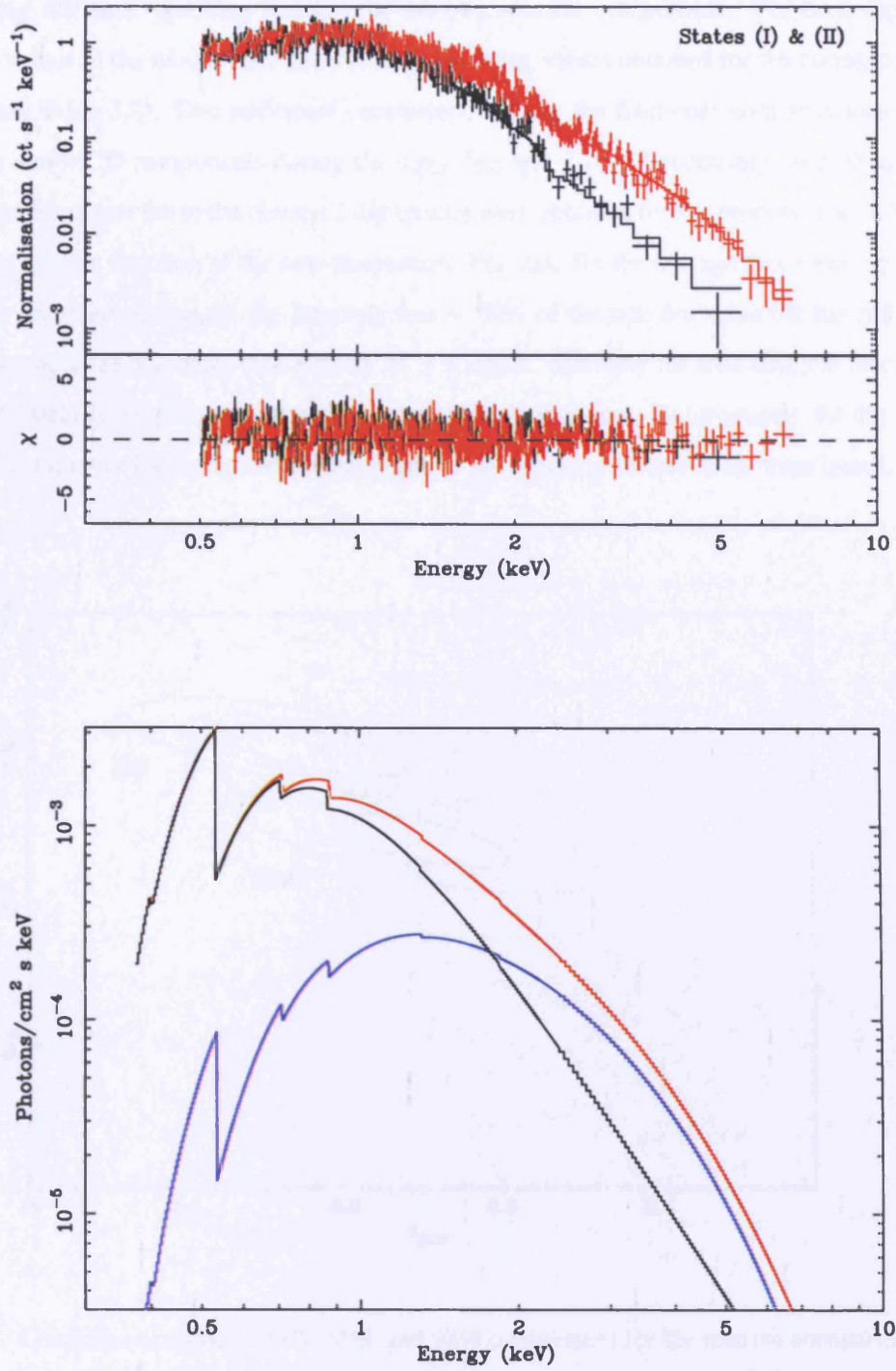


Figure 3.6: *Top panel*: EPIC pn count rate spectra for states I (black) and II (red) plus the corresponding best-fitting models. *Bottom panel*: The spectral model used to fit the measured count rate spectra. The model comprises a steep power-law component (black) plus a MCD component (blue). State I requires only the former component whereas state II is best-fitted by the combination of the two (red).

by assuming different ‘blocking factors’ for the two spectral components. For each dip state, the parameter values in the model were fixed at the best-fitting values obtained for the corresponding non-dip data (see Table 3.2). Two additional parameters, namely the fractional normalisations of the soft power-law and MCD components during the dips, f_{PL} and f_{MCD} respectively, were then used to fit the dip data. Excellent fits to the observed dip spectra were obtained by this process. Fig. 3.7 shows the variation in χ^2 as a function of the two parameters. For state IIId the average flux from the power-law component recorded during the dip intervals was $\sim 60\%$ of the non-dip value but the signal loss for the MCD component was more than a factor of > 3 higher. Similarly for state IIId, the blocking of the MCD component is roughly twice that of the power-law continuum. Unfortunately the dip spectra are of insufficient quality for the spectral dependence of the blocking factors to be investigated.

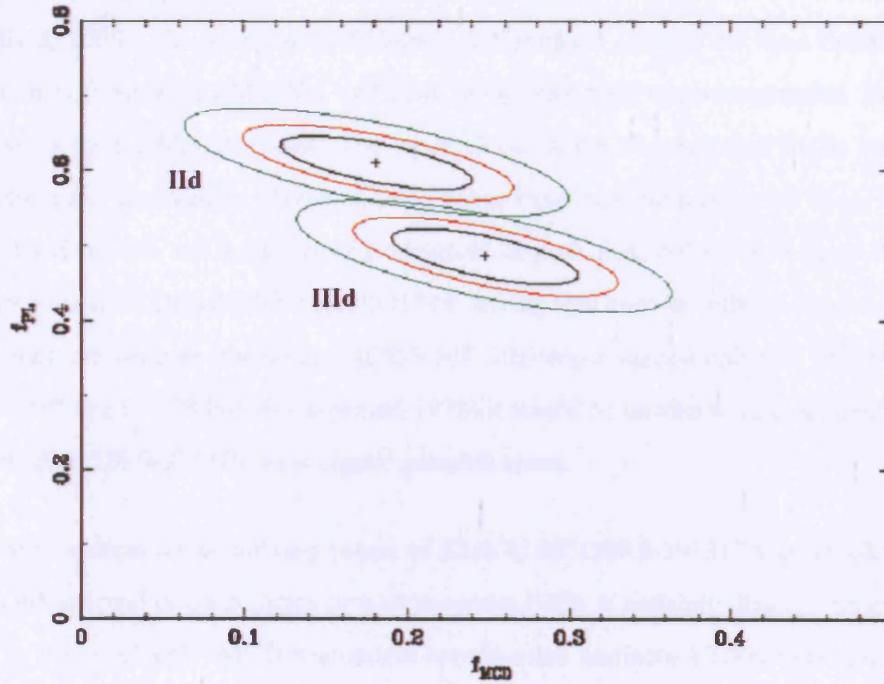


Figure 3.7: Confidence contours (68%, 90% and 98% confidence) for the relative normalisations of the power-law continuum and MCD component during the two dip states.

3.4 Discussion

3.4.1 XMMU J001528.9-391319 as a BHB candidate

Measurements from *ROSAT* (PSPC and HRI), *ASCA*, *Chandra* and *XMM-Newton* spanning ~ 10 yrs confirm that XMMU J001528.9-391319 is a persistent highly luminous source (see Fig. 3.8). The maximum X-ray luminosity observed by *XMM-Newton* of $1.6 \times 10^{39} \text{ erg s}^{-1}$ (0.5–7.0 keV) places the source at the lower boundary of the ULX regime. The variability evident on both long and short timescales is consistent with XMMU J001528.9-391319 being an accretion-powered XRB. If the source is radiating isotropically at or below the Eddington luminosity, then the implied mass of the compact object is $M > 11 M_{\odot}$. This compares to the 3–18 M_{\odot} range inferred for the primary object in the 18 BHBs in our Galaxy and the LMC for which dynamical measurements are available (McClintock & Remillard, 2006). As noted by McClintock & Remillard (2006), the three BHBs classed as persistent sources (Cyg X-1, LMC X-1 and LMC X-3) have high mass secondaries, but generally radiate well below their Eddington limit. The other 15 out of the 18 confirmed BHBs are X-ray novae, and have low-mass secondaries. Three of these novae have maximum observed X-ray luminosities firmly in the ULX regime and were ‘super-Eddington’ at peak flux, but of these three only GRS1915+105 appears similar to XMMU J001528.9-391319, having also been in outburst for more than 10 yrs. However, since the neutron star binary A0535-668 achieved a super-Eddington luminosity at its peak of $L_X \sim 10^{39} \text{ erg s}^{-1}$ (White & Carpenter, 1978) it would be unwise to rule out neutron star models for XMMU J001528.9-391319 on energetic grounds alone.

In order to address the underlying nature of XMMU J001528.9-391319 we can ask whether the source shows the spectral characteristics of a stellar-mass BHB. It certainly displays no evidence of the cool ($kT_{in} \sim 0.1 - 0.2 \text{ keV}$) MCD component seen in more luminous ULXs. In fact, the derived 0.86 keV inner-disc temperature is firmly in the observed regime ($kT_{in} \sim 0.7 - 2.0 \text{ keV}$) for Galactic BHBs in either the high/soft or the very high (steep power-law) state described by McClintock & Remillard (2006). Furthermore, the $\Gamma \sim 4.2$ steep power-law slope is also consistent with either of these states (for which typically $\Gamma > 2.4$). Following McClintock & Remillard (2006), the best-fitting model (soft power-law plus MCD) was extrapolated to find the flux balance between the two spectral components in the 2–20 keV range, in an attempt to distinguish between the two spectral states (HS or VH state). At the start of the observation 100% of the flux arises in the power-law continuum (using the adopted

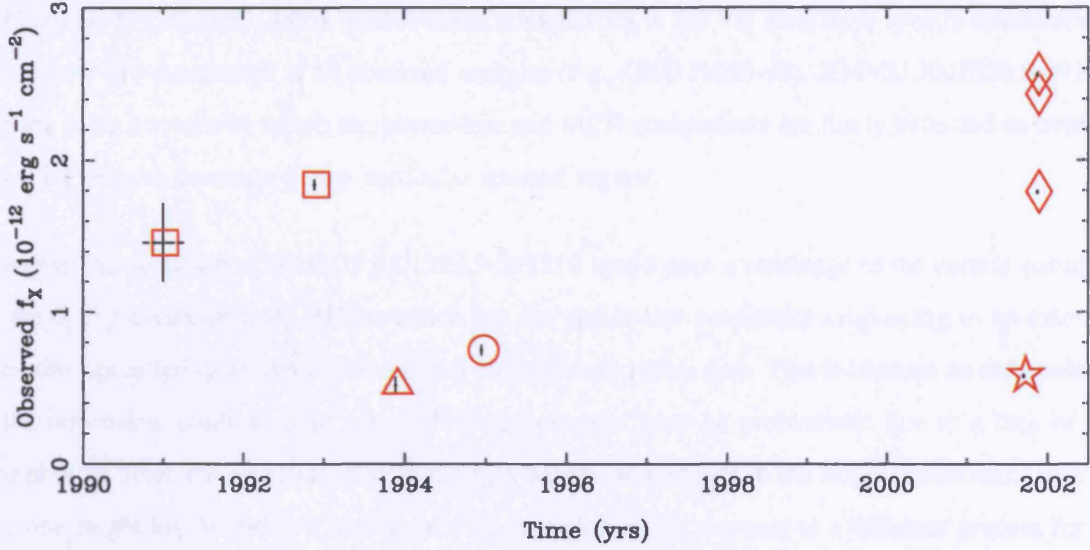


Figure 3.8: Long term variation of XMMU J001528.9-391319. Flux measurements shown are from *ROSAT* PSPC (squares), *ASCA* (triangle), *ROSAT* HRI (circle), *Chandra* (star) and the three *XMM* states of this analysis (diamonds), in the 0.5–2.0 keV band. All data were retrieved from archives using the standard techniques (courtesy of T. P. Roberts).

model of a single power-law fit to the low state data [I], but see earlier), falling to $\gtrsim 27\%$ by the end of the observation. This points to the VH state, but the detection of a QPO in the 0.1-30.0 Hz range is really required in order to completely resolve the ambiguity. This VH state has frequently been associated with the highest accretion rates in Galactic BHBs, consistent with the high luminosity of XMMU J001528.9-391319.

However, there is a potential problem with this interpretation. In XMMU J001528.9-391319 the spectral components are inverted with respect to the ‘standard’ spectral description of Galactic BHBs, *i.e.*, the soft end of the spectrum is dominated by the power-law continuum, not the MCD component. This is the first example of a BHB candidate in which the power-law continuum ‘re-emerges’ at low energies (*i.e.*, below 2 keV) as the MCD continuum turns down. Such behaviour has not been previously seen even in sources with a relatively low absorption column, similar to the $\sim 4 \times 10^{21} \text{ atoms cm}^{-2}$ determined for XMMU J001528.9-391319; for example, see the recent observations of XTE J1550-564 (Miller et al., 2003) and GX 339-4 (Miller et al., 2004). On the other hand, there are BHBs with higher absorption columns that possess observed spectra in the HS state that, if extrapolated below 2 keV, *would* be dominated by an emergent power-law component (*e.g.*, XTE J1550-564 and GRS 1915-105;

McClintock & Remillard 2006). Furthermore some BHBs in the VH state have spectra dominated by their power-law component at all observed energies (*e.g.*, GRO J1655-40). XMMU J001528.9-391319 appears to be a source in which the power-law and MCD components are finely balanced in terms of which happens to dominate in any particular spectral regime.

However, the spectrum of XMMU J001528.9-391319 could pose a challenge to the current paradigm for the X-ray emission from BHBs, which has the power-law continuum originating in an extended Compton-upscattering medium (the corona) above the accretion disc. This is because an extrapolation of the power-law continuum to very soft X-ray energies may be problematic due to a lack of soft seed photons from the accretion disc at energies below the turnover in the MCD continuum. To solve this, one might invoke either a new source of seed photons or recourse to a different process for the production of the soft continuum. For example, synchrotron radiation from the innermost part of a jet, has been discussed as a possible origin of the power-law component in some BHBs (*e.g.*, Markoff et al. 2001), although jets may be quenched for BHBs in a HS or VH state (*e.g.*, Fender 2004).

A second estimate of the mass of the compact object can be obtained from the parameters of the MCD model. On the basis of the spectral analysis, the peak bolometric flux of the disc component was determined to be $\sim 3.4 \times 10^{-12} \text{ erg cm}^{-2} \text{ s}^{-1}$. Using equation (5) of Makishima et al. (2000), results in an inner-disc radius of $R_{in} = 113 (\cos i)^{-\frac{1}{2}} \text{ km}$, where i is the inclination of the accretion disc to the line of sight. For a Schwarzschild black-hole this converts to a mass of $12.8 (\cos i)^{-\frac{1}{2}} M_{\odot}$ based on equation (8) of Makishima et al. (2000). Table 3.3 shows a comparison of the masses derived via the MCD model with the known dynamical mass for five BHBs. This tabulation may be interpreted either in terms of 3/5 of these systems having very high inclinations ($i > 80^{\circ}$) or the above method tending, in some cases, to underestimate the true black-hole mass by several factors (which might indicate that some of these black-holes carry significant angular momentum, Makishima et al. 2000). Interestingly, in the limit $\cos i = 1$, the MCD method never *overestimates* the mass of the black-hole in this case². As this system is dipping this provides a crude handle on the inclination of its accretion disc. Using a conservative assumption of $i \sim 70^{\circ}$ (see below), this leads to a mass estimate of $M_{MCD} \gtrsim 20 M_{\odot}$, implying that this system may harbour a black-hole more massive than in any confirmed BHB.

²But, see Kubota & Done (2004) who show that the MCD model *can* lead to an overestimate as well as an underestimate of the black-hole mass, depending on the geometry of the corona.

Table 3.3: Mass estimates from the MCD model compared to dynamical measurements.^a

System	$M_{MCD} (M_{\odot})$	$M_{dyn} (M_{\odot})$
4U 1543-475	$8.5(\cos i)^{-\frac{1}{2}}$	7.4 – 11.4
XTE J1550-564	$3.4(\cos i)^{-\frac{1}{2}}$	8.4 – 10.8
GRO J1655-40	$1.7(\cos i)^{-\frac{1}{2}}$	6.0 – 6.6
GX 339-4	$2.7(\cos i)^{-\frac{1}{2}}$	~ 5.8
GRS 1915+105	$1.2(\cos i)^{-\frac{1}{2}}$	10 – 18

NOTES: ^a Based on data presented in McClintock & Remillard (2006).

3.4.2 XMMU J001528.9-391319 as a dipping BHB candidate

The most interesting feature of XMMU J001528.9-391319 is the dipping apparent in its light curve. Such activity has been reported in ~ 20 XRBs including at least two BHBs, *e.g.*, GRO J1655-40 (Orosz & Bailyn 1997) and Cyg X-1 (Kitamoto et al. 1984). However, XMMU J001528.9-391319 is the first extragalactic black-hole candidate seen to exhibit dip behaviour.

A variety of models have been put forward to explain dipping activity with the details dependent on whether the system in question is a LMXB or HMXB. In LMXBs, dipping is thought to be due to the obscuration of the central X-ray source by absorbing material in the region where the accretion flow from the companion star impacts on the outer accretion disc of the system (White & Swank 1982; White et al. 1997). This could be via an interaction of the gas stream from the secondary with the outer edge of the accretion disc, causing a thickening at the rim (*e.g.*, EXO 0748-676; Parmar et al. 1986). Alternatively the obscuration may arise not from a bulge on the accretion disc itself but from a filamentary or clumpy absorbing medium extending above or below the impact region (*e.g.*, GRO J1655-40; Kuulkers et al. 1998a). Often in these cases the dips are observed at certain orbital phases and most of these sources are described as periodic dippers (White & Swank 1982). In contrast, in HMXBs the absorbing material is generally associated with clouds or ‘blobs’ in the stellar wind of the companion star. In these cases there are often sharp transitions into and out of the dip states, accompanied by variations in the column density, giving evidence for nonuniformity (*i.e.*, clumpy material) in the stellar wind. In the case of Cyg X-1 dips occur preferentially at orbital phase $\phi \sim 0.95$ with a secondary peak at $\phi \sim 0.6$, features which have been interpreted in terms of the influence of the stellar wind and

of an accretion stream respectively (Kitamoto et al. 1984; Bałucińska-Church et al. 2000). Although the X-ray flux from Cyg X-1 significantly photoionises the stellar wind of its supergiant companion star (HDE 226868) the factor 100–1000 overdensity of the clumps which give rise to the observed dips, explains the near-neutral characteristics of the absorption in this source (Kitamoto et al. 1984; Bałucińska-Church et al. 2000).

Since XRBs which show dips but not eclipses typically have inclinations in the range $60^\circ - 75^\circ$ (Frank et al. 1987), a relatively edge-on configuration seems very likely for XMMU J001528.9-391319. The short 100–300 s duration of the dips mirrors behaviour seen in the BHBs GRO J1655-40 (Kuulkers et al. 2000) and Cyg X-1 (Kitamoto et al. 1984) which are low-mass and high-mass binary systems respectively. This short timescale constrains the dimensions of the obscuring clumps. For example, if these clumps are orbiting a $20 M_\odot$ black-hole, in or just above its accretion disc, with a typical clump encompassing less than 1% of the disc circumference, then the size of a typical clump must be $\lesssim 10^{10}$ cm at a radius of $\gtrsim 2 \times 10^{11}$ cm. For unity optical depth to electron scattering the required density is $\gtrsim 1.5 \times 10^{14} \text{ cm}^{-3}$ at which point the ionisation parameter $\xi = L/nR^2 \lesssim 200$ and the material may be quite strongly photoionised (Hatchett et al. 1976; Kuulkers et al. 1998b). The orbital timescale of such a clump is ~ 10000 s. However, although there are several dip episodes apparent over a timescale of ~ 20 ks, within the bounds of these limited observations, it is not possible to investigate whether the dips follow a periodic pattern.

This spectral analysis suggests that the MCD component is more strongly obscured than the power-law component during the dips, but there are no constraints on whether the obscuration arises from absorption/scattering (in effect complete blocking) in dense cold clumps or is due to electron scattering in a much hotter medium. A scenario which matches the limited information is one in which the harder thermal disc emission from the inner parts of the accretion disc is almost completely blocked during a dipping episode whereas the more extended softer emission (possibly from a hot corona above the disc, though see the discussion above) is only partially obscured by the same clump. However, there are other plausible explanations of the apparent spectral softening during dips. For example photoionisation may have significantly reduced the soft X-ray opacity of the obscuring medium or alternatively the scattering of X-rays in hot clouds above the accretion disc might induce an apparent soft excess during dips (Frank et al., 1987). Also, Díaz Trigo et al. (2006) demonstrated that the spectral state changes from persistent to dipping phases seen in many LMXBs could be modelled simply by variations in the properties of neutral and ionized absorbers. Contrary to a ‘complex continuum’ model, this approach

does not require any partial covering and therefore does not require an extended corona. Unfortunately the quality of the X-ray spectra recorded during the dips is too poor for us to be able to distinguish between these possibilities.

3.5 Conclusions

XMM-Newton observations have revealed a luminous XRB in the nearby galaxy NGC 55. On the basis of its X-ray luminosity and X-ray spectral properties, this object is most likely a black-hole system. The light curve reveals very interesting spectral variability including, most notably, pronounced dips. Future observations may reveal whether these dips show a pattern of occurrence consistent with an underlying orbital period as is the case for the well-studied BHBs GRO J1655-40 and Cyg X-1. However, detailed investigation of the spectral variations which accompany the dips represents a challenge even for the *XMM-Newton* instrumentation.

Chapter 4

The X-ray properties of the dwarf Magellanic-type galaxy NGC 55

4.1 Introduction

As previously mentioned NGC 55 is a member of the nearby Sculptor Group of galaxies, of which the other prominent members are the starburst galaxy NGC 253 and the spirals NGC 45, NGC 247, NGC 300 and NGC 7793. NGC 55 itself has been classified as a SB(s)m galaxy (de Vaucouleurs, 1961) and is viewed almost edge-on with an optical extent of $32.4' \times 5.6'$ (3rd Reference Catalogue of Galaxies; de Vaucouleurs et al. 1991). The inclination estimates range from 80° (Hummel et al., 1986) to 85° (de Vaucouleurs & Freeman, 1972); a value of 81° is assumed here (Kiszkurno-Koziej, 1988). The optical morphology of NGC 55 is rather asymmetric, with the brightest region displaced $\sim 3'$ from the geometrical centre of the galaxy (Robinson & van Damme, 1966). This feature has been interpreted as a bar viewed near to end-on (de Vaucouleurs, 1961). Although there is active star formation present throughout much of the disc of NGC 55, the radio continuum emission is concentrated on the bar region and at 6 cm is dominated by a triple source (*e.g.*, Hummel et al. 1986). Recent *Spitzer* far-infrared imaging suggests this is a young (< 2 Myr) star formation complex (Engelbracht et al., 2004). The *Spitzer* observations further imply a global star formation rate of $0.22 M_\odot \text{ yr}^{-1}$ for NGC 55 (Engelbracht et al., 2004). The edge-on orientation of NGC 55 affords us a prime view of the effects of this disc-based star formation activity on the extra-planar regions. Spectacular ionized gas features,

including giant shells and possible galactic chimneys, protrude well above the plane of the galaxy (Ferguson et al. 1996; Otte & Dettmar 1999), suggesting that the star formation powers the ejection of gas from the disc into the halo. At least some of this gas appears to cool sufficiently to form new stars in the halo (Tüllmann et al. 2003; Tüllmann & Rosa 2004).

For such a relatively nearby ($d = 1.78 \text{ Mpc}$ ¹, active star-forming system, NGC 55 has been relatively poorly studied at X-ray wavelengths. The first detailed X-ray information came from *ROSAT* PSPC and HRI observations (Read et al. 1997; Roberts 1997; Schlegel et al. 1997; Dahlem et al. 1998), revealing a total of 25 sources in and around the galaxy and evidence of localised diffuse emission. Of these sources, 15 were located within the optical confines of the galaxy as defined by the D_{25} ellipse (Roberts, 1997). New *XMM-Newton* observations established the brightest source in the galaxy as a ULX (see previous chapter). Previous *Chandra* (ACIS-I) observations detect possible extended X-ray emission above the disc of the galaxy, as well as a somewhat brighter diffuse component associated with the disc itself (Oshima et al., 2002).

This chapter presents a detailed analysis of the *XMM-Newton* observations of NGC 55, focusing on both the properties of the discrete X-ray source population and the underlying diffuse emission. The chapter is set out as follows: § 4.2—description of the observations and preliminary data screening, § 4.3—presents a catalogue of the X-ray sources detected in the NGC 55 field and discusses the number of X-ray sources associated with the galaxy, § 4.4—X-ray properties of four of the brightest X-ray sources in NGC 55, § 4.5—the X-ray colours of the full set of detected sources, § 4.6—the morphology and spectral properties of the faint diffuse X-ray emission observed in NGC 55, § 4.7—discussion on the nature of the brightest X-ray sources in NGC 55 and a consideration for the overall X-ray properties of this galaxy in the context of other nearby Magellanic-type systems. Finally, the results are summarised in § 4.8.

¹The distance to NGC 55 was estimated to be $1.45^{+0.35}_{-0.30} \text{ Mpc}$ by Graham (1982) based on the apparent magnitude of stars at the tip of the red giant branch, whereas Pritchett et al. (1987) obtained a value of $1.34 \pm 0.08 \text{ Mpc}$, via photometry of carbon stars. More recent estimates, using a variety of techniques, place NGC 55 at a distance of between $1.7 - 2.1 \text{ Mpc}$ (Karachentsev et al. 2003; Tikhonov et al. 2005; Van de Steene et al. 2004). This work assumes a distance to NGC 55 of 1.78 Mpc (Karachentsev et al., 2003).

4.2 Observations and data screening

Details of the *XMM-Newton* observations of NGC 55 used in this work are given in § 3.2 of the previous chapter. Images, light curves and spectra were created and filtered as described in § 2.3.3. In addition, three hot columns were removed from the pn data (two in the first observation, and one in the second). Source detection was performed on the sky area encompassed by both *XMM-Newton* observations of NGC 55 via the source detection procedure outlined in § 2.3.4. This was performed separately on the MOS (*i.e.*, MOS-1 plus MOS-2) and pn data from both observations in three energy bands: 0.3–1 keV (S), 1–2 keV (M) and 2–6 keV (H), and the results are described in the following sections.

4.3 X-ray Sources in the Field of NGC 55

4.3.1 The source catalogue

In total, 137 X-ray sources are detected within the FOV encompassed by the two *XMM-Newton* observations, 42 of which are located within the D_{25} ellipse of NGC 55. Fig. 4.1 shows the broad band (0.3–6 keV) X-ray image obtained by merging the MOS and pn data from the two observations (*top panel*) and the equivalent optical DSS-2 blue image of the galaxy (*bottom panel*). The positions of the 137 sources which pass the significance test described earlier are marked with circles on both images.

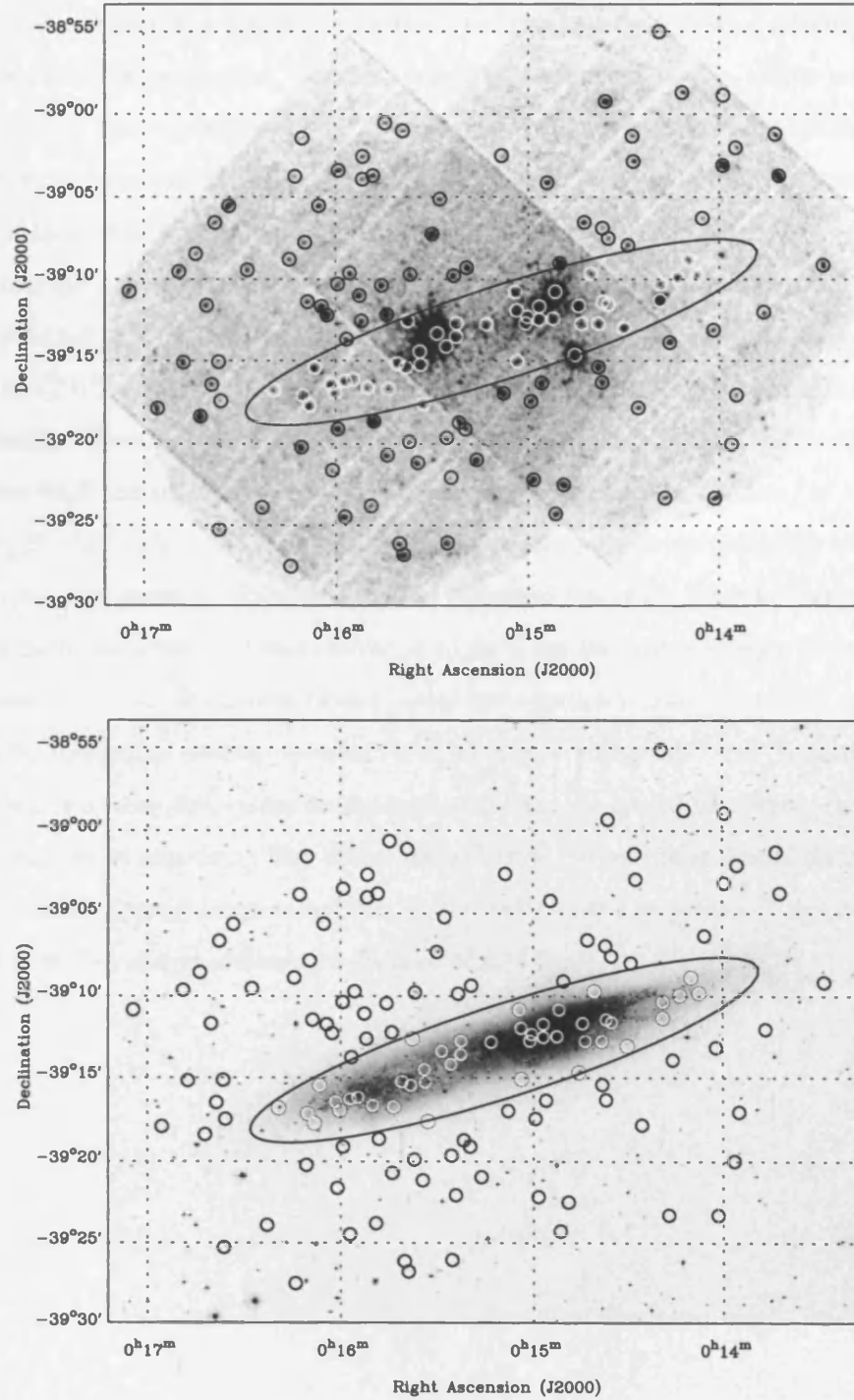


Figure 4.1: *Top panel:* the *XMM-Newton* image of the NGC 55 field in a broad (0.3–6 keV) bandpass. The image has been lightly smoothed using a circular Gaussian mask with $\sigma=1$ pixel (*i.e.*, $4''$). *Bottom panel:* the optical DSS-2 (blue) image of the NGC 55 field. Detected sources are identified with circles and the optical D_{25} ellipse of NGC 55 is also shown.

The full X-ray source catalogue appears in Table 4.1 and provides the following information:

(1) the source identification number. Sources located within the optical D_{25} ellipse are marked with an asterisk. (2)–(3) The source RA and DEC positions (J2000). The correct IAU designated title for each source can be produced by truncating the coordinates in these columns, *e.g.*, source 1 becomes XMMU J001328.3-390903. (4) The 1σ uncertainty in the source position plus a $0.5''$ systematic error. (5)–(7) The measured count rate (corrected for the vignetting) in the pn camera in the S, M & H bands. For sources detected in both observations, these count rates are the weighted mean values from the two exposures. (8)–(10) The measured count rate (corrected for the vignetting) in the MOS cameras in the S, M & H bands. Where appropriate, weighted mean values are quoted as for the pn data. Values are quoted for one MOS camera. (11)–(12) Two hardness ratios calculated as $HR1 = (M - S)/(M + S)$ and $HR2 = (H - M)/(H + M)$. The weighted mean hardness ratios are quoted for sources detected in more than one instrument or exposure. (13) The measured flux in the 0.3–6 keV energy range. The count rate in each detection band was converted to an X-ray flux using Energy Conversion Factors (ECFs) calculated for each instrument from a power-law continuum spectrum with $\Gamma = 1.7$ absorbed by the Galactic foreground column towards NGC 55 ($N_H = 1.55 \times 10^{20} \text{ cm}^{-2}$; Stark et al. 1992). Again, the weighted mean flux values for the particular band are quoted for sources detected in more than one instrument or exposure. The fluxes derived from the individual bands were subsequently added to provide the quoted instrumental flux (0.3–6 keV). (14) The derived X-ray luminosities for sources within the D_{25} ellipse, assuming a distance of 1.78 Mpc.

Table 4.1: The full catalogue of sources detected in the *XMM-Newton* observations

SRC	RA	DEC	$r_1\sigma$	pn cts ks ⁻¹			MOS cts ks ⁻¹			HR1	HR2	f_X	L_X
ID	(hh:mm:ss)	(° : ' : ")	(")	S	M	H	S	M	H			($\times 10^{-14}$)	($\times 10^{36}$)
(1)	(2)	(3)	(4)	(5)	(6)	(7)	(8)	(9)	(10)	(11)	(12)	(13)	(14)
1	00:13:28.37	-39:09:03.0	1.14	–	–	–	3.4±0.4	3.0±0.4	1.4±0.4	-0.06±0.09	-0.36±0.12	4.6±0.5	
2	00:13:42.33	-39:03:38.3	0.60	40.5±2.8	16.9±1.8	14.4±1.7	13.2±1.1	10.6±1.0	7.9±0.8	-0.28±0.05	-0.12±0.08	17.1±0.8	
3	00:13:43.61	-39:01:07.2	0.87	17.7±2.9	7.4±1.8	4.0±1.5	4.2±0.6	2.2±0.5	0.0±0.1	-0.36±0.12	-0.88±0.15	3.0±0.3	
4	00:13:46.83	-39:11:55.7	1.49	4.3±0.8	2.3±0.5	1.3±0.4	–	–	–	-0.31±0.13	-0.26±0.19	1.5±0.3	
5	00:13:55.16	-39:16:58.4	1.41	2.1±0.6	1.2±0.3	2.0±0.5	0.2±0.2	0.9±0.2	0.4±0.2	-0.01±0.19	0.06 ±0.23	1.3±0.2	
6	00:13:55.87	-39:01:56.5	1.28	2.6±0.8	1.9±0.6	1.0±0.6	1.3±0.3	1.1±0.3	0.9±0.3	-0.12±0.19	-0.17±0.27	1.5±0.3	
7	00:13:56.62	-39:19:58.3	1.36	0.5±0.4	1.8±0.6	2.9±0.8	0.0±0.2	0.8±0.2	1.3±0.3	0.73±0.34	0.23 ±0.18	2.0±0.3	
8	00:13:59.88	-39:03:01.8	0.69	28.7±2.0	11.3±1.2	6.3±1.0	–	–	–	-0.44±0.05	-0.28±0.09	8.1±0.6	
9	00:13:59.90	-38:58:46.0	1.73	4.5±1.0	0.0±0.3	0.0±0.2	–	–	–	-1.00±0.13	–	0.5±0.2	
10	00:14:01.76	-39:23:16.0	0.72	–	–	–	11.8±1.0	8.4±0.9	4.5±0.6	-0.17±0.07	-0.31±0.08	14.6±1.0	
11	00:14:02.49	-39:13:02.5	1.01	3.8±0.6	1.4±0.3	0.1±0.2	0.7±0.2	0.4±0.1	0.3±0.1	-0.42±0.20	-0.69±0.24	0.7±0.1	
12	00:14:06.13	-39:06:14.7	1.91	0.3±0.3	1.2±0.3	0.8±0.4	–	–	–	0.61±0.32	-0.20±0.26	0.7±0.2	
13*	00:14:07.84	-39:09:44.0	1.24	0.8±0.3	1.4±0.4	1.2±0.3	0.4±0.2	0.7±0.2	0.4±0.2	0.30±0.21	-0.17±0.20	1.0±0.1	3.8
14*	00:14:10.33	-39:08:47.3	1.53	0.7±0.4	2.2±0.4	0.8±0.3	0.4±0.1	0.8±0.2	0.3±0.2	0.40±0.20	-0.44±0.20	0.9±0.1	3.3
15	00:14:12.66	-38:58:36.6	0.96	8.3±1.2	3.7±0.8	2.4±0.7	2.7±0.6	2.0±0.5	2.2±0.6	-0.30±0.16	-0.08±0.17	3.2±0.4	
16*	00:14:13.87	-39:09:51.9	0.83	1.4±0.4	1.9±0.4	2.2±0.4	0.5±0.1	1.9±0.2	1.4±0.2	0.47±0.14	-0.06±0.11	2.1±0.2	7.9
17	00:14:16.12	-39:13:48.5	0.73	5.8±0.7	2.8±0.4	1.8±0.4	1.8±0.2	1.4±0.2	1.5±0.2	-0.26±0.11	-0.09±0.12	2.5±0.1	
18	00:14:17.33	-39:23:16.4	1.16	3.3±0.9	3.8±0.8	1.1±0.3	2.6±0.5	1.5±0.4	0.5±0.3	-0.13±0.15	-0.53±0.19	1.7±0.2	
19*	00:14:19.24	-39:10:16.2	1.22	0.0±0.2	1.4±0.3	1.1±0.3	0.3±0.1	0.4±0.1	0.7±0.2	0.65±0.26	0.06 ±0.18	1.0±0.2	3.8
20*	00:14:19.31	-39:11:15.2	0.53	27.1±1.4	33.3±1.5	27.9±1.4	8.1±0.5	18.4±0.8	16.5±0.8	0.24±0.03	-0.07±0.03	27.0±0.7	102.4
21	00:14:19.89	-38:54:55.4	2.46	6.5±1.4	2.5±0.9	1.2±0.9	–	–	–	-0.44±0.17	-0.35±0.35	1.7±0.5	
22	00:14:25.86	-39:17:47.6	1.12	2.7±0.5	1.5±0.4	1.0±0.4	1.1±0.2	0.8±0.2	0.6±0.1	-0.23±0.15	-0.19±0.19	1.3±0.1	
23	00:14:27.81	-39:02:48.6	0.94	3.7±0.7	1.6±0.4	1.6±0.4	1.1±0.2	1.7±0.3	0.8±0.2	-0.11±0.13	-0.20±0.16	1.8±0.2	
24	00:14:28.17	-39:01:16.1	1.46	3.4±0.7	1.3±0.4	0.4±0.3	0.9±0.2	0.6±0.2	0.9±0.3	-0.37±0.23	-0.06±0.33	1.0±0.2	
25	00:14:29.36	-39:07:54.3	1.23	1.4±0.4	1.6±0.3	0.4±0.3	0.6±0.1	0.6±0.1	0.6±0.2	0.02±0.17	-0.20±0.20	0.9±0.1	
26*	00:14:30.48	-39:12:57.5	0.69	5.6±0.7	3.9±0.5	2.2±0.4	1.3±0.2	2.3±0.3	1.1±0.2	0.03±0.09	-0.31±0.10	2.6±0.2	10.0
27*	00:14:35.45	-39:11:32.2	1.50	2.2±0.5	0.0±0.2	0.5±0.3	0.9±0.2	0.2±0.1	0.0±0.1	-0.85±0.18	-0.19±0.69	0.5±0.1	1.8
28	00:14:35.50	-39:07:29.6	1.66	0.6±0.3	0.6±0.3	0.9±0.3	0.1±0.1	0.7±0.2	0.5±0.1	0.53±0.30	-0.06±0.21	0.8±0.1	

SRC ID	RA (hh:mm:ss)	DEC (° : ' : ")	$r_1 \sigma$ (")	pn cts ks ⁻¹			MOS cts ks ⁻¹			HR1 (11)	HR2 (12)	f_X ($\times 10^{-14}$) (13)	L_X ($\times 10^{36}$) (14)
				S (5)	M (6)	H (7)	S (8)	M (9)	H (10)				
29	00:14:36.56	-38:59:10.4	1.12	11.4±1.4	4.6±0.9	1.0±0.6	4.7±0.6	3.5±0.5	0.3±0.3	-0.28±0.09	-0.78±0.17	3.0±0.3	
30*	00:14:37.18	-39:11:22.0	2.26	-	-	-	0.9±0.2	0.0±0.1	0.1±0.1	-0.92±0.14	0.53±0.76	0.5±0.2	2.0
31	00:14:37.19	-39:16:15.4	1.46	1.6±0.4	1.6±0.3	0.5±0.3	-	-	-	-0.03±0.16	-0.49±0.22	0.7±0.2	
32	00:14:37.31	-39:06:52.4	1.38	0.0±0.1	0.2±0.2	1.3±0.3	0.0±0.1	0.3±0.1	1.0±0.2	1.00±0.57	0.65±0.22	1.0±0.2	
33	00:14:38.39	-39:15:19.7	0.83	2.7±0.4	1.6±0.3	1.1±0.3	1.1±0.2	0.7±0.1	0.6±0.1	-0.22±0.11	-0.14±0.14	1.3±0.1	
34*	00:14:38.54	-39:12:41.3	1.03	0.7±0.3	1.8±0.4	0.7±0.3	0.5±0.1	0.8±0.2	0.7±0.2	0.33±0.17	-0.25±0.17	1.0±0.1	3.6
35*	00:14:40.88	-39:09:38.6	1.42	-	-	-	0.5±0.1	0.9±0.2	0.7±0.2	0.33±0.16	-0.14±0.16	1.6±0.3	6.0
36	00:14:42.95	-39:06:31.0	0.85	0.0±0.2	2.9±0.5	3.3±0.5	0.2±0.1	1.6±0.3	2.3±0.3	0.90±0.13	0.13±0.11	2.8±0.2	
37*	00:14:43.74	-39:12:41.5	1.49	0.2±0.3	1.2±0.3	0.9±0.3	0.1±0.1	0.7±0.2	0.3±0.2	0.72±0.31	-0.25±0.22	0.7±0.1	2.8
38*	00:14:44.62	-39:11:35.9	0.58	6.7±0.6	10.1±0.7	8.7±0.6	2.1±0.2	4.8±0.4	4.3±0.3	0.30±0.05	-0.07±0.05	7.7±0.3	29.1
39	00:14:45.73	-39:14:35.3	0.51	198.5±2.9	64.0±1.6	9.8±0.7	51.2±1.0	25.1±0.7	3.6±0.3	-0.45±0.01	-0.73±0.02	35.9±0.4	
40	00:14:49.00	-39:22:29.9	0.82	1.8±0.6	6.3±1.0	2.3±0.7	1.0±0.2	2.3±0.2	2.1±0.2	0.45±0.08	-0.11±0.10	3.4±0.3	
41	00:14:50.55	-39:09:01.0	0.62	8.8±0.7	4.9±0.5	2.7±0.4	3.1±0.5	3.0±0.4	2.5±0.4	-0.23±0.10	-0.22±0.08	3.5±0.2	
42	00:14:51.52	-39:24:16.1	0.88	-	-	-	3.6±0.4	2.5±0.3	1.0±0.2	-0.19±0.08	-0.42±0.11	4.1±0.4	
43*	00:14:52.02	-39:10:45.2	0.50	106.0±2.1	119.6±2.3	53.3±1.6	32.3±0.8	56.5±1.1	25.6±0.8	0.16±0.01	-0.38±0.01	64.0±0.7	242.8
44*	00:14:52.68	-39:12:23.9	1.26	-	-	-	1.0±0.2	0.8±0.2	0.4±0.2	-0.11±0.17	-0.30±0.20	1.4±0.3	5.3
45	00:14:54.54	-39:04:07.4	0.85	5.6±0.8	3.2±0.6	0.5±0.3	2.6±0.4	2.3±0.3	0.2±0.2	-0.16±0.10	-0.77±0.16	1.7±0.2	
46	00:14:56.04	-39:16:17.9	0.84	3.0±0.4	1.9±0.3	1.1±0.3	0.5±0.1	0.8±0.1	0.4±0.1	-0.04±0.11	-0.27±0.13	1.2±0.1	
47*	00:14:57.00	-39:11:39.2	0.51	20.3±1.0	42.2±1.3	37.2±1.3	6.3±0.4	20.0±0.6	17.8±0.6	0.44±0.02	-0.05±0.02	31.6±0.6	119.7
48*	00:14:57.04	-39:12:26.8	1.54	2.6±0.6	1.3±0.4	0.2±0.2	0.8±0.2	0.5±0.2	0.1±0.1	-0.29±0.20	-0.75±0.32	0.6±0.1	2.2
49	00:14:58.48	-39:22:11.1	0.69	7.0±0.8	2.2±0.4	1.7±0.3	1.1±0.2	1.4±0.2	0.6±0.1	-0.30±0.08	-0.26±0.12	2.0±0.2	
50	00:14:59.39	-39:17:24.9	1.32	0.3±0.3	0.8±0.3	1.4±0.4	0.0±0.0	0.5±0.1	0.5±0.1	0.87±0.17	0.12±0.20	0.9±0.1	
51*	00:15:00.62	-39:12:16.4	1.16	-	-	-	0.4±0.1	0.7±0.1	0.8±0.1	0.31±0.15	-0.04±0.12	1.7±0.2	6.6
52*	00:15:01.18	-39:12:40.6	0.98	5.0±0.6	1.6±0.3	0.2±0.2	1.4±0.2	0.5±0.2	0.2±0.1	-0.49±0.12	-0.72±0.22	0.9±0.1	3.5
53*	00:15:03.79	-39:14:59.8	1.52	2.1±0.3	0.2±0.1	0.1±0.2	-	-	-	-0.84±0.11	-0.18±0.73	0.3±0.1	1.2
54*	00:15:04.01	-39:11:53.3	0.67	0.9±0.3	4.0±0.4	3.6±0.4	0.2±0.1	1.6±0.2	1.5±0.2	0.68±0.11	-0.04±0.08	2.8±0.2	10.6
55*	00:15:04.47	-39:10:45.9	0.83	2.2±0.4	1.6±0.3	0.9±0.3	0.5±0.1	1.0±0.2	0.7±0.1	0.09±0.12	-0.19±0.11	1.2±0.1	4.6
56	00:15:07.98	-39:16:55.8	0.91	0.4±0.2	2.4±0.3	3.1±0.4	0.0±0.0	0.9±0.1	1.5±0.2	0.87±0.12	0.19±0.09	2.3±0.2	

SRC ID	RA (hh:mm:ss)	DEC (° : ' : ")	$r_1 \sigma$ (")	pn cts ks ⁻¹				MOS cts ks ⁻¹				HR1 (11)	HR2 (12)	f_X ($\times 10^{-14}$) (13)	L_X ($\times 10^{36}$) (14)
				S	M	H	(5)	S	M	H	(10)				
(1)	(2)	(3)	(4)	(5)	(6)	(7)	(8)	(9)	(10)	(11)	(12)	(13)	(14)		
57	00:15:08.77	-39:02:29.1	1.39	1.9±0.6	1.3±0.4	0.2±0.3	2.0±0.4	1.2±0.3	0.4±0.3	-0.24±0.17	-0.59±0.30	0.7±0.2			
58*	00:15:13.44	-39:12:45.0	2.49	-	-	-	0.7±0.2	0.1±0.1	0.0±0.1	-0.69±0.20	-0.50±0.64	0.4±0.1	1.5		
59	00:15:16.42	-39:20:59.0	0.87	4.9±0.6	2.7±0.4	2.0±0.4	1.2±0.2	0.9±0.2	0.7±0.2	-0.25±0.13	-0.13±0.14	2.0±0.2			
60	00:15:19.57	-39:09:17.6	1.48	2.3±0.5	0.9±0.3	0.3±0.3	-	-	-	-0.42±0.14	-0.52±0.33	0.5±0.2			
61	00:15:19.97	-39:19:07.2	1.45	-	-	-	0.5±0.1	0.5±0.1	0.3±0.1	-0.06±0.16	-0.25±0.21	0.8±0.2			
62	00:15:21.94	-39:18:43.5	0.99	-	-	-	0.4±0.1	1.5±0.2	1.1±0.2	0.61±0.10	-0.18±0.10	2.3±0.3			
63*	00:15:22.83	-39:12:41.1	1.31	3.4±0.8	0.0±0.2	0.0±0.1	-	-	-	-1.00±0.09	-	0.3±0.1	1.3		
64*	00:15:22.93	-39:13:30.0	2.70	-	-	-	0.3±0.1	0.8±0.2	0.2±0.1	0.46±0.16	-0.64±0.19	0.7±0.2	2.7		
65	00:15:23.64	-39:09:47.2	1.13	0.6±0.3	1.5±0.3	1.3±0.3	0.2±0.1	0.7±0.2	0.8±0.2	0.49±0.20	-0.01±0.16	1.2±0.2			
66	00:15:24.45	-39:22:04.5	2.42	1.3±0.3	0.0±0.1	0.3±0.2	-	-	-	-1.00±0.21	1.00±0.89	0.3±0.1			
67	00:15:25.61	-39:26:02.5	1.14	5.6±0.8	1.5±0.5	0.2±0.3	1.1±0.2	0.8±0.2	0.3±0.2	-0.43±0.15	-0.51±0.30	1.1±0.2			
68	00:15:25.82	-39:19:40.2	1.27	1.8±0.4	0.9±0.2	0.5±0.3	0.2±0.1	0.1±0.1	0.2±0.1	-0.31±0.24	-0.10±0.31	0.5±0.1			
69*	00:15:26.01	-39:14:05.9	1.00	3.9±0.5	4.9±0.4	1.7±0.4	-	-	-	0.12±0.08	-0.48±0.09	2.1±0.2	8.0		
70	00:15:27.91	-39:05:07.7	1.28	2.8±0.5	0.3±0.2	0.1±0.2	0.5±0.2	0.4±0.2	0.0±0.0	-0.68±0.14	-0.95±0.61	0.4±0.1			
71*	00:15:28.87	-39:13:18.7	0.50	833.6±5.9	772.8±5.8	225.1±3.2	110.6±1.9	158.8±2.3	43.9±1.2	0.04±0.01	-0.52±0.01	247.3±1.5	937.6		
72	00:15:30.29	-39:07:15.0	0.72	2.3±0.5	2.7±0.5	4.4±0.6	0.6±0.1	1.5±0.2	3.1±0.3	0.28±0.13	0.32±0.08	4.0±0.3			
73*	00:15:33.18	-39:17:35.3	1.13	1.0±0.3	1.0±0.2	0.7±0.2	0.4±0.1	0.2±0.1	0.2±0.1	-0.12±0.21	-0.10±0.26	0.6±0.1	2.3		
74*	00:15:33.98	-39:15:12.2	0.67	9.9±0.7	2.7±0.4	0.6±0.3	2.0±0.2	1.4±0.2	0.0±0.1	-0.44±0.06	-0.87±0.13	1.6±0.1	6.0		
75*	00:15:34.27	-39:14:24.8	0.52	27.6±1.1	35.1±1.2	30.0±1.1	6.2±0.3	13.2±0.5	11.7±0.5	0.24±0.03	-0.07±0.03	24.5±0.5	93.0		
76	00:15:34.80	-39:21:10.4	1.00	2.1±0.4	2.5±0.4	2.7±0.4	0.3±0.1	0.8±0.1	0.3±0.1	0.29±0.13	-0.19±0.11	1.1±0.1			
77	00:15:37.13	-39:09:42.7	1.35	2.3±0.4	0.5±0.2	0.1±0.2	-	-	-	-0.67±0.10	-0.82±0.39	0.4±0.1			
78	00:15:37.43	-39:19:54.1	1.58	0.4±0.3	1.0±0.2	0.2±0.2	0.4±0.1	0.2±0.1	0.0±0.0	-0.02±0.28	-0.77±0.36	0.3±0.1			
79*	00:15:38.00	-39:12:32.8	0.69	3.7±0.4	3.1±0.4	1.4±0.3	1.1±0.1	1.4±0.2	0.9±0.1	0.02±0.08	-0.27±0.09	1.9±0.1	7.2		
80*	00:15:38.54	-39:15:22.5	1.71	1.3±0.3	2.3±0.4	1.2±0.3	-	-	-	0.27±0.14	-0.31±0.13	1.2±0.2	4.4		
81	00:15:39.24	-39:26:44.9	0.83	8.9±1.0	3.3±0.6	3.0±0.6	2.0±0.3	1.2±0.2	1.4±0.3	-0.38±0.09	0.01±0.14	3.1±0.3			
82	00:15:39.41	-39:00:59.0	1.50	5.4±1.0	4.9±0.8	1.5±0.7	-	-	-	-0.05±0.13	-0.53±0.18	2.1±0.4			
83	00:15:40.45	-39:26:06.5	1.25	2.4±0.6	1.5±0.4	0.8±0.4	0.7±0.2	0.6±0.2	0.3±0.1	-0.15±0.17	-0.31±0.25	1.0±0.2			
84*	00:15:41.26	-39:15:09.3	1.15	3.8±0.6	0.7±0.3	0.0±0.1	0.7±0.1	0.2±0.1	0.0±0.0	-0.66±0.14	-0.98±0.33	0.4±0.1	1.6		

SRC ID	RA (hh:mm:ss)	DEC (° : ' : ")	$r_1\sigma$ (")	pn cts ks ⁻¹			MOS cts ks ⁻¹			HRI (11)	HR2 (12)	f_X ($\times 10^{-14}$) (13)	L_X ($\times 10^{36}$) (14)
				S	M	H	S	M	H				
(1)	(2)	(3)	(4)	(5)	(6)	(7)	(8)	(9)	(10)	(11)	(12)	(13)	(14)
85*	00:15:43.82	-39:16:41.8	2.27	1.4±0.3	0.1±0.1	0.0±0.1	-	-	-	-0.93±0.13	-1.00±3.57	0.2±0.1	0.6
86	00:15:44.17	-39:20:43.5	0.94	2.8±0.4	1.5±0.3	0.7±0.2	0.5±0.1	0.4±0.1	0.2±0.1	-0.22±0.14	-0.37±0.17	0.8±0.1	
87	00:15:44.28	-39:12:09.2	0.72	6.6±1.2	3.1±0.8	2.7±0.8	1.7±0.2	1.8±0.2	1.0±0.1	-0.06±0.14	-0.27±0.17	2.8±0.2	
88	00:15:44.79	-39:00:30.4	1.09	3.7±0.9	5.5±1.0	2.4±0.7	-	-	-	0.20±0.15	-0.39±0.15	2.6±0.4	
89	00:15:45.87	-39:10:23.0	0.96	2.5±0.4	1.0±0.2	0.9±0.3	0.3±0.1	0.4±0.1	0.3±0.1	-0.20±0.12	-0.09±0.17	0.8±0.1	
90	00:15:48.35	-39:18:39.3	0.59	11.9±0.8	6.3±0.5	2.8±0.4	3.3±0.3	2.3±0.2	1.3±0.2	-0.26±0.06	-0.33±0.07	3.9±0.2	
91	00:15:48.54	-39:03:42.0	1.08	4.4±0.7	2.9±0.6	1.0±0.5	1.7±0.3	1.1±0.3	0.5±0.2	-0.20±0.14	-0.43±0.21	1.7±0.2	
92	00:15:49.27	-39:23:48.2	1.47	0.9±0.3	0.5±0.3	0.8±0.3	0.3±0.1	0.5±0.1	0.3±0.1	0.11±0.29	-0.15±0.24	0.7±0.1	
93*	00:15:50.29	-39:16:36.8	2.24	1.2±0.3	0.0±0.1	0.0±0.1	-	-	-	-1.00±0.18	-	0.1±0.1	0.5
94	00:15:51.69	-39:02:32.5	1.53	1.3±0.5	1.6±0.5	2.6±0.6	0.3±0.2	1.1±0.3	0.7±0.3	0.39±0.23	0.05±0.20	1.7±0.3	
95	00:15:51.79	-39:03:55.4	1.34	0.6±0.5	1.7±0.5	1.9±0.6	0.1±0.1	0.1±0.1	1.2±0.3	0.40±0.32	0.46±0.20	1.5±0.3	
96	00:15:52.19	-39:12:32.1	1.31	0.9±0.3	1.0±0.2	0.9±0.3	-	-	-	0.08±0.18	-0.04±0.18	0.8±0.2	
97	00:15:52.80	-39:10:59.8	0.87	3.1±0.5	1.0±0.3	0.9±0.3	0.6±0.1	0.6±0.1	0.4±0.1	-0.33±0.11	-0.17±0.19	1.0±0.1	
98*	00:15:54.92	-39:16:06.9	1.34	0.5±0.3	0.7±0.2	0.4±0.2	0.0±0.1	0.0±0.0	0.5±0.1	0.16±0.31	-0.23±0.30	0.5±0.1	2.0
99	00:15:55.83	-39:09:37.8	1.02	3.2±0.5	1.4±0.3	0.4±0.2	1.4±0.4	0.6±0.2	0.6±0.2	-0.38±0.19	-0.38±0.24	0.9±0.1	
100	00:15:56.82	-39:13:39.5	1.06	0.1±0.1	0.8±0.2	2.1±0.4	0.0±0.0	0.3±0.1	0.4±0.1	0.97±0.12	0.32±0.16	0.8±0.1	
101*	00:15:57.33	-39:16:12.9	1.14	3.7±0.5	0.3±0.2	0.0±0.1	0.7±0.1	0.0±0.1	0.0±0.0	-0.87±0.11	-1.00±1.00	0.4±0.1	1.4
102	00:15:57.40	-39:24:27.9	0.79	5.6±0.7	2.1±0.4	1.2±0.4	1.8±0.2	0.7±0.2	0.7±0.2	-0.46±0.10	-0.13±0.17	1.7±0.2	
103	00:15:59.24	-39:03:23.8	1.00	6.8±1.0	2.2±0.6	1.3±0.5	2.2±0.4	0.8±0.2	0.7±0.2	-0.50±0.14	-0.13±0.22	1.9±0.2	
104	00:15:59.52	-39:10:18.1	1.56	1.9±0.4	1.1±0.3	0.7±0.3	-	-	-	-0.27±0.15	-0.23±0.22	0.8±0.2	
105	00:15:59.54	-39:19:07.2	0.74	4.1±0.5	2.8±0.4	1.3±0.3	0.9±0.2	1.0±0.1	0.6±0.1	-0.09±0.10	-0.34±0.12	1.6±0.1	
106*	00:16:00.50	-39:16:55.0	1.45	0.0±0.1	0.5±0.2	1.7±0.3	0.0±0.0	0.1±0.1	0.4±0.1	0.85±0.51	0.55±0.21	0.7±0.1	2.8
107	00:16:01.26	-39:21:38.3	1.61	0.4±0.3	0.5±0.2	0.9±0.3	0.0±0.1	0.2±0.1	0.4±0.1	0.50±0.38	0.26±0.25	0.6±0.1	
108*	00:16:01.75	-39:16:23.1	0.75	0.2±0.1	0.5±0.2	5.1±0.5	0.0±0.0	0.1±0.1	2.1±0.2	0.57±0.40	0.86±0.06	2.9±0.2	11.1
109	00:16:02.79	-39:12:11.5	0.62	9.8±0.7	4.9±0.5	2.4±0.4	2.0±0.2	2.0±0.2	1.3±0.2	-0.21±0.07	-0.27±0.08	3.3±0.2	
110	00:16:04.47	-39:11:39.4	0.63	6.3±0.6	5.2±0.5	2.7±0.4	2.3±0.3	2.1±0.3	1.6±0.2	-0.07±0.08	-0.24±0.09	3.3±0.2	
111	00:16:05.24	-39:05:31.8	1.05	1.3±0.4	3.2±0.6	2.2±0.5	0.4±0.2	1.8±0.3	1.3±0.3	0.52±0.15	-0.18±0.14	2.2±0.3	
112*	00:16:06.67	-39:15:22.5	0.86	1.2±0.3	2.0±0.3	2.6±0.4	0.2±0.1	0.9±0.2	1.0±0.2	0.41±0.16	0.08±0.12	1.9±0.2	7.0

SRC	RA	DEC	$r_1 \sigma$	pn cts ks ⁻¹			MOS cts ks ⁻¹			HR1	HR2	f_X	L_X
ID	(hh:mm:ss)	(° : ' : ")	(")	S	M	H	S	M	H			($\times 10^{-14}$)	($\times 10^{36}$)
(1)	(2)	(3)	(4)	(5)	(6)	(7)	(8)	(9)	(10)	(11)	(12)	(13)	(14)
113*	00:16:08.34	-39:17:41.1	0.87	2.1±0.4	3.4±0.5	2.1±0.4	0.5±0.1	1.0±0.2	0.3±0.1	0.27±0.12	-0.35±0.12	1.3±0.1	5.0
114	00:16:08.81	-39:11:22.2	1.15	1.7±0.4	0.8±0.2	0.7±0.3	0.5±0.1	0.5±0.1	0.2±0.1	-0.23±0.16	-0.19±0.23	0.7±0.1	
115	00:16:09.59	-39:07:45.4	1.90	1.9±0.4	1.2±0.3	0.0±0.2	–	–	–	-0.24±0.16	-1.00±0.28	0.4±0.1	
116	00:16:10.33	-39:01:25.6	2.45	2.4±0.6	0.8±0.5	1.5±0.6	–	–	–	-0.48±0.24	0.28 ±0.32	1.2±0.4	
117*	00:16:10.37	-39:17:05.3	2.80	1.0±0.4	1.2±0.3	0.0±0.1	–	–	–	0.06±0.22	-0.92±0.19	0.3±0.1	1.2
118	00:16:10.81	-39:20:13.7	0.76	4.5±0.6	3.4±0.5	1.9±0.4	0.6±0.1	1.0±0.2	1.0±0.2	-0.02±0.13	-0.16±0.13	2.1±0.2	
119	00:16:12.59	-39:03:45.0	2.79	2.1±0.6	0.3±0.4	0.8±0.5	–	–	–	-0.74±0.26	0.45 ±0.50	0.7±0.3	
120	00:16:14.28	-39:27:27.3	1.62	–	–	–	0.5±0.2	0.9±0.2	0.8±0.2	0.24±0.23	-0.02±0.18	1.7±0.3	
121	00:16:14.39	-39:08:48.1	1.24	0.6±0.3	1.5±0.3	0.6±0.3	0.6±0.1	0.4±0.1	0.3±0.1	0.15±0.22	-0.32±0.24	0.7±0.1	
122*	00:16:19.34	-39:16:45.5	2.61	0.2±0.2	1.3±0.3	0.5±0.3	–	–	–	0.75±0.26	-0.48±0.24	0.5±0.2	1.8
123	00:16:23.06	-39:23:53.7	1.75	2.2±0.5	0.9±0.3	0.4±0.3	–	–	–	-0.43±0.18	-0.42±0.37	0.6±0.2	
124	00:16:27.39	-39:09:26.6	1.66	1.4±0.4	1.6±0.4	0.7±0.4	–	–	–	0.08±0.20	-0.42±0.25	0.8±0.2	
125	00:16:33.07	-39:05:32.6	0.73	13.6±1.4	6.1±1.0	3.7±0.7	4.9±0.6	3.3±0.5	1.4±0.4	-0.30±0.08	-0.33±0.12	4.7±0.4	
126	00:16:35.81	-39:17:24.4	1.39	2.0±0.4	0.0±0.1	0.3±0.3	–	–	–	-1.00±0.08	1.00 ±0.53	0.4±0.2	
127	00:16:36.45	-39:15:01.5	2.17	–	–	–	0.1±0.1	0.7±0.2	0.0±0.1	0.78±0.22	-1.00±0.22	0.3±0.1	
128	00:16:36.48	-39:25:14.6	1.45	–	–	–	1.9±0.4	0.9±0.3	0.8±0.2	-0.36±0.15	-0.04±0.20	2.3±0.4	
129	00:16:37.43	-39:06:33.3	1.47	3.8±0.9	2.1±0.6	1.2±0.6	–	–	–	-0.29±0.17	-0.29±0.26	1.4±0.3	
130	00:16:38.59	-39:16:24.1	1.42	2.3±0.5	1.9±0.4	0.6±0.3	–	–	–	-0.11±0.15	-0.54±0.22	0.8±0.2	
131	00:16:40.12	-39:11:35.3	1.19	3.4±0.6	2.2±0.5	0.8±0.4	1.0±0.2	0.9±0.2	0.3±0.2	-0.15±0.15	-0.47±0.23	1.2±0.2	
132	00:16:42.18	-39:18:20.2	0.70	11.0±1.1	7.3±0.9	5.0±0.8	2.3±0.3	3.4±0.4	2.9±0.4	-0.04±0.08	-0.14±0.09	5.5±0.4	
133	00:16:43.46	-39:08:26.8	1.84	0.2±0.3	2.0±0.5	1.3±0.5	–	–	–	0.86±0.28	-0.23±0.22	1.0±0.3	
134	00:16:47.41	-39:15:02.9	1.13	4.0±0.7	3.2±0.6	0.9±0.5	1.2±0.3	1.0±0.3	1.6±0.3	-0.10±0.16	-0.11±0.17	1.8±0.2	
135	00:16:48.71	-39:09:32.0	0.97	6.0±1.0	4.3±0.8	1.1±0.5	1.5±0.4	1.3±0.3	1.1±0.3	-0.14±0.18	-0.37±0.17	2.1±0.3	
136	00:16:55.54	-39:17:50.6	1.11	6.1±0.9	3.9±0.7	2.4±0.7	2.1±0.4	1.3±0.3	1.7±0.4	-0.23±0.14	-0.06±0.16	2.93±0.3	
137	00:17:04.21	-39:10:43.4	1.09	12.6±1.6	5.9±1.0	2.7±0.8	–	–	–	-0.36±0.09	-0.36±0.15	3.7±0.5	

NOTES: (1) source number (objects within the D₂₅ ellipse are marked by *); (2) RA in hh:mm:ss (J2000 coordinates); (3) DEC in ° : ' : " (J2000 coordinates); (4) 1σ error radius including a 0.5'' systematic error; (5), (6) & (7) and (8), (9) & (10) source count rates in the soft (0.3–1 keV), medium (1–2 keV) & hard (2–6 keV) bands for the pn and MOS cameras respectively, with significant source detections ($> 4\sigma$) highlighted in bold; (11) & (12) soft (HR1) and hard (HR2) hardness ratios (as defined in the text); (13) source X-ray flux (0.3–6 keV) in units of 10^{-14} erg cm⁻² s⁻¹; (14) source X-ray luminosity (0.3–6 keV) in units of 10^{38} erg s⁻¹ (assuming a distance to NGC 55 of 1.78 Mpc).

4.3.2 X-ray sources associated with NGC 55

Table 4.2 gives a breakdown of the number of detected sources as a function of instrument and energy band. The D_{25} ellipse of the galaxy occupies $\sim 13\%$ of the total FOV, but encompasses $\sim 30\%$ of the sources. A Monte Carlo simulation was performed to investigate whether the 42 sources detected within the D_{25} ellipse of NGC 55 represent an excess compared to the number of background objects expected by chance. The predictions are based on the $\log N$ – $\log S$ curves published by Giacconi et al. (2001).

Table 4.2: The number of sources detected in each energy band in the pn and MOS images.

Camera	S	M	H	S/M/H
pn	25[91]	25[93]	18[55]	35[119]
MOS	19[70]	22[83]	20[64]	32[103]
pn/MOS	29[105]	30[110]	23[76]	42[137]

NOTES: The numbers quoted are for the D_{25} ellipse with the full-field values given in square brackets. The total number of individual sources detected in various instrument and energy band combinations is also indicated.

Simulations were initially performed to investigate the source statistics in the medium (1–2 keV) band. Here the comparison was between the number of actual detections in this band and the numbers predicted on the basis of the 0.5–2 keV $\log N$ – $\log S$ relation². The simulation involved distributing sources over a sky area encompassing the full FOV of the NGC 55 observations with a surface density and flux distribution consistent with a random sampling of the input $\log N$ – $\log S$ curve. The X-ray flux of each simulated source was then converted to counts using the 1–2 keV exposure maps, applying the relevant 0.5–2 keV flux to 1–2 keV counts conversion (assuming the spectral form defined earlier) and finally Poisson deviating the predicted count. A given source was deemed to be ‘detected’ if its estimated count exceeded a threshold value in either the pn or MOS channels (or both) in either of the EPIC observations. The full process involved the determination of the average number of source detections in 5000 simulation runs. The threshold count used in the analysis was set by requiring the number of

²In the simulation the flux range from which input sources were randomly selected, subject to the $\log N$ – $\log S$ weighting, was constrained to be $9 \times 10^{-16} \text{ erg cm}^{-2} \text{ s}^{-1} - 2 \times 10^{-13} \text{ erg cm}^{-2} \text{ s}^{-1}$.

simulated detections to match the number of actual detections for the off-galaxy regions of the EPIC fields. In practice a threshold of 15 counts gave a reasonable approximation to the detection criteria actually employed in extracting 1–2 keV band sources.

On the basis of the medium band analysis the number of sources detected within the D_{25} ellipse of NGC 55 exceeds the source count prediction by 17 *i.e.*, $\sim 55\%$ of the total. However, this must represent a lower limit since the simulation ignores the effect of absorption in the disc of the galaxy, which will tend to suppress the count rates of background sources below the predicted levels. Allowing for column densities within the disc of NGC 55 of up to 10^{22} cm^{-2} , it is estimated that the above fraction should be increased by a further 5%–10%, implying that roughly two-thirds of the medium band sources within the D_{25} ellipse are probably associated with the galaxy. These sources presumably comprise the bright end of the intrinsic X-ray source population of NGC 55.

The extension of the above analysis to the soft band is complicated by the increased impact of the absorption in the disc of NGC 55. For the hard band, similar results to the above were obtained, albeit with poorer statistics. However, few of the D_{25} sources detected solely in the soft band are likely to be background objects given the softness of their spectra, whereas the hard band only detections represent just a few sources in total. In summary, it is estimated that there may be 10–15 background interlopers in the sample of 42 sources detected within the D_{25} ellipse of NGC 55.

4.3.3 Cross-correlation with other catalogues

The *XMM-Newton* source list was cross-correlated with other multi-wavelength data, including the catalogues available in the NED and SIMBAD databases, by searching for matches within the 3σ error radius (including a $1''$ systematic error) of each *XMM-Newton* source position. The results are summarised in Table 4.3. Of the 14 sources with possible identifications, 6 lie within the confines of the D_{25} ellipse of NGC 55. Four of these are likely to be objects within the galaxy itself, *i.e.*, sources 48, 52 and 58 which coincide with radio sources and have hardness ratios commensurate with SNRs (see § 4.5), and source 71, a likely BHB system in NGC 55 as discussed in the previous chapter. The other two ‘identified’ D_{25} sources are classed optically as galaxies and are presumably background AGN. Of the remaining 8 identified sources, 6 are similarly associated with background galaxies, whilst source 90, which lies just outside the D_{25} ellipse, is coincident with a possible globular cluster located in the

halo of NGC 55 (Liller & Alcaïno 1983; Olsen et al. 2004) and source 39 is coincident with a variable (foreground) star.

Table 4.3 also lists the matches between the *XMM-Newton* sources and previous *ROSAT* X-ray source detections (again within a 3σ position error, but also incorporating a $15''$ or a $10''$ systematic uncertainty in the *ROSAT* PSPC or HRI data respectively). A total of 15 X-ray sources within the D_{25} ellipse have previously been catalogued by *ROSAT*, as have 12 outside this region. Finally, the *XMM-Newton* source list was briefly compared to a *Chandra* source list of galaxy (Obs ID 2255) produced via the standard CIAO processing tools. From this comparison, the *XMM-Newton* sources 29, 34, 55 and 56 are potentially subject to source confusion, as they could be resolved into two separate sources by the sub-arcsecond spatial resolution of *Chandra*. Fig. 4.2 shows the central part of the 0.3–6 keV *XMM-Newton* image with sources of interest marked with different symbols.

Table 4.3: Matches of the *XMM-Newton* sources with sources in other catalogues.

<i>XMM</i> ID	<i>ROSAT</i> ID		Other ID	Source type
	PSPC	HRI		
8			APM B001129.07-391943.0	Galaxy
17	N55-1			
20*	R1, S19, N55-2	N55-2		
27*	N55-3			
29	S18			
35*			BS2000-17	Galaxy
38*	R2, S17, N55-4	N55-4		
39	S16, N55-5	N55-5	UY Scl	Variable Star
41	N55-6	N55-6		
42	S14, RXJ 001451.5-392417			
43*	R3, S15, N55-7	N55-7		
46	1WGA J0014.9-3916, N55-8			
47*	R4, S13	N55-9		
48*			HDW86 - RS	Radio Source
52*	R5, S11, N55-10		HDW86 - RS	Radio Source
55*	N55-11			
58*			HK83-08, HDW86 - RS	HII region, Radio Source
71*	R6, S7, N55-14	N55-14	XMMU J001528.9-391319	ULX, XRB
72			LCRS B001300.1-392355	Galaxy
74*	R7, N55-15			
77			LCRS B001306.8-392624	Galaxy
79*	N55-16			
81	1WGA J0015.6-3926			
84*	N55-17			
87	N55-18			
90	N55-19		LA43	Globular cluster
94			APM B001321.45-391912.8	Galaxy
101*	N55-20			
110	N55-22			
112*	N55-23			
117*	N55-24			
118	1WGA J0016.1-3920, N55-25			
122*			LCRS B001349.4-393325	Galaxy
123			APM B001352.34-394040.4	Galaxy
125	1WGA J0016.5-3905			
132			LCRS B001412.2-393501	Galaxy
137	1WGA J0017.0-3910			

NOTES: *ROSAT* ID numbers refer to Read et al. (1997) (R#), Schlegel et al. (1997) (S#) and Roberts (1997) (N55-#). Other references: APM - Maddox et al. (1990); 1WGA - White et al. (2000), BS2000 - Beasley & Sharples (2000); UY Scl - Perryman et al. (1997); RXJ - Barber et al. (1996); HK83- Hodge & Kennicutt (1983); HDW86 - Hummel et al. (1986) (*i.e.*, the triple radio source); XMMU - Chapter 3; LCRS - Shectman et al. (1996); LA43 - Liller & Alcaïno (1983).

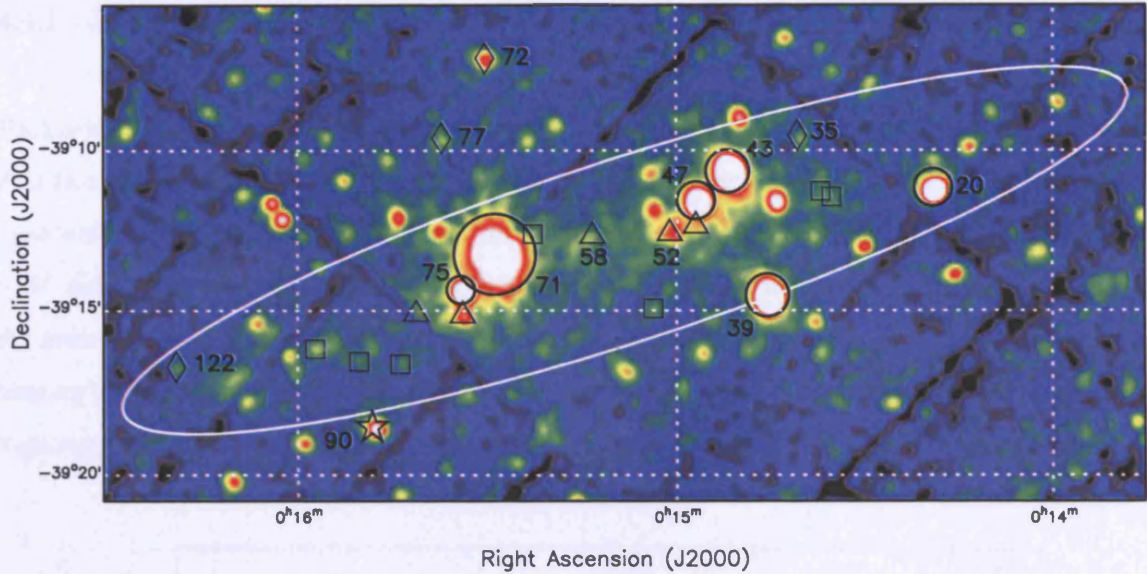


Figure 4.2: The central regions of the *XMM-Newton* image of the NGC 55 field in a broad (0.3–6 keV) bandpass. The ellipse marks the optical extent of the galaxy as measured by the D_{25} isophote. The six brightest X-ray sources are highlighted with circles denoting the spectral extraction radius used. The triangles mark the positions of sources with hardness ratios commensurate with SNRs, whereas the squares mark very soft sources (see § 4.5). An X-ray source possibly located within a globular cluster (Beasley & Sharples, 2000) lies at the position of the star symbol. Sources identified with background galaxies are indicated by diamonds.

4.4 The brightest discrete X-ray sources

Six catalogued sources with observed fluxes in excess of 10^{-13} erg cm $^{-2}$ s $^{-1}$ lie within or close to the D_{25} ellipse of NGC 55. These sources (20, 39, 43, 47, 71 and 75 in Table ??) have been detected with sufficiently high count rates to permit reasonably detailed spectral and temporal analyses of their X-ray properties. A study of the brightest source (71) was presented in Chapter 3, therefore this work concentrates on four of the next five brightest sources, excluding only source 75 for reasons of practicality. The emission from this latter source was contaminated by the wings of the PSF of source 71 in both observations (and furthermore it lay at the very edge of the FOV in the second observation, where it was detected only in the MOS data). It is worth mentioning that source 20 was only within the FOV of the second observation, and source 39 may be identified with a foreground star.

4.4.1 Light curves

Background-subtracted light curves were extracted for each source based on the combined 0.3–6 keV data from the three EPIC cameras. For sources 20 and 47, circular source extraction apertures were used with radii of $35''$. For the marginally brighter sources 39 and 43, circular extraction regions with a $40''$ radius were used. The background data were extracted from same-sized apertures, positioned in the nearest source-free regions visible in all three detectors. The resulting light curves with 200 s time binning are shown in Fig. 4.3. In each case the count rate from each observation was corrected for vignetting effects so as to plot the equivalent on-axis count rate.

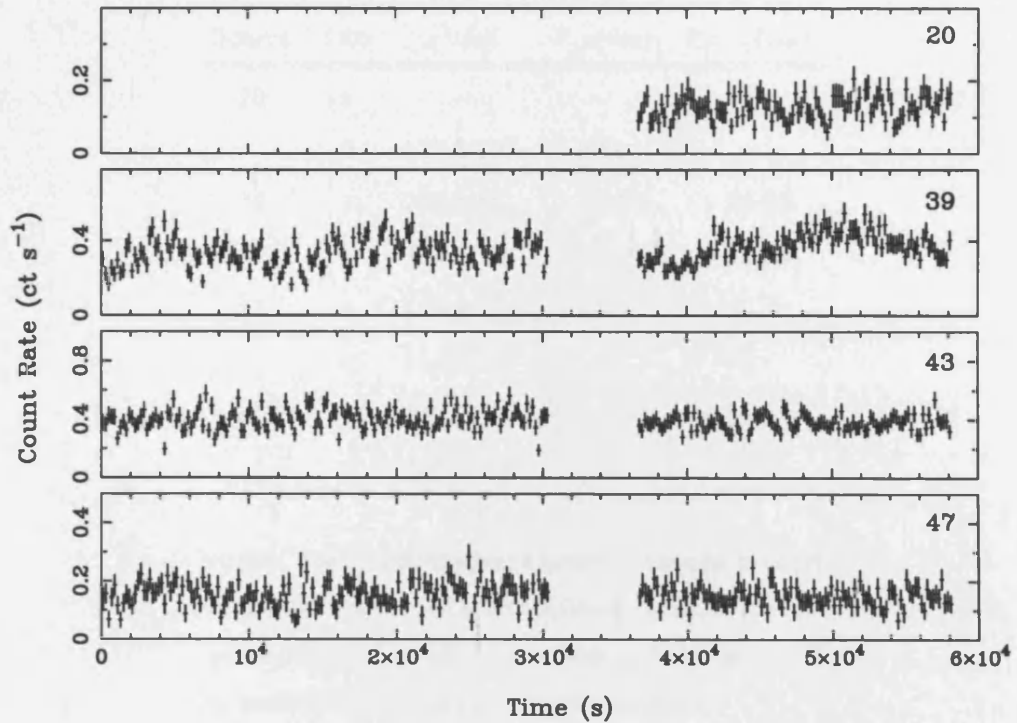


Figure 4.3: The background-subtracted 0.3–6 keV light curves of four bright sources, displayed in 200 s time bins. The light curves are based on the combined data from the MOS-1, MOS-2 and pn cameras. The error bars correspond to $\pm 1\sigma$.

The short-term X-ray variability of each source was investigated by carrying out a χ^2 test (against the hypothesis of a constant flux) on the raw 200 s binned light curves. A Kolmogorov-Smirnov (K-S) test was also performed to search for additional variability characteristics, such as low amplitude underlying trends in the light curve, that a χ^2 test might not detect. For the latter purpose, only the pn light curves with 1s time bins were used. The results of both tests are summarised in Table 4.4. It appears that source 39 (the foreground star) is the only object in the set for which there is strong evidence for short-term X-ray variability ($> 99.9\%$ probability in each test). Of the three remaining sources, sources 20 and 47 show limited evidence (at $\gtrsim 2\sigma$ significance) of variability in one of the tests. However, source 43 shows no evidence at all of short-term variability.

Table 4.4: Tests for short-term variability

Source	Obs	χ^2/dof	$P_{\chi^2}(\text{var})$	$P_{K-S}(\text{var})$
20	I	–	–	–
	II	137.3/107	97%	–
39	I	228.5/151	$> 99.9\%$	$> 99.9\%$
	II	274.5/107	$> 99.9\%$	$> 99.9\%$
43	I	155.2/151	–	–
	II	114.7/107	–	–
47	I	153.2/151	–	98%
	II	105.8/107	–	–

NOTES: The probability that a source is variable in either observation (Obs I: 0028740201 Obs II: 0028740101) according to the χ^2 and K-S tests. Only probabilities $>95\%$ are quoted so as to highlight possible variability.

All four sources were also previously detected in both the *ROSAT* PSPC (performed on 22nd–24th November 1992) and HRI (12th–14th December 1994) observations indicating that these are all relatively persistent sources. A comparison of the measured X-ray fluxes (based on the simple spectral models derived in the next section) reveals that sources 20, 39 and 43 varied by factors of ~ 2 , ~ 2 and ~ 3 respectively, but that the flux of source 47 remained remarkably steady at $1.4 \pm 0.2 \times 10^{-13} \text{ erg cm}^{-2} \text{ s}^{-1}$ (0.5–2 keV) over the 9 yr baseline.

4.4.2 X-ray Spectra

X-ray spectra were extracted in the 0.3–10 keV band (with `especget` as described in § 2.3.3) using circular extraction apertures with radii of 35'' (sources 20 and 47) or 40'' (sources 39 and 43). Background data were again extracted from nearby source-free regions, in this case with radii of 50'' for sources 39 and 43, and 60'' for sources 20 and 47; as far as possible, the chosen regions were located at similar distances from the pn readout nodes to the sources, and free of diffuse emission from the galaxy (see § 4.6).

The spectral analysis was performed using XSPEC v.11.3.0. As in the previous chapter, the pn, MOS-1 and MOS-2 spectra from both observations were fitted simultaneously, including constant multiplicative factors to allow for calibration differences between the cameras. This value was frozen at unity for the pn data and allowed to vary for the MOS detectors, with the values typically agreeing within 15%.

Initial fits to the X-ray spectra of the three bright sources most likely associated with NGC 55 (*i.e.*, 20, 43, 47), were made using single component models in XSPEC. These included power-law (`po`), black-body (`bbody`), MCD (`diskbb`), bremsstrahlung (`bremss`) and solar-abundance optically-thin thermal plasma (`mekal`) spectral forms. An intervening absorption column (`tbabs`, utilising the relative interstellar abundances and absorption cross-sections tabulated by Wilms et al. 2000) was applied in each case. Typically, the best fits were obtained with either the `po` or the `diskbb` models as summarised in Table 4.5, together with the observed 0.3–10 keV fluxes and the observed and intrinsic (unabsorbed) luminosities for the best fitting model. The spectra of sources 20 and 47 are best described by a simple absorbed power-law continuum with $\Gamma \sim 1.7$ and 1.8 respectively, although in both cases the `diskbb` model also provides a statistically acceptable fit (with $kT_{in} \sim 1.7$ keV and 1.5 keV respectively). However, a power-law model is rejected (at $> 99.99\%$ probability) for source 43, which is instead very well fitted by a `diskbb` model with an inner disc temperature of ~ 0.8 keV. Fig. 4.4 shows the spectra and best fitting single component model in each case.

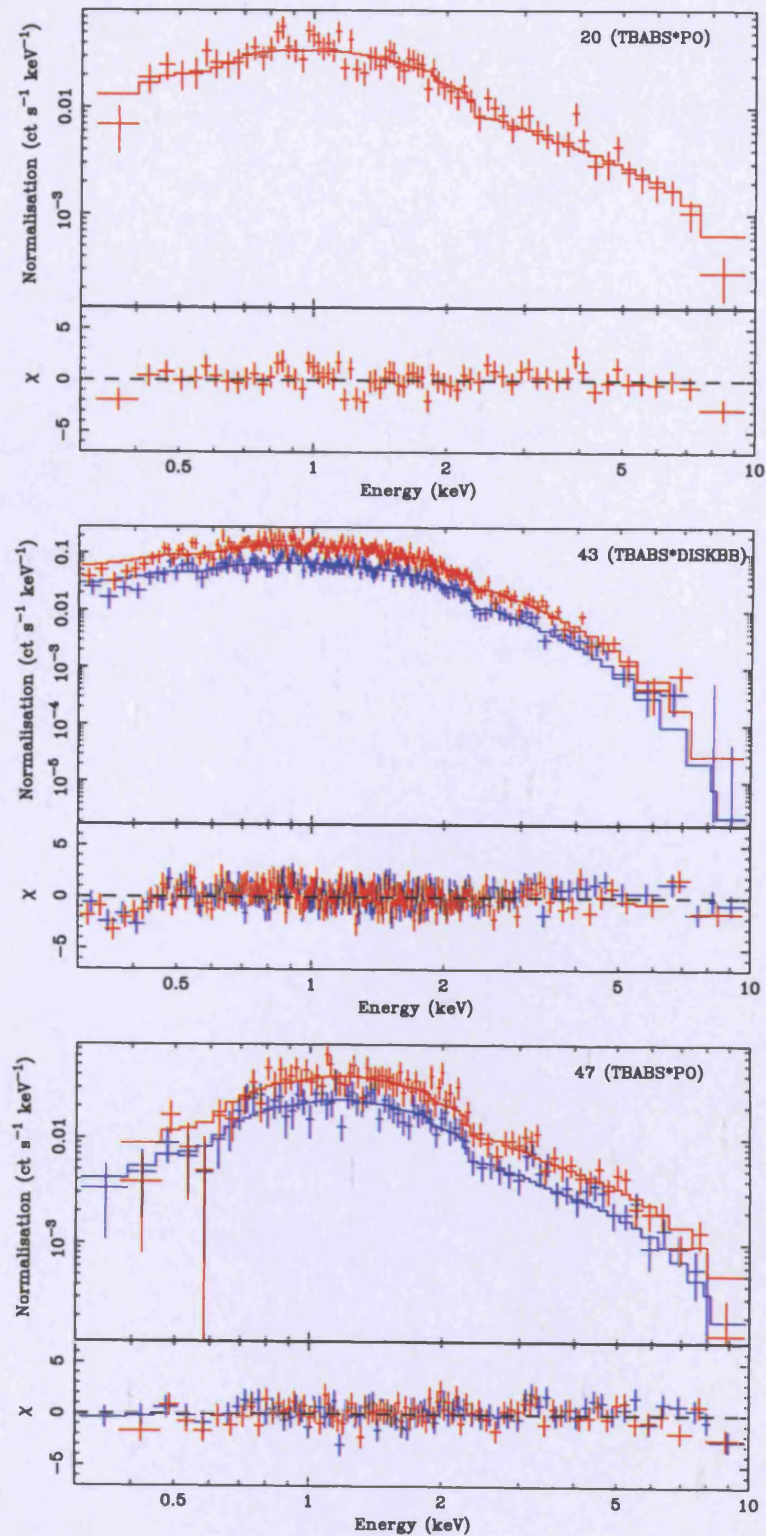


Figure 4.4: EPIC pn count rate spectra and $\Delta\chi$ residuals with respect to the best-fitting single component model specified in Table 4.5, for sources 20, 43 and 47. Data from the first and second observations are shown as blue and red respectively.

Table 4.5: Spectral fitting of single component models for three bright sources in NGC 55

Source	Model	N_H^a	Γ/kT_{in}	χ^2/dof	$f_X(\text{obs})^b$	$L_X(\text{obs})^c$	$L_X(\text{int})^d$
20	po	2.6 ± 0.4	1.7 ± 0.1	125.6/119	$3.5^{+0.2}_{-0.3}$	1.3 ± 0.1	1.7 ± 0.1
	diskbb	$0.8^{+0.3}_{-0.2}$	1.7 ± 0.1	130.9/119	–	–	–
43	po	4.2 ± 0.2	2.7 ± 0.1	715.0/573	–	–	–
	diskbb	1.3 ± 0.1	0.8 ± 0.1	551.3/573	6.3 ± 0.1	2.4 ± 0.1	2.9 ± 0.1
47	po	$4.6^{+0.5}_{-0.4}$	1.8 ± 0.1	252.0/276	4.6 ± 0.2	1.7 ± 0.1	2.6 ± 0.1
	diskbb	2.1 ± 0.3	1.5 ± 0.1	278.2/276	–	–	–

NOTES: The best fitting model for each source is highlighted by showing the χ^2/dof values in bold face. ^a Column density including Galactic ($\times 10^{21} \text{ cm}^{-2}$); ^b Observed 0.3–10 keV X-ray flux ($\times 10^{-13} \text{ erg cm}^{-2} \text{ s}^{-1}$) for the best fitting model; ^c Observed 0.3–10 keV X-ray luminosity ($\times 10^{38} \text{ erg s}^{-1}$) for the best fitting model. ^d Intrinsic 0.3–10 keV X-ray luminosity ($\times 10^{38} \text{ erg s}^{-1}$) for the best fitting model.

Given the high apparent X-ray luminosities of these sources, *i.e.*, close to or exceeding the Eddington limit for spherical accretion on to a $\sim 1.4 M_\odot$ neutron star, attempts were also made to fit the data with the canonical model for BHB spectra, namely a po+diskbb model. This two component model provided an improvement to the spectral fits for all three sources, albeit with varying degrees of improvement ($\Delta\chi^2 \sim 4.5 - 44$ for two extra degrees of freedom).

However, the model provided unusually low inner-disc temperatures for sources 20 and 47 than expected for ‘normal’ luminous stellar-mass BHBs (which typically have $kT_{in} \sim 0.7 - 2 \text{ keV}$, *c.f.* McClintock & Remillard 2006). Therefore alternative models for the soft component in these sources were attempted using bbody and mekal spectral forms. These produced equally good fits to the data, although in all cases the soft components only account for a small fraction ($\sim 6\%$) of the total observed X-ray flux. The po+diskbb fits to source 43 provided an even more puzzling result; the power-law fitted to the soft end of the X-ray spectrum. Similar results have been seen for several ULXs, including source 71 in the same host galaxy (*e.g.*, Chapter 3; Roberts et al. 2005). However, the presence of such a power-law component is difficult to explain physically, and as such the power-law is most likely a proxy for another soft component. Hence attempts were also made to fit the soft component in this source with the bbody and mekal models (as per sources 20 and 47).

Table 4.6: Spectral fitting of two component models for two bright sources in NGC 55

Source	Model ^a	N_H	$\Gamma/kT/kT_{in}$ ^b	kT_{in}/Γ ^c	χ^2/dof	$\Delta\chi^2$ ^d	f_{soft} ^e	f_{hard} ^f
43	po+diskbb	5.6 ± 0.11	$4.91^{+0.74}_{-0.78}$	0.82 ± 0.04	507.3/571	44.0	27%	73%
	bbody+diskbb	$2.6^{+0.9}_{-0.4}$	0.14 ± 0.02	$0.81^{+0.03}_{-0.04}$	513.5/571	37.8	10%	90%
	mekal+diskbb	$1.7^{+0.3}_{-0.2}$	$0.28^{+0.06}_{-0.04}$	0.80 ± 0.02	522.9/571	28.4	4%	96%
47	diskbb+po	$11.0^{+1.6}_{-2.2}$	$0.11^{+0.02}_{-0.01}$	$2.08^{+0.09}_{-0.13}$	234.1/274	17.9	6%	94%
	bbody+po	$10.4^{+2.4}_{-2.2}$	0.10 ± 0.01	$2.06^{+0.11}_{-0.12}$	234.1/274	17.9	6%	94%
	mekal+po	$9.3^{+2.4}_{-2.5}$	$0.24^{+0.09}_{-0.05}$	$1.99^{+0.12}_{-0.14}$	234.3/274	17.7	6%	94%

NOTES: ^a Two component model with the soft component listed first; ^b value of characteristic parameter for the soft component; ^c value of characteristic parameter for the hard component; ^d χ^2 improvement over the best-fitting single component fit, for two extra degrees of freedom; ^e fraction of the total observed flux in the soft component; ^f fraction of the total observed flux in the hard component. The significance probability of the fit improvement over the single component fit is 100% in each case, based on the resolution of the Monte Carlo simulations described in the text (200 simulations per source).

The statistical significance of the improvement offered by these additional components (above the simple single component fits) was quantified using the prescription described in section 5.2 of Protassov et al. (2002)³. This uses a Monte Carlo recipe for XSPEC to simulate the expected reference distribution of F-values based on an input null-hypothesis spectrum (*i.e.*, the best fitting single component model in each case). This reference distribution yields a confidence probability for the fit improvement using additive model components. These simulations show that the two-component modelling provide significant improvements ($\gtrsim 3\sigma$, at the best resolution of the simulations) over a diskbb for source 43, and over a simple power-law model for source 47. However, the $\Delta\chi^2 \sim 5$ improvements for source 20, for two extra degrees of freedom, were not significant (at a probability of $< 90\%$) for any of the two component modelling. Therefore only the results of the two-component modelling to sources 43 and 47 are shown in Table 4.6. This table also shows the percentage of the total flux in each of the model components. In all cases the hard components dominate the total observed X-ray flux. The plausibility of these spectral solutions are discussed in § 4.7.

The final source for which spectral analysis was performed was source 39 which, unlike the other three sources, did not have a simple continuum spectral shape (see Fig. 4.5). This source is in fact

³The F-test **should not** be used in the case of additive model components, because it does not follow its expected theoretical reference distribution in this case (Protassov et al., 2002).

coincident with the $m_v = 11.5$ variable foreground star UY Scl and is presumably a stellar coronal source. Therefore an initial fit to its X-ray spectrum was made using a thermal plasma (`mekal`) model. However, a single temperature `mekal` model resulted in an unacceptable fit, with $\chi^2_\nu \sim 1.7$ (i.e., $\chi^2_\nu = \frac{\chi^2}{\text{dof}}$), even after allowing the abundance to vary from solar. This was due, in part, to an apparent increase in the hardness of the source at energies > 2 keV in the second observation (c.f. Fig. 4.5). Attempts to model this apparent increase were made by allowing the `mekal` temperature and normalisation to vary between the two observations, but this approach proved unsuccessful. However, the addition of a second, hotter `mekal` component, with a normalisation free to vary between the observations did lead to a significant improvement in the fit ($\chi^2_\nu \sim 1.2$), although residuals remained evident above 2 keV. An acceptable fit was finally provided by the addition of a third, hotter `mekal` component, and again allowing the normalisation of this hottest `mekal` to vary between the observations (while the other normalisations were tied across the two observations). All `mekal` components were fitted with the same abundance. Details of the best fit are given in Table 4.7. The variation in the hottest component was considerable, implying at least a factor 10 increase in its strength between the two observations, although even at its brightest level (in the second observation) its contribution to the total 0.3–10 keV source flux amounts to only $\sim 20\%$.

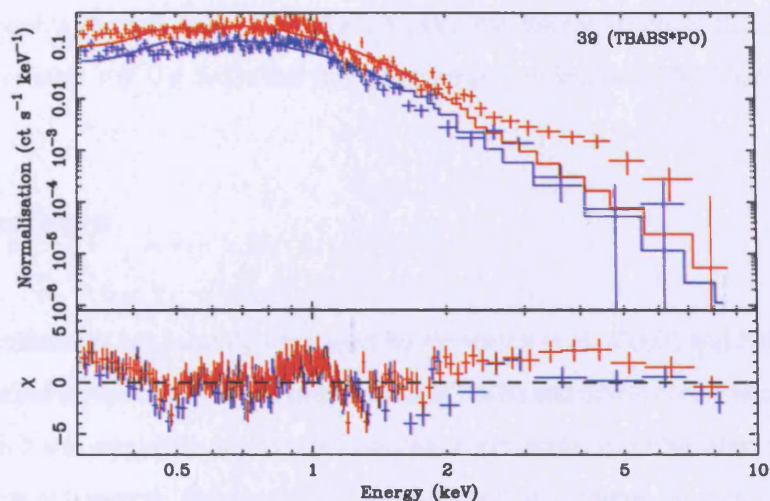


Figure 4.5: EPIC pn count rate spectra and $\Delta\chi$ residuals for a simple power-law continuum model fit to source 39 (the putative foreground star). The data are displayed as in Fig. 4.4.

The low absorption column (set at Galactic) and multi-temperature thermal plasma spectrum provide strong support for the origin of the X-ray emission to be in the stellar corona of an active star in our own Galaxy. Temperatures of ~ 0.3 keV and 1 keV are typical for such objects, however a prominent

Table 4.7: Spectral fitting results to source 39

Parameter	Value
$N_H(\times 10^{21} \text{ cm}^{-2})$	0.155 (<i>fixed</i>)
kT_1 (keV)	0.33 ± 0.02
kT_2 (keV)	1.00 ± 0.04
kT_3 (keV)	$3.44^{+2.39}_{-1.27}$
Abundance (Z_\odot)	$0.43^{+0.08}_{-0.07}$
χ^2/dof	512.6/463

NOTES: Three temperature mekal spectral fit results (modified by Galactic absorption) to the putative foreground star.

emission component at temperatures at or above 2 keV is commonly seen only in young stars or active binaries (such as RS CVns), and rarely in main sequence stars except during flares (Güdel, 2004). A published optical spectrum reveals radial velocity variations of $\sim 40 \text{ km s}^{-1}$ (Solano et al., 1997), characteristic of a close binary star system, and the 2MASS colours of UY Scl reveal it to have a late (possibly K-giant) spectral type. Therefore, a plausible interpretation of the X-ray and optical properties of the variable star UY Scl is that it is a previously-unidentified RS CVn system.

4.5 X-ray colours

X-ray colour classification has recently been used by Prestwich et al. (2003) and Kilgard et al. (2005) to provide a statistical distinction between populations of XRBs and SNRs observed in nearby galaxies. This scheme, which was originally applied to *Chandra* observations, is useful when the X-ray data are too limited for detailed spectral diagnostics to be considered on a source by source basis. This work uses an adaptation of this X-ray colour classification scheme tuned to *XMM-Newton* data (Jenkins et al., 2005)⁴.

The basic approach is to divide the HR1 versus HR2 colour space into sub-regions so as to distinguish different classes of X-ray source, albeit within the limits set by the overlapping spread of spectral form

⁴An alternative classification scheme developed specifically for *XMM-Newton* data is described in Pietsch et al. (2004).

which characterises the various populations. The measurement uncertainties on the X-ray colours (HR1 and HR2) also serve to blur the population boundaries. The sources detected within the D_{25} ellipse of NGC 55 are divided into four broad source categories: ‘absorbed’, ‘XRB’, ‘SNR’ and ‘background’ using the same criteria as employed by Jenkins et al. (2005) in their study of M101⁵. Details of these X-ray colour classifications (in terms of HR1–HR2 colour space) are given in Table 4.8⁶.

These categories are also plotted as ellipses on the HR1–HR2 diagram shown in Fig. 4.6 (*top*). The XRB range encompasses sources with spectral shapes equivalent to $\Gamma \sim 1\text{--}2.5$, which is typical of LMXBs and HMXBs (Prestwich et al. 2003 and references therein). The SNR range covers soft sources ($\Gamma \gtrsim 2$) with low absorption, typical of the soft thermal spectra exhibited by known SNRs. The absorbed range applies to sources with $N_H \gtrsim 5 \times 10^{21} \text{ cm}^{-2}$ and the background range cover sources with highly absorbed X-ray spectra. However, sources located in this ‘background source’ category would possess significant hard and soft counts but few medium band counts. A possible explanation for such sources is that they are highly absorbed AGN (hard emission) with a starburst component (soft counts from thermal emission), and hence do not represent typical background source colours.

A further sub-division of the soft X-ray source population has been included using the criterion, $\text{HR1} < -0.8$, to classify objects as ‘very soft’ sources (VSSs)⁷. This class could contain a menagerie of exotic sources, including true supersoft sources (SSSs). SSSs emit X-rays predominantly below 0.5 keV (Greiner, 2000). Most are believed to be accreting white dwarfs undergoing nuclear burning on their surface (van den Heuvel et al. 1992; Rappaport et al. 1994). Other possibilities for very soft emitters include some SNRs, accreting neutron stars with large photospheres, IMBHs, symbiotic systems, the hot cores of young planetary nebulae and stripped cores of tidally disrupted stars (*e.g.*, Di Stefano & Kong 2004). The VSS classification used here will also contain those sources classed as ‘quasi-soft’ by Di Stefano & Kong (2004), which could include slightly hotter and/or absorbed variants on the above source types. However, while the chosen energy bands provide good signal to noise coverage for the data in general, extra soft energy sub-bands are required for more confident identifications of true SSSs.

⁵Table 3 of Jenkins et al. (2005) also refers to indeterminate soft/hard source categories, however these are not included here as no sources in NGC 55 fall into this range.

⁶These broad source categories are defined by Jenkins et al. (2005).

⁷This definition is similar, although not identical, to the definition of VSSs used by Di Stefano & Kong (2003). For example, they base their work on *Chandra* ACIS-S data, use slightly different bands and have additional selection criteria.

Table 4.8: X-ray colour classifications for *XMM* EPIC observations in the 0.3–6 keV range.

Classification	EPIC (PN & MOS)	PN only	MOS only
SNR	$\text{HR1} < -0.24, \text{HR2} < -0.10$	$\text{HR1} < -0.34, \text{HR2} < -0.14$	$\text{HR1} < -0.15, \text{HR2} < -0.07$
XRB	$-0.24 < \text{HR1} < 0.57, -0.8 < \text{HR2} < 0.8$	$-0.34 < \text{HR1} < 0.52, -0.8 < \text{HR2} < 0.8$	$-0.15 < \text{HR1} < 0.62, -0.8 < \text{HR2} < 0.8$
Background source	$\text{HR1} < -0.24, \text{HR2} > -0.10$	$\text{HR1} < -0.34, \text{HR2} > -0.14$	$\text{HR1} < -0.15, \text{HR2} > -0.07$
Absorbed source	$\text{HR1} > 0.57$	$\text{HR1} > 0.52$	$\text{HR1} > 0.62$

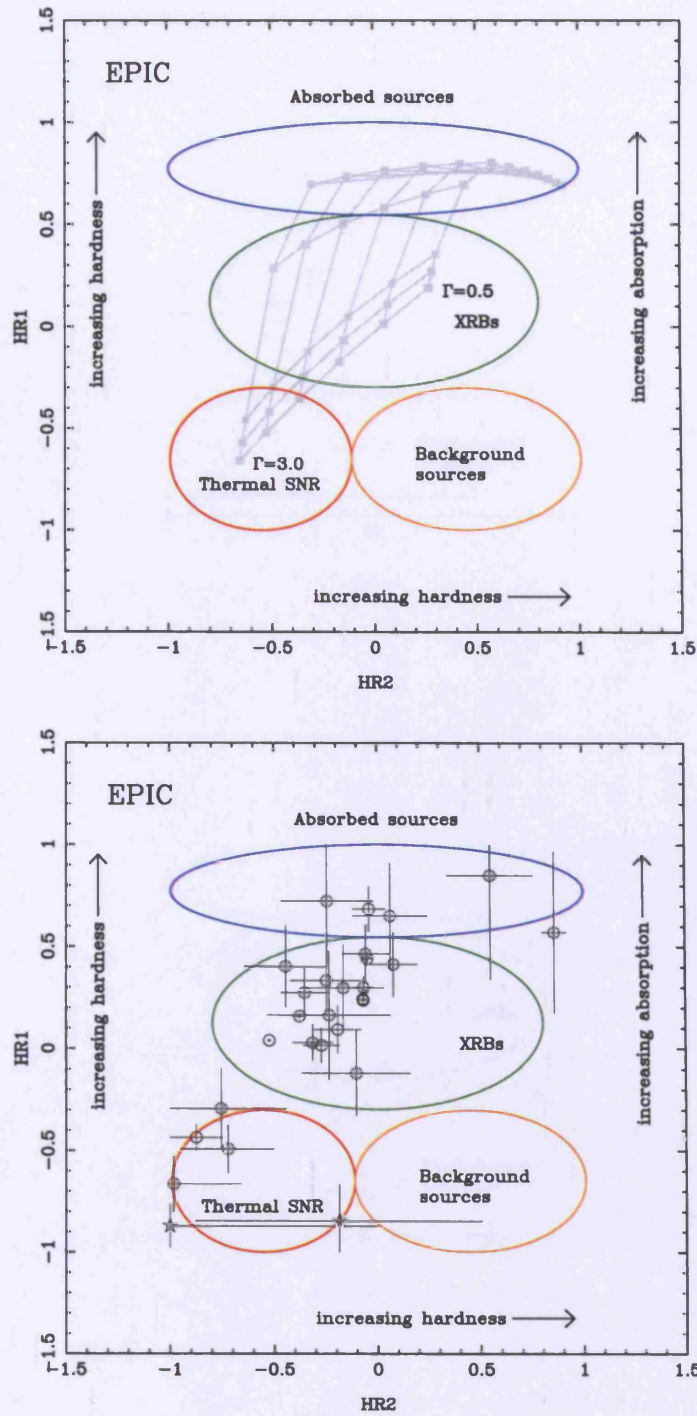


Figure 4.6: *Top:* the X-ray colour source classification scheme of Prestwich et al. (2003) and Kilgard et al. (2005), adapted for *XMM-Newton* data by Jenkins et al. (2005). The ellipses mark the appropriate colour ranges for each source category. The model grid shows a range of absorbed power-law continua, with Γ increasing from 0.5–3.0. The effect of absorption on these spectral shapes is shown by the vertically-rising lines (N_H increasing from 1×10^{20} to $5 \times 10^{22} \text{ cm}^{-2}$). *Bottom:* classification of the NGC 55 D₂₅ sources detected by both MOS and pn. The VSSs are shown with star symbols.

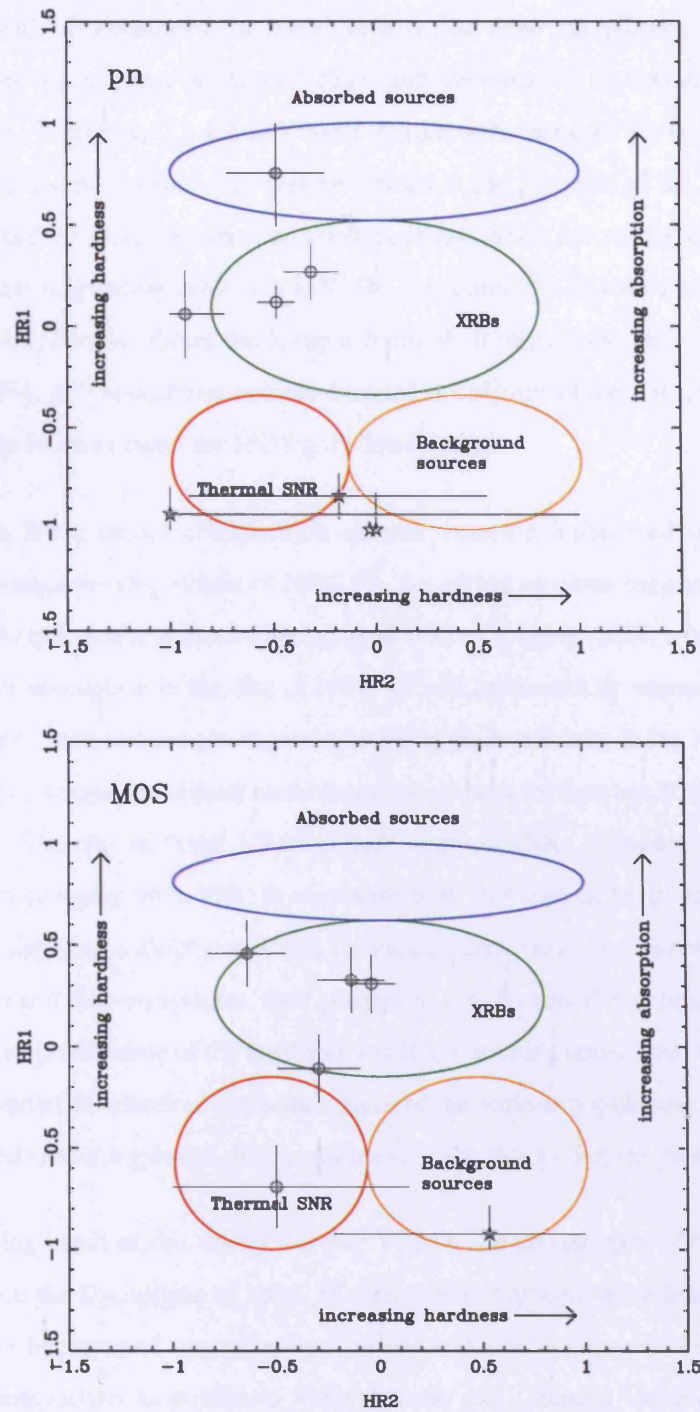


Figure 4.7: *Top:* NGC 55 D₂₅ source classification for sources only detected by the pn camera. *Bottom:* similarly, for sources only detected by the MOS cameras. In both figures, the VSSs are shown with star symbols as before.

This has been explicitly demonstrated for *XMM-Newton* data from the galaxies M33 (Pietsch et al., 2004) and M31 (Pietsch, Freyberg & Haberl, 2005) and the emission of optical novae within them (Pietsch et al., 2005). Therefore, 0.3–0.5 keV band images were extracted for each of the two *XMM-Newton* datasets, and aperture photometry was performed at the positions of the VSSs. On the basis of this, sources 53 and 63 were identified as good candidate SSSs due to the vast majority of their detected source counts originating below 0.5 keV. The remaining 5 VSSs were all dominated by 0.5–1 keV counts. Fig. 4.6 (*bottom*) shows the X-ray colours of all sources detected in *both* the MOS and pn detectors, while Fig. 4.7 shows those sources detected in only one of the instruments ((*top* panel for pn only detections and *bottom* panel for MOS only detections).

On the basis of this X-ray colour classification scheme there are 6 absorbed sources, 24 XRBs, 5 SNRs and 7 VSSs within the D_{25} ellipse of NGC 55. An earlier estimate suggested that 10–15 of the sources within D_{25} ellipse might in fact be background sources (largely AGN) seen through the disc of the galaxy. Since the absorption in the disc of NGC 55 will preferentially suppress the soft emission of background objects, such sources are expected to reside predominantly in the XRB (and ‘absorbed’ source) colour range. Background objects could therefore account for between 30%–50% of the sources in the XRB category. The ratio of ‘hard’ XRBs to ‘soft’ sources (SNRs, VSSs and background sources) observed in NGC 55 (roughly 60%:40%) is very similar to that seen in M101 (Jenkins et al., 2005), after (in both cases) applying a rough correction for background source contamination. Since these are respectively edge-on and face-on systems, then perhaps to zeroth order the inclination of a galaxy does not impact the relative prominence of the hard and soft X-ray source populations. Of course in practice, factors such as the radial distribution and scale height of the various populations and the depth of the absorption associated with the galactic disc, combine to make this a complex problem.

Perhaps one surprising result of this analysis is that VSSs make up one sixth of the total source population detected within the D_{25} ellipse of NGC 55, and could constitute more than one in four sources after the exclusion of background contamination. Whether this is an unusually large fraction has been investigated via a comparison to published *XMM-Newton* and *Chandra* studies that detect VSSs in other nearby galaxies. Firstly, only $\sim 12\%$ of the D_{25} sources of M101 in an *XMM-Newton* observation are classified as VSSs using the criterion presented here (*c.f.* Jenkins et al. 2005). As a wider comparison, the VSS population of M101 was looked at in a much deeper *Chandra* (ACIS-S) observation, as well as those of M83 (face-on spiral), M51 (interacting galaxy) and NGC 4697 (elliptical) (Di Stefano & Kong, 2004). The *XMM-Newton* HR1 VSS criterion was converted to the equivalent

Chandra ACIS-S value (via WEBPIMMS), using the appropriate energy bands, to facilitate comparison. Solely on the basis of this criterion, the fraction of VSSs were 31% for M101, 25% for M83, 15% for M51 and 4% for NGC 4697. At first glance, it therefore appears that there are quite large variations in the VSS population fractions of different galaxies. However, this fraction could be extremely susceptible to observational effects such as the effective (foreground and intrinsic) extinction and the luminosity threshold of the observations. For example, as typical SSSs in particular have luminosities below $\sim 10^{37} \text{ erg s}^{-1}$, this latter effect should result in more SSSs being observed in deeper, more sensitive observations, as may be the case when comparing the deep *Chandra* observation of M101 with the shallower *XMM-Newton* data. The Galactic foreground absorption is certainly a very important factor on the number of VSSs detected—this is small in M101, M83 and NGC 55 but is significantly higher in M51 and NGC 4697. An additional influence on the number of VSSs detected is the choice of filter used in the observations. The *XMM-Newton* observations of M101 were made using the medium filter while the NGC 55 observations utilised the thin filter. Therefore although the differences between galaxies appear large, selection effects may dominate.

4.6 Residual disc emission

The individual *XMM-Newton* observations were flat-fielded by subtracting a constant particle rate from the image (estimated by taking an average of the count rates in the edge regions of the detector not exposed to the sky) and then dividing by the appropriate exposure map. In the same process, bad pixels, a hot column (for the pn detector) and spurious data along chip gaps were excised. The flat-fielded data from the two observations were then mosaiced into a single exposure-corrected image. This next section focuses on the pn soft-band data.

Fig. 4.8 shows the mosaiced pn soft-band image of the central region of the galaxy. In order to highlight unresolved or possible diffuse emission (which is referred to hereafter as the residual disc emission), regions around the catalogued discrete sources listed in Table 4.1 were blanked out. For this purpose, circular exclusion regions were used of radius $20''$, $40''$, $1'$ or $2'$ depending on the strength of the source⁸. An exception was made for sources 48, 52 and 58, which have X-ray colours characteristic of SNRs and are here considered as part of the diffuse component of the galaxy.

⁸These sizes were determined empirically based on the need to suppress high levels of contamination from point sources, consistent with the size and shape of the PSF over the wide range of offset angles sampled.

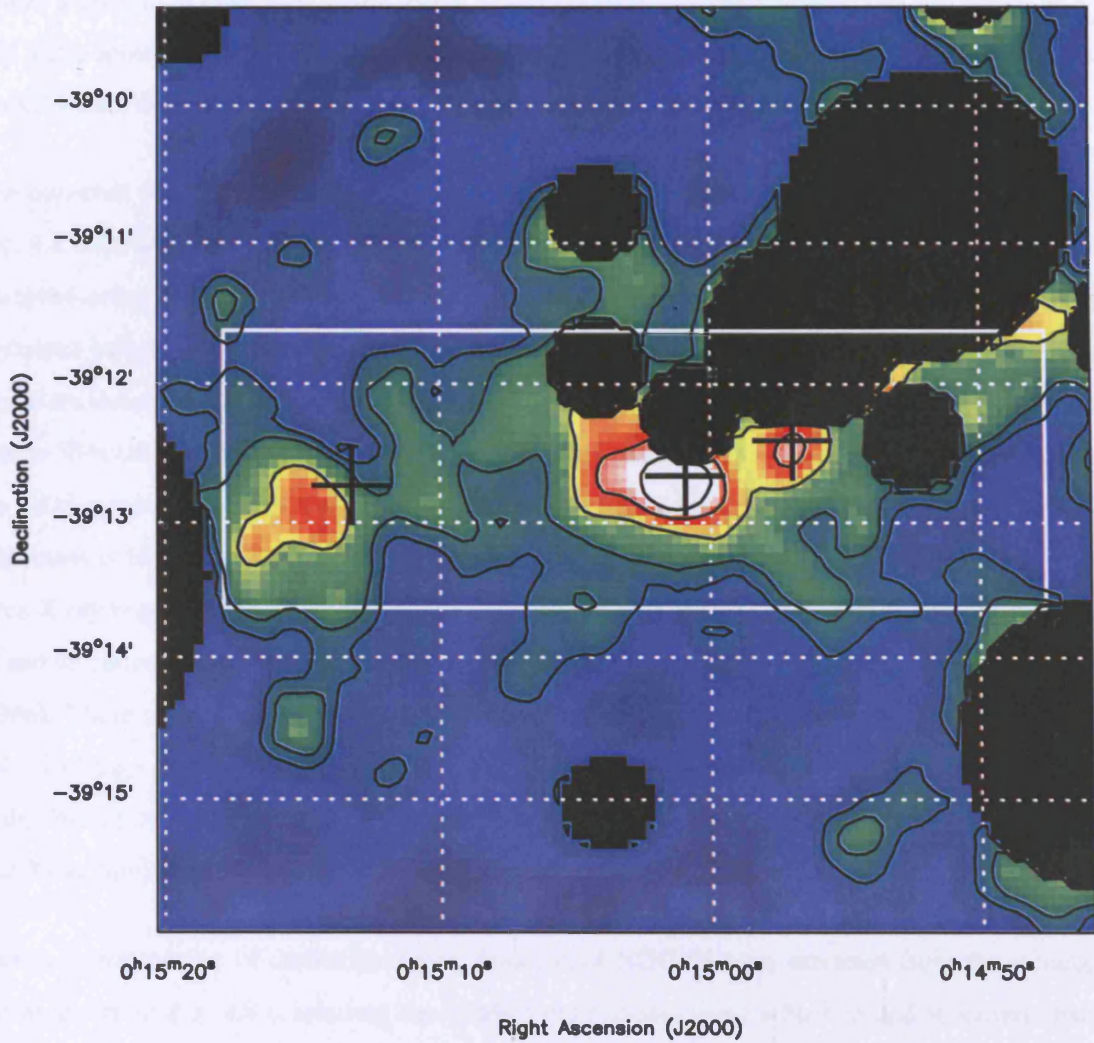


Figure 4.8: Close up of the composite flat-fielded pn image in the soft (0.3–1.0 keV) bandpass. Regions around catalogued sources have been blanked out so as to reduce the contamination of the diffuse signal by relatively bright resolved point sources. An exception was made for three sources in the region (sources 48, 52 and 58) whose positions are indicated by crosses, which have HR1 values characteristic of SNRs (see text). The large rectangle, excluding the blanked out sections, corresponds to the region used to estimate the diffuse luminosity of the disc of NGC 55 and from which the diffuse spectrum was extracted.

The residual emission is concentrated in the central disc of NGC 55 encompassing both the bar region and the region to the immediate east of the bar. The presence of several relatively bright X-ray sources makes it difficult to delineate the full extent of this component along the disc, although on the basis of Fig. 4.2 it appears to be $\lesssim 12'$. The residual emission is most evident within $\pm 1'$ of the plane, which is well within the extent of the thin disc component (Davidge, 2005).

The *observed* (0.3–1 keV) luminosity of the disc within the $6' \times 2'$ rectangular region illustrated in Fig. 4.8 (excluding the blanked out regions) is estimated to be $\sim 2.5 \times 10^{37} \text{ erg s}^{-1}$ (based on the observed count rate in this band, and energy conversion factors derived from the spectral analysis discussed below). Several regions of enhanced surface brightness are evident within this region, two of which are clearly related to sources 48 and 52. The easternmost bright region appears to be offset from source 58 but it is worth mentioning that this source was detected at relatively low significance only in the MOS soft band channel. Judging from the pn soft band image, the position of peak X-ray surface brightness is located approximately 1^s (of time) east of the catalogued position of source 58⁹. The three X-ray bright regions identified above, all coincide with radio sources and, in fact, X-ray sources 52 and 48 correspond to the core and eastern component of the triple source identified by Hummel et al. (1986). These regions are also prominent in H_α (Ferguson et al., 1996) and in the *Spitzer* far-infrared ($24 \mu\text{m}$) image of NGC 55 (Engelbracht et al., 2004) and correspond to sites of current star formation in the disc of the galaxy. Together the three bright regions contribute $\sim 30\%$ of the inferred residual disc X-ray luminosity.

Spectra representative of the residual disc emission of NGC 55 were extracted from the rectangular region shown in Fig. 4.8 (excluding the blanked out regions) using a background spectrum obtained from a nearby region of the same dimension (from which catalogued sources were also excluded). The diffuse spectra were grouped to give a minimum of 30 counts per bin. The six available spectral datasets (pn, MOS-1 and MOS-2 data from two observations) were fitted simultaneously, but with the relative normalisations untied so as to allow for calibration differences between the cameras. The spectral analysis was confined to the 0.3–6 keV energy range for which there was a reasonable signal to noise ratio.

⁹The fact that this region was not detected as a discrete source in the pn data may reflect a limitation in the background modelling in the vicinity of the brightest X-ray source in NGC 55.

Initially, the X-ray spectra were modelled with an absorbed `mekal` component, with the abundance free to vary. This yielded $N_H \sim 2 \times 10^{21} \text{ cm}^{-2}$ and $kT \sim 0.5 \text{ keV}$, with a very low inferred abundance of $Z \sim 0.04 Z_\odot$ ($\chi^2/\text{dof}=307/217$). An improved fit to the data was achieved with the inclusion of an additional harder spectral component, either in the form of a power-law or higher temperature `mekal` emission. The best-fit parameters for these two-component models are given in Table 4.9 and the observed pn spectra and the best-fitting `mekal+pwo` model is shown in Fig 4.9.

The derived flux using the `mekal+pwo` model is $\sim 1.6 \times 10^{-13} \text{ erg cm}^{-2} \text{ s}^{-1}$ (0.3–6 keV), corresponding to an absorbed luminosity of $6 \times 10^{37} \text{ erg s}^{-1}$. Roughly half of this luminosity is contributed by the soft thermal emission. The measured column density of $5.1 \times 10^{21} \text{ cm}^{-2}$ is much greater than the foreground column in our own Galaxy, and is consistent with the location of this residual component within the central disc region of NGC 55. Correcting for this absorption increases the inferred luminosity of the soft component to $\sim 3 \times 10^{38} \text{ erg s}^{-1}$. A reasonable hypothesis is that the soft emission represents a truly diffuse component energised by processes linked to regions of recent star formation (collision of stellar winds in dense environments, supernovae and shock heating in SNRs), whereas the harder spectral component (most appropriately modelled as a power-law) arises largely in unresolved XRBs.

The derived temperature of the soft residual disc emission in NGC 55 is $\sim 0.2 \text{ keV}$ (Table 4.9). This is fairly typical of the softest emission seen in more luminous star-forming galaxies where the temperature range for diffuse disc components may extend up to $\sim 2 \text{ keV}$ (e.g., Pietsch et al. 2001, Fabbiano et al. 2003). By analogy to these systems, it is very likely that the hot diffuse gas in NGC 55 is, in fact, a multi-temperature medium. The very low abundance derived for this hot gas component (Table 4.9) is almost certainly an artefact of fitting a complex spectrum with a very simplified model.

On the one hand the above determination of the luminosity of the residual disc component in NGC 55 represents only a lower limit estimate given that the true extent of the disc component has not been measured and, even within the inner $6' \times 2'$ region (corresponding to $3 \text{ kpc} \times 1 \text{ kpc}$ at the distance of NGC 55) regions around bright sources have been excluded out of necessity. On the other hand the *observed* X-ray flux of the residual disc emission is only $\sim 3\%$ of that of the resolved sources in the broad 0.3–6 keV band or a 6% fraction if only the soft band is considered. Since the PSF of the *XMM-Newton* optics has wings extending well beyond the blanked-out regions in Fig. 4.8, some contamination of the residual disc component by the nearby bright sources is inevitable.

Table 4.9: Spectral modelling results for the residual disc emission

Model	N_H^a	kT_1^b	kT_2^b	$Z (Z_\odot)^c$	Γ	χ^2/dof	$f_X(\text{obs})^d$	$L_X(\text{obs})^e$	$L_X(\text{int})^f$
mekal	$2.0^{+0.4}_{-0.6}$	$0.52^{+0.09}_{-0.05}$	–	0.04 ± 0.02	–	307/217	0.9	0.4	0.8
mekal+po	$5.1^{+1.8}_{-2.0}$	$0.21^{+0.01}_{-0.03}$	–	$0.07^{+0.07}_{-0.03}$	$1.9^{+0.4}_{-0.3}$	230.1/215	1.6	0.6	3.9
mekal+mekal	$5.3^{+0.9}_{-2.0}$	$0.20^{+0.06}_{-0.04}$	$4.52^{+9.19}_{-2.12}$	$0.06^{+0.10}_{-0.03}$	–	231/215	1.4	0.6	4.5

NOTES: ^a Column density (including Galactic, $\times 10^{21} \text{ cm}^{-2}$); ^b Temperatures of the cool (kT_1) and hot (kT_2) thermal components (keV); ^c Relative metal abundance of the thermal plasma component; ^d Observed 0.3–6 keV X-ray flux ($\times 10^{-13} \text{ erg cm}^{-2} \text{ s}^{-1}$); ^{e(f)} Observed (intrinsic) 0.3–6 keV X-ray luminosity respectively ($\times 10^{38} \text{ erg s}^{-1}$).

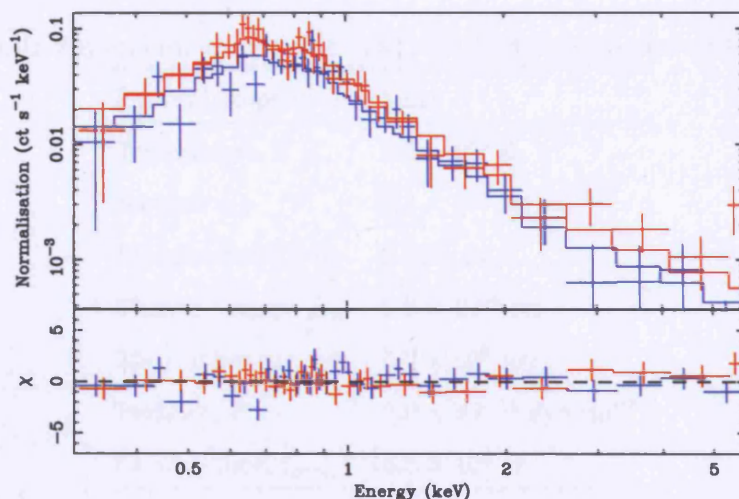


Figure 4.9: EPIC pn count rate spectra for the residual disc emission in NGC 55 from the first (blue) and second (red) observations. The best-fit `mekal` plus power-law model is shown along with the corresponding $\Delta\chi$ residuals (lower panel). N.B. The data have been rebinned for illustrative purposes using `SETPLOT REBIN` in `XSPEC`.

However, since the morphology of the extended emission (in Fig. 4.8) does not closely track the distribution of the bright sources, the residual signal (net of the local background) is unlikely to be dominated by such contamination, at least in the soft band. Unfortunately the surface brightness of the residual emission is too low to apply a similar imaging test above 1 keV.

The physical properties of the soft residual disc component have been derived from the `mekal+po` model, as summarised in Table 4.10 (this table includes a description of the parameters of the diffuse emission introduced below). Similar values have been obtained by Summers et al. (2003) for the cool diffuse disc component seen in the Magellanic irregular galaxy NGC 4449. These authors note that the diffuse medium is likely to be clumpy with a filling factor $f < 1$, implying that the quoted values for n_e and P are underestimates, whereas M , E_{th} and t_{cool} are overestimated. The derived pressure of the hot gas in NGC 55 ($P/k \sim 1.5 \times 10^5 \text{ K cm}^{-3}$) is similar to the pressure inferred for the interior of the Loop 1 superbubble within our own Galaxy (Willingale et al., 2003). This is broadly consistent with the view that there has been sufficient recent star formation in the disc of this low-mass dwarf system to form expanding hot bubbles, which result in the ejection of material out of the disc of the galaxy into the halo. However, the absence of an extended extra-planar soft X-ray component in NGC 55 (contrary to the findings of Oshima et al. 2002) suggests that the gas in such bubbles cools relatively quickly

Table 4.10: Physical parameters of the soft residual disc component (0.3–6 keV).

Physical property	Value
Temperature, T	2.4×10^6 K
Intrinsic L_X	3.3×10^{38} erg s $^{-1}$
Electron density, n_e	0.029 cm $^{-3}$
Thermal energy, E_{th}	6.8×10^{54} erg
Mass of hot gas, M	$5.7 \times 10^6 M_\odot$
Pressure, P	2.0×10^{-11} dyn cm $^{-3}$
Cooling time, t_{cool}	6.5×10^8 yr

ASSUMPTIONS: $V = 2 \times 10^{65}$ cm 3 (cylindrical volume subtending $6' \times 2'$ on the sky); $D = 1.78$ Mpc; filling factor, $f = 1$; $n_e = (EI/Vf)^{1/2}$, where EI is the emission integral ($norm \times 4\pi D^2$)/ 10^{-14} , and $norm$ is the mekal normalisation obtained from the spectral fitting; $E_{th} = 3n_e kTV$; $M = n_e m_P V f$; $P = 2n_e kT$ and $t_{cool} \sim (3kT)/(\Lambda n_e)$, where $\Lambda = L_X/EI$.

through adiabatic losses (given the relatively long radiative cooling timescale in Table 4.10), retaining insufficient energy to power a superwind of the form frequently seen in systems with star-formation rates, $SFR > 1M_\odot \text{ yr}^{-1}$ (Strickland, 2004).

4.7 Discussion

4.7.1 The brightest sources in NGC 55

What is the nature of the luminous X-ray source population observed in NGC 55? This question is most easily addressed for the brightest subset of X-ray sources, wherein the information provided by X-ray diagnostics is at its richest. The brightest X-ray source in NGC 55 (XMMU J001528.8-391318, source 71) has an X-ray luminosity $L_X \sim 10^{39}$ erg s $^{-1}$ placing it on the boundary of the ULX classification. As discussed in Chapter 3 this source is a candidate luminous BHB. § 4.4 reported the

details of four out of the five next brightest X-ray sources in the NGC 55 field. One of these sources (39) is spatially coincident with a bright variable foreground star at the edge of the D_{25} ellipse, and its X-ray properties suggest that it may be a previously unidentified RS CVn system. Of the other three sources, two are located in the bar region and one in the western limb of the NGC 55 disc. A combination of their high luminosities ($L_X > 10^{38} \text{ erg s}^{-1}$), measured absorption columns far in excess of the Galactic foreground, and power-law continuum or accretion disc dominated X-ray spectral shapes (see § 4.4.2), argues that these sources are likely to be XRBs in NGC 55, though a clearer detection of short-term variability is required to confirm this. Indeed, since the apparent high intrinsic X-ray luminosities of these sources are close to or in excess of the Eddington limit for a $1.4 M_\odot$ neutron star, the primary accreting object in these systems may be a black-hole. This hypothesis is supported by the X-ray spectroscopy. It is expected that a bright neutron star XRB spectrum would be described by a combination of a $\sim 1.5 \text{ keV}$ accretion disc and a $\sim 2 \text{ keV}$ blackbody spectral component with the latter originating in the neutron star envelope (*c.f.* Jenkins et al. 2004). Instead these X-ray spectra appear to be more typical of ‘low’ (hard power-law dominated) and ‘high’ (thermal accretion disc dominated) black-hole spectral states (*c.f.* McClintock & Remillard 2006). The long-term ($\sim 9 \text{ yr}$) persistence of these sources, and their locations close to the star-forming regions in the disc of NGC 55, suggest that these may be systems containing a high-mass secondary star. However, neutron star LMXBs at $L_X \sim 10^{38} \text{ erg s}^{-1}$ are also persistent so this cannot be confirmed without further information.

One interesting result from the spectral analysis of sources 43 and 47 is the detection of a very soft component in each spectrum (a similar component is seen in source 20, but does not provide a statistically robust improvement to the fit). The temperature of this component in source 47, when modelled by a `diskbb`, is $\sim 0.1 \text{ keV}$. This is remarkably similar to the $\sim 0.1 - 0.3 \text{ keV}$ temperatures derived for the very soft components seen in some nearby ULXs which, it has been argued, may be evidence for the presence of a $\sim 1000 M_\odot$ IMBHs (*e.g.*, Miller et al. 2003). So should the soft spectra of this source (which is one to two orders of magnitude less luminous than ULXs) be interpreted in the same way? If ULXs are accreting IMBHs, then a range of accretion rates and hence luminosities perhaps should be seen across the population, as is commonly the case for Galactic BHBs. However, on this basis the spectrum is perhaps expected to change to a low state as the luminosity decreases, whereas the spectra for the NGC 55 sources appear very similar to the apparent high state spectrum of IMBH candidates (though in these cases, as in some ULXs, the power-law slope is anomalously hard for a true high state; see Roberts et al. 2005). The overall spectral shape ($\Gamma \sim 2$ power-law, $kT_{in} \sim 0.1 \text{ keV}$

`diskbb`) might actually also describe the low state for an ordinary BHB, which (at a luminosity of $\sim 1 - 2 \times 10^{38} \text{ erg s}^{-1}$) must be a plausible alternative for this source.

The shape of the spectrum of source 43 potentially mirrors another result to emerge from recent ULX studies, an X-ray spectrum described by a hot $0.7 - 2 \text{ keV}$ `diskbb` with a very soft power-law dominant at low energies. The physical implausibility of this spectral description is discussed by various authors, who note alternative empirical solutions (*e.g.*, replacing the power-law with a black-body emission spectrum) or physical models (*e.g.*, optically-thick Comptonisation) that can explain the spectrum (see Feng & Kaaret 2005; Chapter 6).

However, a more mundane alternative for the nature of the soft emission in both sources is suggested by the fact that they are also well-fitted by a `mekal` component. The derived `mekal` temperature ($\sim 0.2 - 0.3 \text{ keV}$) in each case is similar to the temperature of the residual emission detected in the galaxy. Also, the surface brightness required to produce the observed signal within the source extraction regions is within a factor of ~ 2 of the average surface brightness seen elsewhere in the NGC 55 disc (see § 4.6). It seems quite likely, therefore, that this very soft component is simply the underlying emission of the disc of NGC 55 contaminating the source signal¹⁰.

4.7.2 NGC 55 - a typical Magellanic-type galaxy

Although the near edge-on orientation has complicated efforts to study the morphology of NGC 55, the current consensus is that this galaxy is a dwarf irregular, structurally similiar to the Large Magellanic Cloud (LMC; see Davidge 2005). In order to address the question of whether NGC 55, from an X-ray perspective, is a typical Magellanic-type galaxy, its overall X-ray properties need to be considered. An earlier estimate was that there might be up to ~ 16 XRBs associated with NGC 55 in the sample of sources detected within its D_{25} ellipse, down to an effective luminosity threshold of $2 \times 10^{36} \text{ erg s}^{-1}$ ($0.3 - 6 \text{ keV}$). In addition, 7 VSSs were identified in the D_{25} sample. The integrated X-ray luminosity of these source categories together with the luminosity inferred for the residual disc emission (including SNRs) is summarised in Table 4.11¹¹.

¹⁰N.B. similar results are emerging in other *XMM-Newton* datasets, *e.g.*, the soft excesses of ULXs in M51 are readily explained as local diffuse emission (Dewangan et al., 2005).

¹¹Note that the discrete source luminosities are from Table 4.1 and are, in effect, observed luminosities, *i.e.*, uncorrected for absorption intrinsic to NGC 55.

Table 4.11: The components of the integrated X-ray luminosity of NGC 55.

Component	L_X (0.3–6 keV)
Brightest (ULX) source	$9.4 \times 10^{38} \text{ erg s}^{-1}$
Next 20 brightest sources	$6.9 \times 10^{38} \text{ erg s}^{-1}$
VSSs	$0.1 \times 10^{38} \text{ erg s}^{-1}$
Residual soft disc ^a	$3.3 \times 10^{38} \text{ erg s}^{-1}$
Residual hard disc ^a	$0.5 \times 10^{38} \text{ erg s}^{-1}$

^a Corresponding to the $6' \times 2'$ inner disc region and corrected for absorption intrinsic to NGC 55.

Other nearby examples of actively star-forming Magellanic-type systems include NGC 4449 and the LMC, both of which have been extensively studied in X-rays (*e.g.*, Wang et al. 1991; Vogler & Pietsch 1997; Bomans et al. 1997; Sasaki et al. 2002; Summers et al. 2003). Table 4.12 compares various properties of these two galaxies with those of NGC 55 and illustrates the striking similarities of these systems.

Total mass, mass in neutral hydrogen, SFR and the X-ray luminosity in discrete sources and diffuse components (more precisely the residual disc in the case of NGC 55) differ by no more than a factor of 3 across the three galaxies. All three systems would appear to follow the paradigm of strong spatial association of the bright X-ray emitters with the sites of current star-formation, with a scaling of X-ray luminosity to SFR broadly consistent with the L_X versus SFR correlation established for much more active systems (Ranalli et al. 2003; Gilfanov et al. 2004).

Table 4.12: A comparison of the properties of NGC 55 with two other Magellanic-type dwarf galaxies.

Property	LMC	NGC 55	NGC 4449
Assumed Distant (Mpc) ^a	0.05	1.78	2.93
L_X (sources) ^b (10^{38} erg s ⁻¹)	5	17	15
L_X (diffuse) ^b (10^{38} erg s ⁻¹)	3	4	10
M_{25} ^c ($10^9 M_\odot$)	3.3	8.5	4.2
M_{HI} ^d ($10^9 M_\odot$)	0.6	2.0	1.6
SFR ^e (M_\odot yr ⁻¹)	0.25	0.22	0.2

NOTES: ^aDistances from Panagia (1999); Karachentsev et al. (2003); Karachentsev & Drozdovsky (1998) respectively. ^bX-ray luminosities from Wang et al. (1991); this chapter; Summers et al. (2003) respectively. ^c ‘Indicative’ mass of the galaxy within its D_{25} diameter from Karachentsev et al. (2004). ^d HI mass of the galaxy from Karachentsev et al. (2004). ^e Star formation rates from Grimm et al. (2003); Engelbracht et al. (2004); Thronson et al. (1987) respectively. Quoted values are scaled to the assumed distant.

4.8 Summary

Recent *XMM-Newton* EPIC observations have been used to investigate the X-ray properties of the Magellanic type galaxy NGC 55. A total of 137 X-ray sources were detected in the NGC 55 field of which 42 were located within the optical confines of the galaxy as defined by the D_{25} ellipse. The source detections cover a flux range of $\sim 5 \times 10^{-15} - 2 \times 10^{-12}$ erg cm⁻² s⁻¹ (0.3–6 keV) corresponding to a luminosity range of $\sim 3 \times 10^{35} - 9 \times 10^{38}$ erg s⁻¹ for sources at the distance of NGC 55. After allowing for some contamination of the sample by background AGN, the best estimate, based largely on X-ray colour classification, is that within the D_{25} region, there are ~ 4 absorbed sources, 16 XRBs, 5 SNRs and 7 VSSs associated with NGC 55. Also, an X-ray source just outside the D_{25} ellipse was revealed to be coincident with a globular cluster in NGC 55.

Detailed X-ray spectral and timing analysis on four bright X-ray sources (> 500 counts) in the FOV were performed (excluding the brightest source which was studied in Chapter 3). One of these objects is identified with a Galactic foreground star (UY Scl) and exhibits many of the properties of an RS

CVn system. The other three are persistent X-ray sources with spectra indicative of accreting XRBs. A residual emission component is also evident in the disc of NGC 55, concentrated on the bar region. The extent of this emission is at least $6'$ (3 kpc) along the plane of the galaxy and $\pm 1'$ (± 500 pc) perpendicular to the plane. This soft component is interpreted as thermal diffuse emission with $kT \sim 0.2$ keV associated with regions of current star formation in the disc of NGC 55. After correcting for absorption, the X-ray luminosity of this soft emission is $\sim 3 \times 10^{38}$ erg s $^{-1}$ (0.3–6 keV).

NGC 55 is categorised as a Magellanic-type dwarf galaxy. From a comparison of its properties with those of other nearby Magellanic systems, specifically the LMC and NGC 4449, then from a high energy perspective, NGC 55 is quite typical of its class.

Chapter 5

The X-ray properties of the spiral galaxy NGC 4945

5.1 Introduction

NGC 4945 is a nearby (3.7 Mpc; Mauersberger et al. 1996) edge-on ($i \sim 78^\circ$; Ott et al. 2001) spiral galaxy, believed to be a member of the Centaurus group (Hesser et al., 1984). The galaxy has been classified as a SB(s)cd or SAB(s)cd (de Vaucouleurs 1964; Braatz et al. 1997) and has an optical extent of $20' \times 4'$ (3rd Revised Catalogue of Galaxies; de Vaucouleurs et al. 1991). NGC 4945 exhibits intense nuclear infra-red emission, concentrated in a $12'' \times 9''$ region (Brock et al., 1988) and is the third brightest extragalactic source in the *IRAS* point source catalogue (Fullmer & Lonsdale, 1989). The nucleus also shows a rich variety of molecular emission lines (*e.g.*, Henkel et al. 1994) including the first known H₂O megamaser emission (Dos Santos & Lepine, 1979). Optical observations showed extended line emitting gas outflowing along the galaxy minor axis which was thought to be driven by a central starburst (Heckman et al., 1990). Further optical and IR observations revealed a conical wind-blown cavity close to the nucleus, providing direct evidence for the starburst driven superwind (Moorwood et al., 1996). However, it had also been suggested that the infra-red emission could be powered by a non-stellar source, such as a Seyfert 2 or a compact low ionisation nuclear emission line region (LINER) nucleus (*e.g.*, Brock et al. 1988).

Evidence of a Seyfert 2 active nucleus was finally revealed through the first X-ray observations of the galaxy, which were made with the Japanese X-ray astronomy satellite, *Ginga* (Iwasawa et al., 1993). These observations showed a highly obscured, strongly variable hard X-ray source thus establishing the composite nature (starburst plus Seyfert) of the nucleus of this galaxy.

Seyfert 2 galaxies are generally heavily absorbed in soft X-rays, which is thought to be a consequence of a thick molecular torus obscuring the nucleus. Indeed, in this case the AGN X-ray emission is completely absorbed below ~ 10 keV due to the large absorbing column of $\sim \text{few} \times 10^{24} \text{ cm}^{-2}$ (Iwasawa et al. 1993; Done et al. 1996; Madejski et al. 2000). However, the OSSE instrument on board the *Compton Gamma Ray Observatory* revealed that NGC 4945 is actually one of the brightest Seyfert 2 galaxies in the sky at 100 keV (Done et al., 1996). The nuclear power-law dominates the spectrum above 10 keV and the hard X-ray emission has been shown to be rapidly variable on timescales of < 1 day. In addition to this hard power-law emission, previous X-ray observations have also shown softer emission (2–10 keV) which can also be fitted with a simple power-law ($\Gamma \sim 1.7$), interpreted as scattering of the primary nuclear continuum (Iwasawa et al., 1993). This interpretation is also applicable to non-simultaneous *Ginga*, *ASCA* and *OSSE* spectra (Done et al., 1996). A third component of the X-ray emission was also detected in the form of an Fe K_{α} line at ~ 6.5 keV with an equivalent width of ~ 1.5 keV (*e.g.*, Iwasawa et al. 1993).

BeppoSax observations confirmed the previous indications of variability from the *Ginga* observations and provided an improved high energy X-ray spectrum of the galaxy (Guainazzi et al., 2000). The X-ray emission above 10 keV was again shown to be dominated by a nuclear non-thermal continuum, seen through an absorber of $\sim \text{few} \times 10^{24} \text{ cm}^{-2}$ (Guainazzi et al., 2000). These observations also suggest that the active nucleus dominates the bolometric energy output of NGC 4945 and estimate that the inferred intrinsic luminosity of the galaxy is $\sim 1.8 \times 10^{43} \text{ erg s}^{-1}$ (0.1–200 keV). The 0.1–5 keV emission was shown to be extended along the plane of the galaxy, most likely due to a population of unresolved binaries. However, Guainazzi et al. (2000) also suggested that part of the soft (> 1 keV) extended X-ray emission may originate in a superwind component, although the low spatial resolution of the X-ray data up to this point could not confirm this.

Detailed X-ray spectroscopy of the core of NGC 4945 with *Chandra* and *XMM-Newton* also revealed a complex nuclear morphology including a hard nuclear source and a soft X-ray plume extending to the North-West of the nucleus (Schurch et al., 2002). These observations detected considerable emission

from the galaxy disc including at least 12 discrete X-ray sources. A more detailed spatially resolved analysis of the nuclear region was performed by Done et al. (2003) using simultaneous *Chandra* and *RXTE* data. The excellent spatial resolution of *Chandra* enabled the nucleus, starburst and superwind regions to be separated, while the *RXTE* data extended the spectrum to higher energies. The authors also found that the nucleus was only directly seen above $\sim 8\text{--}10$ keV, while the lower energy nuclear spectrum was dominated by reflection. However, the superwind regions were dominated by hot plasma emission, while the starburst region contained both hot plasma and reflection signatures.

An important feature of NGC 4945 is that it is a H_2O megamaser source, which traces underlying cool, dense molecular structures around the central engine. Mapping of this emission implies an edge-on inner disc geometry and provides an estimate of the central black hole mass of $\sim 1.4 \times 10^6 M_\odot$ (Greenhill et al., 1997). This black-hole mass in combination with estimates of the AGN luminosity, implies that the central engine radiates at $\sim 10\%$ of the Eddington limit. This is one of the few AGNs for which the luminosity in Eddington units can be reliably estimated.

Although the nuclear region of NGC 4945 has been well studied and X-ray observations have detected diffuse emission along the plane of the galaxy and several discrete sources (*e.g.*, Guainazzi et al. 2000), there has not been a detailed analysis of this diffuse emission or the off-nuclear point source population. However, individual sources have been studied in more detail, *e.g.*, *ROSAT* observations revealed a highly variable off-nuclear X-ray source, which increased in flux by almost an order of magnitude on a timescale of 11 months or less (Brandt et al., 1996). The maximum observed luminosity (0.8–2.5 keV) of this source was measured to be $\gtrsim 8 \times 10^{38} \text{ erg s}^{-1}$. An additional 2 sources in the galaxy have been previously analysed and classified as ULXs (Colbert et al. 2004, Swartz et al. 2004, Feng & Kaaret 2005).

This chapter presents an analysis of recent *XMM-Newton* observations of NGC 4945, studying both the properties of the bright discrete X-ray source population and the underlying diffuse emission. § 5.2 describes the observations and preliminary data reduction techniques. § 5.3 presents the source catalogue and discusses the number of X-ray sources associated with the galaxy. Spectral and temporal analyses of the bright sources are presented in § 5.4, and § 5.5 presents the results of applying the X-ray colour classification scheme of the previous chapter to the NGC 4945 data. The morphology and spectral properties of the detected diffuse X-ray emission is presented in § 5.6. A brief discussion of this work is presented in § 5.7 and finally the results are summarised in § 5.8.

5.2 Observations and data analysis

The analysis presented in this work is based on a 66 ks observation of NGC 4945 with *XMM-Newton* on January 11, 2004 (Obs. ID 0204870101) during revolution 749 (see Table 5.1). The EPIC MOS and pn (Turner et al. 2001; Strüder et al. 2001) instruments were operated in the full frame mode using the medium filter. The EPIC data were extracted from the observation data files (ODF) using the `emchain` and `epchain` tasks within the XMM-SAS software v.6.0.0. The `emchain` and `epchain` tasks process the data from the MOS and pn instruments respectively, producing calibrated photon event files.

The observation was affected by soft proton flaring such that preliminary cleaning of the full field X-ray (0.3–10 keV) light curves was necessary (see § 2.3.2 & § 2.3.3). Flares were screened using GTI files based on countrate criteria. Also, only those data recorded when all EPIC instruments were in operation were selected, resulting in a net good exposure time of 41.4ks.

For the analysis of the bright sources, events were extracted in a circle centred on the source position given in Table 5.2. The background was taken from a circular region near to the source in the pn camera at the same readout node distance, and as far as possible, free of diffuse emission from the galaxy. The chosen background regions were the same in all three detectors.

A source catalogue for this observation was produced using the source detection procedure outlined in § 2.3.4. As before, this was performed on the combined MOS (*i.e.*, MOS-1 plus MOS-2) and pn data in three energy bands: 0.3–1keV (soft), 1–2 keV (medium) and 2–6 keV (hard), and the results are described in the following sections.

Table 5.1: The *XMM-Newton* observation of NGC 4945

Obs ID	RA (J2000)	Dec (J2000)	Date	UT _{start}
0204870101	13 05 26.10	-49 28 15.0	2004-01-10	18:11:10

5.3 X-ray Sources in the Field of NGC 4945

5.3.1 Source catalogue

There are 69 X-ray sources detected within the field of view encompassed by the *XMM-Newton* observations, 24 of which are located within the D_{25} ellipse of the galaxy¹. Fig. 5.1 shows the combined (*i.e.*, merged MOS and pn) broad band (0.3–6 keV) X-ray image (*top panel*) and the optical DSS-2 blue image of the galaxy (*bottom panel*). The positions of the 69 sources which pass the significance test are marked with circles on both of the images.

The full X-ray source catalogue appears in Table 5.2 and provides the following information:

(1) the source identification number. Sources located within the optical D_{25} ellipse are marked with an asterisk. (2)–(3) The source RA and DEC positions (J2000). (4) The 1σ uncertainty in the source position including a $1.5''$ systematic error added in quadrature. (5)–(7) The measured count rate (corrected for the vignetting) in the pn camera in the S, M & H bands. (8)–(10) The measured count rate (corrected for the vignetting) in the MOS cameras in the S, M & H bands. Values are quoted for one MOS camera. (11)–(12) Two hardness ratios calculated as $HR1 = (M - S)/(M + S)$ and $HR2 = (H - M)/(H + M)$. The weighted mean hardness ratios are quoted for sources detected in both instruments. (13) The measured flux in the 0.3–6 keV energy range. The count rate in each detection band was converted to an X-ray flux using Energy Conversion Factors (ECFs) calculated for each instrument from a power-law continuum spectrum with $\Gamma = 1.7$ absorbed by the Galactic foreground column towards NGC 4945 ($N_H = 1.6 \times 10^{21} \text{ cm}^{-2}$; Stark et al. 1992). Again, for sources detected in both instruments, these are the weighted mean flux values for the particular band. The fluxes derived from the individual bands were subsequently added to provide the quoted instrumental flux (0.3–6 keV). (14) The derived X-ray luminosities for sources within the D_{25} ellipse, assuming a distance of 3.7 Mpc.

¹ Actually there are 23 sources within the ellipse but source 13 is a bright X-ray source located just on the ellipse boundary and has also been included (see later).

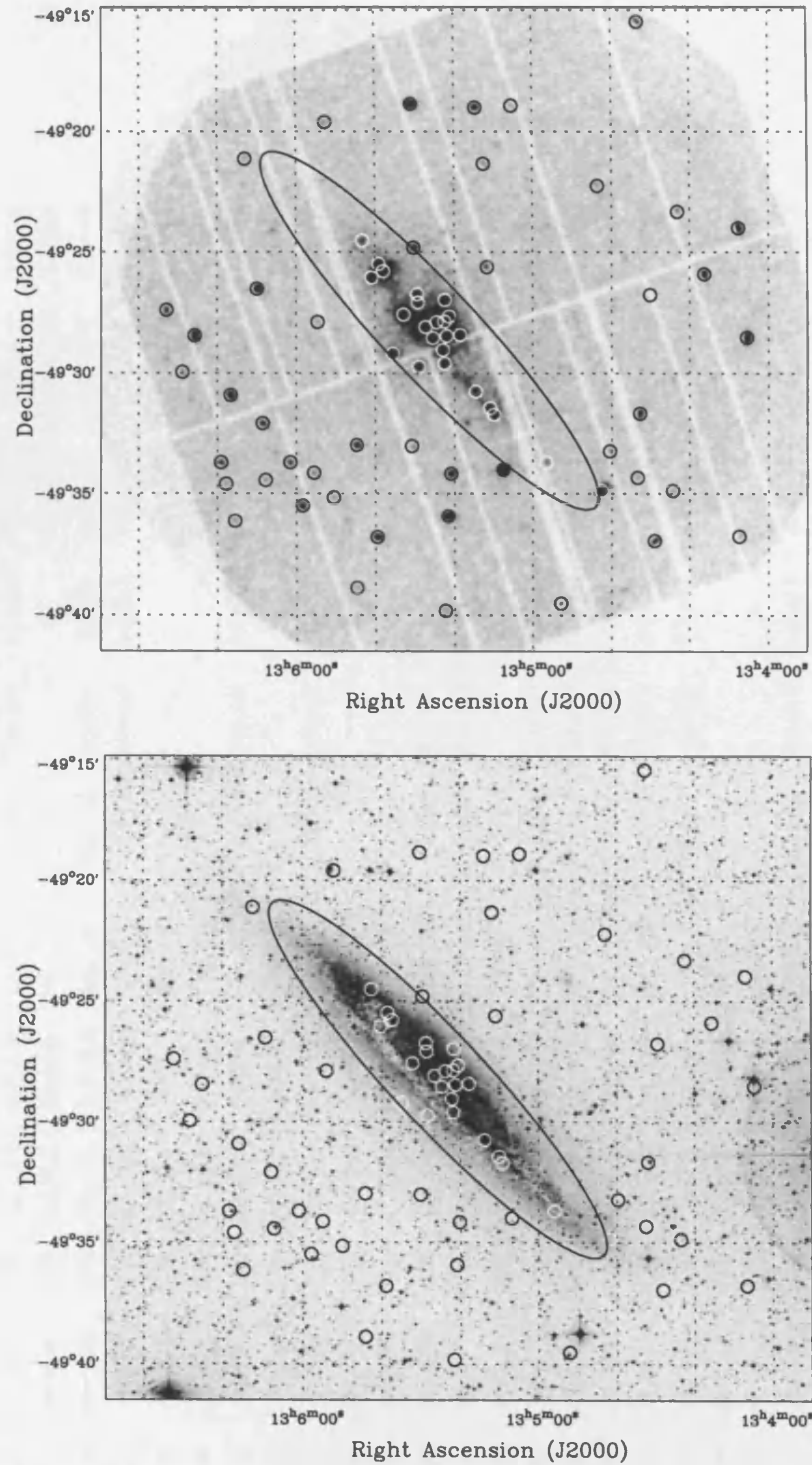


Figure 5.1: *Top panel:* the *XMM-Newton* image of the NGC 4945 field in a broad (0.3–6 keV) band-pass. The image has been lightly smoothed using a 1σ ($4''$) Gaussian mask. *Bottom panel:* the optical DSS-2 (blue) image of the NGC 4945 field. Detected sources are identified with circles and the optical D_{25} ellipse of NGC 4945 is also shown. North is up and East is to the left.

Table 5.2: The full catalogue of sources detected in the *XMM-Newton* observations

SRC	RA	DEC	$r_1 \sigma$	pn cts ks ⁻¹			MOS cts ks ⁻¹			HR1	HR2	f_X	L_X
ID	(hh:mm:ss)	(° : ' : ")	(")	S	M	H	S	M	H			($\times 10^{-14}$)	($\times 10^{36}$)
(1)	(2)	(3)	(4)	(5)	(6)	(7)	(8)	(9)	(10)	(11)	(12)	(13)	(14)
1	13:04:05.78	-49:28:30.0	1.59	32.1±1.9	6.7±0.9	1.5±0.8	7.9±0.7	2.6±0.4	0.5±0.3	-0.61±0.04	-0.65±0.11	9.0±0.6	
2	13:04:07.54	-49:36:45.4	1.88	6.1±1.1	5.4±1.0	3.6±1.1	–	–	–	-0.06±0.13	-0.20±0.17	6.1±1.1	
3	13:04:08.04	-49:23:58.2	1.60	9.0±1.1	10.0±1.2	8.8±1.2	1.0±0.3	3.9±0.5	3.5±0.5	0.28±0.06	-0.05±0.07	12.3±0.9	
4	13:04:16.63	-49:25:53.4	1.63	2.8±0.6	7.0±0.8	6.7±0.9	0.5±0.2	3.2±0.4	2.4±0.4	0.58±0.07	-0.07±0.07	8.5±0.7	
5	13:04:23.50	-49:23:18.6	2.09	0.9±0.5	2.1±0.5	3.8±0.8	–	–	–	0.41±0.25	0.30±0.15	4.3±0.8	
6	13:04:24.48	-49:34:51.2	2.31	3.1±0.7	1.5±0.5	1.2±0.7	–	–	–	-0.35±0.19	-0.10±0.35	2.1±0.7	
7	13:04:29.04	-49:36:56.6	1.60	6.2±1.0	7.7±1.0	5.1±1.0	1.8±0.4	4.0±0.6	0.9±0.4	0.22±0.08	-0.39±0.09	7.2±0.7	
8	13:04:30.41	-49:26:45.6	2.10	3.2±0.6	0.0±0.2	0.0±0.4	–	–	–	-1.00±0.14	0.00±0.00	0.6±0.4	
9	13:04:32.88	-49:31:39.7	1.61	13.1±0.9	2.0±0.4	0.0±0.2	2.3±0.3	0.8±0.2	0.2±0.2	-0.68±0.05	-0.84±0.15	3.0±0.2	
10	13:04:33.43	-49:34:18.8	2.23	1.4±0.5	1.6±0.5	1.9±0.6	–	–	–	0.08±0.22	0.08±0.21	2.5±0.6	
11	13:04:33.67	-49:15:27.7	1.64	11.4±1.3	10.7±1.3	7.5±1.3	–	–	–	-0.03±0.08	-0.17±0.10	12.1±1.3	
12	13:04:40.54	-49:33:13.3	1.86	1.0±0.4	2.3±0.5	0.7±0.5	0.4±0.1	0.8±0.2	0.4±0.1	0.36±0.13	-0.42±0.15	1.7±0.3	
13*	13:04:42.62	-49:34:51.6	1.52	3.2±0.6	29.7±1.4	32.2±1.6	0.8±0.2	10.8±0.6	12.6±0.7	0.84±0.02	0.06±0.03	38.6±1.1	632.3
14	13:04:43.78	-49:22:14.9	2.17	0.5±0.4	1.9±0.4	1.4±0.5	–	–	–	0.59±0.26	-0.14±0.21	1.9±0.5	
15	13:04:52.87	-49:39:33.1	1.71	0.7±0.5	3.4±0.7	3.3±0.8	0.0±0.1	1.7±0.3	1.3±0.3	0.91±0.09	-0.09±0.11	4.2±0.5	
16*	13:04:56.83	-49:33:42.5	1.88	0.4±0.3	1.7±0.4	1.6±0.5	0.1±0.1	0.8±0.2	0.9±0.2	0.72±0.15	0.01±0.12	2.4±0.3	38.8
17	13:05:05.47	-49:18:56.5	2.42	6.3±1.3	7.8±1.2	7.9±1.6	0.3±0.1	0.5±0.2	0.5±0.2	0.15±0.11	0.00±0.11	2.4±0.4	
18	13:05:07.58	-49:33:59.4	1.56	2.2±0.8	2.3±0.7	4.1±1.0	1.7±0.2	5.3±0.3	4.4±0.3	0.49±0.05	-0.07±0.05	10.7±0.6	
19*	13:05:10.01	-49:31:43.3	1.70	–	–	–	0.4±0.1	1.8±0.2	1.1±0.2	0.68±0.11	-0.26±0.09	4.2±0.4	68.6
20*	13:05:10.94	-49:31:27.5	1.76	4.2±0.5	3.6±0.5	0.0±0.3	–	–	–	-0.07±0.09	-1.00±0.17	1.8±0.3	29.3
21	13:05:11.64	-49:25:37.6	2.02	0.4±0.3	1.9±0.3	0.9±0.3	–	–	–	0.64±0.19	-0.35±0.17	1.5±0.3	
22	13:05:12.50	-49:21:20.5	1.94	1.7±0.4	0.8±0.3	0.2±0.3	0.4±0.1	0.6±0.1	0.4±0.1	-0.04±0.13	-0.31±0.18	1.1±0.2	
23	13:05:14.59	-49:19:01.2	1.59	11.1±0.9	2.9±0.5	1.1±0.3	1.8±0.2	1.0±0.2	0.2±0.1	-0.50±0.05	-0.56±0.11	3.1±0.3	
24*	13:05:14.59	-49:30:46.1	2.02	2.2±0.5	1.5±0.4	0.0±0.1	0.6±0.2	0.7±0.1	0.1±0.1	-0.07±0.12	-0.93±0.12	0.9±0.1	15.1
25*	13:05:18.55	-49:28:26.0	1.51	10.6±0.7	19.0±0.9	18.4±0.9	2.1±0.2	6.4±0.3	7.3±0.4	0.38±0.03	0.02±0.02	23.8±0.6	390.6
26	13:05:20.83	-49:34:09.8	1.59	1.8±0.4	4.0±0.5	3.9±0.5	0.5±0.1	1.5±0.2	1.5±0.2	0.45±0.07	-0.01±0.06	5.0±0.4	
27*	13:05:21.34	-49:27:40.0	1.52	6.1±0.6	11.4±0.7	9.1±0.7	1.1±0.2	4.3±0.3	4.0±0.3	0.43±0.04	-0.08±0.03	13.0±0.5	213.7

SRC	RA (hh:mm:ss)	DEC (° : ' : ")	$r_1\sigma$ (")	pn cts ks ⁻¹				MOS cts ks ⁻¹				HR1	HR2	f_X ($\times 10^{-14}$)	L_X ($\times 10^{36}$)
ID	(2)	(3)	(4)	S	M	H	(7)	S	M	H	(10)	(11)	(12)	(13)	(14)
(1)				(5)	(6)	(7)		(8)	(9)	(10)					
28	13:05:21.50	-49:35:56.0	1.54	0.1±0.2	3.2±0.5	19.9±1.1	0.1±0.1	1.3±0.2	7.3±0.4	0.93±0.07	0.71±0.03	18.9±0.7			
29*	13:05:21.96	-49:28:28.2	1.50	17.8±0.9	68.0±1.5	50.3±1.4	4.3±0.3	22.9±0.6	18.7±0.6	0.63±0.01	-0.13±0.01	66.8±1.0	1094.9		
30	13:05:22.27	-49:39:51.5	1.93	0.3±0.4	0.4±0.4	3.3±0.7	0.0±0.1	0.4±0.2	1.3±0.3	0.80±0.33	0.65±0.13	3.3±0.5			
31*	13:05:22.42	-49:26:58.9	1.57	1.9±0.4	4.5±0.5	3.7±0.5	0.7±0.2	1.5±0.2	1.6±0.2	0.37±0.08	-0.02±0.06	5.3±0.3	86.6		
32*	13:05:22.54	-49:27:52.6	1.56	3.3±0.6	12.1±0.8	8.5±0.4	0.5±0.2	3.7±0.3	3.5±0.1	0.67±0.05	-0.11±0.03	11.6±0.3	189.6		
33*	13:05:22.54	-49:29:36.6	1.57	1.1±0.4	4.0±0.5	4.7±0.5	0.3±0.1	1.4±0.2	1.7±0.2	0.63±0.08	0.09±0.06	5.5±0.3	89.7		
34*	13:05:22.92	-49:29:03.1	1.51	3.5±0.5	14.3±0.8	21.1±0.9	0.6±0.1	5.4±0.3	8.0±0.4	0.71±0.03	0.19±0.02	23.7±0.6	388.5		
35*	13:05:24.53	-49:27:54.7	1.58	5.5±1.0	5.4±0.4	2.9±0.8	-	-	-	-0.00±0.09	-0.30±0.12	5.3±0.7	86.1		
36*	13:05:25.44	-49:28:33.2	1.52	1.3±0.4	9.4±0.7	23.2±1.0	0.0±0.0	3.2±0.3	8.7±0.4	0.97±0.02	0.44±0.02	23.7±0.7	387.6		
37*	13:05:27.29	-49:28:06.2	1.51	4.1±0.6	25.7±1.0	73.0±1.6	1.0±0.2	10.3±0.4	25.9±0.7	0.78±0.02	0.46±0.01	72.5±1.1	1187.6		
38*	13:05:29.01	-49:29:45.2	1.61	1.6±0.4	2.8±0.4	2.2±0.4	0.2±0.1	1.1±0.2	1.3±0.2	0.50±0.09	0.01±0.07	3.5±0.3	57.1		
39*	13:05:29.26	-49:27:05.8	2.09	-	-	-	0.0±0.1	0.6±0.2	0.7±0.2	1.00±0.31	0.06±0.16	2.1±0.4	34.9		
40*	13:05:29.40	-49:26:44.9	1.92	1.3±0.4	2.2±0.4	0.6±0.3	-	-	-	0.25±0.15	-0.57±0.18	1.4±0.3	23.5		
41	13:05:30.19	-49:24:49.3	1.61	1.4±0.3	2.4±0.3	1.6±0.4	0.3±0.1	0.6±0.1	1.2±0.2	0.31±0.10	0.10±0.08	2.9±0.3			
42	13:05:30.77	-49:33:01.4	2.31	-	-	-	0.3±0.1	0.5±0.1	0.1±0.1	0.18±0.19	-0.80±0.24	0.7±0.2			
43	13:05:30.82	-49:18:52.2	1.54	7.4±0.7	12.4±0.8	10.6±0.9	1.6±0.2	4.7±0.4	4.9±0.4	0.36±0.04	-0.03±0.04	15.3±0.7			
44*	13:05:32.86	-49:27:35.3	1.51	7.7±0.6	36.8±1.2	39.9±1.2	2.0±0.2	13.6±0.5	14.8±0.5	0.70±0.02	0.04±0.02	47.6±0.9	780.6		
45*	13:05:35.54	-49:29:12.5	1.52	7.6±0.6	13.8±0.7	11.7±0.7	1.6±0.2	5.2±0.3	4.6±0.3	0.40±0.03	-0.07±0.03	16.0±0.5	262.3		
46*	13:05:37.94	-49:25:48.0	1.51	6.6±0.7	25.9±1.1	27.1±1.2	2.0±0.2	10.6±0.5	11.3±0.5	0.64±0.03	0.03±0.02	34.7±0.9	568.4		
47*	13:05:39.07	-49:25:29.6	1.59	2.5±0.3	5.5±0.6	5.1±0.7	0.5±0.1	1.7±0.1	2.0±0.3	0.43±0.05	0.03±0.06	6.6±0.5	107.6		
48	13:05:39.55	-49:36:48.6	1.59	3.5±0.5	5.0±0.6	3.8±0.6	0.8±0.2	1.9±0.2	1.5±0.2	0.27±0.07	-0.13±0.07	5.5±0.4			
49*	13:05:40.85	-49:26:03.5	1.57	-	-	-	0.1±0.1	2.1±0.2	4.9±0.3	0.94±0.07	0.40±0.05	12.9±0.7	211.8		
50*	13:05:43.15	-49:24:31.3	1.95	0.1±0.2	1.2±0.3	1.7±0.4	-	-	-	0.85±0.28	0.16±0.16	2.0±0.4	32.4		
51	13:05:44.71	-49:32:58.9	1.60	1.4±0.3	2.9±0.4	2.5±0.4	0.5±0.1	1.0±0.2	0.9±0.2	0.33±0.08	-0.07±0.08	3.4±0.3			
52	13:05:44.76	-49:38:54.6	2.47	0.3±0.3	0.0±0.2	2.5±0.6	-	-	-	-0.70±1.00	0.96±0.14	2.5±0.6			
53	13:05:50.64	-49:35:09.2	1.97	0.1±0.2	1.1±0.3	1.3±0.4	0.0±0.1	0.5±0.1	0.4±0.1	0.91±0.20	-0.03±0.15	1.3±0.2			
54	13:05:52.56	-49:19:37.2	2.00	1.3±0.4	1.1±0.4	2.5±0.5	0.3±0.1	0.4±0.1	0.3±0.1	0.02±0.17	0.24±0.14	1.8±0.3			

SRC	RA	DEC	$r_{1\sigma}$	pn cts ks ⁻¹			MOS cts ks ⁻¹			HR1	HR2	f_X	L_X
ID	(hh:mm:ss)	(° : ' : ")	(")	S	M	H	S	M	H			(×10 ⁻¹⁴)	(×10 ³⁶)
(1)	(2)	(3)	(4)	(5)	(6)	(7)	(8)	(9)	(10)	(11)	(12)	(13)	(14)
55	13:05:54.55	-49:27:53.6	2.30	1.8±0.3	0.3±0.2	0.0±0.1	–	–	–	-0.71±0.17	-1.00±0.36	0.4±0.1	
56	13:05:55.61	-49:34:07.7	2.28	0.5±0.3	1.3±0.3	0.7±0.4	–	–	–	0.41±0.25	-0.27±0.25	1.2±0.4	
57	13:05:58.49	-49:35:29.0	1.58	4.5±0.5	5.8±0.6	6.2±0.7	0.8±0.2	1.6±0.2	1.7±0.2	0.20±0.06	0.02±0.06	6.8±0.4	
58	13:06:01.59	-49:33:41.4	1.87	–	–	–	0.5±0.1	0.9±0.2	0.8±0.2	0.27±0.15	-0.03±0.14	2.9±0.4	
59	13:06:07.77	-49:34:25.7	2.33	2.3±0.5	0.6±0.3	0.0±0.1	–	–	–	-0.57±0.17	-1.00±0.33	0.6±0.1	
60	13:06:08.47	-49:32:04.6	1.62	2.3±0.4	2.4±0.4	1.4±0.4	0.8±0.1	0.7±0.1	0.6±0.2	-0.00±0.09	-0.18±0.11	2.5±0.3	
61	13:06:09.74	-49:26:30.8	1.55	10.5±0.8	6.2±0.6	3.6±0.5	1.5±0.2	2.4±0.2	1.5±0.2	-0.09±0.04	-0.25±0.06	6.7±0.4	
62	13:06:12.70	-49:21:07.6	2.27	2.1±0.5	1.0±0.3	0.0±0.3	–	–	–	-0.39±0.17	-1.00±0.59	0.6±0.1	
63	13:06:15.51	-49:36:07.9	2.80	0.8±0.4	1.5±0.4	0.6±0.5	–	–	–	0.30±0.27	-0.43±0.34	2.4±0.4	
64	13:06:16.46	-49:30:54.4	1.57	3.6±0.5	5.6±0.6	4.8±0.6	0.6±0.2	2.5±0.3	2.0±0.3	0.41±0.06	-0.10±0.06	6.8±0.4	
65	13:06:17.69	-49:34:34.7	2.42	–	–	–	0.2±0.1	0.4±0.1	0.7±0.2	0.31±0.28	0.25±0.21	2.1±0.5	
66	13:06:18.91	-49:33:41.4	1.63	5.7±0.6	1.7±0.4	0.1±0.2	1.1±0.2	1.0±0.2	0.4±0.1	-0.39±0.07	-0.54±0.14	1.9±0.2	
67	13:06:25.44	-49:28:26.0	1.55	18.1±1.0	4.4±0.6	1.2±0.4	3.9±0.3	1.4±0.2	0.2±0.1	-0.57±0.04	-0.66±0.10	4.9±0.3	
68	13:06:28.58	-49:29:56.8	1.84	0.1±0.2	0.0±0.1	4.0±0.6	0.0±0.1	0.1±0.1	1.2±0.2	0.57±1.57	0.96±0.06	3.2±0.4	
69	13:06:32.52	-49:27:22.7	1.67	1.7±0.5	4.3±0.6	1.9±0.5	0.9±0.2	1.1±0.2	1.0±0.2	0.29±0.09	-0.25±0.09	3.5±0.4	

NOTES: (1) source number (objects within the D₂₅ ellipse are marked by *); (2) RA in hh:mm:ss (J2000 coordinates); (3) DEC in ° : ' : " (J2000 coordinates); (4) 1 σ error radius including a 1.5'' systematic error added in quadrature; (5,6 & 7) and (8,9 & 10) source count rates in the soft (0.3–1 keV), medium (1–2 keV) & hard (2–6 keV) bands for the pn and MOS cameras respectively, with significant source detections (> 4 σ) highlighted in bold; (11 & 12) soft (HR1) and hard (HR2) hardness ratios (as defined in the text); (13) source X-ray flux (0.3–6 keV) in units of 10⁻¹⁴ erg cm⁻² s⁻¹; (14) source X-ray luminosity (0.3–6 keV) in units of 10³⁸ erg s⁻¹ (assuming a distance to NGC 4945 of 3.7 Mpc).

5.3.2 X-ray sources associated with NGC 4945

A breakdown of the total number of detected sources as a function of instrument and energy band is shown in Table 5.3. An estimate of the number of detected sources that may be background AGN was made using the Giacconi et al. (2001) hard band (2–10 keV) $\log N$ – $\log S$ relationship. Sources at the detection threshold (4σ) in the medium (1–2 keV) band of this work correspond to ~ 30 counts in pn and 22 counts in MOS, compared to the hard (2–6 keV) band values of ~ 38 counts for pn and 28 counts for MOS. These counts were folded through the corresponding exposure map in each case (to correct for sensitivity changes across the EPIC FOV), providing a minimum count rate for a detected source at each point across the image, specific to each detector and energy band. These were then converted into a 2–10 keV flux per pixel based on the spectrum for a typical faint AGN ($\Gamma=1.4$, $N_H=3\times 10^{20} \text{ cm}^{-2}$). This flux was then used with the $\log N$ – $\log S$ relationship mentioned above and normalised to the detector area to give an estimated contamination of background sources in each of the pn and MOS datasets, as shown in Table 5.4. These calculations predict a medium band contamination of ~ 38 background AGN in the pn data and ~ 37 in the MOS, and a hard band contamination of ~ 24 background AGN for both pn and MOS. Scaling this to the area on the detector occupied by NGC 4945 (based on the size of the D_{25} ellipse), predicts a contamination of ~ 3 background AGN in the medium band and ~ 2 background AGN in the hard band for each detector.

Table 5.3: The number of significant sources detected in each energy band in the pn and MOS images.

Camera	S	M	H	S/M/H
pn	16[42]	21[51]	17[40]	21[62]
MOS	10[29]	20[47]	19[38]	20[50]
pn/MOS	16[44]	24[59]	21[47]	24[69]

NOTES: The numbers quoted are for the D_{25} ellipse with the full-field values given in square brackets. The total number of individual sources detected in various instrument and energy band combinations is also indicated.

Table 5.4: Predicted number of background sources

Camera	M	H
pn	3[38]	2[24]
MOS	3[37]	2[24]

NOTES: The numbers quoted are for D_{25} ellipse (with the full-field values given in square brackets) in the medium and hard energy bands of the pn and MOS images, based on the $\log N$ – $\log S$ relationship of Giacconi et al. (2001). The D_{25} values were estimated by scaling the full-field numbers to the NGC 4945 area.

5.3.3 Cross correlation

Following the procedure described in Chapter 4, the *XMM-Newton* source list was cross-correlated with other sources in the NED and SIMBAD databases, using a 3σ error search radius (including a $1''$ systematic error) of each *XMM* source position. The results are summarised in Table 5.5. While there are 25 sources with other possible identifications, 21 of these lie within the confines of the D_{25} ellipse of NGC 4945 and all simply correspond to previously detected X-ray sources. The remaining 4 identified sources consist of a foreground star, a radio source, a *ROSAT* X-ray source and a background galaxy (sources 1, 4, 9 and 54 respectively). Importantly, source 37 corresponds to the hard nuclear source, while source 35 is consistent with the soft X-ray plume reported by Schurch et al. (2002), rather than a true discrete X-ray source.

Table 5.5: Previous identifications of the *XMM-Newton* sources.

<i>XMM</i> ID	<i>ROSAT</i> ID PSPC[P]/HRI[H]	<i>Chandra</i> ID	Other ID	Source type
1			CD-487895	Star
4			SUMSS J130416-492550	Radio source
9			1WGA J1304.5-4931	X-ray source
19*		[CHP2004] J130509.7-493143		X-ray source
20*	[GMB2000] 4 [P]	[CHP2004] J130511.0-493126		X-ray source
25*		[CHP2004] J130518.5-492824		X-ray source
27*		[CHP2004] J130521.2-492741		X-ray source
		[CHP2004] J130521.7-492737		X-ray source
29*		[CHP2004] J130521.9-492827		X-ray source
		[SGT2004] J130521.94-492826.6		X-ray source
31*		[CHP2004] J130522.4-492657		X-ray source
32*		[CHP2004] J130522.7-492753		X-ray source
		[CHP2004] J130523.2-492755		X-ray source
33*	NGC 4945: [R97] 05 [P]	[CHP2004] J130522.5-492935		X-ray source
34*	NGC 4945: [BIR96] X-1 [P+H]	[CHP2004] J130522.8-492901		X-ray source
		[CHP2004] J130523.3-492910		X-ray source
35*	[GMB2000] 1 [P]	[SRW2002] J130525.5-492754		X-ray source (plume)
36*		[CHP2004] J130525.4-492824		X-ray source
		[CHP2004] J130525.5-492832		X-ray source
37*		[SRW2002] J130527.5-492805	NGC 4945	Sy-2 nucleus
38*		[CHP2004] J130528.9-492945		X-ray source
39*		[CHP2004] J130529.0-492705		X-ray source
40*		[CHP2004] J130529.8-492643		X-ray source
44*	[GMB2000] 2 [P]	[SGT2004] J130532.89-492734.1		X-ray source
45*		[CHP2004] J130535.5-492912		X-ray source
46*	NGC 4945: [R97] 03 [P]	[CHP2004] J130538.1-492545		X-ray source
	[GMB2000] 3 [P]			X-ray source
47*		[CHP2004] J130539.0-492530		X-ray source
49*		[CHP2004] J130540.8-492604		X-ray source
50*		[CHP2004] J130543.4-492431		X-ray source
54			ESO 219- G 025	Galaxy

NOTES: *ROSAT* ID numbers correspond to PSPC [P] and HRI [H] detections; [GMB2000] Guainazzi et al. (2000); [BIR96] Brandt et al. (1996); [R97] Radecke (1997). *Chandra* ID numbers from [CHP2004] Colbert et al. (2004); [SGT2004] Swartz et al. (2004) and [SRW2002] Schurch et al. (2002). Other ID references: SUMSS - (Sydney University Molonglo Sky Survey) Mauch et al. (2003); CD - Hog et al. (1998); 1WGA - White et al. (2000); ESO - Lauberts (1982).

5.4 The brightest discrete X-ray sources

The bright variable source detected by Brandt et al. (1996) corresponds to source 34 of this work and on the basis of the *XMM-Newton* observation, is the 7th brightest source in this galaxy with an observed 0.3–6 keV luminosity of $\sim 4 \times 10^{38} \text{ erg s}^{-1}$. However, this source, as well as the 6th brightest source within the D_{25} ellipse (source 25), lies on a pn chip gap in this observation. Therefore temporal and spectral analyses have been restricted to the 4 brightest sources within the D_{25} ellipse (excluding the AGN). These sources are labelled 13, 29, 44, and 46 in Table 5.2, and have observed fluxes (0.3–6 keV) in excess of $10^{-13} \text{ erg cm}^{-2} \text{ s}^{-1}$ ($L_X \gtrsim 6 \times 10^{38} \text{ erg s}^{-1}$).

In the analysis, the extraction regions were chosen to minimise contamination by neighbouring point sources or underlying diffuse emission. However, only the data for source 13 could be extracted without strict limitations as this source is located near the edge of the D_{25} ellipse, away from the central region which hosts the strongest diffuse emission and other detected sources. Source 29 is located very near to the centre of the galaxy in a densely populated source region and as such is likely to suffer the most contamination. Source 44 lies further away from the centre of the galaxy and nearby sources but may still be contaminated by the underlying emission from the galaxy. Source 46 is located far enough from the centre of the galaxy such that the diffuse emission component will not be as significant but it lies very close to two other catalogued sources. Therefore smaller extraction regions have been employed than otherwise would have been, to limit the amount of contamination in each case.

5.4.1 Light curves

Background-subtracted light curves were extracted for each source based on the combined 0.3–6 keV data from the three EPIC cameras. In each case the background data were extracted from the nearest source-free regions to the source, visible in all three detectors. The size of the circular source and background extraction apertures are listed in Table 5.6. Before subtracting the background data from each source, an area scaling factor was applied to the background counts to account for the different extraction sizes. As previously mentioned, it was necessary to use quite small extraction regions for the three brightest sources (29, 44, 46), to avoid contamination from neighbouring point sources and the underlying galaxy emission. The light curves were binned to provide at least 20 counts per bin, ensuring Gaussian statistics are valid.

Table 5.6: Light curve and spectral extraction apertures

ID	Extraction radius	
	Source	Background
(1)	(2)	(3)
13	20	40
29	12	17.5
44	15	22.5
46	12	30

NOTES: (1) Source designation; (2)–(3) Aperture radii in " .

The resulting light curves with 500 s time binning for source 13 and 250 s time binning for sources 29, 44 and 46 are shown in Fig. 5.2. The short-term X-ray variability of each source was investigated using the methods described in Chapter 4, namely, a χ^2 test on the raw light curves with the aforementioned binning and K-S test on the pn light curves with 1 s time bins. However, no evidence of such variability was found for any source using either method.

5.4.2 X-ray Spectra

The SAS task `especget` was used to produce a source and background spectrum together with the necessary ARF and RMF files for four bright sources in NGC 4945. The X-ray spectra were extracted in the 0.3–10 keV band, using circular source and background extraction apertures as listed in Table 5.6. Although care has been taken to avoid contamination by the underlying diffuse emission and nearby sources, it is possible that some of this emission still remains. As previously mentioned, this is especially true for source 29 which lies in the central region where the diffuse emission is strongest.

For sources 13 and 46, the background regions were taken from regions relatively free of diffuse emission from the galaxy. However, as sources 29 and 44 are located closer to the centre of the galaxy in a region of intense diffuse emission, the background regions for these sources were taken from nearby regions containing some of this emission. Fig. 5.3 show the positions of the bright sources in the galaxy and the size of the extraction regions. As previously mentioned, the extraction regions are relatively small in most cases in an attempt to limit the contamination.

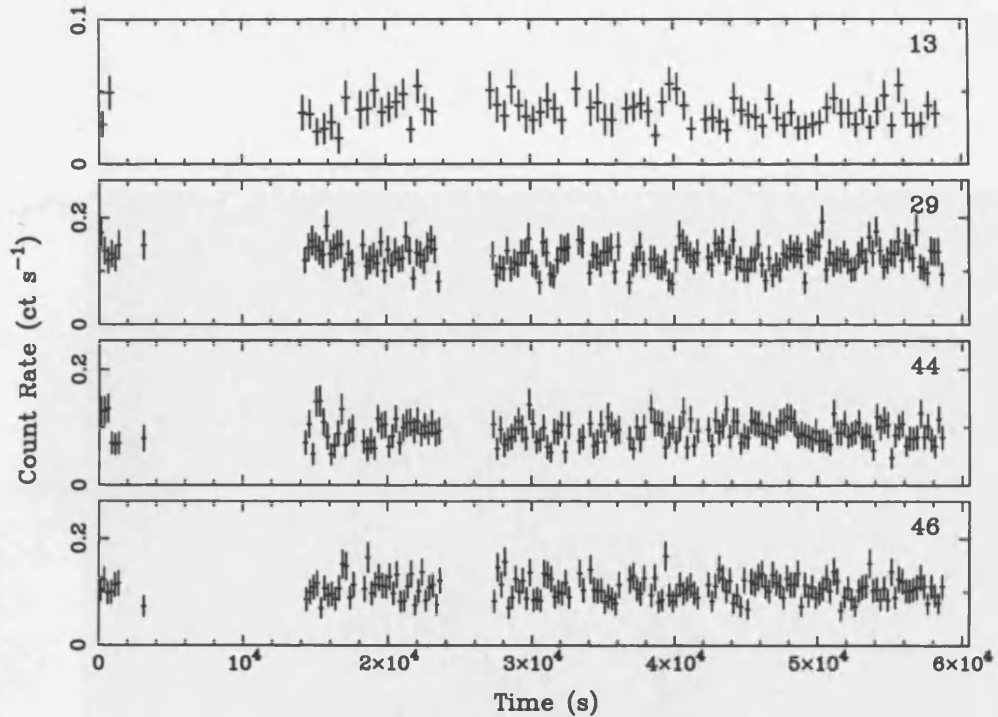


Figure 5.2: The background-subtracted 0.3–6 keV light curves of four bright sources, displayed in 500 s (13) and 250 s (29, 44, 46) time bins. The light curves are based on the combined data from the MOS-1, MOS-2 and pn cameras. The error bars correspond to $\pm 1\sigma$.

A close up of the central region of the galaxy in the soft, medium, hard and broad bands is shown in Fig. 5.4. This clearly shows that source 35 is dominant in the soft X-ray band, whereas the nuclear source emerges at harder X-ray energies.

The spectral analysis was performed using XSPEC (v.11.3.0) and spectral channels were grouped so as to give a minimum of 20 counts per bin. The pn, MOS-1 and MOS-2 spectra were fitted simultaneously, using constant multiplicative factors in each model to allow for calibration differences between the cameras. This value was frozen at unity for the pn data and allowed to vary for the MOS detectors, with the values typically agreeing within 15%.

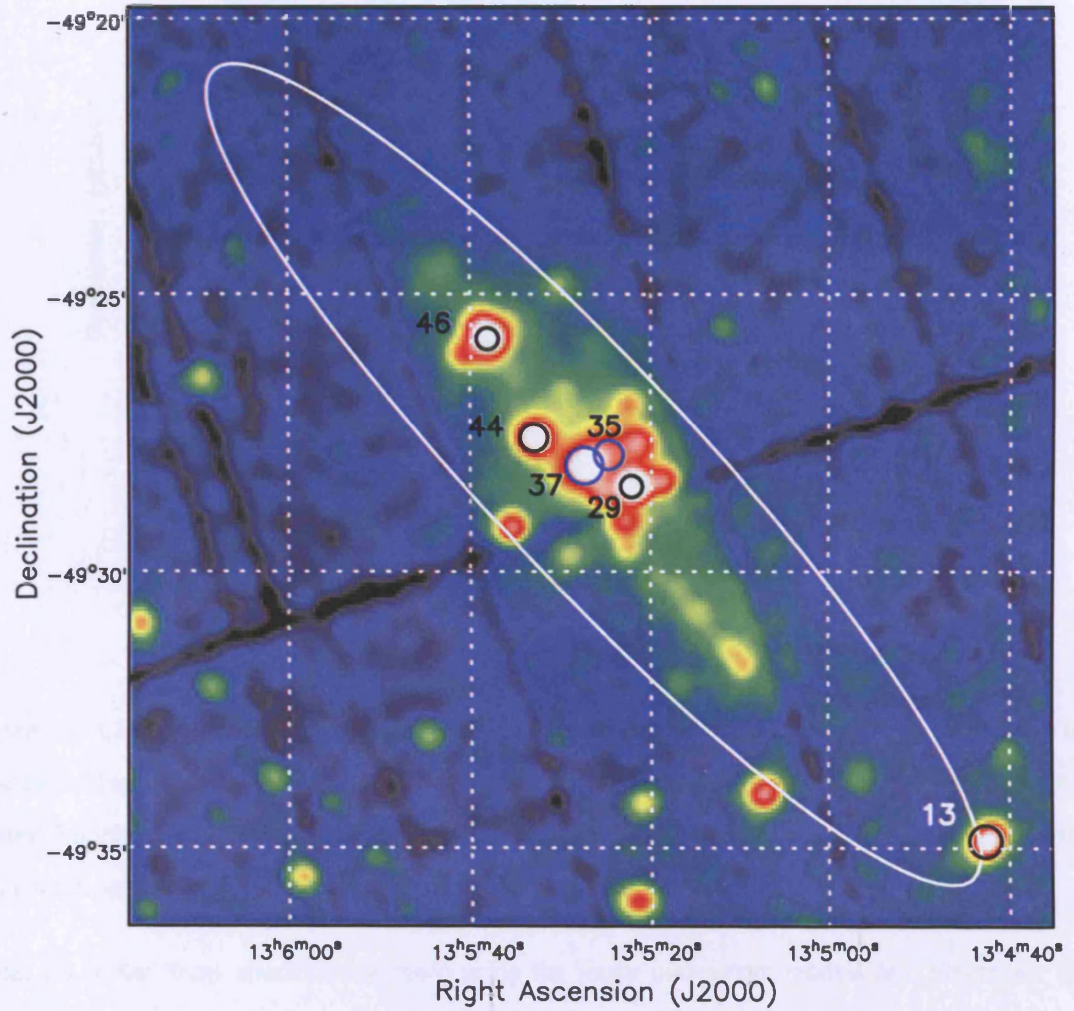


Figure 5.3: The *XMM-Newton* image of the NGC 4945 field in a broad (0.3–6 keV) bandpass. The ellipse marks the optical extent of the galaxy as measured by the D_{25} isophote. The four bright X-ray sources studied here are highlighted with black circles denoting the spectral extraction radius used. The blue circles highlight the position of the Seyfert 2 nucleus (37) and the position of the X-ray plume (35) as reported in Schurch et al. (2002).

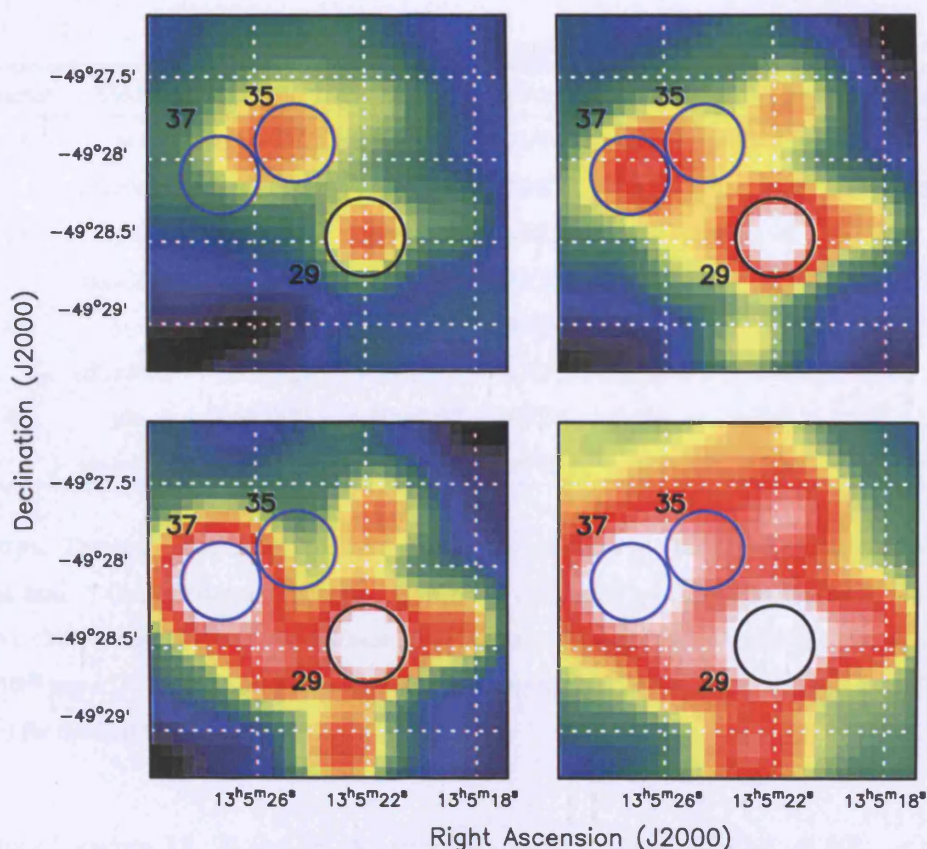


Figure 5.4: Close up of the central region of NGC 4945 in the soft (*top left*), medium (*top right*), hard (*bottom left*) and broad (*bottom right*) X-ray bands. Again, the blue circles highlight the position of the Seyfert 2 nucleus (37) and the position of the X-ray plume (35). As expected, the Sy-2 nucleus emerges at harder X-ray energies while source 35 is dominant in the softest band.

Initial fits to the X-ray spectra were made using the single component models of a power-law (`po`), blackbody (`bbbody`), multi-colour disc blackbody (`diskbb`) and solar-abundance optically-thin thermal plasma (`mekal`) spectral forms. Each model was modified for absorption using the `tbabs` model with abundances and absorption cross-sections tabulated by Wilms et al. (2000). Typically, the best fits were obtained with either the `po` or the `diskbb` models. These results are summarised in Table 5.7, which also lists the observed 0.3–10 keV fluxes and the observed and intrinsic (unabsorbed) luminosities for the best fitting model².

²These fluxes are an average of those measured in the three detectors

Table 5.7: Single component spectral fitting results

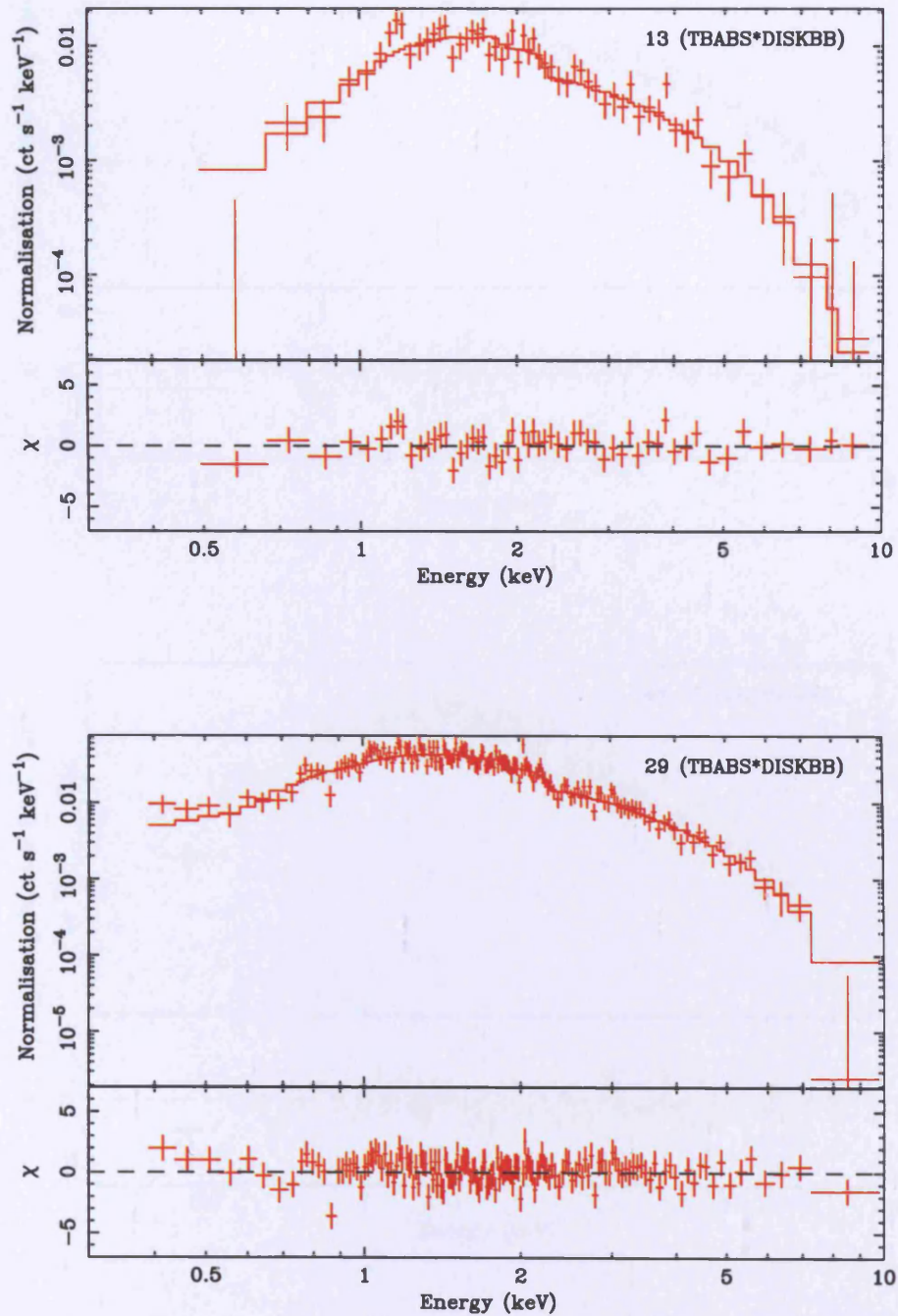
Source	Model	N_H^a	Γ/kT_{in}	χ^2/dof	$f_X(\text{obs})^b$	$L_X(\text{obs})^c$	$L_X(\text{int})^d$
13	po	$15.76^{+2.24}_{-1.89}$	$2.34^{+0.18}_{-0.17}$	94/93	–	–	–
	diskbb	$9.59^{+1.40}_{-1.23}$	$1.21^{+0.11}_{-0.10}$	78/93	2.55	4.18	6.23
29	po	$10.68^{+0.71}_{-0.66}$	2.64 ± 0.08	387/254	–	–	–
	diskbb	$5.01^{+0.40}_{-0.37}$	1.05 ± 0.04	222/254	4.02	6.58	9.23
44	po	$7.77^{+0.75}_{-0.62}$	$1.80^{+0.08}_{-0.07}$	206/204	4.00	6.56	10.22
	diskbb	$4.32^{+0.44}_{-0.41}$	$1.71^{+0.11}_{-0.10}$	222/204	–	–	–
46	po	$7.49^{+0.64}_{-0.59}$	1.87 ± 0.07	282/221	–	–	–
	diskbb	$3.99^{+0.39}_{-0.36}$	1.59 ± 0.08	248/221	4.56	7.47	9.00

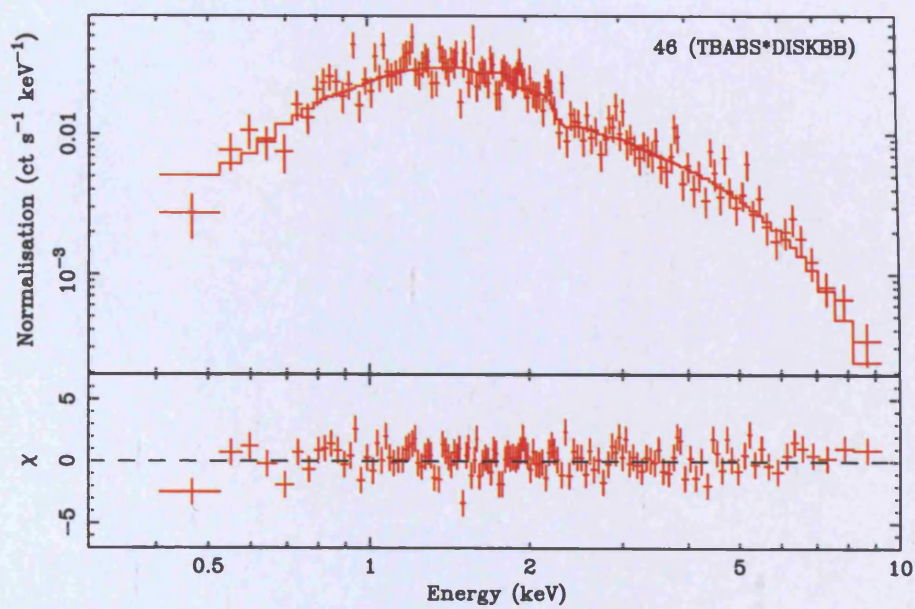
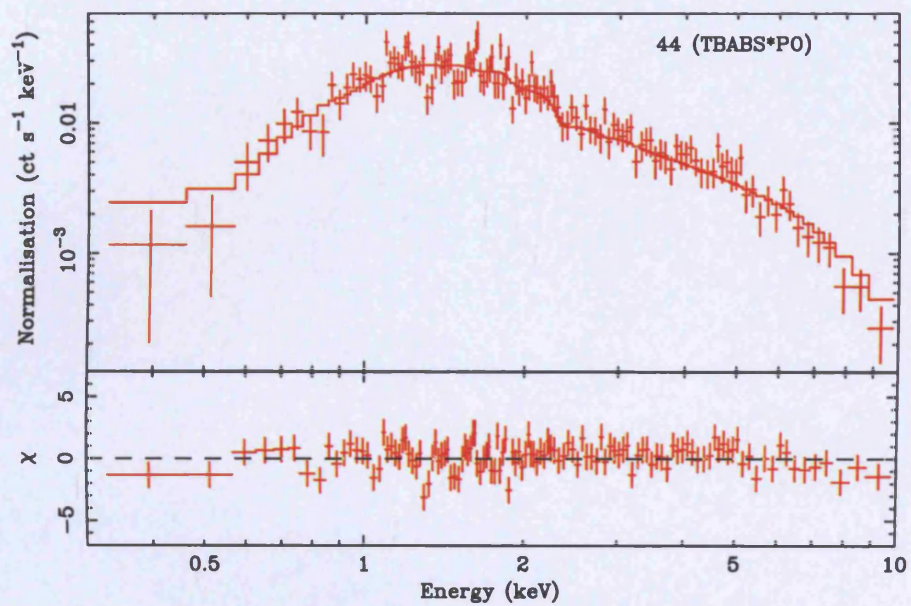
NOTES: The best fitting model for each source is highlighted by showing the χ^2/dof values in bold face. ^a Column density including Galactic ($\times 10^{21} \text{ cm}^{-2}$); ^b Observed 0.3–10 keV X-ray flux ($\times 10^{-13} \text{ erg cm}^{-2} \text{ s}^{-1}$) for the best fitting model; ^c Observed 0.3–10 keV X-ray luminosity ($\times 10^{38} \text{ erg s}^{-1}$) for the best fitting model. ^d Intrinsic 0.3–10 keV X-ray luminosity ($\times 10^{38} \text{ erg s}^{-1}$) for the best fitting model.

The spectra of sources 13, 29 and 46 all prefer the diskbb model with $1.1 < kT_{in} < 1.6$, while source 44 is best fitted by the power-law model with $\Gamma \sim 2$. The bbody and mekal models are not shown in this table as they did not provide better fits than the best fitting po or diskbb model. Fig. 5.5 shows the spectra and best fitting single component model in each case.

Two component modelling was unnecessary in each case as the X-ray spectra are adequately described by the single component models. As confirmation of this, attempts to model the X-ray spectra with two component models (*i.e.*, a power-law plus either a diskbb, bbody or mekal component) did not provide a significant improvement over the single model fits in any case.

Figure 5.5: EPIC pn count rate spectra and $\Delta\chi$ residuals with respect to the best-fitting single component model specified in Table 5.7, for sources 13, 29, 44 and 46.





5.5 X-ray colours

The D_{25} sources in this galaxy were plotted on an X-ray colour diagram, using the same method as described in Chapter 4. All of the sources fall into either the absorbed source category or the XRB regime using these classification boundaries (see Fig. 5.6). This is most likely a consequence of the high column density towards NGC 4945, which absorbs most of the soft X-ray emission resulting in larger HR1 values than expected. This colour classification is intended to be a general scheme that can be applied to any galaxy regardless of the Galactic column density, with the absorption increasing in the Y-direction on the powerlaw grid (see model grid in the top panel of Fig 4.7). Most nearby galaxies chosen for point source studies are selected against such high absorption for this very reason. Therefore, in the case of NGC 4945, this X-ray colour scheme cannot accurately be used to derive information on the types of sources present.

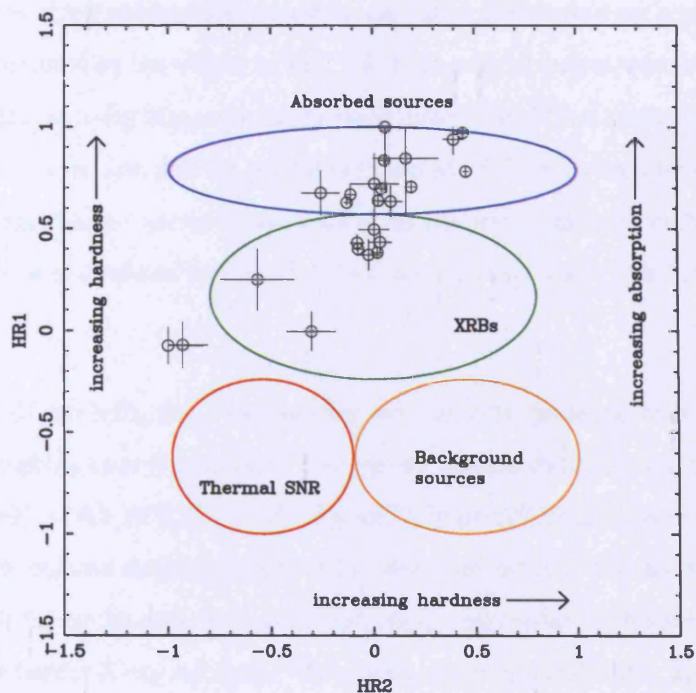


Figure 5.6: Classification of the NGC 4945 D_{25} sources detected by either MOS or pn based on the classification scheme described in Chapter 4.

5.6 Residual disc emission

Following the procedure from Chapter 4, the X-ray images were flat-fielded by subtracting a particle component and then dividing by the appropriate exposure map. As before, bad pixels, a hot column (for the pn detector) and spurious data along chip gaps were excised. Fig. 5.7 shows a close up of the flat-fielded pn soft band data with blanked out regions around the catalogued discrete sources listed in Table 5.2. A few additional regions with emission thought to originate from point sources have also been removed in an attempt to limit contamination of the underlying diffuse emission. The size of the circular exclusion regions were $25''$, $30''$ and $35''$ depending on the brightness of the sources. Unfortunately the bulk of the diffuse emission is concentrated in the centre of the galaxy which also harbours the majority of the point sources; it follows that in removing contamination from point sources, much of the diffuse flux is also excluded. However, it is apparent from Fig. 5.7 that some regions of enhanced diffuse brightness remain, which can be used to sample the spectrum of the extended emission.

Representative spectra of the residual disc emission (excluding the blanked out regions), were extracted from the region represented by the ellipse in Fig. 5.7. Background spectra were obtained with exactly the same extraction region using blank-sky background maps. The diffuse spectra were grouped to give a minimum of 30 counts per bin and the pn, MOS-1 and MOS-2 data were fitted simultaneously, but with the relative normalisations untied so as to allow for calibration differences between the cameras. The spectral analysis was confined to the 0.3–6 keV energy range for which there was a reasonable signal to noise ratio.

Following the NGC 55 analysis, the X-ray spectra were initially modelled with an absorbed `mekal` component, with the abundance free to vary. This model yielded the following fit parameters: $N_H \sim 1.4 \times 10^{21} \text{ cm}^{-2}$, $kT \sim 0.5 \text{ keV}$, $Z \sim 0.07 Z_\odot$ and $\chi^2/\text{dof}=551/362$. However, this absorption is less than the Galactic column density towards NGC 4945 and the very low abundance is unrealistic. As before, improved fits to the data were achieved using a power-law or higher temperature `mekal` component to fit the harder X-ray energies. The results of the spectral fitting are shown in Table 5.8 and the best-fitting `mekal` plus power-law model fit to the data is shown in Fig 5.8.

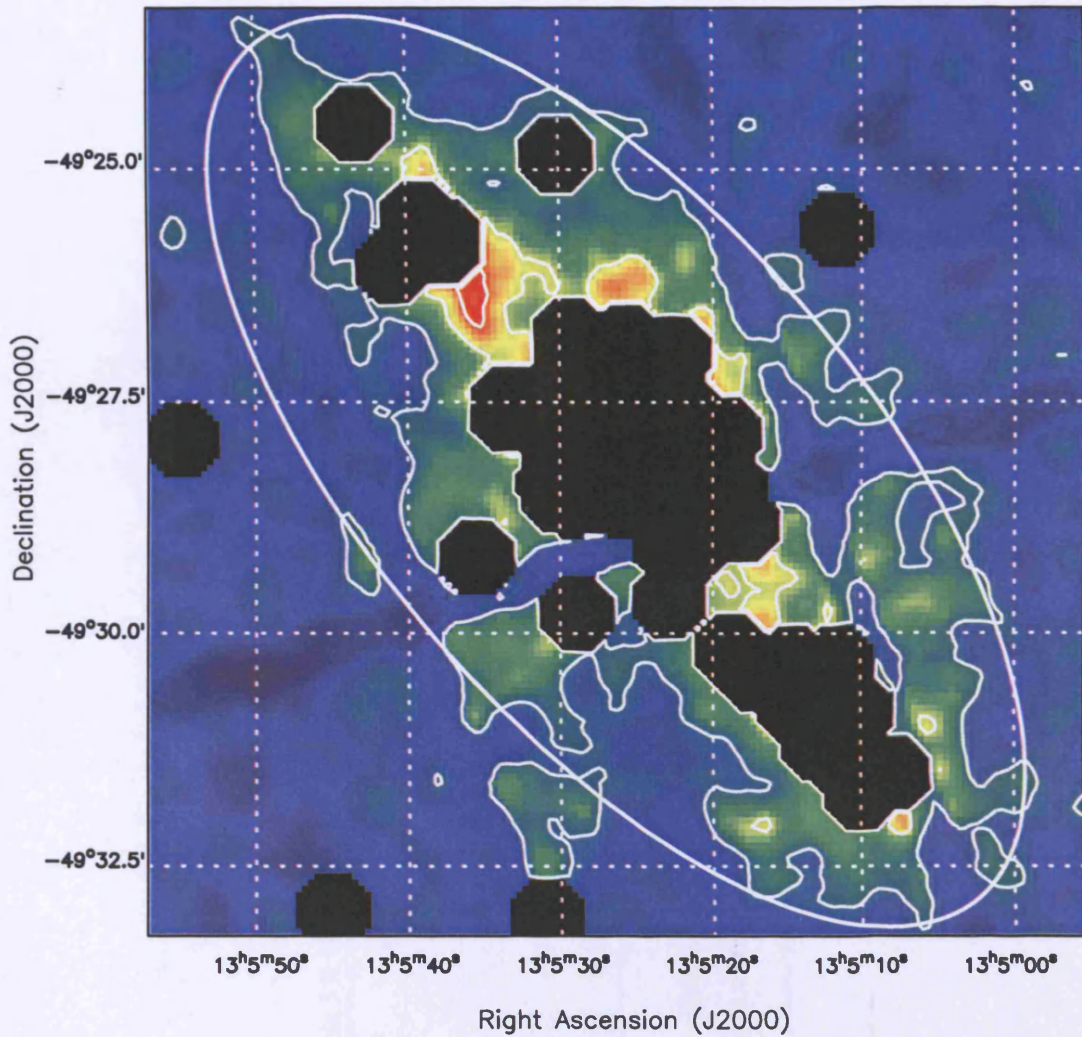


Figure 5.7: Close up of the composite flat-fielded pn image in the soft (0.3–1.0 keV) bandpass. Regions around catalogued sources have been blanked out so as to reduce the contamination of the diffuse signal by relatively bright resolved point sources. A few additional regions thought to be contaminated by relatively bright point sources were also removed. The ellipse, excluding the blanked out sections, corresponds to the region used to estimate the diffuse luminosity of the disc of NGC 4945 and from which the diffuse spectrum was extracted.

Table 5.8: Spectral modelling results for the residual disc emission

Model	N_H^a	kT_1^b	kT_2^b	$Z (Z_\odot)^c$	Γ	χ^2/dof	f_X^d			L_X^e
							Obs	Obs	Unabs	
mekal	<1.70	$0.51^{+0.05}_{-0.04}$	–	0.07 ± 0.01	–	551/362	2.33	3.8	7.4	
mekal+po	$2.36^{+1.98}_{-0.59}$	$0.24^{+0.02}_{-0.01}$	–	$0.41^{+5.53}_{-0.13}$	$2.22^{+0.30}_{-0.34}$	398/360	3.17	5.2	12.2	
mekal+mekal	$2.89^{+4.93}_{-2.05}$	$0.24^{+0.02}_{-0.05}$	$3.78^{+3.20}_{-1.44}$	$0.11^{+0.13}_{-0.06}$	–	403/360	3.15	5.2	16.0	

NOTES: ^a Column density (including Galactic, $\times 10^{21} \text{ cm}^{-2}$). ^b Temperatures of the cool (kT_1) and hot (kT_2) thermal components in keV. ^c Relative metal abundance of the thermal plasma component. ^d Observed 0.3–6 keV X-ray flux ($\times 10^{-13} \text{ erg cm}^{-2} \text{ s}^{-1}$). ^e Observed and intrinsic (absorption-corrected) 0.3–6 keV X-ray luminosity ($\times 10^{38} \text{ erg s}^{-1}$).

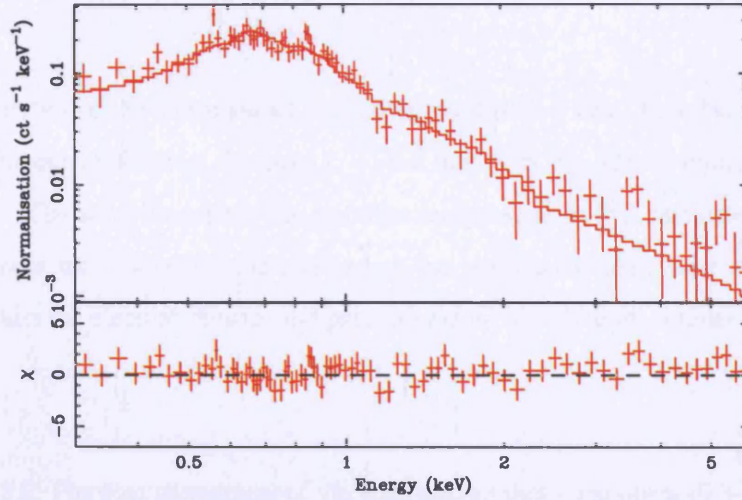


Figure 5.8: EPIC pn count rate spectra for the residual disc emission in NGC 4945. The best-fit `mekal` plus power-law model is shown along with the corresponding $\Delta\chi$ residuals (lower panel).

The `mekal` plus power-law model ($N_H \sim 2.4 \times 10^{21} \text{ cm}^{-2}$, $kT \sim 0.2 \text{ keV}$, $Z \sim 0.4 Z_\odot$, $\Gamma \sim 2$ and $\chi^2/\text{dof}=398/360$) yields an observed X-ray flux of $\sim 3 \times 10^{-13} \text{ erg cm}^{-2} \text{ s}^{-1}$ (0.3–6 keV), corresponding to an absorbed luminosity of $5 \times 10^{38} \text{ erg s}^{-1}$. About 40% of this luminosity originates in the soft thermal emission. After correcting for absorption, the luminosity of this soft component increases to $\sim 7 \times 10^{38} \text{ erg s}^{-1}$ and contributes about 60% of the total. While it is likely that this soft `mekal` component represents real diffuse emission in the galaxy, the harder emission modelled with the power-law component may be due to a contamination of unresolved point sources and/or the possible scattering of the primary nuclear continuum into our line of sight (*e.g.*, Iwasawa et al. 1993, Guainazzi et al. 2000).

The soft diffuse emission has a temperature of $\sim 0.2 \text{ keV}$ (Table 5.8), which as stated in the previous chapter is fairly typical for the softest emission in star forming galaxies (*e.g.*, Pietsch et al. 2001, Fabbiano et al. 2003). The *observed* X-ray flux of the residual disc emission is only $\sim 10\%$ of that of the resolved sources in the broad 0.3–6 keV band but contributes approximately the same amount of flux in the soft band. This supports the argument that a bright soft X-ray disc in this galaxy is being detected. The full extent of the soft diffuse component is $\sim 12' \times 5'$ (which roughly corresponds to the area encompassed by the lowest contour in Fig. 5.7) albeit with a concentration in the central $\sim 3' \times 2'$. Allowing for the fraction of the bright disc region which is masked in Fig. 5.7, the true luminosity of the disc is estimated to be a factor 1.7 larger than determined on the basis of the spectral

extraction region.

The physical properties of the soft residual disc component (0.3–6 keV) have been derived based on the `mekal` component of the best fit `mekal + po` model to the diffuse emission, and are tabulated in Table 5.9. The soft component has a similar temperature to that calculated for NGC 55 and NGC 4449. However, the luminosity, thermal energy, gas mass and cooling time are noticeably larger for NGC 4945, while the electron density and pressure are up to ~ 6 times smaller.

Table 5.9: Physical parameters of the soft residual disc component (0.3–6 keV).

Physical property	Value
Temperature, T	2.8×10^6 K
Intrinsic L_X	1.2×10^{39} erg s $^{-1}$
Electron density, n_e	0.0054 cm $^{-3}$
Thermal energy, E_{th}	4.8×10^{55} erg
Mass of hot gas, M	$3.5 \times 10^7 M_\odot$
Pressure, P	4.2×10^{-12} dyn cm $^{-3}$
Cooling time, t_{cool}	12.8×10^8 yr

ASSUMPTIONS: $V = 8 \times 10^{66}$ cm 3 (cylindrical volume subtending $12' \times 5'$ when projected on the sky); $D = 3.7$ Mpc; filling factor, $f = 1$; the intrinsic L_X is scaled by a factor of 1.7 as described in the text; $n_e = (EI/Vf)^{1/2}$, where EI is the emission integral ($norm \times 4\pi D^2$)/ 10^{-14} , and $norm$ is the `mekal` normalisation obtained from the spectral fitting (also scaled by a factor of 1.7); $E_{th} = 3n_e kTV$; $M = n_e m_P V f$; $P = 2n_e kT$ and $t_{cool} \sim (3kT)/(\Lambda n_e)$, where $\Lambda = L_X/EI$.

Finally, there is evidence from the soft band X-ray images (see Fig. 5.9) that the diffuse component is extended as far as $\sim 3'$ (~ 3 kpc) along the minor axis to the South-East (with a width along the major axis direction of $\sim 2'$). This extended emission (a possible outflow?) is orientated in the opposite direction to that of the soft X-ray plume, which is extended to the North-West by $\sim 30''$ (Schurch et al., 2002). It is at least a plausible hypothesis that this South-East to North-West axis defines the normal to an accretion disc in the nucleus of the galaxy, and hence is the natural axis for an outflow to occur.

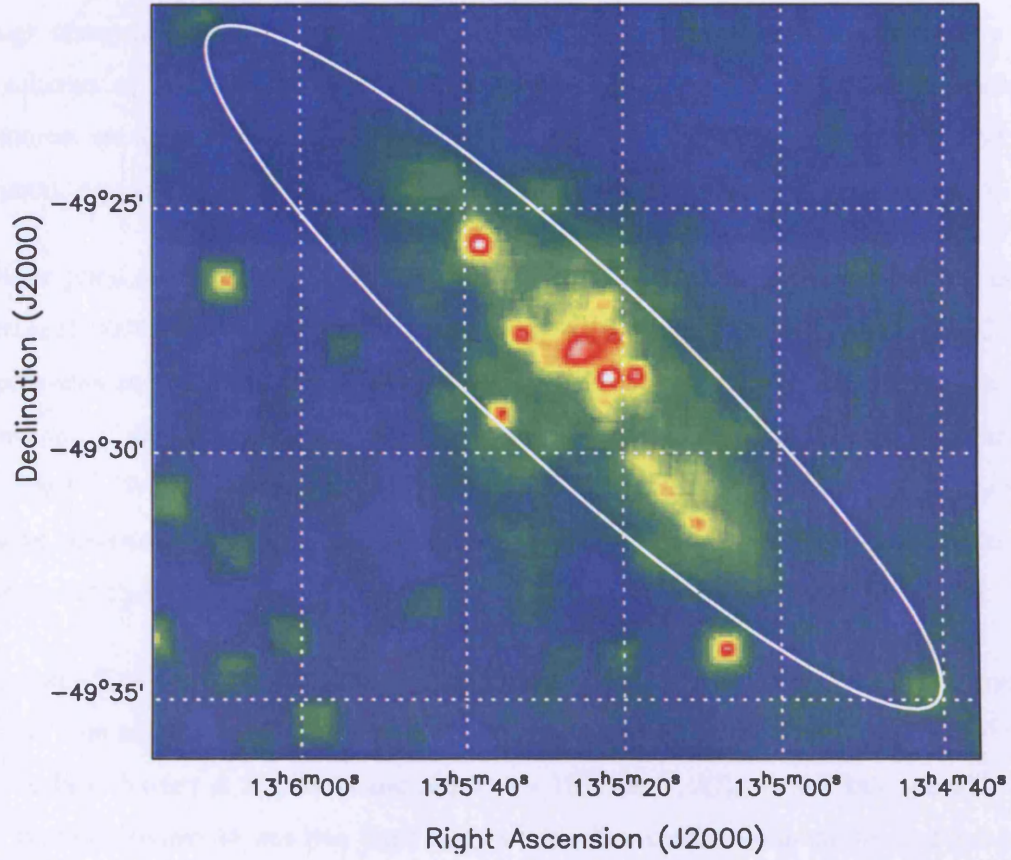


Figure 5.9: Adaptively smoothed soft band (0.3–1 keV) EPIC image of the NGC 4945 field. Evidence of an outflow extending up to $\sim 3'$ in the South-East direction can be clearly seen.

5.7 Discussion

5.7.1 The bright sources

The most luminous X-ray source in the NGC 4945 field (source 37) is coincident with the Seyfert nucleus. The galaxy's nuclear region has been the subject of many previous analyses (*e.g.*, Done et al. 1996, Schurch et al. 2002, Done et al. 2003), and as such is not re-analysed here. Instead, this work concentrates on the four next brightest sources which have not been as well studied. These sources have high observed X-ray luminosities ($\sim 4 - 7 \times 10^{38} \text{ erg s}^{-1}$) and are best described by power-law continuum or accretion disc dominated X-ray spectral shapes (see § 5.4.2). It is possible that these sources are accreting XRBs, however they do not show any variability over the course of this observation. As such, future observations would be necessary to confirm their accreting nature.

The two brightest of these sources (29 and 44 from Table 5.2) have previously been classified as ULXs (Colbert et al. 2004, Swartz et al. 2004). However, Colbert et al. (2004) use a distance to NGC 4945 of 5.2 Mpc compared to 3.7 Mpc throughout this work, which resulted in higher luminosity estimates for these sources. If the authors had used 3.7 Mpc then these sources would not have X-ray luminosities $> 10^{39} \text{ erg s}^{-1}$. While Swartz et al. (2004) do use a 3.7 Mpc distance, they classify ULXs as sources possessing *intrinsic* X-ray luminosities $> 10^{39} \text{ erg s}^{-1}$, rather than *observed* X-ray luminosities which have been used to define ULXs in this thesis.

Swartz et al. (2004) and Feng & Kaaret (2005) also presented spectral characteristics of sources 29 and 44. In both analyses, source 29 was best fitted using a MCD model with $N_H \sim 4 \times 10^{21} \text{ cm}^{-2}$, $kT_{in} \sim 1 \text{ keV}$ (Swartz et al., 2004) and $N_H \sim 4 \times 10^{21} \text{ cm}^{-2}$, $kT_{in} \sim 0.9 \text{ keV}$ (Feng & Kaaret, 2005). Whereas, source 44 was best fitted using a power-law continuum in the work of Swartz et al. (2004) with $N_H \sim 8 \times 10^{21} \text{ cm}^{-2}$, $\Gamma \sim 1.8$, but preferred a MCD model with $N_H \sim 4 \times 10^{21} \text{ cm}^{-2}$, $kT_{in} \sim 1.7 \text{ keV}$ according to Feng & Kaaret (2005).

Modelling of source 29 presented in this work agrees with the MCD interpretation and produced a similar disc temperature to those of Swartz et al. (2004) and Feng & Kaaret (2005) (*i.e.*, $kT_{in} \sim 1 \text{ keV}$), but a slightly higher absorption component (*i.e.*, $N_H \sim 5 \times 10^{21} \text{ cm}^{-2}$). Modelling of source 44 in this work agrees with the power-law interpretation of Swartz et al. (2004), with almost identical fit parameters (*i.e.*, $N_H \sim 8 \times 10^{21} \text{ cm}^{-2}$, $\Gamma \sim 1.8$).

Table 5.10: The components of the integrated X-ray luminosity of NGC 4945.

Component	L_X (0.3–6 keV)
AGN	$12 \times 10^{38} \text{ erg s}^{-1}$
Discrete sources	$58 \times 10^{38} \text{ erg s}^{-1}$
Residual soft disc ^a	$12 \times 10^{38} \text{ erg s}^{-1}$
Residual hard disc ^a	$9 \times 10^{38} \text{ erg s}^{-1}$

^a Corresponding to the $12' \times 5'$ ellipsoidal inner disc region. Corrected for absorption intrinsic to NGC 4945 and including the area scaling factor.

5.7.2 Comparison with NGC 55

In addition to the Seyfert 2/starburst nucleus, ~ 20 of the detected discrete X-ray sources are likely to be associated with NGC 4945, the majority of which are located in the central region. Unfortunately not much can be said about the nature of these sources based on their X-ray colours, as the high intrinsic absorption tends to suppress the soft X-ray emission, causing all the sources to lie in the XRB/absorbed source categories. However, based on their relatively high luminosities ($\gtrsim 6 \times 10^{38} \text{ erg s}^{-1}$), it is likely that most of the discrete sources are XRBs. The integrated X-ray luminosity of the nucleus and the discrete sources together with the luminosity inferred for the residual disc emission is summarised in Table 5.10 (the discrete source luminosities are from the source catalogue given in Table 5.2 and are therefore observed luminosities, *i.e.*, uncorrected for absorption intrinsic to NGC 4945). The quoted values for the residual disc emission are scaled-up values based on the area scaling factor determined earlier.

A comparison of the integrated luminosity of NGC 4945 with NGC 55 reveals that the 23 discrete sources in NGC 4945 (excluding the AGN) are ~ 3.5 times more luminous than the 21 brightest sources in NGC 55 (including the ULX). In other words NGC 4945 has a somewhat more luminous discrete source population than NGC 55. Also, as the majority of the discrete sources in NGC 55 were classified as accreting binaries based on their X-ray colour classification, then based on a luminosity argument, the majority of sources in NGC 4945 are also likely to be accreting binaries.

The diffuse X-ray emission detected in NGC 4945 has been shown to cover a region of $\sim 12' \times 5'$. A

previous study of the diffuse emission in NGC 4945 using high resolution *Chandra* X-ray and ground-based optical $H\alpha$ imaging, revealed a total (*i.e.*, halo+disc+nuclear regions) observed flux (0.3–2 keV) for the galaxy of $\sim 4 \times 10^{-13}$ erg cm $^{-2}$ s $^{-1}$ (Strickland, 2004). The estimated observed flux of the diffuse emission based on this *XMM-Newton* spectral analysis in the same energy band (*i.e.*, 0.3–2 keV) is similarly $\sim 4 \times 10^{-13}$ erg cm $^{-2}$ s $^{-1}$ after applying the 1.7 scaling factor discussed earlier. This is entirely consistent with that derived by Strickland (2004), and corresponds to an observed luminosity of $\sim 7 \times 10^{38}$ erg s $^{-1}$ (0.3–2 keV).

A comparison of the properties of NGC 4945 with those of NGC 55 is given in Table 5.11. While NGC 55 and NGC 4945 are both edge-on galaxies (which makes it difficult to study their detailed morphologies) the key difference is that NGC 4945 is a much more massive and actively star forming than NGC 55. Also, it is believed that the origin of the diffuse X-ray emission differs between normal galaxies like NGC 55 and galaxies with both starburst/Seyfert contributions like NGC 4945. In normal galaxies the diffuse emission tends to trace the optical disc, which largely agrees with the NGC 55 results, which show that the diffuse emission is concentrated in the central disc at sites of current star formation. X-ray studies of edge-on galaxies with both starburst/Seyfert contributions, (*e.g.*, Levenson et al. 2001) have shown that the soft X-rays extend perpendicular to the plane and are not confined to the disc. Indeed, this analysis (as well as other X-ray studies *e.g.*, Guainazzi et al. 2000) shows the presence of diffuse emission along the plane of NGC 4945, as well as possible evidence of a ~ 3 kpc outflow perpendicular to the disc. Comparing the properties in Table 5.11, the most important point to notice is that NGC 4945 is ~ 7 times more massive than NGC 55, and this difference is generally reflected in the X-ray luminosities, which are ~ 5 times larger for NGC 4945. On the other hand, the difference in the diffuse X-ray luminosities between the two systems does not seem to fully scale with the star formation rate (SFR), which is a factor ~ 14 larger for NGC 4945. However, this may be due to the fact that the nuclear starburst region of NGC 4945 was unfortunately largely excluded in this analysis due to the bright source confusion.

A number of studies have argued that the X-ray luminosity can be used as an estimate of the SFR of the galaxy (*e.g.*, Gilfanov et al. 2004). Looking at this in more detail for NGC 55 and NGC 4945, by considering the L_X –SFR relation plotted in Fig. 4 of Gilfanov et al. (2004), the predicted luminosity band for the given SFR of each galaxy is $\sim 6 \times 10^{37} - 10^{39}$ erg s $^{-1}$ for NGC 55 and $\sim 9 \times 10^{39} - 3 \times 10^{40}$ erg s $^{-1}$ for NGC 4945. These luminosities are consistent with those derived in this analysis.

Table 5.11: A comparison of the properties of NGC 4945 with NGC 55(0.3–6 keV).

Property	NGC 55	NGC 4945
Assumed Distant (Mpc)	1.78	3.7
L_X (AGN) ^a (10^{38} erg s ⁻¹)	–	16
L_X (sources) ^a (10^{38} erg s ⁻¹)	17	77
L_X (diffuse) ^a (10^{38} erg s ⁻¹)	4	21
M_{25} ^b ($10^9 M_\odot$)	8.5	61.7
M_{HI} ^c ($10^9 M_\odot$)	2.0	1.3
SFR ^d (M_\odot yr ⁻¹)	0.22	3.1

NOTES: ^aX-ray luminosities from Chapter 4, this chapter respectively. Quoted values are corrected for absorption, and in the case of the diffuse emission, are scaled using the 1.7 factor derived earlier (NGC 4945). Also, for NGC 4945, the source luminosity includes source 35, previously identified as a soft X-ray plume, which has an intrinsic luminosity of 1×10^{38} erg s⁻¹ ^b ‘Indicative’ mass of the galaxy within its D₂₅ diameter from Karachentsev et al. (2004). ^c HI mass of the galaxy from Karachentsev et al. (2004). ^d Star formation rates from Grimm et al. (2003). Quoted values are scaled to the assumed distant.

5.8 Summary

The X-ray properties of the spiral galaxy NGC 4945 have been investigated using recent *XMM-Newton* EPIC observations. These data revealed a total of 69 X-ray sources in the FOV, of which 24 were located within the D₂₅ ellipse of the galaxy. Source detection covered a flux range of $\sim 9 \times 10^{-15} - 7 \times 10^{-13}$ erg cm⁻² s⁻¹ (0.3–6 keV) for sources within the D₂₅ ellipse, corresponding to a luminosity range of $\sim 2 \times 10^{35} - 1 \times 10^{39}$ erg s⁻¹ assuming a distance to NGC 4945 of 3.7 Mpc ³. Estimates of background AGN contamination of the D₂₅ sources leads to a prediction of ~ 20 actual members of the galaxy. Their high luminosities coupled with their high density in the central starburst region suggests the majority of these sources may be accreting XRBs.

X-ray spectral and timing analyses were performed on four of the brightest X-ray sources (excluding

³The faintest source detected in the field had an observed X-ray flux of $\sim 4 \times 10^{-15}$ erg cm⁻² s⁻¹

the AGN) in the galaxy. While the timing studies did not reveal evidence of an accreting nature, the spectra of three of the four sources were best described by an accretion disc model (MCD) with $1.1 < kT_{in} < 1.6$. The remaining source preferred a simple absorbed power-law spectral fit with $\Gamma \sim 1.8$. Additional observations of NGC 4945 are needed to monitor the bright X-ray sources and search for variability, to support the binary interpretation.

The galaxy shows evidence for diffuse emission along the disc with an extent of $12' \times 5'$, as well as a possible outflow perpendicular to the plane extending up to $\sim 3'$. This apparent outflow is aligned in the opposite direction to the soft X-ray plume which emanates from the nucleus, suggesting that both are linked to nuclear activity. The diffuse emission is best described by a soft thermal component with $kT \sim 0.2$ keV plus a hard power-law contribution with $\Gamma \sim 2$, which may be due to unresolved binaries or reflection from the nuclear continuum. After correcting for absorption and an area scaling factor, the X-ray luminosity of this soft emission is $\sim 12 \times 10^{38}$ erg s $^{-1}$ (0.3–6 keV). However, as noted by Guainazzi et al. (2000), there may be substantial contribution to the emission above 1 keV due to unresolved binaries.

A comparison of the properties of NGC 4945 with NGC 55 show that the X-ray luminosities from the source and diffuse components appear to scale with the total mass of the system. In addition to this, the expected luminosities based on the SFR of each system are entirely consistent to those calculated in this analysis.

Chapter 6

XMM-NEWTON observations of the brightest ultraluminous X-ray sources

6.1 Introduction

Einstein X-ray observations were the first to reveal point-like, extranuclear sources in some nearby galaxies with luminosities in excess of 10^{39} erg s $^{-1}$ (Fabbiano, 1989). Subsequently, many of these so-called ultraluminous X-ray sources (ULXs) have displayed short and long term variability, which suggests they are predominantly accreting objects (see Miller & Colbert 2004 and references therein). However, the observed luminosities of most ULXs exceed the Eddington limit for spherical accretion onto a stellar-mass (~ 10 - M_{\odot}) black-hole. In fact, their luminosities are intermediate between those of normal stellar mass BHBs and AGN. Therefore, the accretion of matter onto IMBHs of $\sim 10^2$ – 10^4 M_{\odot} provides an attractive explanation for ULXs, and could represent the long sought-after ‘missing link’ between stellar mass black-holes and the supermassive black-holes in the nuclei of galaxies. However, the large populations of ULXs associated with sites of active star formation (*e.g.*, in the Cartwheel galaxy, Gao et al. 2003) demand rather too high formation rates of IMBHs if they are to explain the ULX class as a whole (King, 2004). An alternative to accreting IMBHs is that ULXs may be a type of stellar-mass BHB with geometrically (King et al., 2001) or relativistically (Körding et al., 2002) beamed emission, such that their intrinsic X-ray luminosity does not exceed the Eddington limit. Another possibility is that they are stellar-mass BHBs that can achieve truly super Eddington luminosities via

slim (Ebisawa et al., 2003) or radiation pressure dominated (Begelman, 2002) accretion discs.

As ULXs are probably the brightest class of XRB fueled by the accretion of matter onto a black-hole¹, a knowledge of the properties of Galactic BHBs could be vital in interpreting their characteristics. Traditionally the X-ray spectra of BHBs have been fitted empirically with two components, namely a power-law continuum and a MCD component (Mitsuda et al. 1984; Makishima et al. 1986). In the standard picture, the power-law component is thought to represent inverse-Compton scattering of thermal photons from the accretion disc by hot electrons in a surrounding corona. As such, the power-law represents the hard tail of the X-ray emission while the MCD component models the soft X-ray emission from the accretion disc. The MCD model itself has been formulated based on the best known model for accretion onto black-holes (*i.e.*, the thin accretion disc model, Shakura & Sunyaev 1973).

As previously mentioned (§ 1.3.4), BHBs exhibit thermal and non-thermal components of X-ray emission, typically modelled by a MCD and power-law respectively, both of which can vary widely in intensity. It has long been recognised that BHBs undergo transitions between various X-ray spectral states when one or the other of these emission components dominates the X-ray luminosity: the LH state where the emission is dominated by a power-law, the HS state which is dominated by MCD emission and the VH state where the emission is usually dominated by steep power-law emission.

The idea of ULXs as analogues to Galactic BHBs in the HS state was supported by *ASCA* observations, which revealed that their 0.5–10 keV spectra were successfully fitted with the MCD model with relatively high disc temperatures (1.0–1.8 keV, Makishima et al. 2000). As such, the ULXs were considered to be mass-accreting BHs with the X-ray emission originating in an optically-thick accretion disc. In fact, the use of the MCD model to describe these spectra permits an ‘X-ray-estimated’ black-hole mass, M_{XR} , to be calculated from the following equation (*c.f.* Makishima et al. 2000 equations (5)–(8)).

$$M_{\text{XR}} = \frac{\xi \kappa^2}{8.86\alpha} \frac{D}{\sqrt{\cos i}} \sqrt{\frac{f_{\text{bol}}}{2\sigma T_{\text{in}}^4}} M_{\odot} \quad (6.1)$$

Where D is the distance to the X-ray source, which has an inclination i , a full bolometric luminosity (from the MCD model) of f_{bol} and an observed maximum disc colour temperature T_{in} . In addition

¹Although the most likely reservoir of fuel for a ULX is a companion star, others have been suggested, for example the direct accretion of matter from molecular clouds (Krolik, 2004).

σ is the Stefan-Boltzmann constant, κ is the ratio of the colour temperature to the effective temperature (‘spectral hardening factor’), and ξ is a correction factor reflecting the fact that T_{in} occurs at a radius somewhat larger than R_{in} (one assumption here is that R_{in} is at the last stable Keplerian orbit). Makishima et al. (2000) use values of $\xi = 0.412$ and $\kappa = 1.7$, though other work has found different values for the spectral hardening factor (e.g. $\kappa = 2.6$ for GRO J1655-40, Shrader & Titarchuk 2003). Finally, α is a positive parameter with $\alpha = 1$ corresponding to a Schwarzschild black-hole. However, the masses inferred from the *ASCA* data and Equation (6.1) are far too low to be compatible with the large black-hole masses suggested by their luminosities (assuming Eddington-limited accretion), for standard accretion discs around Schwarzschild black-holes. Makishima et al. (2000) suggested that this incompatibility could be explained if the black-holes were in the Kerr metric (*i.e.*, rapidly rotating objects), allowing smaller inner disc radii and hence higher disc temperatures.

Chandra observations have provided some support for the Makishima et al. (2000) results, with some ULX spectra being consistent with the MCD model (*e.g.*, Roberts et al. 2002). However, *Chandra* also revealed that some ULX spectra showed a preference for a power-law continuum rather than the MCD model (*e.g.*, Strickland et al. 2001; Roberts et al. 2004; Terashima & Wilson 2004). It has been suggested that this preference for a power-law spectrum could be interpreted in terms of the LH state seen in Galactic BHB candidates, relativistically beamed jets or emission from a Comptonised accretion disc in the VH state. As well as these single component models, *ASCA* and *Chandra* spectroscopy have also suggested the presence of two component spectra for some ULXs, comprising a MCD with a power-law component. For example, previous *ASCA* analyses hinted at evidence for IMBHs, *i.e.*, cool accretion disc components (see below), but these observations were not sensitive enough to statistically require two component modelling (*e.g.*, Colbert & Mushotzky 1999). Similar results have been obtained by *Chandra*, *e.g.*, ULXs in NGC 5408 (Kaaret et al., 2003) and NGC 6946 (Roberts & Colbert, 2003). Conversely, *Chandra* spectra of the Antennae ULXs (Zezas et al. 2002a; Zezas et al. 2002b) revealed an accretion disc (MCD) component consistent with the high temperature *ASCA* results (*i.e.*, $kT_{\text{in}} \sim 1$ keV), together with a hard power-law component ($\Gamma \sim 1.2$).

It is only recently, using high quality *XMM-Newton*/EPIC spectroscopy of ULXs, that it has been demonstrated that the addition of a soft thermal disc component to a power-law continuum spectrum provides a strong statistical improvement to the best fitting models to ULX data (*e.g.*, Miller et al. 2003; Miller et al. 2004b). These particular observations have provided strong support for the IMBH hypothesis by revealing disc temperatures in these sources up to 10 times lower than commonly measured in

stellar mass BHs, consistent with the expectation for the accretion disc around a $\sim 1000 M_{\odot}$ IMBH² (c.f. Equation (6.1)). However, in a few cases, *XMM-Newton*/EPIC observations have revealed a more unusual two-component X-ray spectrum. A detailed analysis of such a source is presented in Chapter 3. In this case, the ULX is the brightest X-ray source in the nearby (1.78 Mpc) Magellanic-type galaxy NGC 55 and, although its X-ray luminosity only marginally exceeds $10^{39} \text{ erg s}^{-1}$, it represents one of the highest quality ULX datasets obtained to date. The initial low flux state data were best fitted with an absorbed power-law continuum ($\Gamma \sim 4$), while a subsequent flux increase was almost entirely due to an additional contribution at energies $> 1 \text{ keV}$, adequately modelled by a MCD component ($kT_{\text{in}} \sim 0.9 \text{ keV}$).

Whilst this accretion disc component is reasonable for stellar-mass black-holes, the dominance of the power-law continuum at soft X-ray energies is problematic. Such a soft power-law cannot represent Comptonised emission from a hot corona, as the coronal component is not expected to extend down below the peak emissivity of the accretion disc, where there would be insufficient photons to seed the corona. Alternative sources of seed photons for the corona are unlikely; for example, the incident photon flux of the secondary star at the inner regions of the accretion disc is too low to provide the seeding (c.f. Roberts et al. 2005). It also seems unlikely that the power-law emission could arise from processes at the base of a jet, as these are typically represented by much harder photon indices than measured here ($\Gamma \sim 1.5\text{--}2$; Markoff et al. 2005 and references therein). Indeed, with the possible exception of NGC 5408 X-1 (Kaaret et al., 2003), there is no evidence that ULXs do display bright radio jets, though this cannot be excluded by current observations (Körding et al., 2005). The possibility of the soft component resulting from an outflow of material from the accretion disc may also be discounted as this would produce a thermal spectrum rather than a power-law continuum.

Although this spectral description has not been seen in Galactic systems, a second case has been reported independently for the nearest persistent extragalactic ULX (M33 X-8) by Foschini et al. (2004). The non-standard model provided the best fit to this ULX with $\Gamma \sim 2.5$ and $kT_{\text{in}} \sim 1.2 \text{ keV}$. However, this source is also at the low luminosity end of the ULX regime with $L_X \sim 2 \times 10^{39} \text{ erg s}^{-1}$. A further possi-

²It is common for the generic range of masses for IMBHs to be quoted as $20\text{--}10^6 M_{\odot}$. The lower limit comes from a consideration of the measured masses of black-holes in our own Galaxy (McClintock & Remillard, 2006), and a theoretical limit for the mass of a black-hole formed from a single massive star (Fryer & Kalogera, 2001). However, more recent population synthesis analyses show that black-holes of up to $\sim 80 M_{\odot}$ may be formed in young stellar populations (Belczynski et al., 2004). Hence, when referring to IMBHs in this chapter, it is a reference specifically to the larger $\sim 1000 M_{\odot}$ IMBHs implied by the cool accretion disc measurements.

ble case, in a more luminous ULX, has arisen from the *XMM-Newton* data analysis of NGC 5204 X-1 (Roberts et al., 2005). In this case the authors show that there is spectral ambiguity between the non-standard fit ($\Gamma \sim 3.3$, $kT_{\text{in}} \sim 2.2$ keV) and the IMBH model ($\Gamma \sim 2.0$, $kT_{\text{in}} \sim 0.2$ keV), with both providing statistically acceptable fits to the data. Even more recently, two additional examples of this spectral form have been uncovered in an *XMM-Newton* survey of ULXs by Feng & Kaaret (2005).

Although it is difficult to derive a literal physical interpretation from the non-standard model, it does provide an accurate empirical description of ULX spectra in some cases, and as such it has the potential to provide new insights into the nature of these sources. Therefore in this chapter, current *XMM-Newton* data has been re-evaluated in an attempt to determine the best spectral description for the shape of high quality ULX spectra, and to ask what consequences this has for the idea of ULXs as accreting IMBHs. The chapter is structured as follows: § 6.2 – introduction to the ULX sample; § 6.3 – details of the observations and data reduction; § 6.4 – description of the spectral analysis; § 6.5 – a comment on the luminosity and inner disc temperature relationship of these ULXs; § 6.6 – a discussion of the results; and finally § 6.7 – the conclusions.

6.2 The Sample

As the primary goal of this analysis is to find the best description(s) of the shape of ULX spectra, only the highest quality datasets were chosen. The ULXs were initially selected from the *ROSAT* catalogues of Roberts & Warwick (2000) and Colbert & Ptak (2002) to provide a list of historically-bright ULXs that are resolved at a spatial resolution similar to *XMM-Newton*³. A source selection criteria of observed count rates of > 10 counts ks^{-1} in the *ROSAT* HRI camera, combined with > 10 ks of *XMM-Newton*/EPIC data available in the archive by December 2004, was applied to select ten ULXs with potentially sufficient counts for very detailed spectral analysis. In addition, three more high quality ULX datasets were included: proprietary data for Holmberg II X-1 (hereafter Ho II X-1), and two sources not quite bright enough in the *ROSAT* bandpass to be classified as ULXs, namely the ULX in NGC 55 and M33 X-8. Whilst some of the sources in this sample have been observed more than once, only the longest individual exposure in each case was selected to provide the clearest single view of their spectra. The final sample of 13 sources from 12 different galaxies is listed in Table 6.1.

³This was deemed appropriate as most bright ULXs are persistent and vary by factors of no more than 2–3 in flux over a baseline of years, *c.f.* Roberts et al. (2004).

Table 6.1: The sample

Source	Alternate name(s)	R.A. (J2000)	DEC (J2000)	N_H (10^{20} cm^{-2})	d (Mpc)	L_X ($10^{39} \text{ erg s}^{-1}$)
(1)	(2)	(3)	(4)	(5)	(6)	(7)
NGC 55 ULX ¹	XMMU J001528.9–391319 ^a NGC 55 6 ^c Source 7 ^d	00 15 28.9	–39 13 19.1 ^a	1.74	1.78 ^b	1.3
M33 X-8 ²	–	01 33 50.9	+30 39 37.2 ^e	5.69	0.70 ^f	1.0
NGC 1313 X-1 ³	Source 6 ^g IXO 7 ^j	03 18 20.0	–66 29 11.0 ^h	3.96	3.70 ⁱ	4.7
NGC 1313 X-2 ³	Source 4 ^g IXO 8 ^j	03 18 22.3	–66 36 03.8 ^k	3.94	3.70 ⁱ	1.7
NGC 2403 X-1 ⁴	Source 21 ^l	07 36 25.5	+65 35 40.0 ^l	4.17	4.20 ^f	2.7
Ho II X-1 ⁵	IXO 31 ^j	08 19 29.0	+70 42 19.3 ^m	3.41	4.50 ⁱ	17
M81 X-9 ⁶	Holmberg IX X-1 ⁿ IXO 34 ^j NGC 3031 10 ^q H 44 ^r	09 57 53.2	+69 03 48.3 ^o	4.25	3.55 ^p	12
NGC 3628 X-1 ⁴	IXO 39 ^j	11 20 15.8	+13 35 13.6 ^s	2.22	7.70 ^f	5.2
NGC 4395 X-1 ⁴	NGC 4395 X2 ^t IXO 53 ^j	12 26 01.5	+33 31 30.5 ^u	1.36	3.60 ^f	0.6
NGC 4559 X-1 ⁴	X-7 ^v IXO 65 ^j	12 35 51.7	+27 56 04.1 ^w	0.82	9.70 ^f	9.1
NGC 4861 ULX ¹	IXO 73 ^j X1 ^y	12 59 01.9	+34 51 13.5 ^x	1.21	17.80 ⁱ	8.8
NGC 5204 X-1 ⁴	IXO 77 ^j HST 3 ^z U1 ^{aa}	13 29 38.6	+58 25 05.7 ^z	1.38	4.80 ^f	4.4
M83 ULX ¹	Source 13 ^{bb} IXO 82 ^j H30 ^{dd} H2 ^{ee}	13 37 19.8	–29 53 48.9 ^{cc}	3.69	4.70 ⁱ	1.0

NOTES: (1) Source designation; (2) Alternative name(s); (3–4) X-ray source position from *XMM-Newton* and *Chandra* data, or position of possible optical counterpart; (5) Galactic absorption column density from the ‘NH’ FTOOLS program (based on the measurements of Dickey & Lockman 1990); (6) Distance to the host galaxy; (7) Observed X-ray luminosity (0.3–10 keV) based on the results of the physically self-consistent modelling (see later). REFERENCES: ¹ This chapter, ² Markert & Rallis (1983), ³ Colbert et al. (1995), ⁴ Roberts & Warwick (2000), ⁵ Dewangan et al. (2004), ⁶ Fabbiano (1988a), ^a Chapter 3, ^b Karachentsev et al. (2003), ^c Read et al. (1997), ^d Schlegel et al. (1997), ^e Foschini et al. (2004), ^f Ho et al. (1997a), ^g Schlegel et al. (2000), ^h Miller et al. (2003), ⁱ Tully (1988), ^j Colbert & Ptak (2002), ^k Zampieri et al. (2004), ^l Schlegel & Pannuti (2003), ^m Kaaret et al. (2004), ⁿ Miller et al. (2004b), ^o Ramsey et al. (2006), ^p Paturel et al. (2002), ^q Radecke (1997), ^r Immler & Wang (2001), ^s Strickland et al. (2001), ^t Lira et al. (2000), ^u Source list (Obs.Id 5302) via *Chandra* X-ray Centre: <http://cxc.harvard.edu/chaser>, ^v Vogler et al. (1997), ^w Cropper et al. (2004), ^x Source list (Obs.Id 014115010) via *XMM-Newton* Science Archive: http://xmm.vilspa.esa.es/external/xmm_data_acc/xsa/index.shtml, ^y Liu & Bregman (2005), ^z Goad et al. (2002), ^{aa} Liu et al. (2004), ^{bb} Ehle et al. (1998), ^{cc} Soria & Wu (2002), ^{dd} Immler et al. (1999), ^{ee} Trinchieri et al. (1985).

The selected ULXs are located at distances of between 800 kpc and 17.8 Mpc, possess *XMM-Newton* count rates between 0.1 count s^{-1} and 8.9 count s^{-1} and cover the full range of ULX luminosities ($\sim 10^{39} \text{ erg s}^{-1}$ – $\text{few} \times 10^{40} \text{ erg s}^{-1}$). Hereafter the sources are referred to by their names as given in column (1) of Table 6.1.

6.3 Observations and data analysis

This work has utilised EPIC data obtained through the *XMM-Newton* public data archive (excluding proprietary Ho II X-1 data), with details of the observations shown in Table 6.2. The data were processed and reduced using the standard tools of XMM-SAS software v.6.0.0. In some cases the observations were affected by soft proton flaring for which preliminary cleaning was necessary. For these observations, full field X-ray (0.3–10 keV) lightcurves were extracted and screened for flaring using GTI files based on either a time or count rate criterion. The NGC 55 ULX and NGC 5204 X-1 observations were not affected by flaring episodes. The NGC 2403 X-1 observation was only affected by flaring at the end of the exposure (the last ~ 20 ks), therefore a time selection was used to exclude this flaring event. For the remaining sources, a count rate cut-off criterion was used to produce a GTI file. The exact value of the cut-off was allowed to vary from field-to-field, to provide the best compromise in each case between excluding high background periods and facilitating the longest available exposure on the ULX. In practise the actual cut-off values varied in the $6.5\text{--}17.5 \text{ count s}^{-1}$ (0.3–10 keV) range. In all cases, only those data recorded when the MOS and pn cameras were in simultaneous operation were used (see Table 6.2 for the net good exposure times).

For each ULX, events were extracted in a circular aperture centred on the source position given in Table 6.1. The background was taken from a circular region, near to the source in the pn camera and at the same distance from the readout node. The chosen background regions were the same in all three detectors where observations were taken using the full-frame observing mode. However, in three cases the MOS cameras were operated in either the large-window or small-window mode, so here a background region closest to the one used for the pn extraction was used. The size of the source and background spectral extraction regions are listed in Table 6.3.

Table 6.2: *XMM-Newton* Observation Log

Source	Obs.ID	Date	Duration (s)	Net exp. (s)	Rate (ct s ⁻¹)	MOS-1	MOS-2	pn	Position	Ref
(1)	(2)	(3)	(4)	(5)	(6)	(7)	(8)	(9)	(10)	(11)
NGC 55 ULX	0028740201	2001-11-14	34025	30410	2.08	FF	FF	FF	on-axis	1
M33 X-8	0102640101	2000-08-04	18672	6850	8.55	SW	SW	FF	on-axis	2,3,4
NGC 1313 X-1	0106860101	2000-10-17	42769	18490	1.15	FF	FF	FF	on-axis	4,5,6
NGC 1313 X-2	0106860101	2000-10-17	42769	18490	0.39	FF	FF	FF	off-axis ^a	4,5,6
NGC 2403 X-1	0164560901	2004-09-12	84600	57063	0.47	FF	FF	FF	on-axis	4
Ho II X-1	0200470101	2004-04-15	111999	47260	4.52	LW	LW	FF	on-axis	7
M81 X-9	0112521101	2002-04-16	11935	8440	3.25	FF	FF	FF	on-axis	4,5
NGC 3628 X-1	0110980101	2000-11-27	60745	45260	0.20	FF	FF	FF	on-axis	4,5
NGC 4395 X-1	0142830101	2003-11-30	118900	98900	0.18	FF	FF	FF	on-axis	4,8
NGC 4559 X-1	0152170501	2003-05-27	43290	37660	0.48	SW	SW	FF	on-axis	4,9
NGC 4861 ULX	0141150101	2003-06-14	29600	14590	0.11	FF	FF	FF	on-axis	–
NGC 5204 X-1	0142770101	2003-01-06	32999	17048	0.87	FF	FF	FF	on-axis	4,10
M83 ULX	0110910201	2003-01-27	31722	21130	0.21	FF	FF	EFF	off-axis ^b	4

NOTES: (1) Source designation; (2) Observation identifier, (3) Observation date (yyyy-mm-dd); (4) Observation duration (NB. this does include calibration observations in some cases); (5) Useful exposure after correcting for flaring episodes and ensuring simultaneous operation of the EPIC cameras; (6) Combined EPIC count rates derived from the combined X-ray light curves (0.3–10 keV); (7–9) Observing mode of each EPIC detector (SW : Small Window, LW : Large Window, FF : Full Frame, EFF : Extended Full Frame); (10) Source position with respect to the centre of the pn field of view: ^a $\sim 7'$ offset, ^b $\sim 6.5'$ offset; (11) References for previous analyses of these datasets (although not all references contain a complete analysis of the ULX): 1–Chapter 3, 2–Foschini et al. (2004), 3–Pietsch et al. (2004), 4–Feng & Kaaret (2005), 5–Wang et al. (2004), 6–Miller et al. (2003), 7–Goad et al. (2006), 8–Vaughan et al. (2005), 9–Cropper et al. (2004), 10–Roberts et al. (2005).

Table 6.3: Spectral extraction apertures

ULX	Extraction radius	
	Source	Background
(1)	(2)	(3)
NGC 55 ULX	60	75
M33 X-8	35	120
NGC 1313 X-1	35	70
NGC 1313 X-2	35	70
NGC 2403 X-1	45	45
Ho II X-1	45	60
M81 X-9	30	45
NGC 3628 X-1	35	70
NGC 4395 X-1	40	40
NGC 4559 X-1	40	80
NGC 4861 ULX	15	45
NGC 5204 X-1	40	50
M83 ULX	35	50

NOTES: (1) Source designation; (2)–(3) Aperture radii in '' .

The data were filtered and spectra were extracted as described in § 2.3.1 & § 2.3.3. Also, ‘FLAG=0’ was used for the pn data to exclude all events at the edge of the CCD and events from bad pixels, while a less conservative screening criterion for the MOS data was employed by using the flag expression #XMMEA_EM to exclude hot pixels and events outside of the FOV. Model spectra were fitted to the data using XSPEC (v.11.3.0). The pn, MOS-1 and MOS-2 spectra for each object were fitted simultaneously, but constant multiplicative factors were included in each model to allow for calibration differences between the cameras. This value was frozen at unity for the pn data and allowed to vary for the MOS detectors, with the values typically agreeing within 20%. Quoted fluxes are an average of the three measurements.

Spectra were initially fitted in the 0.3–10 keV band. However, in several cases, the data below 0.5 keV did not agree with any of the models that were tried, leaving large residuals (particularly with respect to the pn data) to the best fits. The datasets with this problem (NGC 55 ULX, NGC 1313 X-1 & X-2 and NGC 3628 X-1) were all obtained in the years 2000–2001 (in fact M33 X-8 is the only observation

from this epoch without these fitting residuals). This would appear to be a problem with the calibration at early mission times; however the pn calibration at least has remained remarkably static in orbit (EPIC team, priv. comm.). As this variation could not be explained, these data were conservatively excluded in all EPIC cameras, such that spectral fitting was restricted to the 0.5–10 keV range in these four cases. Also, in the case of Ho II X-1 there is a possible pn calibration feature that is particularly prominent at low energies (Goad et al., 2006), therefore this work followed the method of these authors and excluded the pn data below 0.7 keV to account for this, whilst retaining MOS data down to 0.3 keV.

The X-ray spectra were modified for absorption following Balucinska-Church & McCammon (1992), assuming the solar abundances of Anders & Grevesse (1989) (*i.e.*, the `wabs` component in `XSPEC`). Two absorption components were used, one of which was fixed for each source to represent the appropriate foreground column density through our Galaxy (Dickey & Lockman 1990 – see Table 6.1), and the second component was left free to fit the data to represent additional absorption within the host galaxy and/or intrinsic to the ULX. The errors quoted in this work are at the 90% confidence level for one interesting parameter. Throughout this analysis, statistically acceptable fits are distinguished from unacceptable fits using a fixed criterion of $P_{\text{rej}} < 95\%$, where P_{rej} is the probability of rejection derived directly from the χ^2 statistic for the spectral fit.

6.4 Spectral properties

6.4.1 Simple models

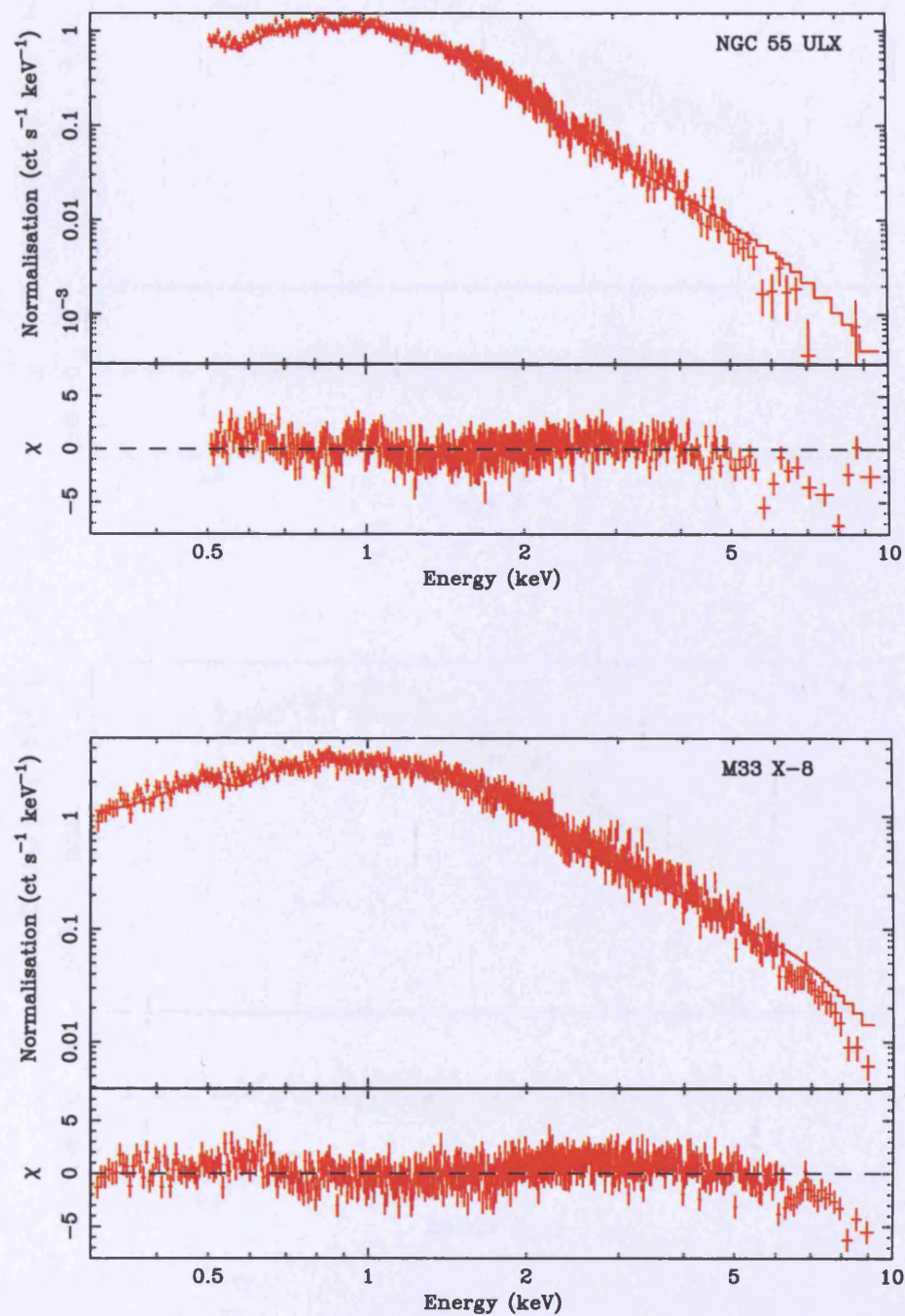
The X-ray spectra appeared relatively smooth and featureless in each case, hence simple continuum models were initially fitted to the data. The two models most often used in the past as single-component descriptions of ULX spectra were used, namely a power-law continuum model and the canonical MCD model. The details of these fits are given in Table 6.4 and the quality of the X-ray spectra is illustrated using the power-law fits in Figure 6.1. Due to the excellent spectral quality, the power-law model could be rejected for 8 out of the 13 cases at $> 95\%$ confidence. Interestingly, the five ULXs for which a power-law is an adequate description of the data (NGC 1313 X-1 & X-2, M83 ULX, NGC 4861 ULX, NGC 5204 X-1) include the three poorest quality datasets. Even more notably, the MCD model does not provide an acceptable fit to any of the spectra.

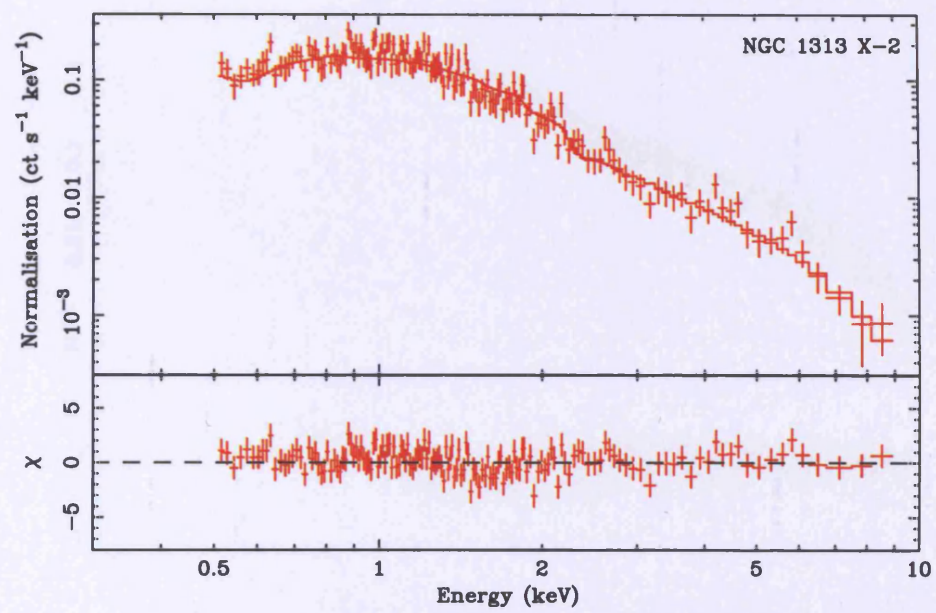
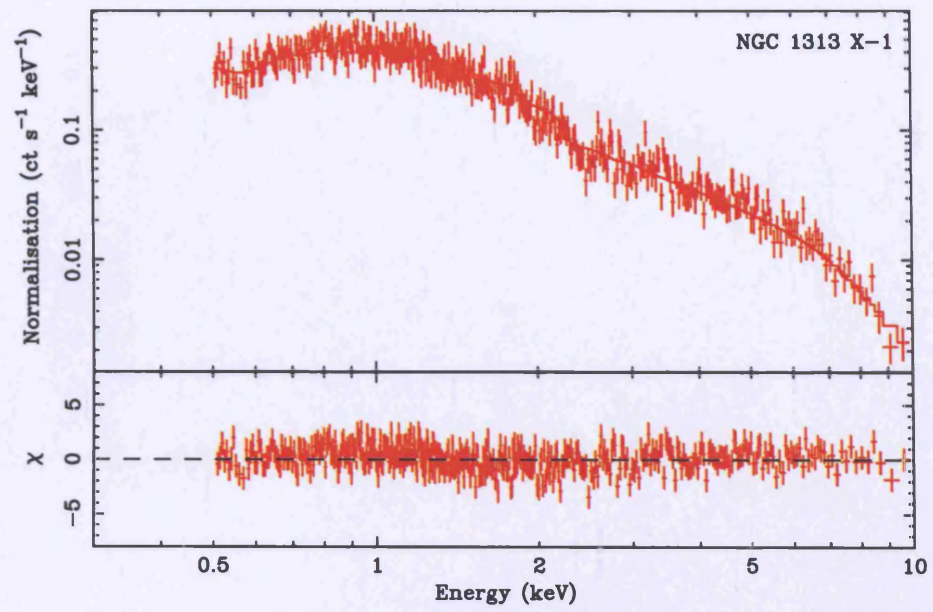
Table 6.4: Single component spectral fits

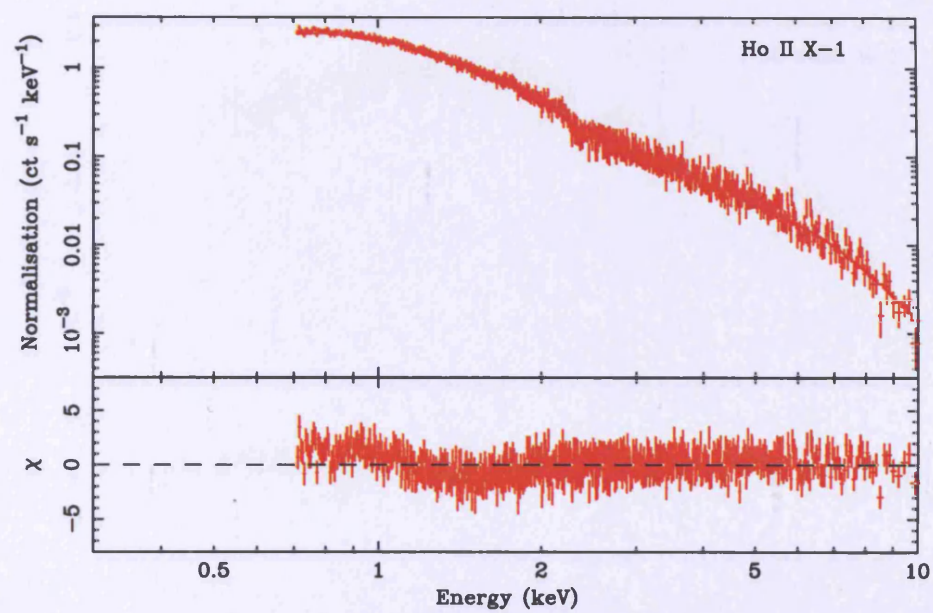
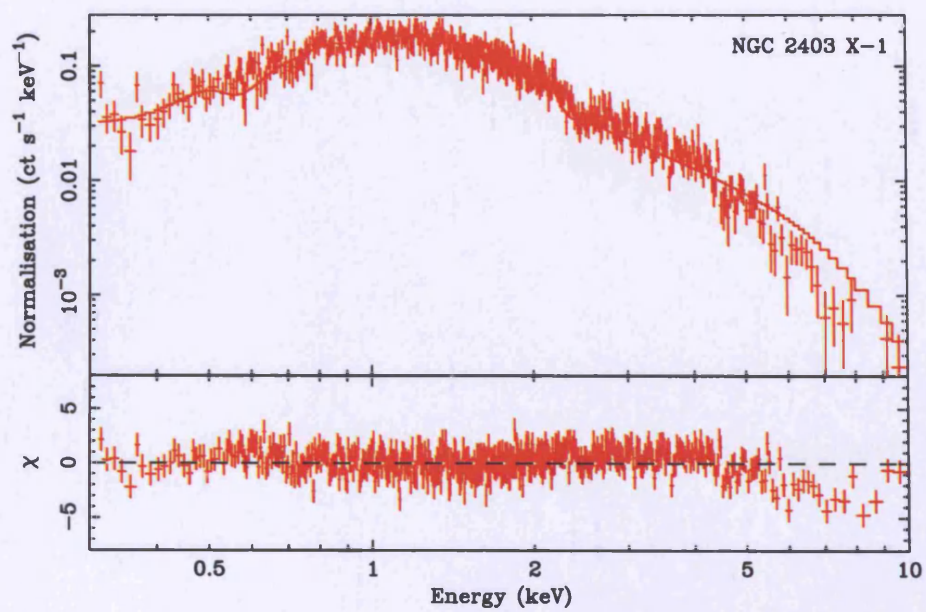
wa*wa*po	N_H^a	Γ^b	A_P^c	χ^2/dof
NGC 55 ULX	3.50 ± 0.08	3.38 ± 0.03	3.09 ± 0.08	1128.9/830
M33 X-8	1.94 ± 0.06	2.28 ± 0.02	6.02 ± 0.12	1790.1/1115
NGC 1313 X-1	1.05 ± 0.11	$1.84^{+0.04}_{-0.03}$	0.55 ± 0.02	723.0/675
NGC 1313 X-2	1.68 ± 0.02	$2.27^{+0.08}_{-0.07}$	0.31 ± 0.02	261.7/257
NGC 2403 X-1	3.78 ± 0.13	2.40 ± 0.03	0.65 ± 0.02	1130.2/851
Ho II X-1	1.53 ± 0.04	2.76 ± 0.02	3.23 ± 0.04	1690.6/1314
M81 X-9	1.57 ± 0.08	1.89 ± 0.03	$1.92^{+0.06}_{-0.05}$	938.1/864
NGC 3628 X-1	2.77 ± 0.03	1.45 ± 0.05	0.10 ± 0.01	459.8/406
NGC 4395 X-1	$2.73^{+0.17}_{-0.16}$	$4.37^{+0.12}_{-0.11}$	0.09 ± 0.01	540.8/368
NGC 4559 X-1	1.15 ± 0.08	$2.38^{+0.05}_{-0.04}$	0.27 ± 0.01	752/599
NGC 4861 ULX	$1.24^{+0.31}_{-0.30}$	$2.49^{+0.17}_{-0.15}$	0.09 ± 0.01	94.0/74
NGC 5204 X-1	0.50 ± 0.08	$2.10^{+0.05}_{-0.04}$	$0.39^{+0.02}_{-0.01}$	572.3/529
M83 ULX	$1.22^{+0.21}_{-0.20}$	$2.51^{+0.11}_{-0.10}$	0.14 ± 0.01	199.2/207
wa*wa*diskbb	N_H^b	kT_{in}^d	A_{MCD}^e	χ^2/dof
NGC 55 ULX	0.37	0.60	1.62	1796.3/830
M33 X-8	0	1.08 ± 0.01	$0.62^{+0.02}_{-0.01}$	1538.7/1115
NGC 1313 X-1	0	1.32	0.04	1409.6/675
NGC 1313 X-2	< 0.02	0.93 ± 0.04	0.05 ± 0.01	443.3/257
NGC 2403 X-1	$1.20^{+0.08}_{-0.07}$	1.04 ± 0.02	0.06 ± 0.01	923.7/851
Ho II X-1	0	0.59	2.74	8646.7/131
M81 X-9	0	1.42	0.09	1758.6/864
NGC 3628 X-1	1.04 ± 0.02	$2.27^{+0.13}_{-0.12}$	$(1.38^{+0.28}_{-0.24}) \times 10^{-3}$	466.6/406
NGC 4395 X-1	0.13 ± 0.09	0.32 ± 0.01	$0.81^{+0.16}_{-0.13}$	693.0/368
NGC 4559 X-1	0	0.69	0.15	1651.4/599
NGC 4861 ULX	0	0.64	0.06	166.9/74
NGC 5204 X-1	0	0.66	0.33	1650.1/529
M83 ULX	< 0.01	0.64 ± 0.03	0.11 ± 0.02	310.7/207

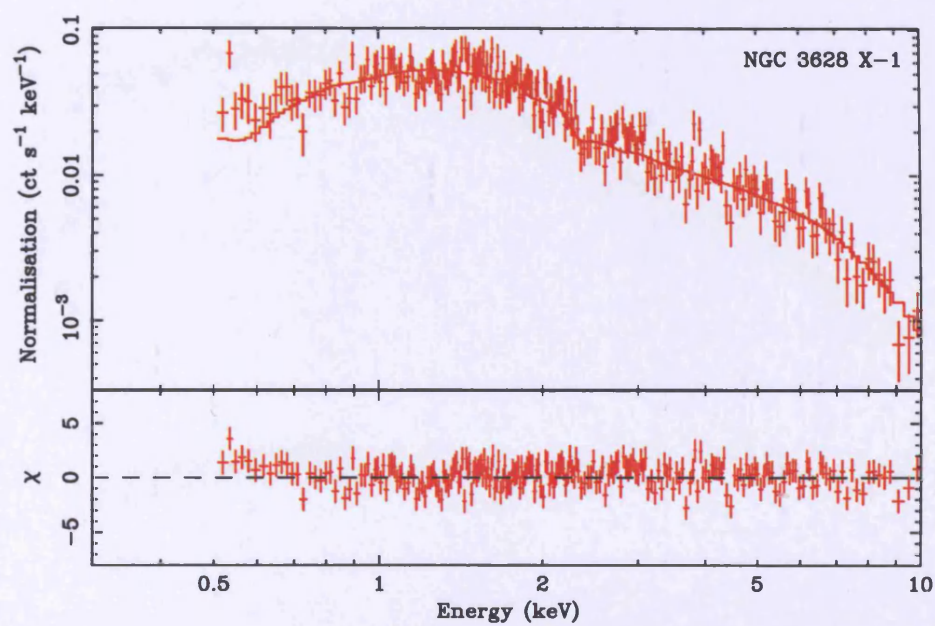
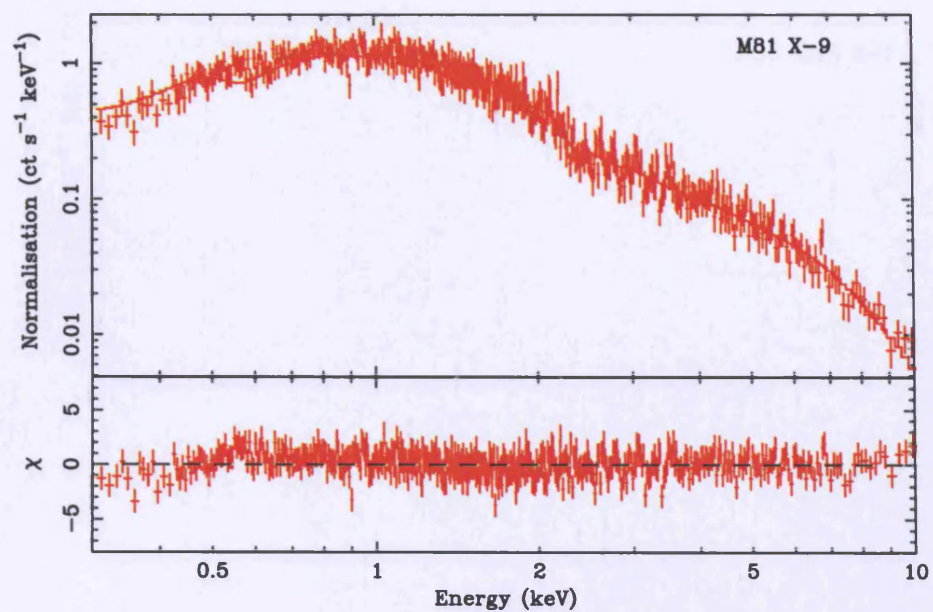
NOTES: ^a External absorption column (10^{21} atoms cm^{-2}), ^b po photon index, ^c po normalisation (10^{-3} photon $\text{cm}^{-2} \text{s}^{-1} \text{keV}^{-1}$ at 1 keV), ^d Inner disc temperature (keV), ^e diskbb normalisation ($((R_{\text{in}}/\text{km})/(D/10 \text{ kpc}))^2 \cos \Theta$; where R_{in} —inner disc radius, D —distance to source, Θ —inclination angle of the disc). Errors are not shown for fits where $\chi^2_{\nu} > 2$. Statistically acceptable fits are highlighted in bold.

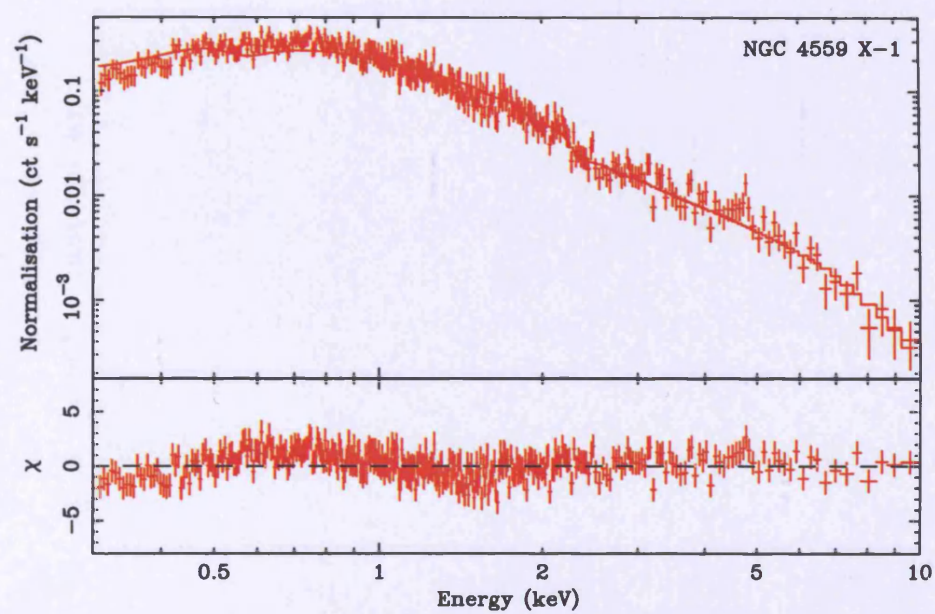
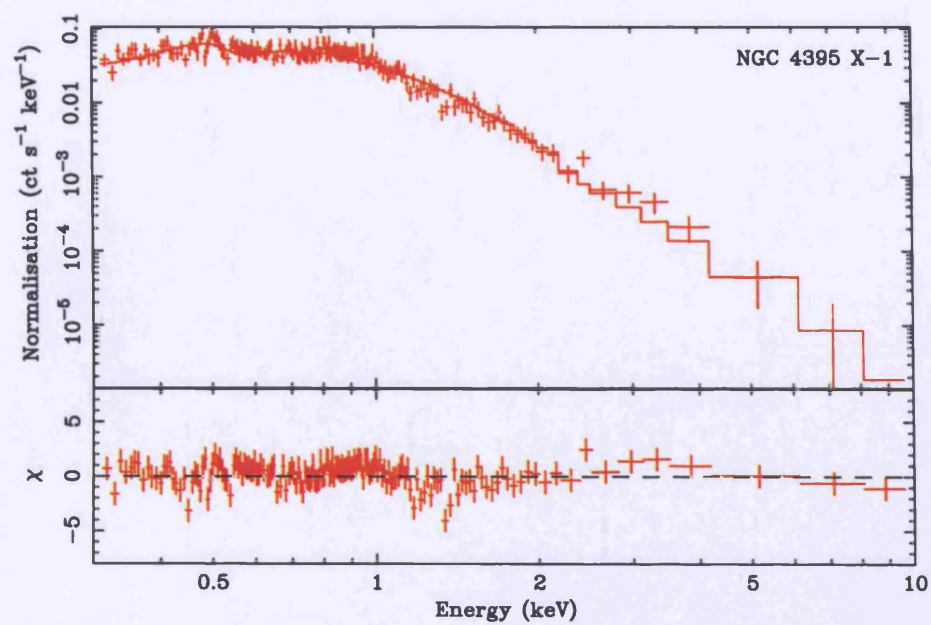
Figure 6.1: EPIC pn count rate spectra and $\Delta\chi$ residuals for a simple power-law continuum model fit for each of the ULXs in the sample.

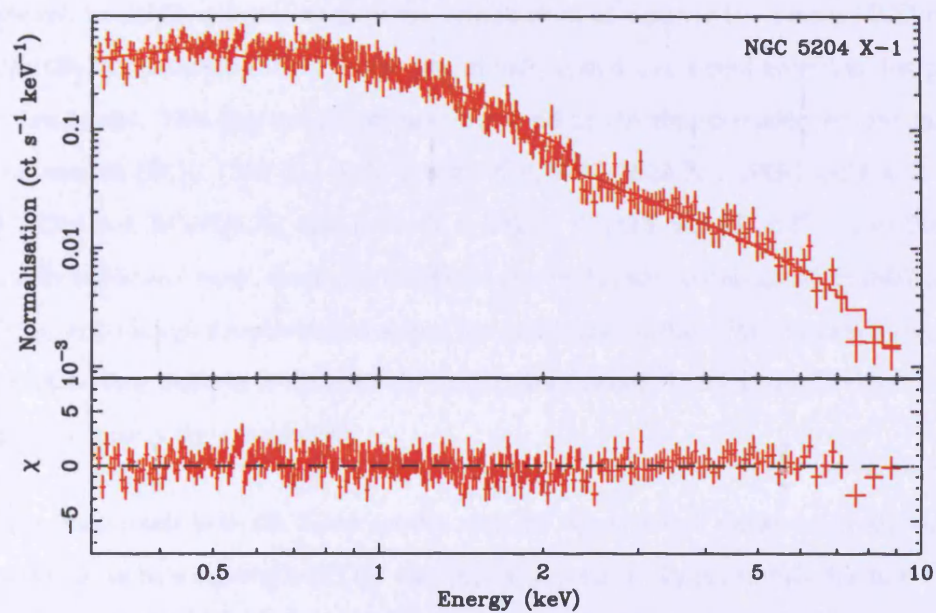
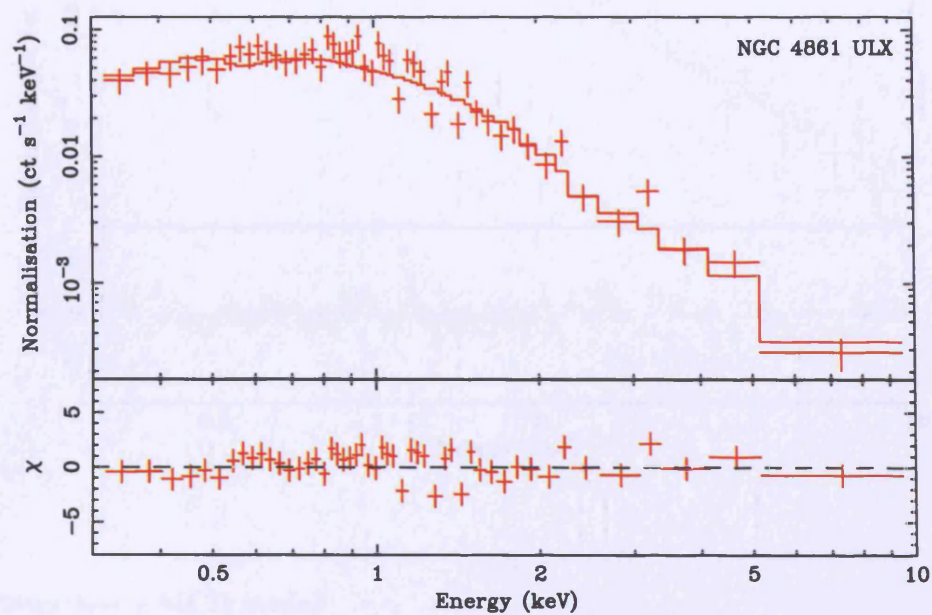


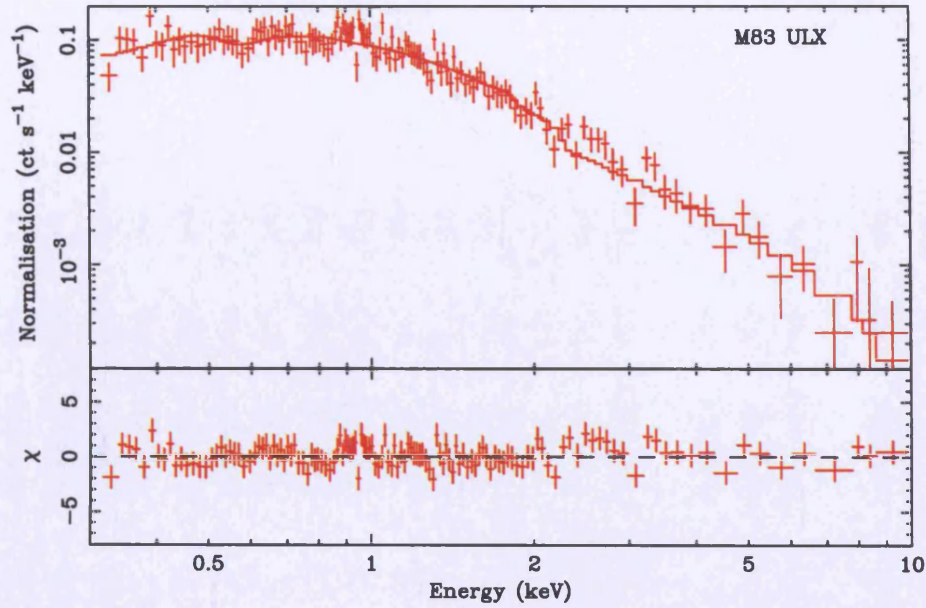












6.4.2 Power-law + MCD model

As simple spectral models were inadequate, the data were fitted with the two component model generally employed for BHB systems, namely the combination of a power-law plus a MCD component. More specifically, the standard IMBH model was initially tested, *i.e.*, a cool accretion disc plus power-law continuum model. This spectral description improved on the simple models by providing acceptable fits to 8 sources (NGC 1313 X-1 & X-2, M81 X-9, NGC 3628 X-1, NGC 4559 X-1, NGC 4861 ULX, NGC 5204 X-1, M83 ULX), with $0.1 \text{ keV} < kT_{\text{in}} < 0.3 \text{ keV}$ and $1.6 < \Gamma < 2.5$ (Table 6.5). As with previously published work, these disc temperatures are broadly consistent with IMBHs of around $\sim 1000 M_{\odot}$ in size, though the power-law slopes are puzzlingly shallow for what are supposed HS (or VH) state sources (see Roberts et al. 2005 for further discussion). In all cases the 0.3–10 keV flux is dominated by the power-law component.

Attempts were then made to fit the X-ray spectra with the non-standard model *i.e.*, with the power-law component dominant at soft energies. This also provided statistically-acceptable fits to 8 ULXs (M33 X-8, NGC 1313 X-2, NGC 2403 X-1, NGC 3628 X-1, NGC 4559 X-1, NGC 4861 ULX, NGC 5204 X-1, M83 ULX), with disc temperatures of $1.2 \text{ keV} < kT_{\text{in}} < 2.2 \text{ keV}$ (excluding M 83 for which the temperature is unconstrained below $\sim 4 \text{ keV}$) and $2.5 < \Gamma < 4.5$ (except NGC 3628 X-1, for which Γ is unconstrained below ~ 1.2) (Table 6.5).

Table 6.5: Two component spectral fits

$wa*wa^*(po+diskbb)^1$	N_H^a	Γ^b	A_P^c	kT_{in}^d	$A_{MCD}^e(\times 10^2)$	χ^2/dof	f_{XPO}^f	f_{XMCD}^g
NGC 55 ULX	$3.50^{+0.42}_{-0.09}$	3.38 ± 0.03	$3.09^{+0.07}_{-0.08}$	< 0.16	$< 9.71 \times 10^4$	1128.8/828	99.9	0.1
M33 X-8	$4.43^{+0.25}_{-0.06}$	$2.52^{+0.02}_{-0.01}$	$8.51^{+0.20}_{-0.12}$	0.09 ± 0.002	3312^{+1694}_{-1055}	1527.0/1113	92.7	7.3
NGC 1313 X-1	$2.37^{+0.52}_{-0.48}$	1.77 ± 0.06	0.51 ± 0.04	0.19 ± 0.02	$0.81^{+1.39}_{-0.55}$	664.5/673	90.9	9.1
NGC 1313 X-2	$1.80^{+0.76}_{-0.42}$	$2.11^{+0.15}_{-0.17}$	$0.25^{+0.05}_{-0.06}$	$0.27^{+0.10}_{-0.09}$	$0.03^{+0.27}_{-0.02}$	255.0/255	91.7	8.3
NGC 2403 X-1	$7.18^{+0.04}_{-0.05}$	$2.68^{+0.02}_{-0.05}$	0.98 ± 0.03	$0.09^{+0.002}_{-0.004}$	527^{+644}_{-224}	1028.5/849	93.6	6.4
Ho II X-1	$1.74^{+0.10}_{-0.09}$	2.63 ± 0.03	2.81 ± 0.09	0.19 ± 0.01	$211^{+1.23}_{-0.78}$	1453.1/1312	89.7	10.3
M81 X-9	$2.17^{+0.43}_{-0.23}$	$1.81^{+0.05}_{-0.04}$	$1.74^{+0.14}_{-0.10}$	0.20 ± 0.03	$1.05^{+2.78}_{-0.61}$	877.2/862	94.0	6.0
NGC 3628 X-1	$4.26^{+0.77}_{-0.70}$	$1.58^{+0.07}_{-0.04}$	0.12 ± 0.01	0.08 ± 0.01	127^{+402}_{-96}	424.6/404	98.1	1.9
NGC 4395 X-1	$1.96^{+0.26}_{-0.40}$	$3.72^{+0.18}_{-0.27}$	0.05 ± 0.01	0.18 ± 0.02	$0.11^{+0.09}_{-0.05}$	492.2/366	71.6	28.4
NGC 4559 X-1	$2.33^{+0.70}_{-0.20}$	$2.23^{+0.07}_{-0.05}$	$0.24^{+0.03}_{-0.01}$	0.14 ± 0.01	$2.74^{+5.64}_{-0.96}$	597.2/597	81.5	18.5
NGC 4861 ULX	$1.75^{+1.13}_{-0.69}$	$2.24^{+0.23}_{-0.24}$	0.07 ± 0.02	$0.18^{+0.08}_{-0.04}$	$0.13^{+0.03}_{-0.12}$	84.4/72	82.4	17.6
NGC 5204 X-1	$0.68^{+0.22}_{-0.18}$	$1.91^{+0.07}_{-0.08}$	0.31 ± 0.03	$0.22^{+0.04}_{-0.03}$	$0.12^{+0.21}_{-0.07}$	529.9/527	88.2	11.8
M83 ULX	$1.28^{+0.54}_{-0.37}$	$2.47^{+0.14}_{-0.17}$	$0.14^{+0.02}_{-0.03}$	$[\sim 0.2]^k$	< 0.98	198.6/205	96.6	3.4
$wa*wa^*(po+diskbb)^2$	N_H^a	Γ^b	A_P^c	kT_{in}^d	$A_{MCD}^e(\times 10^{-3})$	χ^2/dof	f_{XPO}^f	f_{XMCD}^g
NGC 55 ULX	$4.32^{+0.24}_{-0.34}$	$4.31^{+0.19}_{-0.27}$	$3.29^{+0.21}_{-0.27}$	0.86 ± 0.03	$170.47^{+35.51}_{-40.63}$	957.6/828	67.6	32.4
M33 X-8	$1.42^{+0.21}_{-0.18}$	$2.49^{+0.18}_{-0.14}$	$3.15^{+0.31}_{-0.32}$	1.18 ± 0.06	$264.55^{+53.06}_{-43.13}$	1187.0/1113	48.8	51.2
NGC 1313 X-1	—	—	—	—	—	—	—	—
NGC 1313 X-2	$2.52^{+0.97}_{-0.62}$	$2.93^{+0.75}_{-0.47}$	$0.36^{+0.09}_{-0.05}$	$2.65^{+1.06}_{-0.78}$	< 2.19	255.9/255	64.4	35.6
NGC 2403 X-1	$4.77^{+1.01}_{-0.99}$	$4.05^{+0.70}_{-0.75}$	$0.55^{+0.20}_{-0.15}$	$1.16^{+0.04}_{-0.05}$	$36.93^{+10.14}_{-7.95}$	847.7/849	27.3	72.7
Ho II X-1	$2.34^{+0.13}_{-0.12}$	$3.45^{+0.11}_{-0.10}$	$3.78^{+0.11}_{-0.10}$	$1.79^{+0.10}_{-0.09}$	$10.33^{+3.33}_{-2.70}$	1508.8/1312	74.5	25.5
M81 X-9	—	—	—	—	—	—	—	—
NGC 3628 X-1	$1.43^{+0.47}_{-0.26}$	< 1.18	< 0.04	1.40 ± 0.21	$4.68^{+1.65}_{-2.31}$	439.5/404	53.4	46.6
NGC 4395 X-1	—	—	—	—	—	—	—	—
NGC 4559 X-1	$3.35^{+0.46}_{-0.41}$	$4.47^{+0.37}_{-0.34}$	$0.41^{+0.05}_{-0.04}$	$1.61^{+0.13}_{-0.12}$	$4.04^{+1.64}_{-1.59}$	637.0/597	47.3	52.7
NGC 4861 ULX	$3.33^{+1.75}_{-1.30}$	$4.36^{+1.34}_{-1.08}$	$0.13^{+0.08}_{-0.04}$	$1.60^{+0.60}_{-0.32}$	$1.09^{+1.34}_{-0.87}$	85.6/72	51.9	48.1

continued over page

wa*wa* (po+diskbb) ²	N_H^a	Γ^b	A_P^c	kT_{in}^d	$A_{MCD}^e (\times 10^{-3})$	χ^2/dof	f_{XPO}^f	f_{XMCD}^g
NGC 5204 X-1	$1.64^{+0.37}_{-0.33}$	$3.33^{+0.34}_{-0.32}$	$0.44^{+0.05}_{-0.03}$	$2.23^{+0.32}_{-0.26}$	$1.96^{+1.17}_{-0.87}$	525.5/527	50.3	49.7
M83 ULX	$1.37^{+0.92}_{-0.45}$	$2.75^{+0.94}_{-0.45}$	0.14 ± 0.02	< 4.03	< 4.53	198.1/205	82.9	17.1
wa*wa* (bb+diskbb)	N_H^a	kT^h	A_B^i	kT_{in}^d	$A_{MCD}^e (\times 10^{-3})$	χ^2/dof	f_{XBB}^j	f_{XMCD}^g
NGC 55 ULX	$1.43^{+0.16}_{-0.17}$	0.20 ± 0.01	$3.35^{+0.33}_{-0.31}$	0.81 ± 0.01	343^{+53}_{-47}	884.1/828	36.4	63.6
M33 X-8	$0.16^{+0.10}_{-0.09}$	0.27 ± 0.02	$3.09^{+0.31}_{-0.30}$	$1.26^{+0.02}_{-0.03}$	303^{+37}_{-16}	1216.7/1113	11.7	88.3
NGC 1313 X-1	$0.60^{+0.14}_{-0.25}$	$0.25^{+0.02}_{-0.01}$	$0.86^{+0.11}_{-0.10}$	2.20 ± 0.10	$5.07^{+0.31}_{-0.16}$	666.5/673	17.7	82.3
NGC 1313 X-2	< 0.54	$0.27^{+0.04}_{-0.02}$	$0.41^{+0.07}_{-0.06}$	$1.71^{+0.15}_{-0.16}$	$4.02^{+0.49}_{-1.36}$	257.1/255	27.7	72.3
NGC 2403 X-1	2.02 ± 0.30	$0.21^{+0.03}_{-0.02}$	$0.38^{+0.14}_{-0.09}$	$1.12^{+0.04}_{-0.03}$	46.63 ± 3.42	830.0/849	8.7	91.3
Ho II X-1	< 0.01	0.23 ± 0.002	$4.37^{+0.06}_{-0.07}$	1.28 ± 0.02	$77.69^{+6.44}_{-6.05}$	1677.9/1312	41.4	58.6
M81 X-9	$0.64^{+0.14}_{-0.10}$	0.27 ± 0.01	2.56 ± 0.16	$2.21^{+0.12}_{-0.11}$	$15.93^{+3.34}_{-2.83}$	922.3/862	17.5	82.5
NGC 3628 X-1	$0.71^{+0.28}_{-0.24}$	$0.60^{+0.05}_{-0.06}$	$0.16^{+0.04}_{-0.06}$	$4.32^{+0.74}_{-0.87}$	$0.13^{+0.17}_{-0.07}$	429.4/404	17.7	82.3
NGC 4395 X-1	$0.34^{+0.19}_{-0.17}$	0.17 ± 0.01	0.15 ± 0.02	0.61 ± 0.05	$17.66^{+9.56}_{-6.26}$	464.5/366	65.5	34.5
NGC 4559 X-1	$0.80^{+0.17}_{-0.11}$	0.17 ± 0.01	$0.61^{+0.11}_{-0.08}$	$1.33^{+0.07}_{-0.06}$	$9.94^{+2.29}_{-1.82}$	604.9/597	30.6	69.4
NGC 4861 ULX	$0.46^{+0.05}_{-0.03}$	0.20 ± 0.03	$0.15^{+0.09}_{-0.04}$	$1.37^{+0.20}_{-0.08}$	$2.38^{+1.89}_{-1.13}$	77.7/72	34.1	65.9
NGC 5204 X-1	< 0.03	0.20 ± 0.01	0.67 ± 0.03	$1.69^{+0.10}_{-0.09}$	$7.37^{+1.69}_{-1.40}$	527.8/527	28.0	72.0
M83 ULX	< 0.37	$0.21^{+0.02}_{-0.03}$	$0.16^{+0.05}_{-0.02}$	$1.10^{+0.13}_{-0.05}$	$9.28^{+2.76}_{-3.55}$	193.2/205	27.8	72.2

NOTES: Model fitted with a cool¹ or hot² diskbb component. ^a External absorption column (10^{21} atoms cm^{-2}), ^b po photon index, ^c po normalisation (10^{-3} photon $\text{cm}^{-2} \text{s}^{-1} \text{keV}^{-1}$ at 1 keV), ^d inner disc temperature (keV), ^e diskbb normalisation as before ($((R_{in}/\text{km})/(D/10 \text{ kpc}))^2 \cos \Theta$), ^f fraction of the total flux (0.3–10 keV) in the po component, ^g fraction of the total flux (0.3–10 keV) in the diskbb component, ^h blackbody temperature (keV), ⁱ blackbody normalisation, ($10^{-5} L_{39}/D_{10}^2$; where L_{39} –source luminosity in $10^{39} \text{ erg s}^{-1}$, D_{10} –source distance in 10 kpc). ^j Fraction of the total flux (0.3–10 keV) in the bb component. ^k Unconstrained at the 90% confidence level. In the three cases in the central portion of the table where no fit is shown, the χ^2 -minimisation always found the minimum describing the IMBH model. Statistically acceptable fits are highlighted in bold. (NB. In cases where the spectral fitting was not performed over the 0.3–10 keV energy range, a dummy response matrix was created in XSPEC (see §4.5), to determine the fraction of the total flux in each spectral component over 0.3–10 keV, consistent with the other datasets).

The balance in 0.3–10 keV flux between the two components was much more varied for this model, though most sources showed a relatively equitable balance (ratios of no more than 3:1 in either direction, and $\sim 1:1$ in five cases).

In total, the power-law + MCD combination could not be rejected at $> 95\%$ confidence for 10/13 sources in the sample. Two of these sources were unambiguously best fitted with the IMBH model (NGC 1313 X-1, M81 X-9) while two more were best fitted by the non-standard model (M33 X-8, NGC 2403 X-1). Statistically acceptable fits existed *for both models* for the remaining six sources. Three sources in this sample (NGC 55 ULX, Ho II X-1 and NGC 4395) rejected both models at $> 95\%$ confidence, although a comparison of the fits show that the spectrum of the NGC 55 ULX appeared to fit much better to the non-standard model, whilst Ho II X-1 and NGC 4395 X-1 much preferred the IMBH model.

This sample of high quality ULX datasets demonstrates spectral ambiguity for six sources (NGC 1313 X-2, NGC 3628 X-1, NGC 4559 X-1, NGC 4861 ULX, NGC 5204 X-1, M83 ULX). As Roberts et al. (2005) suggest, a key discriminator between the models could be a test for spectral curvature at high energies (> 2 keV). Curvature is not expected in the IMBH model where the power-law component is dominant above 2 keV, whereas sources best-fitted by the non-standard model have the curved MCD component dominant at these hard X-ray energies. Therefore attempts were then made to fit the high energy (2–10 keV) ULX spectra with a broken power-law model (*i.e.*, the `bknpo` model in XSPEC). For comparison, the 2–10 keV ULX spectra were also fitted with a single power-law component, as shown in Table 6.6. Absorption was not included in the fitting in either case, as single- and two-component fits generally limit absorption to $\lesssim 4 \times 10^{21}$ atoms cm^{-2} , which should not strongly affect the data above 2 keV. When absorption is included in these fits, far higher columns are measured in several cases, which is physically unrealistic (and may be a result of the absorption compensating for intrinsic curvature). The results of the broken power-law spectral fits, together with the statistical probability of the fit improvement over the single power-law fits (using the F-test) are shown in Table 6.7.

Table 6.6: Power-law spectral fits (2–10 keV)

wa*wa*po	Γ^a	A_P^b	χ^2/dof
NGC 55 ULX	$3.58^{+0.06}_{-0.07}$	3.57 ± 0.25	459.3/326
M33 X-8	2.59 ± 0.04	$8.90^{+0.41}_{-0.39}$	663.1/548
NGC 1313 X-1	$1.70^{+0.05}_{-0.07}$	$0.44^{+0.03}_{-0.04}$	263.7/259
NGC 1313 X-2	$2.19^{+0.12}_{-0.16}$	$0.27^{+0.04}_{-0.05}$	60.2/70
NGC 2403 X-1	$2.63^{+4.95}_{-0.07}$	$0.82^{+0.05}_{-0.06}$	467.3/340
Ho II X-1	2.61 ± 0.03	2.65 ± 0.10	805.7/824
M81 X-9	1.78 ± 0.05	1.59 ± 0.10	360.4/355
NGC 3628 X-1	$1.50^{+0.06}_{-0.08}$	0.10 ± 0.01	219.5/211
NGC 4395 X-1	$4.48^{+0.31}_{-0.45}$	0.12 ± 0.04	33.1/28
NGC 4559 X-1	$2.28^{+0.08}_{-0.10}$	$0.24^{+0.02}_{-0.03}$	171.3/155
NGC 4861 ULX	2.50 ± 0.38	$0.09^{+0.06}_{-0.04}$	12.3/8
NGC 5204 X-1	1.89 ± 0.09	$0.29^{+0.04}_{-0.03}$	160.8/133
M83 ULX	$2.67^{+0.21}_{-0.28}$	0.17 ± 0.05	45.5/39

NOTES: ^a po photon index, ^b po normalisation (10^{-3} photon $\text{cm}^{-2} \text{s}^{-1} \text{keV}^{-1}$ at 1 keV). Statistically acceptable fits are highlighted in bold.

To demonstrate the validity of this method, the two sources with unambiguous non-standard fits (M33 X-8 and NGC 2403 X-1), plus NGC 55 ULX which clearly prefers this model, show unacceptable power-law fits that are made acceptable by the inclusion of a break. In these cases the improvement is highly statistically significant ($> 9\sigma$ improvement over a simple power-law fit according to the F-test). However, these were the clearest-cut cases. Of the ambiguous spectra, three out of six showed evidence for curvature. This was marginal in the case of M83 ULX ($> 2\sigma$ level), but more significant for NGC 4559 X-1 and NGC 5204 X-1 ($> 3\sigma$), with the latter case having an unacceptable power-law fit. Most interestingly, though, one of the IMBH-fit sources (NGC 1313 X-1) shows evidence for curvature ($> 3\sigma$ improvement), whilst Ho II X-1 also shows a significant break ($> 4\sigma$ improvement). In total 8/13 sources show at least marginal evidence for curvature at the high energy end of their *XMM-Newton* spectrum. This is strongly suggestive that the majority of sources are *not* dominated by a power-law continuum at these energies, such as one might expect to see if the X-ray emission arises

Table 6.7: Broken power-law spectral fits (2–10 keV)

wa*wa*bknpo	Γ_1^a	E_{break}^b	Γ_2^c	A_{BP}^d	χ^2/dof	$\Delta\chi^{2e}$	1-P(F-test) ^f
NGC 55 ULX	3.08 ± 0.11	$3.90^{+0.20}_{-0.18}$	$5.34^{+0.53}_{-0.41}$	$2.32^{+0.26}_{-0.24}$	341.0/324	118.3	>99.9
M33 X-8	2.17 ± 0.09	$3.94^{+0.26}_{-0.21}$	$3.32^{+0.19}_{-0.15}$	$6.07^{+0.56}_{-0.52}$	516.1/546	147.0	>99.9
NGC 1313 X-1	$1.55^{+0.10}_{-0.09}$	$4.93^{+1.37}_{-0.53}$	$2.16^{+0.66}_{-0.25}$	$0.37^{+0.05}_{-0.04}$	250.9/257	12.9	99.8
NGC 1313 X-2	–	–	–	–	–	–	–
NGC 2403 X-1	$2.07^{+0.10}_{-0.11}$	$4.00^{+0.17}_{-0.15}$	$4.05^{+0.33}_{-0.28}$	0.49 ± 0.05	325.4/338	141.9	>99.9
Ho II X-1	2.55 ± 0.04	$5.31^{+0.43}_{-0.56}$	$3.08^{+0.25}_{-0.22}$	$2.50^{+0.11}_{-0.12}$	786.1/822	19.6	>99.9
M81 X-9	–	–	–	–	–	–	–
NGC 3628 X-1	–	–	–	–	–	–	–
NGC 4395 X-1	$2.77^{+1.31}_{-2.58}$	$2.45^{+0.93}_{-0.23}$	$4.92^{+0.77}_{-0.60}$	<0.09	30.0/26	3.1	72.1
NGC 4559 X-1	$2.07^{+0.12}_{-0.14}$	$4.77^{+0.65}_{-0.41}$	$3.14^{+0.62}_{-0.43}$	0.20 ± 0.03	157.7/153	13.6	99.8
NGC 4861 ULX	–	–	–	–	–	–	–
NGC 5204 X-1	$1.65^{+0.10}_{-0.15}$	$4.92^{+0.46}_{-0.41}$	$2.99^{+0.65}_{-0.45}$	$0.23^{+0.03}_{-0.04}$	138.3/131	22.5	>99.9
M83 ULX	<1.79	$2.41^{+0.31}_{-0.15}$	$3.11^{+0.46}_{-0.40}$	< 0.08	37.5/37	8.0	97.2

NOTES: ^a Photon index below the break energy, ^b location of the break point (keV), ^c photon index above the break energy, ^d bknpo normalisation (10^{-3} photon $\text{cm}^{-2} \text{s}^{-1} \text{keV}^{-1}$ at 1 keV), ^e χ^2 improvement over a single po fit, for two extra degrees of freedom, ^f statistical probability (%) of the fit improvement over a single po fit. Results are only shown for constrained fits that showed the requisite behaviour, *i.e.*, $\Gamma_2 > \Gamma_1$ and E_{break} constrained in the 2–10 keV range. Statistically acceptable fits are highlighted in bold.

from the optically thin, hot corona assumed in the IMBH model.

6.4.3 Dual thermal models

The above analysis shows there is (at least marginal) evidence of curvature above 2 keV in the majority of these sources, arguing that a power-law continuum is not an adequate description of this emission, while the hotter accretion disc present in the alternate model may be more appropriate. The situation below 2 keV is less clear cut. Though the alternate model uses a power-law continuum to describe the soft component, this is modified to appear curved by absorption. As this power-law emission is difficult to understand physically, a new variation of the alternate model was explored in which the soft component is also intrinsically curved (*i.e.*, it does not rely solely on absorption to produce the observed

curvature). In this model a cool blackbody (bbody) continuum was fitted to the soft component, and a MCD to the hard component. The physical motivation for the soft component comes from the suggestion that optically-thick outflowing winds from black-holes accreting at or above the Eddington limit could explain ultrasoft components in ULXs (King & Pounds, 2003). Such winds would appear as blackbody continua with temperatures of $\sim 0.1\text{--}0.3$ keV. Emission may then be observed from both the accretion disc and the wind given a favourable accretion disc geometry and viewing angle (A. King, priv. comm.)⁴.

The results of applying this new model to the data are shown in Table 6.5. It proved to be the most successful empirical description of the data, providing statistically acceptable fits to 10 out of the 13 sources, with $0.15 \text{ keV} < kT < 0.3 \text{ keV}$ and $0.8 \text{ keV} < kT_{\text{in}} < 2.2 \text{ keV}$ (excluding NGC 3628 X-1 for which the temperatures are much higher than shown in the other sources, *i.e.*, $kT \sim 0.6 \text{ keV}$ and $kT_{\text{in}} \sim 4.3 \text{ keV}$). This model provided the only acceptable empirical fit to the ULX in NGC 55, and all six ambiguous sources are adequately described by this model. Curiously, this is also true for both IMBH sources (though it does provide a notably worse fit than the IMBH model for M 81 X-9), and for one of the two non-standard model sources (NGC 2403 X-1). However, this model could not provide statistically acceptable fits to the other non-standard source (M 33 X-8) or to the final two ULXs (Ho II X-1 & NGC 4395 X-1, which also do not fit well with the power-law + MCD combination).

6.4.4 Why do Ho II X-1 and NGC 4395 X-1 not conform?

As shown in the previous sections, statistically acceptable fits for Ho II X-1 and NGC 4395 X-1 cannot be found using the chosen two-component models. Interestingly, these are two of the softest sources in the sample which means that their X-ray spectra are relatively dominated by < 1 keV emission, where it is most sensitive to absorption characteristics (*c.f.* Fig. 6.1). The analysis of an RGS spectrum of Ho II X-1 by Goad et al. (2006) revealed that its X-ray emission is subject to absorption by a medium with a sub-solar oxygen abundance. The mis-modelling of absorption, in combination with the exceptionally high signal to noise EPIC spectrum of Ho II X-1, may be responsible for the lack of a good fit to this

⁴Miller et al. (2004b) argue that cool, optically-thick outflows cannot explain the soft excess in ULXs as it would be impossible to form powerful enough shocks to produce a luminous non-thermal power-law continuum component in such systems. If the hard component is not a power-law, but instead originates directly from the accretion disc, then the requirement for shocks to be present is removed and their argument is circumvented.

ULX in the present analysis. However, even after correcting for the sub-solar abundance absorption acting on Ho II X-1, Goad et al. (2006) still did not find acceptable fits using the canonical power-law + MCD model. Instead, a statistically acceptable solution to the spectrum was found through using a more physical model, namely the `diskpn` + `comptt` combination. The utility of a similar model in describing the whole dataset of this Chapter is explored in the next section.

In the case of NGC 4395 X-1, a further inspection of the residuals to a simple power-law fit does suggest some structure, notably including a smooth ‘hump’ at ~ 1 keV, which is unlike the featureless X-ray spectra of the other ULXs. Therefore a fit including a `mekal` component (nominally representing the emission spectrum from hot, collisionally-ionised gas) was tried in addition to a power-law continuum to model this spectrum. The result is shown in Table 6.8. This model does indeed provide the best (and only statistically acceptable) fit to NGC 4395 X-1 with $\chi^2/\text{dof} = 397.5/366$. The model fit to the pn count rate spectrum is shown in Fig. 6.2, as well as the individual additive model components. From this figure, one can clearly see how the `mekal` component effectively models the emission hump at ~ 1 keV. Using a fixed solar-abundance absorber, the temperature of the `mekal` component was found to be ~ 0.75 keV, while the photon index is quite steep at $\Gamma \sim 4$.

Such `mekal` components have been reported in the spectral fits of a small number of ULXs. In fact, two other ULXs within this sample have been described thus in previous analyses, namely Ho II X-1 based on joint *ROSAT* - *ASCA* fits (Miyaji et al., 2001), and NGC 4559 X-1 based on one of two *Chandra* observations (Roberts et al., 2004). Whether such `mekal` + power-law models could be successfully applied to the current data for these sources has been investigated, and the results are shown in Table 6.8. This model is again rejected for Ho II X-1, though it is notable that the quality of the fit is very close to that of the best empirical description of the source (cool MCD plus power-law). In this case the temperature of the `mekal` is again relatively high at ~ 0.66 keV, but the contribution of this component is minimal ($\sim 3\%$ of the 0.3–10 keV flux)⁵. This is both far hotter and far fainter than the ~ 0.3 keV thermal plasma that composed 20%–30% of the 0.5–2 keV emission modelled by Miyaji et al. (2001). On the other hand, the temperature of the best-fitting `mekal` to NGC 4559 X-1 is lower, at ~ 0.25 keV, but it does constitute part of a statistically-acceptable fit to the data. This temperature is similar to the ~ 0.18 keV plasma inferred by Roberts et al. (2004).

⁵The contribution of the `mekal` is so small that its parameterisation is relatively insensitive to changes in metallicity. For example, setting a low abundance (as found by Miyaji et al. 2001) leaves the temperature of the `mekal` unchanged at ~ 0.66 keV.

Table 6.8: mekal + power-law spectral fits

wa*wa* (mekal+po)	N_H^a	kT^b	A_M^c	Γ^d	A_P^e	χ^2/dof	f_{XPO}^f	f_{XM}^g
Ho II X-1	1.42 ± 0.04	0.66 ± 0.03	$15.73^{+1.86}_{-1.52}$	2.67 ± 0.02	2.90 ± 0.05	1463.9/1312	96.7	3.3
NGC 4395 X-1	1.73 ± 0.13	0.75 ± 0.04	1.32 ± 0.15	$3.88^{+0.08}_{-0.09}$	$5.38^{+0.46}_{-0.14}$	397.5/366	84.4	15.6
NGC 4559 X-1	$1.26^{+0.10}_{-0.11}$	0.25 ± 0.02	$7.23^{+1.56}_{-1.54}$	$2.25^{+0.05}_{-0.04}$	0.24 ± 0.01	612.1/597	92.8	7.2

NOTES: ^a External absorption column (10^{21} atoms cm^{-2}), ^b plasma temperature (keV), ^c mekal normalisation ($((10^{-19}/(4\pi[D(1+z)]^2)) \int n_e n_H dV$, where D is the distance to the source (cm), n_e is the electron density (cm^{-3}), n_H is the hydrogen density (cm^{-3})), ^d po photon index, ^e po normalisation (10^{-5} photon $\text{cm}^{-2} \text{s}^{-1} \text{keV}^{-1}$ at 1 keV), ^f fraction of the total flux (0.3–10 keV) in the po component, ^g fraction of the total flux (0.3–10 keV) in the mekal component. Statistically acceptable fits are highlighted in bold. (NB For Ho II X-1 a dummy response matrix was created over the 0.3–10 keV energy range, to determine the fractional flux in each spectral component (see § 6.4.5)).

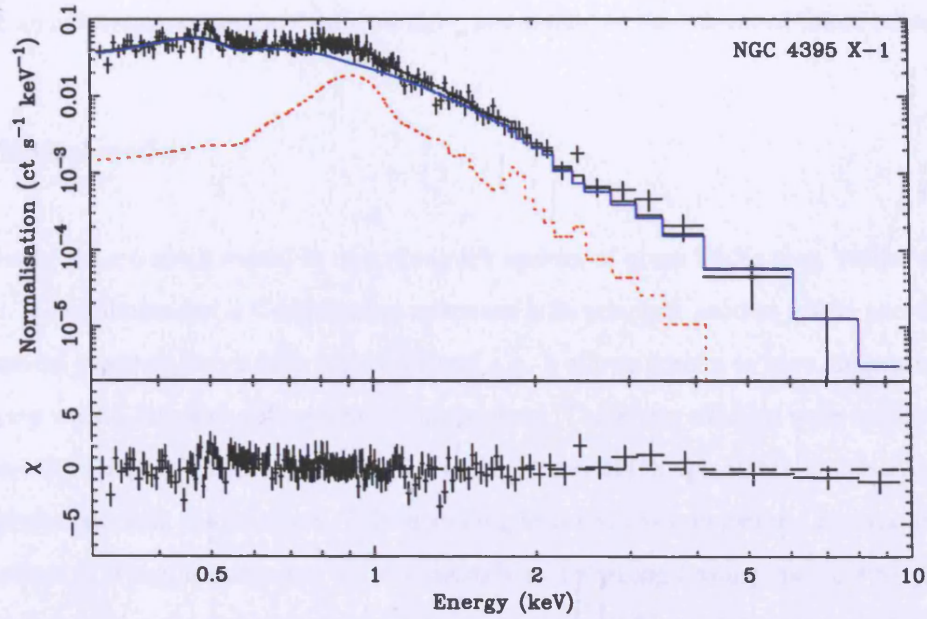


Figure 6.2: EPIC pn count rate spectra and $\Delta\chi$ residuals for the `mekal` + `po` model fit to NGC 4395 X-1. Also shown are the individual additive model components: power-law—blue solid line, `mekal`—red dotted line.

It seems that this latter result just adds to the spectral ambiguity already seen in the case of this ULX.

Finally, if NGC 4395 X-1 really does possess an X-ray line-emitting component, what is its physical origin? Several ideas have been put forward to explain such a component in the spectrum of a ULX. Miyaji et al. (2001) suggest the presence of a young SNR coincident with Ho II X-1, a theme expanded on by Feng & Kaaret (2005). Indeed, these authors independently confirm the presence of the `mekal` component in the spectrum of NGC 4395 X-1, and find two further ULXs with similar characteristics. Alternately, as Roberts et al. (2004) find the `mekal` component in NGC 4559 X-1 to switch on between two *Chandra* observations separated by ~ 5 months, they suggest that the plasma may originate in the collision of a jet or outflow from the ULX with a denser medium in the close proximity of the system. A second alternative is offered by Terashima & Wilson (2004), who suggest that emission lines in the spectrum of a ULX in M51 may originate from a photoionised stellar wind, similar to what is seen in some HMXBs in our own Galaxy. A final point of interest is that a broad ~ 1 keV feature, similar to that driving the `mekal` fit in NGC 4395 X-1, has recently been seen in the *XMM-Newton* spectrum of GRS 1915+105 by Martocchia et al. (2005) (although see their paper for caveats). One intriguing possibility is that this feature could originate in a disc wind. Clearly ULXs possessing `mekal` components in their

spectra are an interesting subject in their own right, and should be the subject of future attention.

6.4.5 Physical models

The success of the `comptt` model in describing the spectra of some ULXs (e.g. Miller et al. 2003, Goad et al. 2006) shows that a Comptonised spectrum is in principle another viable alternative. The `comptt` model however, is not fully self-consistent *e.g.*, it allows spectra to have temperatures higher than expected when Compton cooling is taken into account. Therefore, attempts were made to fit a more physical model to the ULX spectra, namely the `eqpair` model (Coppi, 1999), which allows thermal and non thermal electron distributions. This modelling assumes a purely thermal electron distribution, the temperature of which is computed self-consistently by balancing heating and cooling (the latter of which is mainly due to Compton cooling). A key parameter of this model is the ratio l_h/l_s , where l_h and l_s represent the compactness of the electrons and the compactness of the seed photon distribution respectively. This ratio depends on the geometry of the source as well as the internal mechanisms, and it provides the dominant influence on the spectral shape. The source geometry assumed is either spherical or a disc-corona (slab) geometry. Low energy (UV or X-ray) thermal photons from the accretion disc are assumed to be emitted uniformly inside the source region for the spherical models and enter from the base of the corona in the slab geometry. The seed photons are assumed to have an accretion disc spectrum as described with the `diskpn` model of Gierliński et al. (1999), with the inner edge of the disc at $6GM/c^2$. This model assumes a proper general relativistic potential and has a characteristic temperature kT_{bb} . To allow for a patchy Compton corona, a second `diskpn` component was added to the model, with the temperature coupled to that of the `eqpair` seed photons.

This model ultimately proved the best description of the ULX spectra in this sample, with statistically acceptable fits to 11/13 datasets, all with similar or improved goodness of fits compared to the best empirical modelling, for only one extra degree of freedom. Only Ho II X-1 and NGC 4395 X-1 were rejected at $> 95\%$ confidence (see Table 6.9), although in the case of Ho II X-1 it does provide clearly the best fit of all that were attempted to the data, and is only marginally rejected ($P_{\text{rej}} \approx 97.7\%$). Again the fit to NGC 4395 X-1 is poor, for reasons explained in the previous section.

Table 6.9: diskpn+eqpair spectral fits

wa*wa* (diskpn+eqpair)	N_H^a	kT_{\max}^b	A_D^c	l_h/l_s^d	τ_P^e	A_E^f	χ^2/dof
NGC 55 ULX	$2.12^{+0.12}_{-0.11}$	0.24 ± 0.01	$1.37^{+0.50}_{-0.36}$	$4.54^{+1.90}_{-2.44}$	> 37.2	$0.96^{+3.94}_{-0.24}$	889.3/827
M33 X-8	$1.03^{+0.09}_{-0.13}$	$0.08^{+0.01}_{-0.07}$	$< 4.37 \times 10^{-10}$	$3.22^{+0.48}_{-0.21}$	$18.7^{+0.6}_{-0.5}$	1083^{+21859}_{-78}	1188.0/1112
NGC 1313 X-1	$2.09^{+0.21}_{-0.39}$	$0.21^{+0.03}_{-0.02}$	< 0.44	$2.22^{+2.48}_{-0.46}$	$0.2^{+0.4}_{-0.1}$	$9.99^{+8.72}_{-2.59}$	658.7/672
NGC 1313 X-2	$1.44^{+0.30}_{-0.54}$	$0.26^{+0.09}_{-0.08}$	< 0.27	$1.83^{+0.95}_{-0.40}$	$9.2^{+10.7}_{-7.7}$	$0.72^{+2.80}_{-0.34}$	254.1/254
NGC 2403 X-1	$2.53^{+0.23}_{-0.28}$	$0.27^{+0.05}_{-0.04}$	$0.11^{+0.21}_{-0.06}$	$4.50^{+7.39}_{-1.83}$	> 33.3	$0.36^{+1.21}_{-0.31}$	831.7/848
Ho II X-1	$1.11^{+0.05}_{-0.07}$	$0.20^{+0.02}_{-0.01}$	$2.01^{+0.27}_{-0.19}$	1.01 ± 0.03	$8.5^{+0.6}_{-0.7}$	$26.7^{+4.4}_{-8.5}$	1414.8/1311
M81 X-9	$1.90^{+0.14}_{-0.19}$	$0.23^{+0.01}_{-0.03}$	< 2.08	$3.25^{+2.09}_{-0.47}$	$0.5^{+0.3}_{-0.1}$	$18.9^{+16.2}_{-7.0}$	873.8/861
NGC 3628 X-1	$4.28^{+0.36}_{-0.42}$	$0.07^{+0.02}_{-0.01}$	167^{+972}_{-112}	$26.9^{+12.6}_{-9.4}$	< 7.4	$47.8^{+21.1}_{-11.2}$	424.9/403
NGC 4395 X-1	$1.00^{+0.12}_{-0.08}$	0.20 ± 0.01	$0.15^{+0.08}_{-0.05}$	$5.97^{+0.34}_{-3.17}$	> 30.4	$0.03^{+0.03}_{-0.01}$	467.0/365
NGC 4559 X-1	$1.97^{+0.15}_{-0.08}$	$0.16^{+0.01}_{-0.02}$	$2.21^{+3.57}_{-0.76}$	$2.23^{+0.51}_{-0.71}$	$13.9^{+3.4}_{-0.6}$	$4.12^{+1.49}_{-1.45}$	577.5/596
NGC 4861 ULX	$1.09^{+0.81}_{-0.42}$	0.24 ± 0.06	$0.06^{+0.22}_{-0.03}$	$5.30^{+8.65}_{-3.18}$	> 15.8	$0.06^{+0.55}_{-0.04}$	78.7/71
NGC 5204 X-1	0.24 ± 0.08	$0.29^{+0.03}_{-0.05}$	$0.09^{+0.09}_{-0.05}$	$4.32^{+3.27}_{-1.25}$	$26.3^{+57.0}_{-5.6}$	$0.25^{+0.60}_{-0.13}$	505.8/526
M83 ULX	$0.65^{+0.34}_{-0.33}$	$0.23^{+0.08}_{-0.07}$	$0.05^{+0.21}_{-0.04}$	$1.96^{+7.63}_{-0.85}$	> 15.8	$0.32^{+3.98}_{-0.19}$	193.2/204

NOTES: ^a External absorption column (10^{21} atoms cm^{-2}), ^b maximum temperature in the accretion disc (keV), ^c diskpn normalisation ($10^{-3}(M^2 \cos(i))/(D^2 \beta^4)$); where M–central mass (M_\odot), D–distance to the source (kpc), i–inclination angle of the disc, β –colour/effective temperature ratio), ^d ratio between the compactness of the electrons and the compactness of the seed photon distribution, ^e optical depth, ^f eqpair normalisation (corresponding to the disc component) *i.e.*, $(f_c M^2 \cos(i))/(D^2 \beta^4)$, where f_c is the covering factor. Statistically acceptable fits are highlighted in bold.

The fits provide a uniformly low measurement of the disc temperature across the sample, in the range $0.07 \text{ keV} < kT_{\text{max}} < 0.29 \text{ keV}$ ⁶. Taken in isolation, this might be interpreted as strong support for the presence of IMBHs in ULXs. However, many of the fits show a second remarkable characteristic, which is that the optical depth of the coronae appear to be very high, ranging from $\tau \sim 8$ for Ho II X-1 up to depths well in excess of 30 (NGC 55 ULX, NGC 2403 X-1)⁷. Importantly, this result gives a physical explanation for the curvature noted to be present in the spectra in previous sections. This second characteristic appears irreconcilable with the main assumption behind the IMBH model, which is that they operate as simple scaled-up BHBs (see also Goad et al. 2006), as such sources typically do not possess very optically-thick coronae. This result must therefore strongly challenge the IMBH interpretation for the 9 ULXs (including Ho II X-1) well-described by this model. However, 3 ULXs - NGC 1313 X-1, M81 X-9 and (possibly) NGC 3628 X-1 - may still possess optically-thin coronae, and as such remain viable IMBH candidates.

As this spectral model provides at least the same goodness of fit as the empirical models in all but one case, these fits were used to determine the observed X-ray flux. Due to uncertainties in the low energy spectrum of some ULXs, the spectral fitting was restricted to 0.5–10 keV (and in the case of Ho II X-1 the pn data was restricted to 0.7–10 keV) instead of the 0.3–10 keV range adopted for the other sources. Therefore to determine the absorbed X-ray flux of each ULX over the same energy range, a dummy response matrix was created in XSPEC over the 0.3–10 keV energy range for those cases with calibration uncertainties. This dummy response temporarily supercedes the response matrix used in the spectral fitting of those sources, allowing an examination of the behaviour of the `diskpn+eqpair` model over this energy range. The three EPIC cameras are consistent to within 20% in 12/13 cases, therefore the derived absorbed flux (0.3–10 keV) for each of these ULXs are based on an average of the three measurements. These fluxes were converted to an observed X-ray luminosity for each source in the 0.3–10 keV band (assuming the appropriate distance) and the results are tabulated in Table 6.1⁸.

⁶However, the derived inner disc temperatures using `diskpn` are slightly lower than would be derived using the standard `diskbb` model

⁷Indeed, the optical depth for four sources hit the artificial upper limit of $\tau = 100$ during spectral fitting, therefore values are quoted as > ‘lower limit’ in these cases.

⁸Although the power-law + `mekal` spectral model statistically provided the best fit to NGC 4395 X-1, the measured source flux derived from this model and the `diskpn+eqpair` model were in very close agreement. For consistency, the value from the `diskpn+eqpair` model is quoted. However, as the ULX lay on a hot column in the pn data, the average of the two MOS flux measurements was used to estimate its luminosity.

6.5 L_X – kT relationship

Perhaps the most visually striking evidence for ULXs containing IMBHs was presented by Miller et al. (2004a) (their Figures 1 & 2). These authors selected a sample of ULXs with published estimates of $L_X > 10^{40} \text{ erg s}^{-1}$, that require a soft excess component (at least at the 3σ confidence level) in the low energy part of a two component X-ray spectrum. They then compared the inferred disc temperatures (taken from the soft component) and unabsorbed luminosities (0.5–10 keV) of their ULXs to those of a number of Galactic BHBs, and found that these ULXs and stellar mass BHBs occupy distinct regions of a L_X – kT diagram. More specifically, the ULXs are more luminous but have cooler thermal disc components than standard stellar-mass BHBs, consistent with the ULXs harbouring IMBHs.

Following on from this work, L_X – kT diagrams have been reproduced based on the inferred unabsorbed 0.5–10 keV X-ray luminosities for ULXs in this sample (Fig. 6.3). However, this is done for two cases: (i) disc temperatures measured from the IMBH (cool disc + hard power-law) fits; and (ii) disc temperatures taken from the dual thermal (cool blackbody + warm disc) fits⁹. In both cases, sources are only shown where the spectral fits are statistically acceptable, and the fit parameters are well constrained. For this reason, the values from the IMBH fit to M83 ULX are excluded, as the disc temperature is unconstrained in this case. Additionally, NGC 3628 X-1 does not appear on either plot as its unusual disc temperatures place it outside the range displayed in both cases. In each case the luminosity was derived from an average of the unabsorbed flux (0.5–10 keV) from each detector. The errors on the disc temperature are 90% confidence errors, likewise the luminosity errors are based on the 90% confidence errors in the average measured flux, as calculated by XSPEC. Finally, the regions of parameter space occupied by the BHBs and ULXs in Miller et al. (2004a) are illustrated using ellipses, with the ellipse representing IMBH-candidate ULXs at the upper-left.

The two L_X – kT diagrams in Fig. 6.3 tell very different stories. As would be expected, the IMBH model results of this work reproduce those of Miller et al. (2004a), *i.e.*, the ULXs occupy a very different region of parameter space to the stellar-mass BHBs, consistent with larger black-holes and hence more luminous, cooler accretion discs. However, the dual thermal model disc temperatures suggest an alternative interpretation. In this case, the ULXs appear to be a direct, high luminosity extension of the BHB class, and follow the $L_X \propto T^4$ trend expected from standard accretion discs. Obviously,

⁹N.B. The `diskbb` component in this figure has artificially high temperatures if the optically thick corona idea is correct.

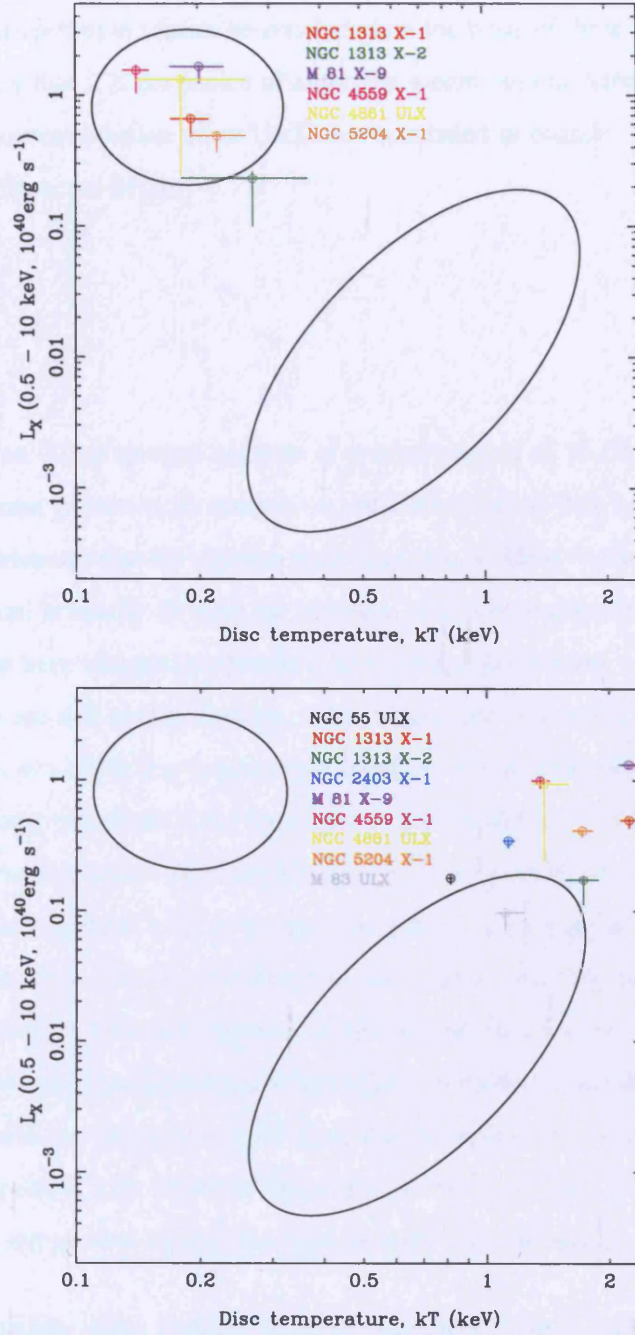


Figure 6.3: Unabsorbed X-ray luminosity (0.5–10 keV) plotted against accretion disc temperatures inferred from the X-ray spectral fits (as per Miller et al. 2004a). The ellipses represent the regions occupied by ULXs (small ellipse) and Galactic BHCs (large ellipse) presented in Figure 2 of Miller et al. (2004a). The values of the data points displayed in these figures are derived from the IMBH spectral fits (*top panel*) or the dual thermal model fits (*bottom panel*), for sources with statistically acceptable and well constrained fits for that model. (NOTE: IMBH data points neglect M83 ULX, which has an unconstrained temperature, and NGC 3628 X-1 which has a lower temperature than the other sources [~ 80 eV]; dual thermal data points also neglect NGC 3628 X-1 which has a much higher temperature than the other sources [~ 4 keV]).

which is the correct interpretation cannot be concluded on the basis of these plots. However, it does demonstrate very clearly that it is the choice of empirical model used to determine the characteristics of ULX spectra that governs whether some ULXs are concluded to contain IMBHs, or whether they are more similar to stellar-mass BHBs.

6.6 Discussion

This chapter presents an X-ray spectral analysis of a small sample of 13 ULXs, that constituted the highest quality (*i.e.*, most photon-rich) datasets in the *XMM-Newton* data holdings as of December 2004. This work demonstrates that the superior collecting area of *XMM-Newton* over its rivals leads to better spectral definition, primarily through the rejection of simple single-component spectral models (power-law, MCD) that have adequately described previous spectra of many of these ULXs. However, many of these spectra are still photon-limited, to the extent that in 6 cases, it is not possible to tell whether a combination of a MCD plus a power-law uniquely fits the data with the MCD component at the low or the high energy end of the X-ray spectrum. In each of these six ambiguous spectra, no more than ~ 18000 EPIC counts (pn and MOS combined) were accumulated. For each spectrum where this ambiguity was resolved, or where both cases were excluded as unacceptable fits, had > 20000 EPIC counts (excluding NGC 4395 X-1, as this had both an atypical spectrum and an underestimated pn count rate due to its location on a hot column). Even then, the introduction of a model composed of two thermal components adds an extra layer of ambiguity to many of the datasets. This suggests that very photon-rich datasets are required to make progress in descriptive empirical *XMM-Newton* ULX spectroscopy, equivalent to at least 100 ks of flare-free data for a 0.2 count s^{-1} on-axis ULX observed by the EPIC cameras, and spectral results from poorer quality data should be regarded with caution.

Issues of spectral ambiguity aside, perhaps the most interesting result is the detection of curvature in the high-energy part of the *XMM-Newton* EPIC spectrum in more than half of the sample. Though this has previously been detected in individual ULXs (Chapter 3; Foschini et al. 2004), or as minority populations in ULX samples (Feng & Kaaret, 2005), this is the first suggestion that the majority of ULXs, across the whole range of ULX luminosity, might appear thus. Indeed, the most successful empirical modelling of this sample is achieved using a model in which the high-energy portion of the spectrum is described by the MCD model, with a soft excess modelled as a cool blackbody emitter.

This obviously adds to the challenges in modelling ULXs as IMBHs. Indeed, though 8/13 ULXs present acceptable fits to the simple IMBH model of a cool disc plus a hard power-law continuum, the problem noted by Roberts et al. (2005) occurs again. Namely, if the inner-disc temperature can provide an estimate of the black-hole mass, then the very dominant power-law component detected here ($> 80\%$ of the observed 0.3–10 keV flux) appears too hard for what should be a HS (or perhaps VH) state source *i.e.*, $1.6 < \Gamma < 2.5$ for the IMBH candidates in this sample, compared to approximately $2.1 < \Gamma < 4.8$ for the HS, and $\Gamma > 2.5$ for the VH state - McClintock & Remillard 2006. Curvature above 2 keV compounds these problems further, as the IMBH model assumes that whilst the bigger black-hole results in a cooler accretion disc, the corona remains similar to that observed in Galactic BHBs, *i.e.*, optically-thin and hence modelled with a power-law. In fact, there is no reason to suppose that increasing the mass of the black-hole should alter the state of the corona—timing measurements at least appear to scale linearly with black-hole mass for given spectral states, implying the properties of the states themselves are invariant with mass (*c.f.* Done & Gierliński 2005). But the detection of curvature implies that either the state of the coronae is changing as the black-hole becomes more massive, or a different physical process is responsible for the emission above 2 keV.

The dual thermal model uses a MCD to model this curvature, with inner disc temperatures in the range 1.1–2.2 keV. As Fig 6.3 shows, this provides a natural explanation of ULXs as a simple extension of the behaviour of Galactic BHBs, with more luminous and slightly hotter discs. In this case, assuming the Eddington limit can be exceeded, there is no obvious requirement for IMBHs. However, even this simple empirical model has limitations; for instance, in order to see both the inner regions of the accretion disc and an optically-thick outflow simultaneously, requires a very specific geometry and viewing angle. Therefore further explanations for the origin of the soft excess component may have to be considered; one interesting suggestion, that has recently been found to work in some AGN X-ray spectra, is that the soft excess could arise in relativistically-blurred atomic features found in the reflection spectrum of a photoionised accretion disc (Crummy, 2005). A further concern for this model is that similar spectral shapes have not been commonly found in Galactic BHBs, with the exception of slight soft excesses (modelled by the extension of the power-law component below the MCD) seen in the spectra in LMC X-1 and LMC X-3 (Haardt et al., 2001). One explanation could be that soft excesses, below the MCD component in Galactic BHB spectra, are not seen due to a combination of high absorption columns and lack of detector sensitivity at low X-ray energies. However, the columns to a significant minority of BHBs are not much in excess of the $\sim 10^{21} \text{ cm}^{-2}$ columns inferred for

these ULXs (McClintock & Remillard, 2006), and many have now been observed by *XMM-Newton* and *Chandra* without such soft excesses being reported. Perhaps this is simply suggesting that this spectral shape is unique to the very high accretion rates required if ULXs contain stellar-mass black-holes.

The model that did best in terms of providing acceptable fits to the data was also the only physically self-consistent model used in the analysis, namely the `diskpn+eqpair` spectral model. The best fits provided by this model show, without exception, that the accretion disc photons seeding the corona are cool. In fact they are cool enough, at < 0.3 keV, to be consistent with the accretion disc around an IMBH. However, this model also provides a physical explanation for the curvature above 2 keV: unlike in conventional BHBs, it originates in an optically-thick corona. This combination of a cool disc and optically-thick corona has already been observed in Ho II X-1; Goad et al. (2006) note the cosmetic similarities between this spectral model and the model of Zhang et al. (2000) of a three-layered atmospheric structure in the accretion discs around BHBs. More specifically, their model includes a warm layer ($kT \sim 1\text{--}1.5$ keV, $\tau \sim 10$) between the cool optically-thick accretion disc ($kT \sim 0.2\text{--}0.5$ keV) and the hot optically-thin corona ($kT \sim 100$ keV, $\tau \sim 1$) of BHBs, which is responsible for the dominant component below ~ 10 keV (see also Nayakshin & Melia 1997, Misra et al. 1998). The warm layer appears relatively stable and hence unconnected to the hot corona, which can be highly dynamic and even disappear completely (Misra et al., 1998). In this picture, the cool disc seeds the warm optically thick scattering medium, and as such may explain both components seen in the modelling presented here.

This model has been successful in describing the X-ray spectrum of GRS 1915+105 (Zhang et al., 2000), and so Goad et al. (2006) speculate that this modelling, combined with an upper limit on the mass of the black-hole in Ho II X-1 of $\sim 100 M_{\odot}$ derived from timing properties, implies that Ho II X-1 behaves in an analogous manner to GRS 1915+105 in its χ -class. Therefore by extension, perhaps many of the ULXs in this sample that are well fitted by this spectral model could also be GRS 1915+105 analogues, *i.e.*, stellar-mass black-holes accreting at around and in excess of the Eddington limit. If individual black-holes with mass up to $80 M_{\odot}$ can form from stellar processes as suggested by Belczynski et al. (2004), and these larger stellar-mass black-holes exist in ULXs, then the factors by which the Eddington limit are exceeded need not be large for even the brighter ULXs (factors $\sim 2 - 3$ only). One piece of additional, encouraging evidence in this respect is that, similarly to Ho II X-1 and GRS 1915+105 in its analogous χ -class of behaviour, the light curves of the ULXs in this sample show little or no intrinsic variability on timescales of minutes to hours, with the fractional variability (in

excess of counting noise) limited to $\lesssim 10\%$ in all cases¹⁰.

Recently a second, very plausible explanation for the physically self-consistent spectral modelling presented here has come to light. Done & Kubota (2005) describe spectral modelling of the Galactic BHB XTE J1550-564 in its high-luminosity VH state, using a model in which the energetics of the inner regions of the accretion disc are coupled to a surrounding corona. This results in a cooler apparent disc temperature, as the corona drains energy from the inner disc, and an optically-thick corona, that are both part of the accretion flow. Done & Kubota (2005) note that this may provide an explanation for the low disc temperatures observed in ULXs not reliant upon the presence of an IMBH. As the spectral modelling presented in this chapter also provides evidence that the corona itself is indeed optically-thick in such sources, this model must constitute a very serious physical alternative to IMBHs for the majority of ULXs. However, even here there are caveats, for instance Feng & Kaaret (2005) note that optically-thick coronae should show deep Fe K absorption edges, unless the accreting material has a very low metallicity. Such features are not detected in this analysis.

In this chapter, the empirical spectral fitting has posed new challenges for the IMBH model fits to ULX spectra, and the physical modelling describes scenarios in which the bulk of ULXs could be stellar-mass black-holes accreting at around the Eddington limit. This is perhaps not surprising, as many strands of recent evidence have pointed away from an IMBH model for most ULXs. In fact, excepting the somewhat unique case for M82 X-1 as an IMBH, possibly formed in the dense MGG-11 cluster or captured as the nucleus of an accreted dwarf galaxy (*e.g.*, Strohmayer & Mushotzky 2003; Portegies Zwart et al. 2004; King & Dehnen 2005; Mucciarelli et al. 2005), and the cool disc detections (shown to be somewhat ambiguous in this chapter), observational results have tended to argue in the opposite sense. For example, the probable breaking of the Eddington limit seen in some - perhaps most (see Jonker & Nelemans 2004) - Galactic BHBs, and especially GRS 1915+105, argues that stellar-mass black-holes cannot be excluded from producing ULXs on this basis (McClintock & Remillard, 2006). Also, the shape of the universal XLF for HMXBs, derived by Grimm et al. (2003), is somewhat puzzling if IMBHs constitute a significant part of the ULX population. In particular, why does the XLF appear to cut-off at $\sim 2 \times 10^{40} \text{ erg s}^{-1}$?¹¹ Surely no such cut-off would be present if $\sim 1000 M_{\odot}$ IMBHs constitute a large fraction of the ULX population (no other source population is known to cut off at

¹⁰Excepting the NGC 55 ULX, which shows prominent dips in its *XMM-Newton* light curve (Chapter 3).

¹¹Independent support for this cut-off comes from the empirical L_X -SFR relationship of Grimm et al. (2003), which can only have its linear form above $\sim 10 M_{\odot} \text{ yr}^{-1}$ if the cut-off is real.

~ 0.1 Eddington rate). Therefore, on current evidence, it is unlikely that accreting IMBHs constitute a large proportion of the total ULX population.

6.7 Conclusions

A detailed examination has been conducted of the X-ray spectral shapes in a sample of the highest quality *XMM-Newton* EPIC ULX datasets currently available. Most notably, more than half of the ULXs show at least marginal evidence for curvature in their 2–10 keV spectra, which is somewhat unexpected if they are to be interpreted as the accreting $\sim 1000 M_{\odot}$ IMBHs suggested by modelling the soft spectral components as accretion discs. Physical modelling shows that this curvature is likely to originate in optically-thick coronae, which in turn leads to interpretations of the ULXs in terms of high accretion-rate stellar-mass (or slightly larger) black-holes operating at around the Eddington limit. However, while it is likely that the general ULX population does not have a large contribution from IMBHs, the possibility that some ULXs do possess IMBHs obviously cannot be ruled out. Perhaps the best candidate on the basis of spectral fitting is M81 X-9, which is well fitted by cool disc plus power-law/optically-thin corona models, and does not show explicit curvature in its 2–10 keV spectrum. However, even this ULX may be fitted using a hot (~ 2.2 keV) accretion disc plus soft excess model. Clearly, it is difficult to find unique solutions for these sources even with high quality *XMM-Newton* EPIC data. Ultimately, astronomers may have to wait for radial velocity measurements from the optical counterpart of a ULX, leading to dynamical mass measurements of the compact accretor, before there is conclusive evidence whether any individual ULX does harbour an IMBH.

Chapter 7

Conclusions

7.1 Overview

The analysis in this thesis is based on X-ray data from the EPIC CCD cameras on board the *XMM-Newton* Observatory. This chapter discusses the main highlights of this work and provides a brief summary of the results that are presented in previous chapters. Following on from this, this chapter describes further work that can be performed with improved high-energy observations, both with the present complement of telescopes and with future X-ray missions.

7.2 Thesis highlights

The work in this thesis is based on *XMM-Newton* observations of nearby (< 20 Mpc) galaxies, focusing on bright individual discrete sources (ULXs) as well as the global X-ray properties for two systems; NGC 55 and NGC 4945. The *XMM-Newton* observations of these galaxies revealed an underlying diffuse component in each case, which is most likely due to hot gas associated with current sites of star formation. In addition, a number of discrete X-ray sources have been discovered in these galaxies, the majority of which are consistent with accreting XRBs. NGC 55 also harbours a ULX which was studied in more detail to reveal interesting dips in its X-ray light curve and an unusual X-ray spectrum which shows curvature at high energies.

A more detailed analysis was performed on a sample of ULXs from a number of different galaxies using the best quality available datasets. Although detailed analyses of ULXs are revealing more information about these sources, one of the important results from this thesis is that even for high quality ULX datasets, it is not possible to gain a clear physical insight into their true nature, particularly for low count rate sources, using empirical models. Interestingly though, there is evidence for a break at the high energy end (> 2 keV) of the X-ray spectra, as reported for the NGC 55 ULX, in a number of cases. Such a break is inconsistent with the IMBH model, if IMBHs are thought to be scaled-up XRBs, where the high energy emission is thought to arise in a hot optically thin corona. Instead, such breaks may be better described by an optically thick corona together with a cool accretion disc. More detailed summaries of each data chapter are given in the following sections.

7.2.1 A dipping black-hole X-ray binary candidate in NGC 55

Chapter 3 presented *XMM-Newton* EPIC observations of a bright point-like X-ray source in the nearby Magellanic-type galaxy NGC 55. At the distance of NGC 55, the maximum observed X-ray luminosity of the source, designated as XMMU J001528.9-391319, is $L_X \sim 1.6 \times 10^{39} \text{ erg s}^{-1}$, placing the object in the ULX regime. The X-ray lightcurve was shown to exhibit a variety of features including a significant upward drift over the 60 ks observation. Most notably a series of X-ray dips are apparent with individual dips lasting for typically 100–300 s. Some of these dips reach almost 100% diminution of the source flux in the 2.0–4.5 keV band. The EPIC CCD spectra can be modelled with two spectral components, a very soft power-law continuum ($\Gamma \sim 4$) dominant below 2 keV, plus a MCD component

with an inner-disc temperature $kT \sim 0.8$ keV. The observed upward drift in the X-ray flux can be attributed to an increase in the level of the MCD component, whilst the normalisation of the power-law continuum remains unchanged. The dipping episodes correspond to a loss of signal from both spectral components, although the blocking factor is at least a factor two higher for the MCD component. XMMU J001528.9-391319 can be considered as a candidate BHB system. A plausible explanation of the observed temporal and spectral behaviour is that the accretion disc is viewed close to edge-on and that, during dips, orbiting clumps of obscuring material enter the line of sight and cause significant blocking or scattering of the hard thermal X-rays emitted from the inner disc. In contrast, the more extended source of the soft power-law flux is only partially covered by the obscuring matter during the dips.

7.2.2 The X-ray properties of the dwarf Magellanic-type galaxy NGC 55

This chapter presented an analysis of the X-ray properties of the Magellanic-type galaxy NGC 55 based on two contiguous *XMM-Newton* observations. A total of 137 X-ray sources were detected in the FOV, down to a flux of $\sim 5 \times 10^{-15}$ erg cm $^{-2}$ s $^{-1}$ (0.3–6 keV), 42 of which are located within the optical confines of the galaxy. On the basis of X-ray colour classification and after correcting for background objects, this source sample includes ~ 4 absorbed sources, 16 XRBs, 5 SNRs and 7 VSSs (including 2 good candidate SSSs) associated with NGC 55. In addition, one detected X-ray source is coincident with a previously identified globular cluster in NGC 55. Detailed spectral and timing analyses were carried out on 4 of the brightest X-ray sources (excluding the brightest source, which was the subject of Chapter 3). One of these objects is identified with a Galactic foreground star and is a possible new RS CVn system. The other three are persistent X-ray sources with X-ray spectra well described by either a single absorbed power-law ($\Gamma \sim 2$) or a MCD ($kT_{in} \sim 1$ keV) model. While the observed luminosities of these sources ($L_X \sim 1 - 2 \times 10^{38}$ erg s $^{-1}$) and their X-ray spectra are consistent with accreting XRBs, further evidence of short term variability is required to confirm this. Although the *observed* X-ray emission from NGC 55 is dominated by point sources, there is also evidence of an underlying component, which is concentrated on the bar region but has an extent of at least $6'$ (3 kpc) in the plane of the galaxy and $\pm 1'$ (± 500 pc) perpendicular to it. This emission is best fitted by a *mekal* thermal plasma ($kT \sim 0.2$ keV) plus power-law ($\Gamma \sim 2$) model but with high intrinsic absorption consistent with its location in the central disc of the galaxy. This soft component is interpreted as diffuse thermal emission linked to regions of current star formation, whilst

the hard power-law component may originate in unresolved XRB sources. The *intrinsic* luminosity of this residual disc emission may exceed $L_X \sim 4 \times 10^{38} \text{ erg s}^{-1}$ (0.3–6 keV). A comparison with other Magellanic systems confirms that, in terms of both its discrete X-ray source population and its extended emission, NGC 55 has X-ray properties which are typical of its class.

7.2.3 The X-ray properties of the spiral galaxy NGC 4945

Chapter 5 presented an investigation of the X-ray properties of the spiral galaxy NGC 4945 based on *XMM-Newton* EPIC data. At the centre of this galaxy there is both a heavily absorbed Seyfert nucleus and a starburst region which drives an outflow in the form of a superwind. However, this chapter focused on the less well studied extended galaxy, including the point source population and galactic diffuse emission. A total of 69 X-ray sources have been detected in the EPIC FOV, of which ~ 20 are probably associated with the galaxy. The sources lying within the D_{25} region encompass a flux range of $\sim 9 \times 10^{-15} - 7 \times 10^{-13} \text{ erg cm}^{-2} \text{ s}^{-1}$ (0.3–6 keV), corresponding to a luminosity range of $\sim 2 \times 10^{35} - 1 \times 10^{39} \text{ erg s}^{-1}$ at the distance of NGC 4945. Temporal analyses were performed on four of the brightest X-ray sources (excluding the nuclear source), but no sources appeared to be variable on timescales monitored by this observation. The X-ray spectra were well fitted, in three cases, with absorbed single component MCD models, whereas a power-law provided the best fit in the remaining case. Their high luminosities and X-ray spectra are consistent with XRBs, but further observations are necessary to confirm their accreting nature. In addition to the point source population, the *XMM-Newton* observations have also shown clear evidence for diffuse X-ray emission, with an approximate extent of $12' \times 5'$. This extended emission is best fitted spectrally by a soft thermal plasma component plus a hard power-law continuum. The soft plasma emission is likely to be associated with recent starburst activity throughout the inner region of the galaxy, and has an *intrinsic* luminosity of at least $7 \times 10^{38} \text{ erg s}^{-1}$ (0.3–6 keV), while the hard emission is perhaps due to unresolved X-ray sources.

7.2.4 *XMM-Newton* observations of the brightest ULXs

Chapter 6 presented an analysis of 13 of the best quality ULX datasets available from *XMM-Newton* EPIC observations. The high signal-to-noise in these ULX spectra was utilised to investigate the best descriptions of their spectral shape in the 0.3–10 keV range. Simple models of an absorbed power-law

or MCD proved to be inadequate at describing the spectra. Better fits were found using a combination of these two components, with both variants of this model - a cool (~ 0.2 keV) disc blackbody plus hard power-law continuum, and a soft power-law continuum (dominant at low energies) plus a warm (~ 1.7 keV) disc blackbody - providing good fits to 8/13 ULX spectra. However, by examining the data above 2 keV, there is evidence for curvature in the majority of datasets (8/13 with at least marginal detections), inconsistent with the dominance of a power-law in this regime. In fact, the most successful empirical description of the spectra proved to be a combination of a cool (~ 0.2 keV) classic blackbody spectrum plus a warm disc blackbody, which fitted acceptably to 10/13 ULXs. The best overall fits were provided by a physically self-consistent accretion disc plus Comptonised corona model (`diskpn + eqpair`), which fitted acceptably to 11/13 ULXs. This model provides a physical explanation for the spectral curvature, namely that it originates in an optically-thick corona, though the accretion disc photons seeding this corona still originate in an apparently cool disc. Similarities exist between this fit and models of Galactic BHBs at high accretion rates, most notably the model of Done & Kubota (2005). In this scenario the inner-disc and corona become energetically-coupled at high accretion rates, resulting in a cooled accretion disc and optically-thick corona. In conclusion, this analysis of the best spectral data for ULXs shows it to be plausible that the majority of the population are high accretion rate stellar-mass (perhaps up to $80 M_{\odot}$) black-holes, though the presence of larger, $\sim 1000 M_{\odot}$ IMBHs in individual sources cannot categorically be ruled out with the current X-ray data.

7.3 Future Work

One obvious way in which further progress can be made in the field of ULX research is by performing observations with longer exposures, thus providing more detailed X-ray spectra. On the basis of the study presented in Chapter 6, such datasets should possess > 20000 counts in order to avoid ambiguity and thus make further progress in ULX spectroscopy. Such progress with more detailed EPIC data (in particular, so-called ‘large projects’ with exposures > 300 ks) should be aimed at constraining the shape of the X-ray spectra and investigating the details of the high energy break if present. Another area of interest is whether a significant number of ULXs show evidence for broad Fe K lines. This Fe fluorescence line is believed to be generated by the irradiation of the ‘cold’ accretion disc by a source of hard X-rays (perhaps a corona of hot electrons) and therefore probes the immediate vicinity of the black-hole. Broad Fe lines have been observed in AGNs (*e.g.*, MCG-6-30-15; Wilms et al. 2001) and

Galactic systems (*e.g.*, XTE J1650-500; Miller et al. 2002) but only one questionable claim for a ULX has so far been made (Strohmayer & Mushotzky, 2003). More detailed X-ray spectra will obviously enable better use of more physical models, which could then provide further insights into the physics at work in these systems. Longer observations ($\gtrsim 300$ ks) with *XMM-Newton* would also provide excellent RGS data and provide further clues to the temperature and chemical composition of ULXs and their surrounding environments.

Another approach to study the nature of ULXs and perhaps the best method for determining the mass of the central black-hole, is through short timescale variability measurements via comparisons of their Power Spectral Density (PSD) with those of XRBs and AGN. In particular, the location of the characteristic break frequency in the slope of the PSD scales inversely with the mass of the black-hole (*e.g.*, Uttley et al. 2002, Markowitz et al. 2003, Vaughan et al. 2005) and therefore can be used to infer black-hole masses (assuming a direct scaling of properties between Galactic black-holes and AGN). However, ULXs as a class do not tend to show much short term variability (*e.g.*, Swartz et al. 2004) and so such calculations are not practical in all cases (though see Goad et al. 2006 for an example of the limits that can be placed using data lacking significant variability). An additional way of distinguishing between the IMBH or the stellar mass black-hole model is via the detection of a 3:2 ratio twin peak QPO. The expected frequency for IMBHs is ~ 1 Hz compared to the observed value for Galactic microquasars of ~ 100 Hz (Abramowicz et al., 2004). However the detection of such a signature will require far superior capabilities to those of current X-ray missions.

Many of the ideas regarding the nature of ULXs cannot be confirmed without supportive evidence from multiwavelength observations. In particular, optical/UV observations can provide crucial diagnostics of the nature of ULXs through the identification of optical counterparts. The study of such counterparts can reveal the type of the mass donor star and, with sufficient data quality, enable radial velocity measurements to be made. These measurements would allow the determination of the mass function which would provide constraints on the mass of the black-hole, thus revealing whether the compact objects in ULXs are IMBHs or stellar mass black-holes. Various studies focussing on nearby spiral galaxies (< 10 Mpc) using the excellent capabilities of *Chandra* and the *Hubble Space Telescope* have resulted in a number of possible ULX counterparts (*e.g.*, Goad et al. 2002; Liu et al. 2002, 2004; Kuntz et al. 2005; Terashima et al. 2006). Frequently, the counterparts have magnitudes $m_V \sim 22\text{--}26$ and possess blue colours, consistent with the interpretation of ULXs as HMXBs which possess massive (OB) companions. However, current observations have so far lacked the required quality in the optical

spectra for radial velocity searches.

In addition to optical searches, surveys are currently underway to search for radio counterparts to ULXs. Such a detection has implications for whether ULXs have relativistically beamed jets and are therefore analogues to Galactic microquasars, but perhaps with their jet directed towards the observer (*i.e.*, so-called microblazars). However, radio counterparts are also relatively scarce, with the first detection reported only a few years ago in the dwarf irregular galaxy NGC 5408 (Kaaret et al., 2003). This particular ULX displayed a radio spectrum consistent with optically thin synchrotron emission, interpreted as core radio emission from a ULX jet (Kaaret et al., 2003) or from radio lobes inflated by a relativistic jet from the ULX (Soria et al., 2006). Understanding this radio source is crucial for constraining the nature of ULXs, especially as very few ULXs have a detected radio counterpart (*e.g.*, K rding et al. 2005).

While there may be difficulties in identifying unique counterparts to ULXs, studies of the local stellar population can still yield important information about the nature of the sources. For example, a population of early type stars support the HMXB origin (*e.g.*, Roberts et al. 2001, Liu et al. 2004, Soria et al. 2005). Other interesting results from studies of ULX environments include the discovery that the ULX Holmberg II X-1 is the ionising source which powers the line emission from the surrounding optical nebula (Pakull & Mirioni 2002, Kaaret et al. 2004). Some ULXs have also been shown to be associated with larger (~ 100 s pc) SNR-like structures (*e.g.*, IC 342 X-1; Roberts & Colbert 2003, NGC 1313 X-2; Pakull & Mirioni 2002). Further progress needs to be made in the study of ULX environments in order to improve current understanding of how ULXs are formed and fuelled.

ULXs are critically important in the study of X-ray emission from star-forming galaxies as they may dominate the point-source X-ray luminosity of, *e.g.*, spiral galaxies (Colbert et al., 2004). Although some studies have been made on the relationship between ULXs and their host galaxies (*e.g.*, Colbert et al. 2004, Swartz et al. 2004), there is still a lot more to be done in this area, particularly in extending the studies to higher redshifts via deep surveys. Advances have been made using the Great Observatories Origins Deep Survey (GOODS), which revealed that the fraction of optically luminous galaxies exhibiting ULXs with $L_X \gtrsim 2 \times 10^{39} \text{ erg s}^{-1}$ is $\sim 8\%$ locally and $\sim 36\%$ at $z \sim 0.1$, suggesting that the frequency of ULXs may evolve similarly to the SFR (Hornschemeier et al., 2004). Further progress in this field requires better measurements of the 2–10 keV X-ray luminosity for many galaxies with known high SFRs. This will help to calibrate the L_X (2–10 keV)–SFR relation which will be an

important tool for the next generation X-ray missions that will probe star-forming galaxies out to $z \sim 1$.

7.3.1 Future X-ray missions

In addition to ‘pointed’ instruments like *Chandra* and *XMM-Newton*, ‘wide angle’ telescopes are also needed to enable large areas of sky to be monitored at a particular time in the search for interesting events. In this way, such instruments can providing the information needed to point the highly sensitive, narrow field instruments at these targets. The Leicester-led mission which plans to fulfill this criteria is the *Lobster All-Sky X-ray Monitor*. The *Lobster* instrument will image almost the complete X-ray sky every 90 minutes, permitting real-time monitoring of vast numbers of astronomical objects within our Galaxy and far beyond. Therefore one of the key strengths of this mission is that it will provide, for the first time, a complete census of the time variability of all classes of X-ray sources. Thus, for ULXs (as well as many other objects), *Lobster* will enable the analysis of day by day light curves over a period of months to years, thus providing further insight into their physical nature through a measure of their long term behaviour.

There is also a need for improved sensitivity in the hard X-ray (> 10 keV) and soft γ -ray (\sim several MeV) bands. This will be satisfied with the Japanese New X-ray Telescope (*NeXT*) mission which plans to be launched in the next ~ 5 yrs or so. The *NeXT* project has been proposed as a successor of the joint Japanese-American *Suzaku* (formerly *Astro-E2*) mission which was launched on 10th July 2005. *Suzaku* covers the energy range 0.2–600 keV with two instruments; the X-ray Imaging Spectrometer (XIS; 0.2–10 keV) and the Hard X-ray Detector (HXD; 10–600 keV). There are 4 co-aligned XIS instruments (which are X-ray CCD cameras) and one HXD which is a non-imaging detector. A non-dispersive X-ray spectrometer (XRS) is also onboard and was intended to provide high energy resolution spectroscopy in the 0.3–12 keV energy band but was rendered inoperable due to a failure in the cryogenic system. The *NeXT* project plans to recover the science lost due to the XRS failure and extend the science with wide-band spectroscopy. *NeXT* will carry multiple instruments covering 0.5–300 keV, namely, two hard X-ray telescopes (HXTs) for an X-ray imager which will concentrate hard X-rays up to ~ 80 keV; two soft X-ray telescopes (SXT)—one for a soft X-ray spectrometer (SXS) and the other for a soft X-ray imager (SXI); and a soft γ -ray detector (SGD). *NeXT* will therefore provide the first hard X-ray imaging spectroscopy, enabling spatial studies of non-thermal emission above 10 keV. This will permit mapping of the hard X-ray emission in diffuse sources in *e.g.*, clusters of galaxies and

SNRs. In addition, it would provide images and spectra from a large number of hard X-ray sources which are currently too faint to be studied, including ULXs. Such observations are important for improving current understanding of powerful accretion flows, and in the case of ULXs, will provide a definitive measure of the \sim few keV spectral turnover if present.

Two major future X-ray missions planned for launch in \sim 10 yrs or so, are NASA's *Constellation-X* and ESA's X-ray Evolving Universe Spectroscopy (*XEUS*) missions. The *Constellation-X* observatory is a combination of four X-ray telescopes working in unison to generate the observing power of one giant telescope. The four telescopes will combine to provide a sensitivity \sim 100 times greater than any past or current X-ray satellite mission. Each of the four *Constellation-X* satellites are expected to carry 3 hard X-ray telescope (HXT) systems and one Spectroscopy X-ray Telescope (SXT) which would be shared by a Reflection Grating Assembly (RGA) and an X-ray Microcalorimeter Spectrometer (XMS). *XEUS* is the potential follow-on to ESA's *XMM-Newton* mission and will consist of two spacecraft (one carrying the mirror, the other carrying the detectors) flying in formation 50 metres apart. Novel light weight X-ray optics and advanced imaging detectors will provide an improvement in sensitivity of \sim 200 times better than *XMM-Newton* as well as much improved spatial resolution, high energy coverage and spectral performance. *XEUS* will carry three scientific instruments in the focal plane of the X-ray telescope: a Wide-Field Imager (WFI) for deep-survey pointed observations (FOV of \sim 5'), and two Narrow-Field Instruments (NFI1 and 2) for follow-up observations with high spectral resolution (Wilson & Xeus Instrument Working Group, 2003)¹.

Both observatories emphasise large collecting area, high spectral resolution and a broad energy band-pass (*Constellation-X*: 0.25–40 keV, *XEUS*: 0.05–30 keV) thereby providing high quality spectra for many classes of X-ray sources over a wide range of luminosity and redshift. As previously mentioned, such broad energy bandpasses are essential for sources whose energy output peaks above 10 keV. The Seyfert 2 galaxy NGC 4945 is an example of such a source (*e.g.*, see Fig. 7.1). The highly absorbed continuum X-ray emission from the AGN, which is probably obscured by an optically-thick torus, is visible only above 10 keV. Therefore, at lower X-ray energies (<10 keV), for which *Chandra* and *XMM-Newton* are sensitive, only the X-rays that are scattered around the torus are seen. However, *Constellation-X* and *XEUS* will be able to measure the underlying continuum and the scattering component simultaneously, thus enabling the total energy output to be determined. These missions will permit the study of AGN with the highest X-ray absorbing column densities and will go to much

¹There are also discussions for an Extended Wide-Field Imager (E-WFI) with a 15'–30' FOV

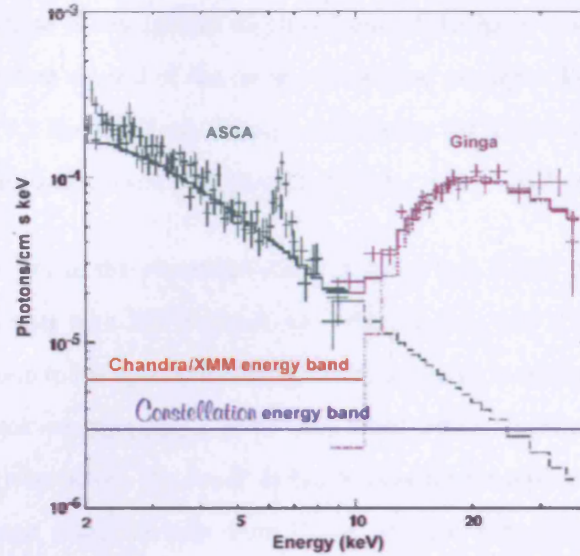


Figure 7.1: A combined *ASCA* and *Ginga* spectrum (the observations were not simultaneous) of NGC 4945, which illustrates the need for a hard X-ray telescope. Figure taken from http://constellation-x.nasa.gov/mission/overview/spectral_resolution.html.

deeper flux levels than before, thus revealing the overall accretion geometry and obtaining spectra for thousands of such objects.

Constellation-X and *XEUS* will have unique capabilities for studying stellar-mass black-holes in Galactic BHBs and in nearby galaxies. For Galactic systems, these missions will be able to study spectroscopic and timing signatures of matter moving near the black-hole event horizon. In the case of ULXs, these observatories will be able to spectroscopically confirm the presence of cool accretion discs in IMBH candidates and detect relativistic Fe-K emission lines if present.

One of the key questions arising from this thesis is whether ULX X-ray spectra typically show a hard energy break. This break can only be constrained for a few of the brightest cases with long *XMM-Newton* exposures but *Constellation-X* and *XEUS* observations should be able to provide much clearer constraints on such breaks if they are present. For example, Fig. 7.2 shows a comparison between the spectral quality expected from a 100 ks *XMM-Newton* EPIC-pn observation and a 100 ks *XEUS* WFI observation of a ULX². The data were simulated based on the `diskpn + eqpair` spectral fit to the

²As ULXs are smooth continuum sources, simulations have not been performed for the NFI instruments which are mainly suitable for identifying emission lines.

ULX NGC 4559 X-1, whose X-ray spectra displayed one of the more moderate examples of a break (lower τ , higher E_{break}) than several of the more pronounced examples like NGC 55 ULX and M33 X-8. It is clear from Fig. 7.2 that the X-ray data are far superior for XEUS with typical parameter errors of $\sim 1\%$ vs. $\sim 10\%$ for pn and a count rate of $\sim 17 \text{ counts s}^{-1}$ vs. $\sim 0.3 \text{ counts s}^{-1}$ for pn.

Also, broken power-law fits to the simulated *XMM-Newton* and *XEUS* data in the 2–10 keV band show much better constraints with *XEUS* (errors of $\sim \text{few } \%$ vs $\sim \text{few } 10\text{s } \%$ for pn). To graphically demonstrate the fall-off due to the optical thickness of the *eqpair* model, the simulated X-ray spectra from 2 keV up to the break energy (E_{break} keV) were fitted with a single power-law component, with the slope fixed to that given before the break in the broken power-law model (*i.e.*, fixed Γ , variable normalisation) in each case. Then the data from E_{break} –10 keV were included, without refitting, and the $\Delta\chi$ residuals were plotted as shown in Fig. 7.2. As can be seen, the residuals for the simulated *XEUS* data show a more noticeable fall-off above the break than for the *XMM-Newton* data.

Finally, the unprecedented high signal-to-noise of the XEUS ULX spectra will permit the detection of faint lines (*i.e.*, Fe K if present) and/or absorption features, for example those possibly originating in an outflowing wind expected to be present round near-Eddington accretors (*e.g.*, Pounds et al. 2003).

While *Chandra* and *XMM-Newton* have enabled huge strides to be made in X-ray astronomy, the proposed X-ray missions of the future are promising to be even more spectacular and should lead to a deeper understanding of the physics in extreme environments in general, and of the nature and properties of the extraordinary X-ray sources discussed in this thesis in particular.

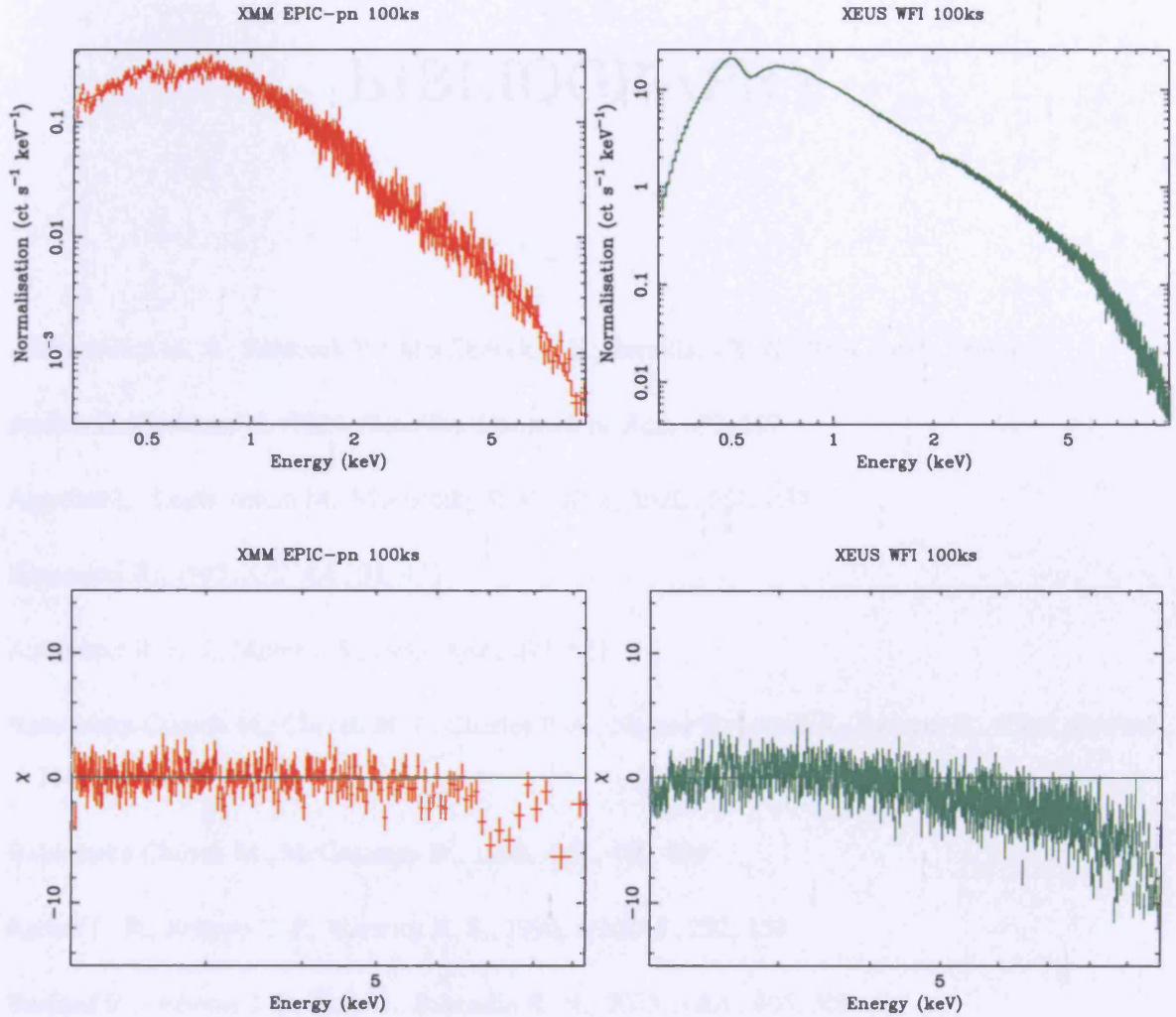


Figure 7.2: *Top panel:* A simulated 100 ks *XMM-Newton* EPIC-pn spectrum (*left*) compared to a simulated 100 ks *XEUS* WFI spectrum (*right*) of a ULX based on a `diskpn+eqpair` spectral model (0.3–10 keV). *Bottom panel:* $\Delta\chi$ residuals for a single power-law fit to the $2\text{--}E_{\text{break}}$ keV regime of the simulated *XMM-Newton* EPIC-pn (*left*) and *XEUS* WFI (*right*) spectra (see text for details).

BIBLIOGRAPHY

- Abramowicz M. A., Kluźniak W., McClintock J. E., Remillard R. A., 2004, *ApJL* , 609, L63
- Anders E., Grevesse N., 1989, *Geochim. Cosmochim. Acta* , 53, 197
- Angelini L., Loewenstein M., Mushotzky R. F., 2001, *ApJL* , 557, L35
- Antonucci R., 1993, *ARA&A* , 31, 473
- Antonucci R. R. J., Miller J. S., 1985, *ApJ* , 297, 621
- Bałucińska-Church M., Church M. J., Charles P. A., Nagase F., LaSala J., Barnard R., 2000, *MNRAS* , 311, 861
- Balucinska-Church M., McCammon D., 1992, *ApJ* , 400, 699
- Barber C. R., Roberts T. P., Warwick R. S., 1996, *MNRAS* , 282, 157
- Barnard R., Osborne J. P., Kolb U., Borozdin K. N., 2003, *A&A* , 405, 505
- Bauer F. E., Brandt W. N., Sambruna R. M., Chartas G., Garmire G. P., Kaspi S., Netzer H., 2001, *AJ* , 122, 182
- Beasley M. A., Sharples R. M., 2000, *MNRAS* , 311, 673
- Begelman M. C., 2002, *ApJL* , 568, L97
- Belczynski K., Sadowski A., Rasio F. A., 2004, *ApJ* , 611, 1068
- Belloni T., Méndez M., van der Klis M., Lewin W. H. G., Dieters S., 1999, *ApJL* , 519, L159

- Bertola F., Boschetti C. S., Cioi S., Corbelli E., Corsini E. M., Danese L., D’Onofrio M., Marconi A., Pizzella A., Rafanelli P., Salucci P., 2003, *Memorie della Societa Astronomica Italiana*, 74, 324
- Blanton E. L., Sarazin C. L., Irwin J. A., 2001, *ApJ* , 552, 106
- Bomans D. J., Chu Y.-H., Hopp U., 1997, *AJ* , 113, 1678
- Bowyer S., Byram E. T., Chubb T. A., Friedman H., 1965, *Science*, 147, 394
- Braatz J. A., Wilson A. S., Henkel C., 1997, *ApJS* , 110, 321
- Brandt W. N., Alexander D. M., Hornschemeier A. E., Garmire G. P., Schneider D. P., Barger A. J., Bauer F. E., Broos P. S., Cowie L. L., Townsley L. K., Burrows D. N., Chartas G., Feigelson E. D., Griffiths R. E., Nousek J. A., Sargent W. L. W., 2001, *AJ* , 122, 2810
- Brandt W. N., et al., 2000, *AJ* , 119, 2349
- Brandt W. N., Iwasawa K., Reynolds C. S., 1996, *MNRAS* , 281, L41
- Bregman J. N., Houck J. C., 1997, *ApJ* , 485, 159
- Bregman J. N., Pildis R. A., 1994, *ApJ* , 420, 570
- Brock D., Joy M., Lester D. F., Harvey P. M., Ellis H. B. J., 1988, *ApJ* , 329, 208
- Carpano S., Wilms J., Schirmer M., Kendziorra E., 2005, *A&A* , 443, 103
- Colbert E. J. M., Heckman T. M., Ptak A. F., Strickland D. K., Weaver K. A., 2004, *ApJ* , 602, 231
- Colbert E. J. M., Mushotzky R. F., 1999, *ApJ* , 519, 89
- Colbert E. J. M., Petre R., Schlegel E. M., Ryder S. D., 1995, *ApJ* , 446, 177
- Colbert E. J. M., Ptak A. F., 2002, *ApJS* , 143, 25
- Coppi P. S., 1999, in ASP Conf. Ser. 161: High Energy Processes in Accreting Black Holes The Physics of Hybrid Thermal/Non-Thermal Plasmas. pp 375–
- Costa E., et al., 1997, *Nature* , 387, 783
- Cropper M., Soria R., Mushotzky R. F., Wu K., Markwardt C. B., Pakull M., 2004, *MNRAS* , 349, 39
- Crummy J., 2005, preprint (astro-ph/0511457)

Dahlem M., Weaver K. A., Heckman T. M., 1998, *ApJS* , 118, 401

Davidge T. J., 2005, *ApJ* , 622, 279

de Vaucouleurs G., 1961, *ApJ* , 133, 405

de Vaucouleurs G., 1964, *ApJ* , 139, 899

de Vaucouleurs G., de Vaucouleurs A., Corwin H. G., 1991, Third Reference Catalogue of Bright Galaxies. Volume 1-3, XII, 2069 pp. 7 figs.. Springer-Verlag Berlin Heidelberg New York

de Vaucouleurs G., Freeman K. C., 1972, *Vistas in Astronomy*, 14, 163

den Herder J. W., et al., 2001, *A&A* , 365, L7

Dewangan G. C., Griffiths R. E., Choudhury M., Miyaji T., Schurch N. J., 2005, *ApJ* , 635, 198

Dewangan G. C., Miyaji T., Griffiths R. E., Lehmann I., 2004, *ApJL* , 608, L57

Di Stefano R., Kong A. K. H., 2003, *ApJ* , 592, 884

Di Stefano R., Kong A. K. H., 2004, *ApJ* , 609, 710

Díaz Trigo M., Parmar A. N., Boirin L., Méndez M., Kaastra J. S., 2006, *A&A* , 445, 179

Dickey J. M., Lockman F. J., 1990, *ARA&A* , 28, 215

Done C., Gierliński M., 2005, *MNRAS* , 364, 208

Done C., Kubota A., 2005, preprint (astro-ph/0511030)

Done C., Madejski G. M., Smith D. A., 1996, *ApJL* , 463, L63+

Done C., Madejski G. M., Życki P. T., Greenhill L. J., 2003, *ApJ* , 588, 763

Dos Santos P. M., Lepine J. R. D., 1979, *Nature* , 278, 34

Ebisawa K., Życki P., Kubota A., Mizuno T., Watarai K.-y., 2003, *ApJ* , 597, 780

Edmunds M. G., 1990, *MNRAS* , 246, 678

Ehle M., Pietsch W., Beck R., 1995, *A&A* , 295, 289

Ehle M., Pietsch W., Beck R., Klein U., 1998, *A&A* , 329, 39

Engelbracht C. W., Gordon K. D., Bendo G. J., 2004, *ApJS* , 154, 248

Fabbiano G., 1988a, *ApJ* , 325, 544

Fabbiano G., 1988b, *ApJ* , 330, 672

Fabbiano G., 1989, *ARA&A* , 27, 87

Fabbiano G., Kim D.-W., Trinchieri G., 1992, *ApJS* , 80, 531

Fabbiano G., Krauss M., Zezas A., Rots A., Neff S., 2003, *ApJ* , 598, 272

Fabbiano G., Trinchieri G., 1987, *ApJ* , 315, 46

Falcke H., Biermann P. L., 1995, *A&A* , 293, 665

Fender R., 2004, preprint (astro-ph/0303339)

Feng H., Kaaret P., 2005, *ApJ* , 633, 1052

Ferguson A. M. N., Wyse R. F. G., Gallagher J. S., 1996, *AJ* , 112, 2567

Forman W., Schwarz J., Jones C., Liller W., Fabian A. C., 1979, *ApJL* , 234, L27

Foschini L., Rodriguez J., Fuchs Y., Ho L. C., Dadina M., Di Cocco G., Courvoisier T. J.-L., Malaguti G., 2004, *A&A* , 416, 529

Frank J., King A. R., Lasota J.-P., 1987, *A&A* , 178, 137

Fryer C. L., Kalogera V., 2001, *ApJ* , 554, 548

Fullmer L., Lonsdale C. J., 1989, JPL D-1932, Version 2, part no 3 (1989)

Gao Y., Wang Q. D., Appleton P. N., Lucas R. A., 2003, *ApJL* , 596, L171

Giacconi R., et al., 1979, *ApJ* , 230, 540

Giacconi R., Gursky H., Paolini F. R., Rossi B. B., 1962, *Physical Review Letters*, 9, 439

Giacconi R., Kellogg E., Gorenstein P., Gursky H., Tananbaum H., 1971, *ApJL* , 165, L27+

Giacconi R., Rosati P., Tozzi P., Nonino M., 2001, *ApJ* , 551, 624

Gierliński M., Zdziarski A. A., Poutanen J., Coppi P. S., Ebisawa K., Johnson W. N., 1999, *MNRAS* , 309, 496

- Gilfanov M., Grimm H.-J., Sunyaev R., 2004, *MNRAS* , 347, L57
- Goad M. R., Roberts T. P., Knigge C., Lira P., 2002, *MNRAS* , 335, L67
- Goad M. R., Roberts T. P., Reeves J. N., Uttley P., 2006, *MNRAS* , 365, 191
- Graham J. A., 1982, *ApJ* , 252, 474
- Greenhill L. J., Moran J. M., Herrnstein J. R., 1997, *ApJL* , 481, L23+
- Greiner J., 2000, *New Astronomy*, 5, 137
- Grimm H.-J., Gilfanov M., Sunyaev R., 2003, *MNRAS* , 339, 793
- Guainazzi M., Matt G., Brandt W. N., Antonelli L. A., Barr P., Bassani L., 2000, *A&A* , 356, 463
- Güdel M., 2004, *A&ARv* , 12, 71
- Haardt F., Galli M. R., Treves A., Chiappetti L., Dal Fiume D., Corongiu A., Belloni T., Frontera F., Kuulkers E., Stella L., 2001, *ApJS* , 133, 187
- Haberl F., Pietsch W., 2001, *A&A* , 373, 438
- Hasinger G., Burg R., Giacconi R., Schmidt M., Trumper J., Zamorani G., 1998, *A&A* , 329, 482
- Hasinger G., et al., 2001, *A&A* , 365, L45
- Hatchett S., Buff J., McCray R., 1976, *ApJ* , 206, 847
- Heckman T. M., 2001, in Hibbard J. E., Rupen M., van Gorkom J. H., eds, ASP Conf. Ser. 240: Gas and Galaxy Evolution Galactic Superwinds at Low and High Redshift. pp 345—+
- Heckman T. M., Armus L., Miley G. K., 1990, *ApJS* , 74, 833
- Helfand D. J., 1984, *PASP* , 96, 913
- Henkel C., Whiteoak J. B., Mauersberger R., 1994, *A&A* , 284, 17
- Hesser J. E., Harris H. C., van den Bergh S., Harris G. L. H., 1984, *ApJ* , 276, 491
- Ho L. C., Filippenko A. V., Sargent W. L. W., 1997a, *ApJS* , 112, 315
- Ho L. C., Filippenko A. V., Sargent W. L. W., 1997b, *ApJ* , 487, 568

- Hodge P. W., Kennicutt R. C., 1983, *AJ* , 88, 296
- Hog E., Kuzmin A., Bastian U., Fabricius C., Kuimov K., Lindegren L., Makarov V. V., Roeser S., 1998, *A&A* , 335, L65
- Hornschemeier A. E., Alexander D. M., Bauer F. E., Brandt W. N., Chary R., Conselice C., Grogin N. A., Koekemoer A. M., Mobasher B., Paolillo M., Ravindranath S., Schreier E. J., 2004, *ApJL* , 600, L147
- Hornschemeier A. E., Brandt W. N., Garmire G. P., Schneider D. P., Barger A. J., Broos P. S., Cowie L. L., Townsley L. K., Bautz M. W., Burrows D. N., Chartas G., Feigelson E. D., Griffiths R. E., Lumb D., Nousek J. A., Ramsey L. W., Sargent W. L. W., 2001, *ApJ* , 554, 742
- Hummel E., Dettmar R.-J., Wielebinski R., 1986, *A&A* , 166, 97
- Immler S., Vogler A., Ehle M., Pietsch W., 1999, *A&A* , 352, 415
- Immler S., Wang Q. D., 2001, *ApJ* , 554, 202
- Irwin J. A., Sarazin C. L., Bregman J. N., 2002, *ApJ* , 570, 152
- Iwasawa K., Koyama K., Awaki H., Kunieda H., Makishima K., Tsuru T., Ohashi T., Nakai N., 1993, *ApJ* , 409, 155
- Jansen F., et al., 2001, *A&A* , 365, L1
- Jenkins L. P., Roberts T. P., Warwick R. S., Kilgard R. E., Ward M. J., 2004, *MNRAS* , 349, 404
- Jenkins L. P., Roberts T. P., Warwick R. S., Kilgard R. E., Ward M. J., 2005, *MNRAS* , 357, 401
- Jonker P. G., Nelemans G., 2004, *MNRAS* , 354, 355
- Kaaret P., Corbel S., Prestwich A. H., Zezas A., 2003, *Science*, 299, 365
- Kaaret P., Prestwich A. H., Zezas A., Murray S. S., Kim D.-W., Kilgard R. E., Schlegel E. M., Ward M. J., 2001, *MNRAS* , 321, L29
- Kaaret P., Ward M. J., Zezas A., 2004, *MNRAS* , 351, L83
- Kaastra J. S., Mewe R., 1993, *Legacy*, 3, 16
- Karachentsev I. D., Drozdovsky I. O., 1998, *A&AS* , 131, 1

- Karachentsev I. D., Grebel E. K., Sharina M. E., 2003, *A&A* , 404, 93
- Karachentsev I. D., Karachentseva V. E., Huchtmeier W. K., Makarov D. I., 2004, *AJ* , 127, 2031
- Kellogg E., Baldwin J. R., Koch D., 1975, *ApJ* , 199, 299
- Kilgard R. E., Cowan J. J., Garcia M. R., Kaaret P., Krauss M. I., McDowell J. C., Prestwich A. H., Primini F. A., Stockdale C. J., Trinchieri G., Ward M. J., Zezas A., 2005, *ApJS* , 159, 214
- Kilgard R. E., Kaaret P., Krauss M. I., Prestwich A. H., Raley M. T., Zezas A., 2002, *ApJ* , 573, 138
- Kim D.-W., Fabbiano G., 2003, *ApJ* , 586, 826
- King A. R., 2003, preprint (astro-ph/0301118)
- King A. R., 2004, *MNRAS* , 347, L18
- King A. R., Davies M. B., Ward M. J., Fabbiano G., Elvis M., 2001, *ApJL* , 552, L109
- King A. R., Dehnen W., 2005, *MNRAS* , 357, 275
- King A. R., Pounds K. A., 2003, *MNRAS* , 345, 657
- Kirsch M. G., et al., 2005, in Siegmund O. H. W., ed., *UV, X-Ray, and Gamma-Ray Space Instrumentation for Astronomy XIV*. Edited by Siegmund, Oswald H. W. *Proceedings of the SPIE*, Volume 5898, pp. 224-235 (2005). Health and cleanliness of the XMM-Newton science payload since launch. pp 224–235
- Kiszkurno-Koziej E., 1988, *A&A* , 196, 26
- Kitamoto S., Miyamoto S., Tanaka Y., Ohashi T., Kondo Y., Tawara Y., Nakagawa M., 1984, *PASJ* , 36, 731
- Kong A. K. H., Garcia M. R., Primini F. A., Murray S. S., Di Stefano R., McClintock J. E., 2002, *ApJ* , 577, 738
- Körding E., Colbert E., Falcke H., 2005, *A&A* , 436, 427
- Körding E., Falcke H., Markoff S., 2002, *A&A* , 382, L13
- Körding E., Falcke H., Markoff S., Fender R., 2001, in Schielicke E. R., ed., *Astronomische Gesellschaft Meeting Abstracts Population X - Are the Super-Eddington Sources just Beamed Jets?*. pp 176–+

- Krauss M. I., Kilgard R. E., Garcia M. R., Roberts T. P., Prestwich A. H., 2005, *ApJ* , 630, 228
- Krolik J. H., 2004, *ApJ* , 615, 383
- Kubota A., Done C., 2004, *MNRAS* , 353, 980
- Kuntz K. D., Gruendl R. A., Chu Y.-H., Chen C.-H. R., Still M., Mukai K., Mushotzky R. F., 2005, *ApJL* , 620, L31
- Kuntz K. D., Snowden S. L., Pence W. D., Mukai K., 2003, *ApJ* , 588, 264
- Kuulkers E., in't Zand J. J. M., Cornelisse R., Heise J., Kong A. K. H., Charles P. A., Bazzano A., Cocchi M., Natalucci L., Ubertini P., 2000, *A&A*, 358, 993
- Kuulkers E., Wijnands R., Belloni T., Mendez M., van der Klis M., van Paradijs J., 1998a, in *The Active X-ray Sky: Results from BeppoSAX and RXTE Absorption Dips in GRO J1655+40: Mapping the Inner Accretion Disk*. pp 324+
- Kuulkers E., Wijnands R., Belloni T., Mendez M., van der Klis M., van Paradijs J., 1998b, *ApJ* , 494, 753
- La Parola V., Damiani F., Fabbiano G., Peres G., 2003, *ApJ* , 583, 758
- Lauberts A., 1982, *ESO/Uppsala survey of the ESO(B) atlas*. Garching: European Southern Observatory (ESO), 1982
- Levenson N. A., Weaver K. A., Heckman T. M., 2001, *ApJ* , 550, 230
- Lewin W., Joss P., 1983, *TITLE*. In *Accretion Driven Stellar X-ray Sources*, Edited by Walter Lewin and Edward P. J. van den Heuvel, pp. 41 Cambridge, UK: Cambridge University Press, 1983.
- Liller W., Alcaïno G., 1983, *ApJ* , 264, 53
- Lira P., Lawrence A., Johnson R. A., 2000, *MNRAS* , 319, 17
- Liu J.-F., Bregman J. N., 2005, *ApJS* , 157, 59
- Liu J.-F., Bregman J. N., Seitzer P., 2002, *ApJL* , 580, L31
- Liu J.-F., Bregman J. N., Seitzer P., 2004, *ApJ* , 602, 249
- Long K. S., Dodorico S., Charles P. A., Dopita M. A., 1981, *ApJL* , 246, L61

- Lynden-Bell D., 1969, *Nature* , 223, 690
- Maddox S. J., Efstathiou G., Sutherland W. J., Loveday J., 1990, *MNRAS* , 243, 692
- Madejski G., Życki P., Done C., Valinia A., Blanco P., Rothschild R., Turek B., 2000, *ApJL* , 535, L87
- Makishima K., Kubota A., Mizuno T., Ohnishi T., Tashiro M., Aruga Y., Asai K., Dotani T., Mitsuda K., Ueda Y., Uno S., Yamaoka K., Ebisawa K., Kohmura Y., Okada K., 2000, *ApJ* , 535, 632
- Makishima K., Maejima Y., Mitsuda K., Bradt H. V., 1986, *ApJ* , 308, 635
- Markert T. H., Rallis A. D., 1983, *ApJ* , 275, 571
- Markoff S., Falcke H., Fender R., 2001, *A&A* , 372, L25
- Markoff S., Nowak M. A., Wilms J., 2005, *ApJ* , 635, 1203
- Markowitz A., Edelson R., Vaughan S., Uttley P., George I. M., Griffiths R. E., Kaspi S., Lawrence A., McHardy I., Nandra K., Pounds K., Reeves J., Schurch N., Warwick R., 2003, *ApJ* , 593, 96
- Martocchia A., Matt G., Belloni T., Feroci M., V. K., G. P., 2005, preprint (astro-ph/0510651)
- Matsumoto H., Tsuru T. G., Koyama K., Awaki H., Canizares C. R., Kawai N., Matsushita S., Kawabe R., 2001, *ApJL* , 547, L25
- Mauch T., Murphy T., Buttery H. J., Curran J., Hunstead R. W., Piestrzynski B., Robertson J. G., Sadler E. M., 2003, *MNRAS* , 342, 1117
- Mauersberger R., Henkel C., Whiteoak J. B., Chin Y.-N., Tieftrunk A. R., 1996, *A&A* , 309, 705
- McClintock J., Remillard R., 2006, Black hole binaries. In Compact Stellar X-ray Sources, Edited by Walter Lewin and Michiel van der Klis, pp. 157-214. ISBN-13: 9780521826594, ISBN-10: 0521826594. Cambridge, UK: Cambridge University Press, April 2006.
- McClintock J. E., Haswell C. A., Garcia M. R., Drake J. J., Hynes R. I., Marshall H. L., Muno M. P., Chaty S., Garnavich P. M., Groot P. J., Lewin W. H. G., Mauche C. W., Miller J. M., Pooley G. G., Shrader C. R., Vrtilik S. D., 2001, *ApJ* , 555, 477
- Metzger M. R., et al., 1997a, *IAUCirc*, 6676, 3
- Metzger M. R., et al., 1997b, *Nature* , 387, 878

Mewe R., Kaastra J. S., Liedahl D. A., 1995, *Legacy*, 6, 16

Miller J. M., Fabbiano G., Miller M. C., Fabian A. C., 2003, *ApJL* , 585, L37

Miller J. M., Fabian A. C., Miller M. C., 2004a, *ApJL* , 614, L117

Miller J. M., Fabian A. C., Miller M. C., 2004b, *ApJ* , 607, 931

Miller J. M., Fabian A. C., Wijnands R., Reynolds C. S., Ehle M., Freyberg M. J., van der Klis M., Lewin W. H. G., Sanchez-Fernandez C., Castro-Tirado A. J., 2002, *ApJL* , 570, L69

Miller J. M., Marshall H. L., Wijnands R., Di Matteo T., Fox D. W., Kommers J., Pooley D., Belloni T., Casares J., Charles P. A., Fabian A. C., van der Klis M., Lewin W. H. G., 2003, *MNRAS* , 338, 7

Miller J. M., Raymond J., Fabian A. C., Homan J., Nowak M. A., Wijnands R., van der Klis M., Belloni T., Tomsick J. A., Smith D. M., Charles P. A., Lewin W. H. G., 2004, *ApJ* , 601, 450

Miller M. C., Colbert E. J. M., 2004, *International Journal of Modern Physics D*, 13, 1

Mirabel I. F., Rodríguez L. F., 1999, *ARA&A* , 37, 409

Misra R., Chitnis V. R., Melia F., 1998, *ApJ* , 495, 407

Mitsuda K., Inoue H., Koyama K., Makishima K., 1984, *PASJ* , 36, 741

Miyaji T., Lehmann I., Hasinger G., 2001, *AJ* , 121, 3041

Moorwood A. F. M., van der Werf P. P., Kotilainen J. K., Marconi A., Oliva E., 1996, *A&A* , 308, L1+

Morrison R., McCammon D., 1983, *ApJ* , 270, 119

Mucciarelli P., Casella P., Belloni T., Zampieri L., Ranalli P., 2005, preprint (astro-ph/0509796)

Mushotzky R., 2004, *Progress of Theoretical Physics Supplement*, 155, 27

Mushotzky R. F., Cowie L. L., Barger A. J., Arnaud K. A., 2000, *Nature* , 404, 459

Nayakshin S., Melia F., 1997, *ApJL* , 490, L13+

Olsen K. A. G., Miller B. W., Suntzeff N. B., 2004, *AJ* , 127, 2674

Orosz J. A., Bailyn C. D., 1997, *ApJ* , 477, 876

- Osborne J. P., Borozdin K. N., Trudolyubov S. P., Friedhorsky W. C., Soria R., Shirey R., Hayter C., La
Palombara N., Mason K., Molendi S., Paerels F., Pietsch W., Read A. M., Tiengo A., Watson M. G.,
West R. G., 2001, *A&A* , 378, 800
- Oshima T., Mitsuda K., Ota N., Yamasaki N., 2002, in 8th Asian-Pacific Regional Meeting, Volume II
Chandra Detection of an Extended Emission around the Edge-on Galaxy NGC 55. pp 287–288
- Ott M., Whiteoak J. B., Henkel C., Wielebinski R., 2001, *A&A* , 372, 463
- Otte B., Dettmar R.-J., 1999, *A&A* , 343, 705
- Pakull M. W., Mirioni L., 2002, preprint (astro-ph/0202488)
- Panagia N., 1999, in Chu Y.-H., Suntzeff N., Hesser J., Bohlender D., eds, IAU Symp. 190: New Views
of the Magellanic Clouds Distance to SN 1987 A and the LMC. pp 549–+
- Parmar A. N., White N. E., Giommi P., Gottwald M., 1986, *ApJ* , 308, 199
- Paturel G., Theureau G., Fouqué P., Terry J. N., Musella I., Ekholm T., 2002, *A&A* , 383, 398
- Perryman M. A. C., Lindegren L., Kovalevsky J., 1997, *A&A* , 323, L49
- Pietsch W., Fliri J., Freyberg M. J., Greiner J., Haberl F., Riffeser A., Sala G., 2005, *A&A* , 442, 879
- Pietsch W., Freyberg M., Haberl F., 2005, *A&A* , 434, 483
- Pietsch W., Haberl F., Vogler A., 2003, *A&A* , 402, 457
- Pietsch W., Mochejska B. J., Misanovic Z., Haberl F., Ehle M., Trinchieri G., 2004, *A&A* , 413, 879
- Pietsch W., Roberts T. P., Sako M., Freyberg M. J., Read A. M., Borozdin K. N., Branduardi-Raymont
G., Cappi M., Ehle M., Ferrando P., Kahn S. M., Ponman T. J., Ptak A., Shirey R. E., Ward M., 2001,
A&A , 365, L174
- Portegies Zwart S. F., Baumgardt H., Hut P., Makino J., McMillan S. L. W., 2004, *Nature* , 428, 724
- Pounds K. A., Nandra K., Stewart G. C., Leighly K., 1989, *MNRAS* , 240, 769
- Pounds K. A., Reeves J. N., King A. R., Page K. L., O’Brien P. T., Turner M. J. L., 2003, *MNRAS* ,
345, 705
- Prestwich A. H., Irwin J. A., Kilgard R. E., 2003, *ApJ* , 595, 719

- Pritchett C. J., Schade D., Richer H. B., Crabtree D., Yee H. K. C., 1987, *ApJ* , 323, 79
- Protassov R., van Dyk D. A., Connors A., Kashyap V. L., Siemiginowska A., 2002, *ApJ* , 571, 545
- Psaltis J., Remillard R., 2006, Accreting neutron stars and black holes: a decade of discovery. In *Compact Stellar X-ray Sources*, Edited by Walter Lewin and Michiel van der Klis, pp. 1-38. ISBN-13: 9780521826594, ISBN-10: 0521826594. Cambridge, UK: Cambridge University Press, April 2006.
- Radecke H.-D., 1997, *A&A* , 319, 18
- Ramsey C. J., Williams R. M., Gruendl R. A., Chen C.-H. R., Chu Y.-H., Wang Q. D., 2006, preprint (astro-ph/0511540)
- Ranalli P., Comastri A., Setti G., 2003, *A&A* , 399, 39
- Rappaport S., Di Stefano R., Smith J. D., 1994, *ApJ* , 426, 692
- Read A. M., Ponman T. J., Strickland D. K., 1997, *MNRAS* , 286, 626
- Read A. M., Stevens I. R., 2002, *MNRAS* , 335, L36
- Roberts T. P., 1997, PhD thesis
- Roberts T. P., Colbert E. J. M., 2003, *MNRAS* , 341, L49
- Roberts T. P., Goad M. R., Ward M. J., Warwick R. S., O'Brien P. T., Lira P., Hands A. D. P., 2001, *MNRAS* , 325, L7
- Roberts T. P., Warwick R. S., 2000, *MNRAS* , 315, 98
- Roberts T. P., Warwick R. S., Ward M. J., Goad M. R., 2004, *MNRAS* , 349, 1193
- Roberts T. P., Warwick R. S., Ward M. J., Goad M. R., Jenkins L. P., 2005, *MNRAS* , 357, 1363
- Roberts T. P., Warwick R. S., Ward M. J., Murray S. S., 2002, *MNRAS* , 337, 677
- Robinson B. J., van Damme K. J., 1966, *Australian Journal of Physics*, 19, 111
- Sarazin C. L., Irwin J. A., Bregman J. N., 2001, *ApJ* , 556, 533
- Sasaki M., Haberl F., Pietsch W., 2002, *A&A* , 392, 103

- Schlegel E. M., Barrett P., Singh K. P., 1997, *AJ* , 113, 1296
- Schlegel E. M., Pannuti T. G., 2003, *AJ* , 125, 3025
- Schlegel E. M., Petre R., Colbert E. J. M., Miller S., 2000, *AJ* , 120, 2373
- Schurch N. J., Roberts T. P., Warwick R. S., 2002, *MNRAS* , 335, 241
- Seyfert C. K., 1943, *ApJ* , 97, 28
- Shakura N. I., Sunyaev R. A., 1973, *A&A* , 24, 337
- Shectman S. A., Landy S. D., Oemler A., Tucker D. L., Lin H., Kirshner R. P., Schechter P. L., 1996, *ApJ* , 470, 172
- Shirey R., et al., 2001, *A&A* , 365, L195
- Shrader C. R., Titarchuk L., 2003, *ApJ* , 598, 168
- Snowden S. L., Freyberg M. J., Plucinsky P. P., Schmitt J. H. M. M., Truemper J., Voges W., Edgar R. J., McCammon D., Sanders W. T., 1995, *ApJ* , 454, 643
- Snowden S. L., Pietsch W., 1995, *ApJ* , 452, 627
- Solano E., Garrido R., Fernley J., Barnes T. G., 1997, *A&AS* , 125, 321
- Soria R., Cropper M., Pakull M., Mushotzky R., Wu K., 2005, *MNRAS* , 356, 12
- Soria R., Fender R. P., Hannikainen D. C., Read A. M., Stevens I. R., 2006, *MNRAS* , 368, 1527
- Soria R., Wu K., 2002, *A&A* , 384, 99
- Stark A. A., Gammie C. F., Wilson R. W., Bally J., 1992, *ApJS* , 79, 77
- Strüder L., et al., 2001, *A&A* , 365, L18
- Strickland D. K., 2004, in IAU Symposium Winds from nuclear Starbursts: Old truths and recent progress on superwinds. pp 249–254
- Strickland D. K., Colbert E. J. M., Heckman T. M., Weaver K. A., Dahlem M., Stevens I. R., 2001, *ApJ* , 560, 707
- Strickland D. K., Heckman T. M., Colbert E. J. M., Hoopes C. G., Weaver K. A., 2004a, *ApJS* , 151, 193

- Strickland D. K., Heckman T. M., Colbert E. J. M., Hoopes C. G., Weaver K. A., 2004b, *ApJ* , 606, 829
- Strohmayer T. E., Mushotzky R. F., 2003, *ApJL* , 586, L61
- Strohmayer T. E., Zhang W., Swank J. H., Smale A., Titarchuk L., Day C., Lee U., 1996, *ApJL* , 469, L9+
- Summers L. K., Stevens I. R., Strickland D. K., Heckman T. M., 2003, *MNRAS* , 342, 690
- Swartz D. A., Ghosh K. K., Tennant A. F., Wu K., 2004, *ApJS* , 154, 519
- Tüllmann R., Rosa M. R., 2004, *A&A* , 416, 243
- Tüllmann R., Rosa M. R., Elwert T., Bomans D. J., Ferguson A. M. N., Dettmar R.-J., 2003, *The Messenger*, 114, 39
- Tanaka Y., Inoue H., Holt S. S., 1994, *PASJ* , 46, L37
- Tanaka Y., Lewin W. H. G., 1997, *Black-Hole Binaries*. In *X-ray Binaries*, Edited by Walter H. G. Lewin and Jan van Paradijs and Edward P. J. van den Heuvel, pp. 126-174. ISBN 0521599342. Cambridge, UK: Cambridge University Press, January 1997.
- Tanaka Y., Nandra K., Fabian A. C., Inoue H., Otani C., Dotani T., Hayashida K., Iwasawa K., Kii T., Kunieda H., Makino F., Matsuoka M., 1995, *Nature* , 375, 659
- Tanaka Y., Shibazaki N., 1996, *ARA&A* , 34, 607
- Tananbaum H., Gursky H., Kellogg E., Giacconi R., Jones C., 1972, *ApJL* , 177, L5+
- Tauris T. M., van den Heuvel E. P. J., 2006, *Formation and evolution of compact stellar X-ray sources*. In *Compact Stellar X-ray Sources*, Edited by Walter Lewin and Michiel van der Klis, pp. 623-666. ISBN-13: 9780521826594, ISBN-10: 0521826594. Cambridge, UK: Cambridge University Press, April 2006.
- Terashima Y., Inoue H., Wilson A. S., 2006, *ApJ* , 645, 264
- Terashima Y., Wilson A. S., 2004, *ApJ* , 601, 735
- Thronson H. A., Hunter D. A., Telesco C. M., Decher R., Harper D. A., 1987, *ApJ* , 317, 180
- Tikhonov N. A., Galazutdinova O. A., Drozdovsky I. O., 2005, *A&A* , 431, 127

- Trinchieri G., Fabbiano G., Paulumbo G. G. C., 1985, *ApJ* , 290, 96
- Trinchieri G., Fabbiano G., Peres G., 1988, *ApJ* , 325, 531
- Tully R. B., 1988, Nearby galaxies catalog. Cambridge and New York, Cambridge University Press, 1988, 221 p.
- Turner M. J. L., et al., 2001, *A&A* , 365, L27
- Urry C. M., Padovani P., 1995, *PASP* , 107, 803
- Uttley P., McHardy I. M., Papadakis I. E., 2002, *MNRAS* , 332, 231
- Van de Steene G., Jacoby G., Praet C., Ciardullo R., Dejonghe H., 2004, preprint (astro-ph/0407348)
- van den Heuvel E. P. J., Bhattacharya D., Nomoto K., Rappaport S. A., 1992, *A&A* , 262, 97
- van der Klis M., 1994, *ApJS* , 92, 511
- van der Klis M., 1997, Rapid aperiodic variability. In X-ray Binaries, Edited by Walter H. G. Lewin and Jan van Paradijs and Edward P. J. van den Heuvel, pp. 257-307. ISBN 0521599342. Cambridge, UK: Cambridge University Press, January 1997.
- van der Klis M., Swank J. H., Zhang W., Jahoda K., Morgan E. H., Lewin W. H. G., Vaughan B., van Paradijs J., 1996, *ApJL* , 469, L1+
- van Paradijs J., et al., 1997, *Nature* , 386, 686
- van Speybroeck L., Epstein A., Forman W., Giacconi R., Jones C., Liller W., Smarr L., 1979, *ApJL* , 234, L45
- Vaughan S., Iwasawa K., Fabian A. C., Hayashida K., 2005, *MNRAS* , 356, 524
- Vogler A., Pietsch W., 1997, *A&A* , 319, 459
- Vogler A., Pietsch W., Bertoldi F., 1997, *A&A* , 318, 768
- Wang Q., Hamilton T., Helfand D. J., Wu X., 1991, *ApJ* , 374, 475
- Wang Q. D., Walterbos R. A. M., Steakley M. F., Norman C. A., Braun R., 1995, *ApJ* , 439, 176
- Wang Q. D., Yao Y., Fukui W., Zhang S. N., Williams R., 2004, *ApJ* , 609, 113

- Watson M. G., Stanger V., Griffiths R. E., 1984, *ApJ* , 286, 144
- White N., Nagase F., A.N. P., 1997, The properties of X-ray binaries. In X-ray Binaries, Edited by Walter H. G. Lewin and Jan van Paradijs and Edward P. J. van den Heuvel, pp. 1-57. ISBN 0521599342. Cambridge, UK: Cambridge University Press, January 1997.
- White N. E., Carpenter G. F., 1978, *MNRAS* , 183, 11P
- White N. E., Giommi P., Angelini L., 2000, VizieR Online Data Catalog, 9031, 0
- White N. E., Swank J. H., 1982, *ApJL* , 253, L61
- Wijnands R., van der Klis M., 1998, *Nature* , 394, 344
- Willingale R., Hands A. D. P., Warwick R. S., Snowden S. L., Burrows D. N., 2003, *MNRAS* , 343, 995
- Wilms J., Allen A., McCray R., 2000, *ApJ* , 542, 914
- Wilms J., Nowak M. A., Dove J. B., Fender R. P., di Matteo T., 1999, *ApJ* , 522, 460
- Wilms J., Reynolds C. S., Begelman M. C., Reeves J., Molendi S., Staubert R., Kendziorra E., 2001, *MNRAS* , 328, L27
- Wilson A., Xeus Instrument Working Group 2003, X-ray Evolving-Universe Spectroscopy - the XEUS instruments. X-ray Evolving-Universe Spectroscopy - the XEUS instruments / Ed.: Andrew Wilson. ESA SP-1273. Noordwijk, Netherlands: ESA Publications Division, ISBN 92-9092-977-4, 2003, 134 pp.
- Wolter A., Trinchieri G., 2004, *A&A* , 426, 787
- Wood K. S., Meekins J. F., Yentis D. J., Smathers H. W., McNutt D. P., Bleach R. D., Friedman H., Byram E. T., Chubb T. A., Meidav M., 1984, *ApJS* , 56, 507
- Zampieri L., Mucciarelli P., Falomo R., Kaaret P., Di Stefano R., Turolla R., Chierigato M., Treves A., 2004, *ApJ* , 603, 523
- Zdziarski A. A., Grove J. E., Poutanen J., Rao A. R., Vadawale S. V., 2001, *ApJL* , 554, L45
- Zezas A., Fabbiano G., Prestwich A., Murray S., Ward M., 2001, in Knapen J. H., Beckman J. E., Shlosman I., Mahoney T. J., eds, ASP Conf. Ser. 249: The Central Kiloparsec of Starbursts and AGN: The La Palma Connection Chandra Observations of the Stellar Populations and Diffuse Gas in Nearby Galaxies. pp 425—

Zezas A., Fabbiano G., Rots A. H., Murray S. S., 2002a, *ApJS* , 142, 239

Zezas A., Fabbiano G., Rots A. H., Murray S. S., 2002b, *ApJ* , 577, 710

Zhang S. N., Cui W., Chen W., Yao Y., Zhang X., Sun X., Wu X.-B., Xu H., 2000, *Science*, 287, 1239